DEEP SUBMARINE SILICIC VOLCANISM: CONDUIT AND ERUPTIVE DYNAMICS OF THE 2012 HAVRE ERUPTION

A DISSERTATION SUBMITTED TO THE GRADUATE DIVISION OF THE UNIVERSITY OF HAWAIʻI AT MĀNOA IN PARTIAL FULFILLMENT OF THE REQUIREMENTS FOR THE DEGREE OF

DOCTOR OF PHILOSOPHY

IN

GEOLOGY AND GEOPHYSICS

December 2018

By

Samuel Johnston Mitchell

Dissertation Committee:

Bruce F. Houghton, Chairperson
Rebecca J. Carey
Thomas Shea
Sarah A. Fagents
Michael J. Mottl

"The sea is everything. It covers seven tenths of the terrestrial globe. Its breath is pure and healthy. It is an immense desert, where man is never lonely, for he feels life stirring on all sides. The sea is only the embodiment of a supernatural and wonderful existence. It is nothing but love and emotion; it is the Living Infinite."

— *Jules Verne*,
Twenty Thousand Leagues Under the Sea

ACKNOWLEDGMENTS

The work within this dissertation reflects the dedication, and combined efforts and collaborations of members of the Havre research group. I want to begin by thanking all of those who contributed in some way to the work presented herein, and to those whose valuable collaborations have enabled me to produce science beyond my original scope and anticipation. I owe a particular debt of gratitude to Iona McIntosh and Michael Manga, whose expertise, guidance, intrigue and insights have helped me to broaden my skillset, and pushed me to explore science outside of my initial focus; your collaborations have become central to this work. Thank you to Kristen, Tom, Meghan, Adam, Chris, Thomas G and Zihan who have all provided constructive and useful critique throughout manuscript preparations, interesting discussions and thoughts, and unsolicited support that has moved our science forward significantly; I look forward to future collaborations. Thank you also to my committee; your continued interest in the project, thoroughness in review, and constructive critique and feedback have helped bind these projects together; mahalo for your guidance on this journey.

The volume of data acquired would not have been possible without those who have assisted me in the lab throughout the past three years through the processing of countless pumice clasts and BSE images. So thank you Zach, Warren, Caroline, Wendy and Hannah for your time and endless effort, I will always be very grateful for your input and hard work. Thank you to the faculty, laboratory managers and staff, peers, and instrument technicians who have assisted and instructed me on analytical equipment, techniques and software through the years: Eric, Julia, Brian M, Kazu, Gary, Murli, Maria, Samantha, Val, Seb, Emily and Benoit. Thank you Eleanor for offering to complete the arduous task of collecting, wrapping and shipping raft pumice from Fiji to Hawai′i; our dataset is enriched because of your efforts. I also want to give a warm mahalo to JoAnn Sinton who can polish thin sections like no else! Thank you for tackling an unworldly number of thin sections for me, your work is phenomenal, and I will truly miss your generosity and our extended lab chats.

None of this work would have been possible without the remarkable science party, ROV and AUV technicians, and crew of the 2015 MESH expedition. I am so proud of what we have achieved so far, and I look forward to seeing where our research takes us next. Thank you for spoiling me

rotten for my first science-at-sea experience, I know it will certainly not be my last. In truth, it is likely that none of this research would have even initiated without the keen eyes of Maggie de Grauw, who first documented the 2012 Havre pumice raft in a chance viewing out of a plane window; we are forever in your debt!

My time here in Hawai′i has been made truly unforgettable due to the friendships and camaraderie of many. Thank you to my incredible officemates throughout the years, the magma chamber support group, the GG grad family and all of those within SOEST, GSO and outside of work who have given me three years well worth remembering. Thank you to our amazing department adminstrators Connie, Susan, Lily, Alison and Arlene for helping me keep my life together and for making GG a wonderful place to work. Thank you to my DHT ′ohana for being my rock this past year, you stuck with me, challenged me, and yet supported me through every second, I will be forever grateful for your time and friendship. My family have always been my greatest fan club and I am continually thankful for your love, belief and unwavering support of my endless endeavors. You may be 7000 miles away, but you have been here for every step. Thank you.

Finally, I owe my time here to Bruce and Rebecca, whose fierce guidance, incredible mentorship, editorial skills and inspiring scientific intrigue have made this experience everything that I could have wanted out of a PhD. You have pushed me far beyond what I expected of myself, guided me swiftly through a challenging project, and continued to stoke my interest in volcanology. Thank you for opening my eyes to the fascinating submarine realm, taking a chance on me, and for giving me an opportunity that I once believed was far out of my reach. I am incredibly grateful to you both for allowing me to explore additional scientific interests and develop my independence of thought as a multidisciplinary researcher. Your unsolicited generosity as advisors and sincere passion for discovery, research and innovation continue to inspire me, and I look forward to pursuing many more science questions with you both in the years to come. Mahalo nui loa.

ABSTRACT

The eruption of the submarine Havre volcano, Kermadec Ridge, New Zealand, in July 2012 was the largest documented silicic submarine eruption for the past 360 years. This event was equivalent in eruptive volume to the May 18 1980 Mt. St Helens subaerial explosive eruption. This deep submarine volcanic system (650 – 1500 meters below sea level) produced an eruption with a resultant broad range of eruptive deposits including: 15 lava flows and domes, a 1.2 km^3 floating pumice raft, and a series of seafloor clastic deposits including a bed of giant (>1 m diameter) pumice blocks that was dispersed kilometers away from the inferred source.

Deep submarine volcanic eruptions rarely breach the ocean surface, and go mostly undetected until exploration of the seafloor via submersible. The pumice raft observations during the 2012 Havre eruption presented the opportunity to study fresh deposits from a recent, voluminous, deep submarine silicic eruption. An expedition to Havre in 2015 observed a range of volcanic products, conducted geological investigations, and collected samples to understand pre-eruptive magma conditions, eruption dynamics, and mechanisms of clast transportation and deposition in seawater.

This dissertation addresses a wide range of research themes regarding the dynamics of the 2012 Havre eruption, in particular focusing on the clastic, pumiceous units found on the seafloor and at the ocean's surface. Using a number of seafloor observations, analytical methods, and computational modelling, we assess the textures, volatile contents and geochemistry of pumice over meter- to micron-scales to answer outstanding yet fundamental questions within the field of submarine volcanology. By considering the effects of overlying hydrostatic pressure on the Havre volcanic system and the thermophysical properties of the surrounding seawater, we investigate the magmatic conditions and address physical and chemical processes driving the submarine eruptive environment. This detailed assessment of the 2012 Havre eruption gives not only an insight into eruptive mechanisms and processes at deep-sea silicic volcanic centers, but also an opportunity to apply knowledge to eruptions on land or in environments of variable pressure.

TABLE OF CONTENTS

LIST OF TABLES

LIST OF FIGURES

LIST OF ABBREVIATIONS AND SYMBOLS

a	Primary major axis of the best-fit ellipse of a vesicle
A	Absorbance of the glass (Chapter 2)
A	Vesicle area observed in 2D (Chapter 3)
$\bar{A}$	Normalized absorbance of the glass (A/d)
A_C	Convex area of a vesicle
AL	Ash and fine-lapilli unit
ALB	Ash-lapilli-block unit
AR	Vesicle (bubble) aspect ratio (major/minor)
AUS	Raft pumice samples collected from the shores of New South Wales
AUV	Autonomous underwater vehicle
Band	Banded pumice
BSE	Backscattered electron (referred to for BSE images)
c	Speed of light (Chapter 2)
c	Vesicle connectivity (Chapters 3 and 4)
cN_A	Cristobalite number density per area
C	Concentration (wt. %)
C_1	Weight % of H_2O_m
C_{OH}	Weight % of OH
C_W	Weight % of H_2O_t
Ca	Capillary number
CT	Computed tomography
d	Glass shard/wafer thickness
dP/dt	Magma decompression rate
dP/dz	Pressure gradient in the z direction

D	Diffusivity coefficient
D_{Ai}	Observed diameter of vesicles in 2D
D_{ch}	Characteristic diffusivity coefficient
D_f	Feret's vesicle diameter
D_{H2O}	Diffusivity coefficient of H_2O
D_Mod2D	Modal vesicle spherical diameter prior to stereo-conversion
D_Mod3D (D_{3V})	Modal vesicle spherical diameter after stereo-conversion
D_Nv3D	Middle spherical diameter of modal vesicle number density bin
DB	Dome talus and autobreccia deposit (subunit of Dome)
Dome	Dome OP samples (talus + carapace)
DRE	Dense rock equivalent density (ρ)
EPMA	Electron probe microanalyzer
EqD	The equivalent spherical-volume or circular-area diameter of a vesicle
FJ	Raft pumice samples collected from the shores of Fiji
FPA	Focal-plane array
FTIR	Fourier transform infrared (spectroscopy)
g	Subscript (gas phase)
GP	Giant pumice block unit
GP290	Banded giant pumice block with sample name HVR_290
GPI	Giant pumice interior
GPX	Giant pumice exterior
h	Planck's constant
H	Projected mean vesicle height (Chapter 3)
H	Higher density value from density distribution (Chapter 4)
HVR	Havre sample number from the 2015 MESH expedition
i	Position along diffusion profile length (Chapter 2)

i	Number of classes analyzed within stereo-conversion (Chapter 3)
I	Corrected light intensity at a particular wavenumber
I_R	Raw intensity of light from scattered μRaman laser beam
IR	Infrared (wavelength of light)
IGSN	International geo sample number
j	Position through time for the diffusion profile (Chapter 2)
j	Chosen class number within stereo-conversion (Chapter 3)
JAMSTEC	Japanese Agency for Marine Science and Technology
k	Boltzmann constant (Chapter 2)
k_1	Darcian permeability
k_2	Inertial permeability
K_{ae}	Equilibrium constant of apparent speciation equilibrium
K_{eq}	Equilibrium constant of speciation interconversion
$_l$	Subscript (melt phase)
L	Half-fall distance within a vesicle edge profile (Chapter 2)
L	Core length (Chapter 3)
L	Lower density value from density distribution (Chapter 4)
L	Mid-size value of vesicle diameter per size bin
LGL	Lava-G-lapilli unit
LOI	Loss on ignition from XRF analysis
m	Number of interference fringes counted in FTIR spectra analysis
mbsl	Meters below sea level
mN	Number of microlites counted per crystal phase
mN_A	Microlite number density per unit area
mN_{Am}	Corrected microlite number density per unit area
M	Molar mass (Chapter 2)

M	Modal density value from density distribution (Chapter 4)
MER	Mass eruption rate
MESH	Mapping, exploration and sampling at Havre (2015 expedition)
MODIS	Moderate Resolution Imaging Spectroradiometer
MI	Melt inclusion
n	Refractive index of glass
N_A	Vesicle number density per unit area
N_{rim}	Northern caldera rim lapilli samples
N_V	Vesicle number density per unit volume
N_{Vm}	Corrected vesicle number density per unit volume
NASA	National Aeronautics and Space Administration
O^0	Bridging oxygen atoms within the silicate structure
pxl	Pixels
P	Pressure
P_i	Probability of vesicle intersection (Chapter 3)
P_Q	Quenching pressure
r	Distance from the conduit center
R^2	Coefficient of determination
R_C	Conduit radius
R/V	Research vessel
RP	Pumice raft unit
Re	Reynolds number
ROV	Remotely operated vehicle
RSD	Mean-relative standard deviation
s	Saturation volume proportion of the connected porosity
SD (σ)	Standard deviation

SIMS	Secondary ion mass spectrometry
t	Set rehydration time within diffusion model
T	Temperature
T_{ae}	Apparent equilibrium temperature
T_g	Glass transition temperature
TC	Sub-unit of ALB containing denser tube pumice
TP	Taupo (1.8 ka eruption)
u	Magma ascent velocity
u_l	Melt ascent velocity
U	Flow rate of gas through pumice for capillary flow porometry
vesic. (Ves)	Vesicularity (%) – same as ϕ and $\emptyset$
V_g	Volume gas fraction
V_H	Volume of a sphere with projected mean height H
V_i	Volume fraction of each class within the stereo-conversion
V_l	Volume glass (melt + crystal) fraction
VB	Vapor bubble
VEI	Volcanic explosivity index
VSD	Vesicle size distribution
VVD	Vesicle volume distribution
wt. %	Weight percentage (element concentration)
W	Weight of the dry melt per mole of oxygen assuming Fe is ferrous
WHOI	Woods Hole Oceanographic Institution
x_b	Bubble size in the conduit
XRF	X-ray fluorescence
(μ)XRT	X-ray (micro)tomography
z	Depth within the conduit / depth step

α	Alpha conversion coefficient for stereo-conversion
γ	Conduit strain
$\dot{\gamma}$	Magma strain rate
γ_t	Cumulative conduit strain
ΔP	Pressure differential
$\Delta\tau$	Duration of each diffusion profile time step
Δx	Spacing along diffusion profile
ε_e	Molar absorptivity coefficient (e = wavenumber / peak of interest)
μ	Viscosity of magma
μ_g	Viscosity of air
µRaman	MicroRaman (spectroscopy)
ν	Wavenumber
ν_1	Highest wavenumber of the selected range for thickness calculation
ν_2	Lowest wavenumber of the selected range for thickness calculation
ν_l	Wavenumber of incident light from microRaman laser
ρ	Density of glass (Chapter 2)
ρ_g	Density of air
σ	Bubble surface tension
Σ_{RMS}	Sum of the root mean square residuals
τ_{max}	Maximum timescale for rehydration to occur
ϕ_c	Connected porosity
ϕ_i	Isolated porosity
ϕ_t (ϕ, $\emptyset$)	Total porosity (whole clast vesicularity)

1. INTRODUCTION

1.1. Dissertation overview and outline

This dissertation analyzes volcanic products of the 2012 eruption of the submarine Havre volcano to further our understanding of deep submarine silicic volcanic eruptions and the role of hydrostatic pressure on eruptive styles. The 2012 Havre eruption is the largest deep-submarine silicic eruption recorded in modern history. The eruption produced a variety of effusive and clastic products on the volcano in addition to the pumice raft produced during July 18-19, 2012. The stratigraphic relationships of eruptive products on the seafloor, observations of the pumice raft, and calculations of the raft's volume and duration, provide one of the best-known chances to study the fundamental controls on deep-submarine silicic conduit and eruptive dynamics, and processes that affect magma and pumice in seawater.

This first chapter provides the geologic setting and background for the submarine 2012 Havre eruption, outlining the findings and interpretations from exploration in 2015 and subsequent published papers. This chapter also presents the motivation behind the broader dissertation topic and then specific aims of each research project included. I address the importance of the field of submarine volcanism, and the fundamental physical volcanology required to understand the proceeding chapters.

Chapter 2 assesses the water contents within matrix glass from all the major 2012 clastic units to address clast quenching depths and cooling rates, the presence and dynamics of a large submarine plume, and the unexpectedly-rapid rehydration within Havre pumice. Chapter 3 analyzes the microtextures and geochemistry of the giant pumice phase of the 2012 eruption and the shallow conduit conditions and post-eruptive processes that produced this deposit. Chapter 4 applies approaches similar to Chapter 3, but for all other clastic units of the 2012 eruption to assess stratigraphic and textural relationships. This textural analysis is coupled with measurements of volatile content from melt inclusions and matrix glasses to assess the degassing history of magma from storage to the main 900-meter deep vent on the seafloor. Chapter 5 summarizes the overall findings, and addresses how I have satisfied the aims established in Chapter 1. The dissertation

concludes by exploring the impact of this work on the broader scientific community and avenues of further research within the Havre project and projects applicable across submarine volcanology.

1.2. Havre volcano

Havre volcano is a large submarine caldera 780 km NE of Auckland, New Zealand along the Kermadec Arc in the Southwest Pacific, situated 30 km behind the forearc ridge (**Figure 1.1a**) (Wright et al., 2006a; Carey et al., 2014). The caldera was first mapped in 2002 by Wright et al. (2006a) who identified a volcano with a 25 km basal diameter, a basal depth of 1750 m, a 720 m deep summit cone, a 5 x 4 km wide caldera with caldera rims averaging 900 – 1000 m deep and a maximum depth of 1520 m; they estimated a total constructional volume of ~91 km^3.

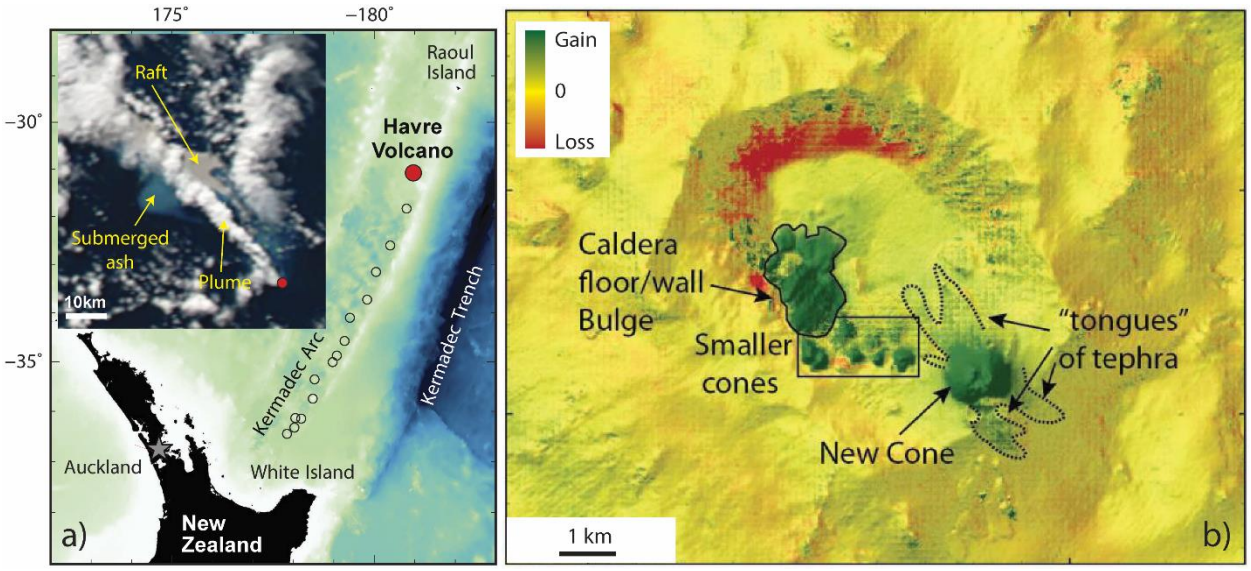

Figure 1.1. a) Location of Havre Volcano along the Kermadec Arc north east of New Zealand from Carey et al. (2018) and elevation difference between 2002 and October 2012 bathymetry of the Havre caldera (Havre NSF proposal). The inset shows the ocean surface raft and subaerial plume from the identified point source. b) Main "elevation gain" features identified possible new features from the July 2012 eruption albeit with poor spatial resolution.

Rocks collected with dredges from the summit of Havre volcano were geochemically analyzed by Wright et al. (2006a). Rocks range from altered pumice to aphyric lava flows with compositions ranging from 52 – 71 wt. % SiO_2. The range of compositions at Havre is typical for a large caldera system along a subduction zone forearc (Ewart et al., 1977; Wright and Gamble, 1999). The composition of dacite and rhyodacite lavas and pumice on the flanks and from the caldera walls of Havre match closely with the higher silica compositions of other large Kermadec calderas (Wright et al., 2006a; Barker et al., 2012a; Rotella et al., 2015). Pumices collected from the flanks of Havre volcano in 2002 were possible evidence of historic, and possibly recent, silicic explosive eruptions at Havre. However prior to 2012, no eruption had ever been physically documented or dated from the Havre system, as is the case with many remote, deep submarine calderas.

1.2.1. Discovery of the 2012 eruption

On July 31, 2012, a passenger aboard a flight from Samoa to Auckland, New Zealand, noted the presence of a "peculiar, large mass floating on the ocean between Tonga and New Zealand" (Carey et al., 2014). Analysis of MODIS images (NASA's Moderate Resolution Imaging Spectrometer) throughout July around the identified location, located the source of a pumice raft (**Figure 1.1a**). July 18-19 images showed a coherent pumice raft and a subaerial plume from a point source with a 30° thermal anomaly (Carey et al., 2014; Jutzeler et al., 2014). The location of the point source corresponded to the Havre volcano (**Figure 1.1a**). Images of this timeframe were used to calculate the duration of pumice raft production – when it was still connected to the point source – of ~21 hours (Carey et al., 2014). This duration and an estimated 1.2 km^3 raft volume led to mass eruption rate (MER) calculations of ~10^7 kg s^{-1}. The volume and intensity of this eruption is comparable to moderately large VEI-5 subaerial explosive eruptions, such as the May 1980 Mt. St. Helens eruption and 2008 Chaitén, Chile eruption (Rutherford and Hill, 1993; Alfano et al., 2011; Carey et al., 2014; Jutzeler et al., 2014).

A research expedition in October 2012 acquired ship-based multibeam bathymetry of the Havre caldera allowing a comparison between 2002 and post-eruptive 2012 bathymetry (**Figure 1.1b**) (Carey et al., 2014). The bathymetry revealed several major new features present at Havre: 1) a large cone-shaped feature on the SE caldera rim 250 m high and 1.2 km wide; 2) a linear field

of small cone-shaped features up to 100 m high on the S caldera rim; 3) a large bulge on the SW caldera floor and walls; 4) several 'tongues' that extended out from the SE cone; and 5) loss of material along the N and E caldera walls (**Figure 1.1b**) (Carey et al., 2014). The volumes of the identified submarine features increased the estimated total erupted volume to 1.5 – 2 km^3. Seafloor dredges collected during the late 2012 expedition sampled white and grey pumice deposits and denser rocks from inside the Havre caldera with 71 – 73 wt. % SiO_2 – similar to the range identified by Wright et al. (2006a). However, without *in situ* submarine exploration, the interpretations of these features and dredge samples were speculative and motivated a specific expedition to assess the seafloor products of the 2012 Havre eruption.

1.2.2. MESH expedition 2015

In March 2015, a team of 17 scientists and students from seven institutions spent 21 days at the Havre caldera aboard the R/V *Roger Revelle* to undertake the Mapping, Exploration and Sampling at Havre expedition (MESH). The ROV *Jason* (remotely operated vehicle) and AUV *Sentry* (autonomous underwater vehicle) were used to map the post-2012-eruption caldera and observe and sample the 2012 eruption products (**Figure 1.2**). An initial ship-based multibeam scan of the entire caldera identified no significant change to the bathymetry between 15 October 2012 and 30 March 2015 (Carey et al., 2018).

The high spatial resolution (1 m) bathymetry collected by AUV throughout the expedition showed features with morphologies akin to effusive dome growth and lava flow features seen in subaerial settings, rather than "cones" (**Figure 1.2;** Tuffen et al., 2013; Embley and Rubin, 2018; Magnall, 2018). Ship-based backscatter overlain with the bathymetry identified an elliptical region of significant scattering (roughness) across the caldera and caldera floor that extended NW out of the surveyed region (**Figure 1.3**). The southern end of the rough ellipse terminates one km SE of the largest dome. This region also corresponds to a rough terrain observed in high resolution AUV data (**Figure 1.3**). The same two datasets also identified "tongues" of smooth material that extended up to one km from the largest dome (**Figure 1.3**; Carey et al., 2014). A total of 290 samples was collected using the ROV manipulator to collect large fragments, and scoops, push

cores and a vacuum to collect finer clastic samples (**Figure 1.2**). Deposits from 2012, and several pre-2012 samples, were collected from the caldera floor and rim, and from the caldera walls.

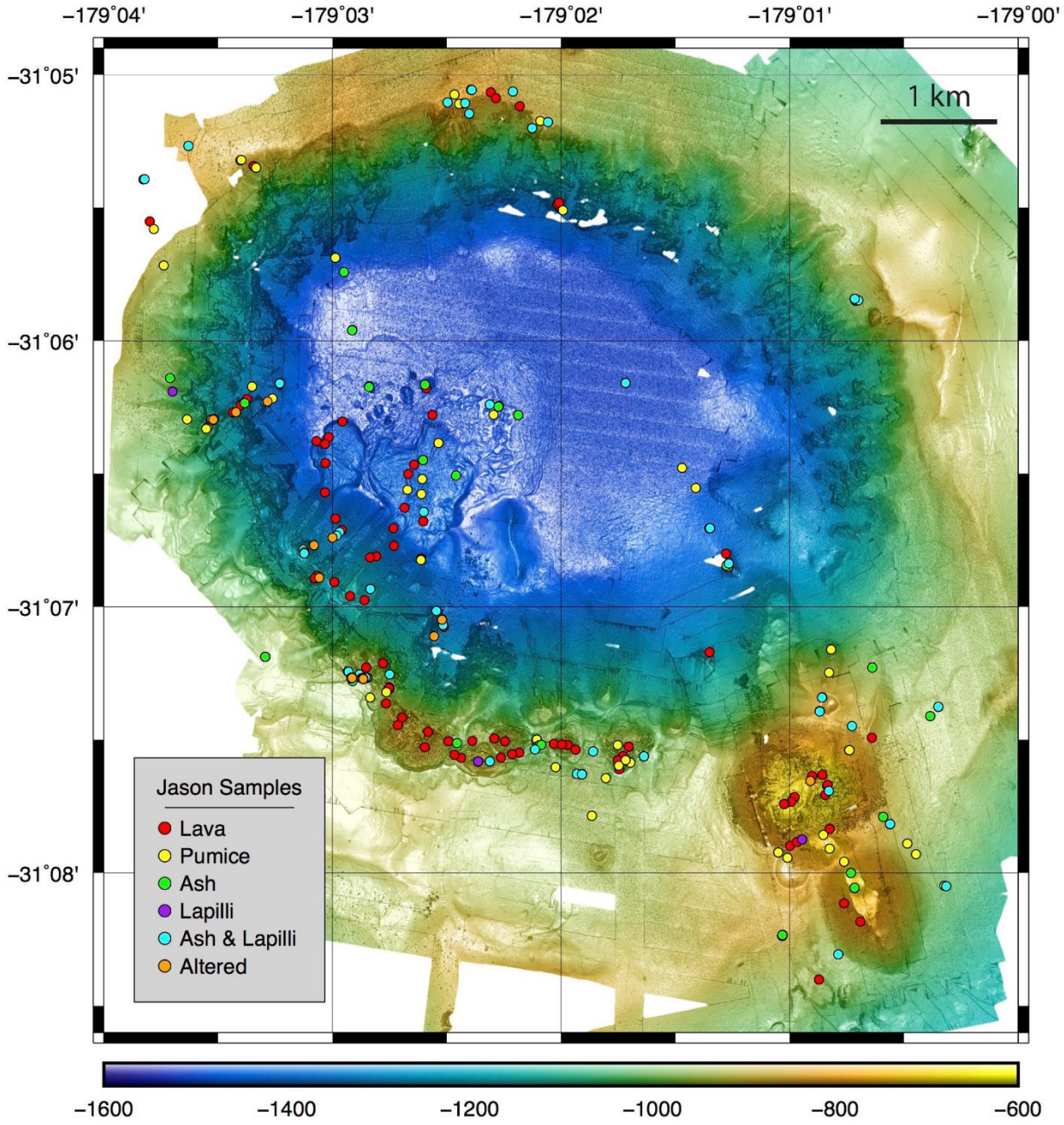

Figure 1.2. Distribution of samples collected by the ROV *Jason* during the 2015 MESH expedition at the Havre caldera. Sample locations overlain over the obtained AUV *Sentry* map (MESH cruise report, 2015).

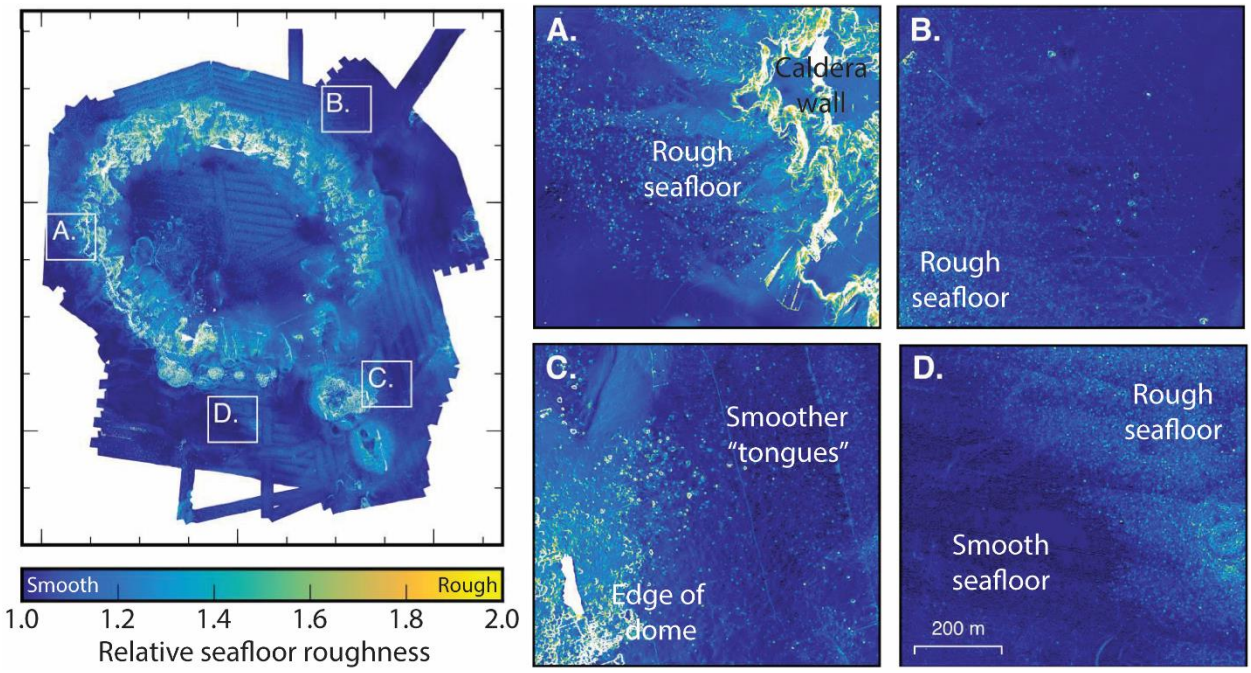

Figure 1.3. Backscattered roughness of the seafloor overlain over the AUV bathymetry data given as a relative scale of roughness (adapted from Carey et al. 2018 (supplement)). Insets A-D identity areas of relatively smooth and rough seafloor at 1 m spatial resolution; steep caldera walls display the highest roughness.

1.2.2.1. Lava flows and lava domes

Volumetrically, the majority of 2012-erupted material preserved on the seafloor consisted of rhyolite (70 – 72 wt. % SiO_2) lava flows and domes (~ 0.21 km^3) (**Figure 1.4**; **Table 1.1**; Carey et al., 2018). Five lava flows (A-E) were erupted from vents at depths of 1280 – 1140 m on the SW caldera walls and flowed into the caldera (**Figure 1.4**). Lava flows A and C were the most voluminous (0.009 and 0.034 km^3 respectively), with thicknesses of up to 30 m, high aspect ratios and lengths of >1 km from their vents (Ikegami et al., 2018). Lava flows A-E (and F) make up the 'bulge' present in 2012 low-resolution bathymetry (**Figure 1.1b**). Lava flows A-E have 70.6 – 71.0 wt. % SiO_2 and loss on ignition (LOI) values of 1.3 – 1.6 wt. %; i.e., the amount of volatiles lost on heating samples during X-ray fluorescence (XRF) analysis (**Table 1.1;** Carey et al., 2018).

Table 1.1. Bulk volumes and SiO_2 content of lava flows and domes, and the pumice raft and giant pumice block deposits (Carey et al., 2018). LOI is the loss on ignition volatile mass released during X-ray fluorescence (XRF) analysis. } represents the total calculated volume of two combined lavas. *data from Rotella et al., 2015.

Unit/deposit	Volume ($\times 10^6$ m^3)	SiO_2 (wt. %)	L.O.I. (wt. %)
Lava flow A	8.9	70.66	1.62
Lava flow B	2.8	No data	No data
Lava flow C	34	70.89	1.53
Lava flow D	}8.2	70.95	1.31
Lava flow E		70.67	1.48
Lava flow F	26	70.92	1.48
Lava flow G	0.4	71.72	0.43
Lava dome H	}10.6	71.95	0.65
Lava dome I		71.95	1.42
Lava dome K	2.3	71.97	1.22
Lava dome L	1.7	71.86	1.79
Lava dome M	}5.9	72.01	1.32
Lava dome N		71.89	1.64
Lava dome O	}109.9	72.20	0.59
Lava dome P		72.21	0.41
Pumice raft	>1,200	72.11*	1.08*
Giant pumice	>100	71.92	1.27

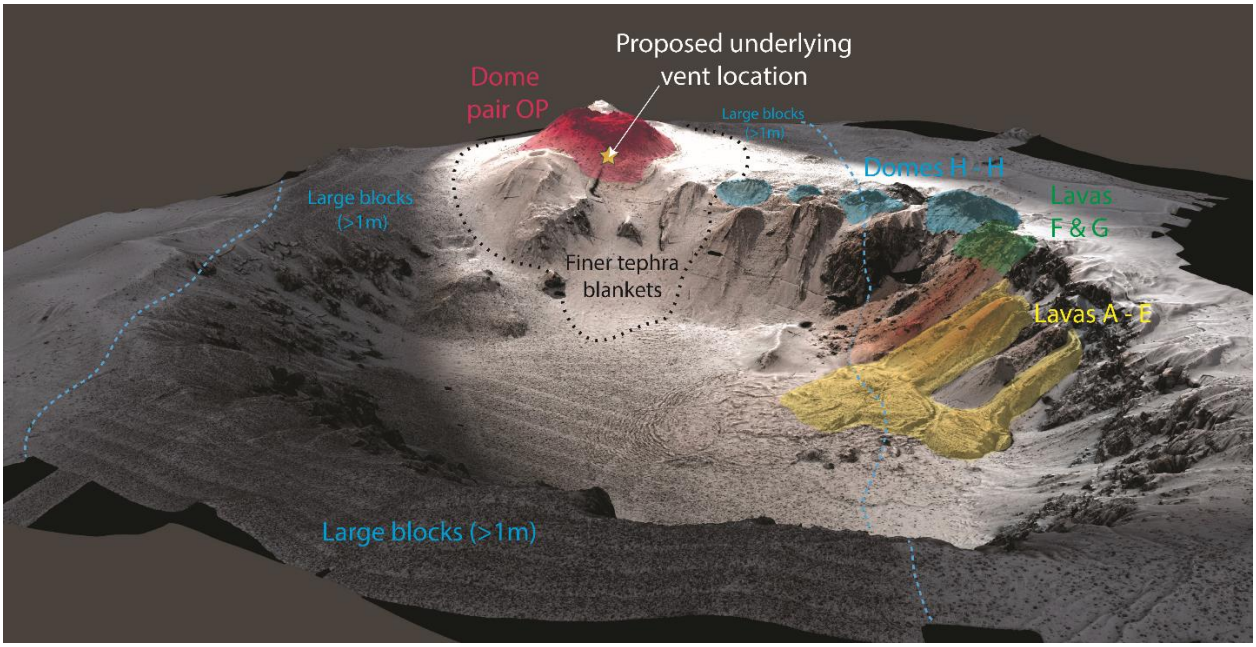

Figure 1.4. 3D rendering of the AUV *Sentry* map looking SE across the Havre caldera with extent of elevation gain given in red (from media release associated with Carey et al. (2018)). Important new features (Dome OP, lavas A – N, proposed pumice vent location, block field and fine tephra blankets) are outlined by colors and dashed lines.

Lava flows and domes F-P were all erupted along the southern caldera rim with depths of 900 – 1000 m (**Figure 1.4**). Lava domes H-N have more regular, dome-like morphologies with lower aspect ratios. K, L, M and N are each isolated on the seafloor (Ikegami et al., 2018). Lava domes H-N, excluding pre-2012 J, have 71.8 – 72.0 wt. % SiO_2 and 1.2 – 1.8 wt. % LOI (**Table 1.1**). The tops of these domes do not have pumiceous carapaces, but have blocky spines. Lava flow G is particularly interesting given its distinctive flow morphology not observed in other lavas and domes present on the S caldera rim (Ikegami et al., 2018), anomalously low LOI (0.4 wt. %) and pumiceous carapace up to 2 m thick. Lava G is also associated with a locally dispersed, adjacent clastic deposit made up of clasts with a tube/woody pumice nature (Kato, 1987; Dingwell et al., 2016; Mundana and Carey, 2017; Murch, 2018).

Dome OP forms a ~250 m high edifice on the SE caldera rim and comprises 50% of the total 2012 lava volume (~0.11 km^3) (**Figure 1.4; Table 1.1**). The 1.2 km-wide dome erupted from a vent at 900 mbsl, and has two distinct summit morphologies: Lava O, a blocky dome with spines and talus deposits (particularly so on the NE flank), and lava P on its western margin with a smoother, blocky carapace. Like lava flow G, Dome OP has lower LOI values than the other lavas and domes (~0.48 wt. %) despite the similar bulk geochemistry (**Table 1.1**).

1.2.2.2. Submarine pumiceous deposits

There are five major clastic units identified on the seafloor that, along with the pumice raft (RP), are the primary focus of the dissertation: GP, ALB, AL, DB and LGL (Carey et al., 2018). The giant pumice unit (GP) is a 1-5 clast-thick discontinuous blanket of giant pumiceous blocks with diameters 1.0 to 1.6 m in diameter, although some observed are up to 9 m across (a first-order increasing block diameter with distance relationship was inferred in Carey et al. (2018)). Individual giant pumice blocks can be identified in the AUV *Sentry* bathymetry due to its 1 m spatial resolution (**Figure 1.4**). GP forms a NW-SE oriented envelope that extends around and from Dome OP in a northwesterly direction, presumably from a vent beneath Dome OP at 900 m depth (**Figure 1.3** and **1.4**). This deposit extends outside of the study area (>35 km^2). The apparent limit to the GP distribution seen in AUV bathymetry data is bound by clasts >1 m in diameter, as smaller GP clasts are not observable in the AUV survey data. Based on ROV dives crossing this apparent

boundary, there is a sharp change in GP grainsize and deposit thickness; however, this boundary was neither quantified nor systematically observed in all sectors (**Figure 1.3**). Using a bulk deposit density of 550 kg m^{-3} (calculated previously from pumice density measurements and clast packing) for the GP deposit gives a minimum bulk volume of 0.1 km^3; however, an unknown volume lies outside of the *Sentry* map (Carey et al., 2018). Carey et al. (2018) hypothesize a genetic link between GP and the pumice raft due to their similar dispersal direction, inferred common point source beneath Dome OP, and identical geochemistry. In stratigraphy, GP underlies Dome OP, but is found on the surface of a number of lava flows.

The ash-lapilli-block deposit (ALB) comprises mostly of white pumiceous lapilli and blocks (cm to sub-meter diameter clasts); there is a minor ash component. The ALB unit forms local lobes in multiple directions up to 1.5 km from Dome OP that correspond to the "smoother areas" identified in AUV bathymetry (**Figure 1.1b** and **1.2**) which correlate to a lack of meter-scale clasts (**Figure 1.3**). The lobe deposit geometry and rapid changes of thickness and mean grain size with distance suggests a lateral transport mechanism syn- or post- the GP-forming phase; however this is not yet quantified (Carey et al., 2018). The estimated total volume of ALB is significantly smaller than GP (<0.01 km^3). Proximal to Dome OP, GP appears to have been buried due to ALB deposition. Dome OP then overlies the most proximal ALB deposits.

The ash with lapilli deposit (AL) is rich in ash with minor lapilli. It overlies everything except for Lava Dome P (Murch, 2018). AL was dispersed across the volcanic edifice, observed throughout the survey area, and extends outside of the 2015 survey area. The thickness of AL ranges from 50 cm close to Dome OP, to 10 cm at the outer extent of the survey area (up to 7 km from Dome OP). A total calculated volume is estimated at >0.1 km^3 (Carey et al., 2018). AL has a complex internal stratigraphy that is made up of four main subunits with different grainsize distributions, componentry, dispersal characteristics, inferred origins and stratigraphic relationships between other units (Murch, 2018). AL has proven a valuable marker for assessing the timing of lava emplacement and pumice deposition (Ikegami et al., 2018; Murch, 2018). Murch (2018) describes all AL subunits and their respective origins in full; I will introduce the AL subunit stratigraphy as needed later within the dissertation.

The Dome Breccia deposit (DB) is a clastic unit comprised of lapilli to block sized dense dome fragments and ALB-like pumice preserved on the NE and E flanks of, and up to 700 m from,

Dome OP (**Figure 1.3c**). The mechanism of formation of DB is unknown, although it is likely to be the result of an earlier dome flank collapse due to slope instability or seismic events during and after Dome OP emplacement.

Lava-G-Lapilli (LGL) is a lapilli deposit locally and sporadically dispersed around Lava G (Ikegami et al., 2018; Murch, 2018). Lapilli clasts with LGL have a distinct textural fabric that differentiates them from most other pumice and clastic deposits within the Havre 2012 eruptive sequence. Most LGL clasts exhibit woody, tubular fabrics that are identical to the pumiceous carapace of Lava G itself and show distinct similarities to ash within one of the subunits of the AL deposit (Murch, 2018).

1.3. Motivation and aims of the dissertation

This dissertation focuses on elucidating the relationships between and within the pumice-bearing units associated with the 2012 eruption (GP, RP, ALB, AL, DB and LGL), and using this information to understand the role of hydrostatic pressure on submarine volcanism. In particular, there is a need to define the spatial and temporal relationships between units inferred to have erupted primarily from the main vent beneath Dome OP (GP, RP, ALB and the dome itself). I will test the hypothesized synchronous timing relationship between the pumice raft and GP (Carey et al., 2018), as this has implications for considering the mass eruption rate and duration of the GP phase (previously assumed to be that of RP: ~10^7 kg s^{-1}), and the evolution of magma within the conduit from the pumice-producing to dome-forming phases.

Detailed textural and volatile geochemical analysis of pumice from all of these units will provide insight into the ascent history of the parent magma, shallow conduit dynamics, eruption mechanisms, and post-eruption magma–water interactions in the ocean. The transportation and deposition of pumice from the 2012 eruption are considered within the discussion of the following chapters and in the conclusions; however, these processes are not the integral focus of each project. The aims of this dissertation are to:

- Assess and estimate quenching depths and cooling rates of submarine pumice produced from a deep submarine vent by analyzing residual water in volcanic glass.

- Provide a detailed textural and geochemical assessment of the giant pumice block deposit. Textures from the meter to micron scale are used in interpretation of conduit and eruptive dynamics and processes within the water column.
- Support or challenge previous interpretations of origin and eruptive mechanism of pumice-bearing units (RP, GP, ALB, LGL) from the 2012 Havre eruption.
- Assess to what extent hydrostatic pressure controls eruption styles and conduit conditions in deep submarine silicic volcanic systems.

With the aims of the dissertation established, it is vital to assess the broader field of submarine volcanism and the challenges associated with this field of research, specifically with regards to deep submarine silicic volcanism; the rest of this chapter addresses this. I also provide the basic physical volcanology framework required to understand the processes of magma ascent, degassing and the development of textures within pumice.

1.4. Submarine volcanism

Over 70% of current global volcanic activity occurs on the seafloor (**Figure 1.5**; Crisp, 1984; Wessel et al., 2010; Rubin et al., 2012; White et al., 2015). The increasing development of submersible technology has allowed scientists to sample, observe, and monitor volcanism at the bottom of the oceans (Tan et al., 2008; Rubin et al., 2012; Campbell et al., 2015; Kelley, 2017; Embley and Rubin, 2018). Challenges remain in that submarine exploration is costly, and access to deep sites is limited by the technology available.

Submarine volcanic eruptions present a lower risk to life than subaerial eruptions, but there are still a number of hazards associated with submarine volcanism. Shallow submarine explosive eruptions, for example, Surtsey, Iceland 1963-64 (Thorarinsson et al., 1964; Kokelaar, 1983), Hunga Ha'apai, Tonga 2009 (Vaughan and Webley, 2010; Bohnenstiehl et al., 2013), and Bogoslof, Alaska 2016-2017 (Wech et al., 2018), present similar hazards to subaerial explosive eruptions: ash-laden plumes affecting aviation, proximal tephra fallout, and blasts and density currents proximal to nearby coastlines or marine vessels (Casadevall, 1994; Vougioukalakis et al., 1994; Nomikou et al., 2012; Jenkins et al., 2015).

Submarine volcanic centers are also sites of shallow crustal earthquake activity and thus, possible tsunami generation, where large earthquakes or submarine landslides can displace the overlying water column (Smith and Shepherd, 1993; Dawson, 1999; Dominey-Howes et al., 2000; Nanayama et al., 2003; Masson et al., 2006; Mellors et al., 2007; Ibáñez et al., 2012; Nomikou et al., 2014). Shallow eruptions can also increase fluxes of acidic, and potentially toxic, species into the water, e.g., CO_2, CH_4, SO_2, H_2S, HS^-, HCl and HF (Frogner et al., 2001; Sauter et al., 2006; Hall-Spencer et al., 2008; Carracedo et al., 2012).

Voluminous, pumice-producing submarine eruptions, such as the 2012 Havre eruption, can form pumice rafts that remain afloat on the ocean surface for months to many years due to the low density of pumice relative to seawater (Coombs and Landis, 1966; Francis and Self, 1983; Bryan et al., 2004; Bryan et al., 2012; Jutzeler et al., 2014).

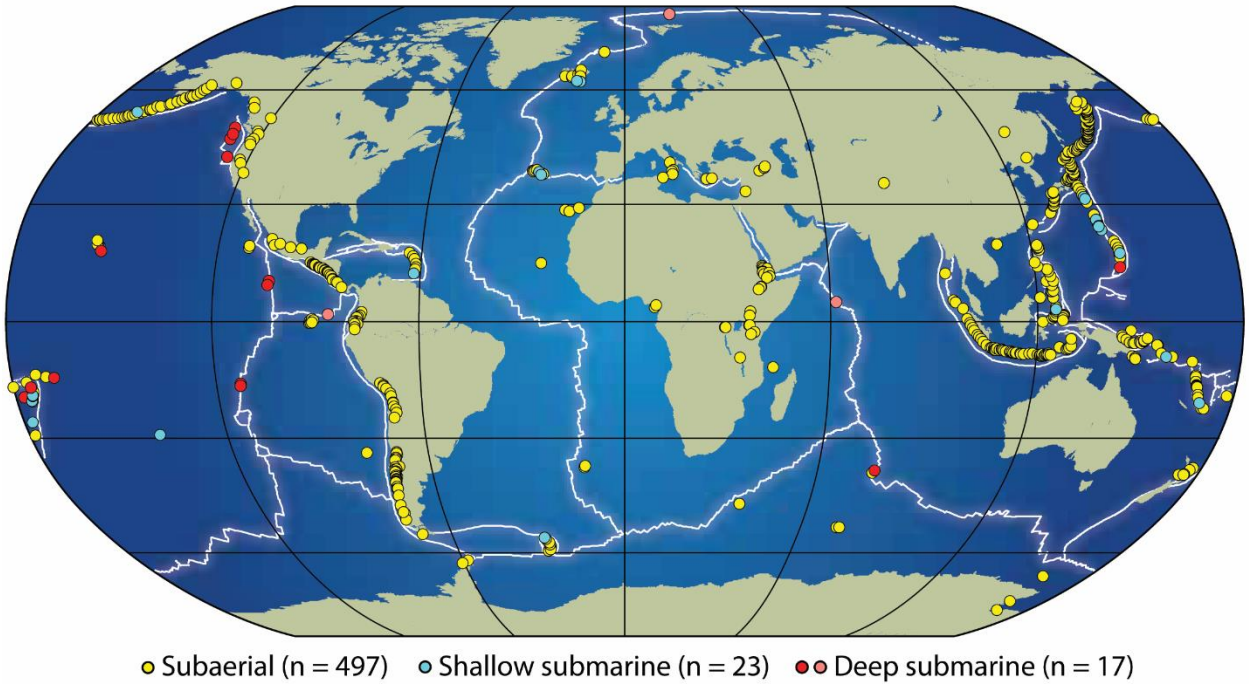

Figure 1.5. Locations of known historic subaerial and submarine volcanism over the last 500 years from Rubin et al. (2012). The figure highlights how little is known about seafloor volcanism in comparison to subaerial volcanism. Red dots (confirmed sites), pink dots (likely sites).

Pumice rafts can affect ship traffic and ship engines where, similar to plane engines, ingestion and melting of volcanic glass can present a risk to operating machinery (Gass et al., 1963; Casadevall, 1994; Grindle and Burcham, 2003; Song et al., 2016). Pumice rafts have the advantage of being used as a tracer for submarine volcanic activity and, potentially, as a tracking system for locating eruptions that breach the sea surface (Vaughan et al., 2007); this resulted in the discovery of the 2012 Havre eruption (Jutzeler et al., 2014).

1.4.1. Effects of seawater on volcanic eruptions

A critical part of understanding submarine volcanism is accounting for the different physical conditions of magma erupting into seawater vs. erupting into air, and ocean currents that affect eruptive and clast-transportation dynamics (**Table 1.2**). As a physical medium, seawater exhibits higher density, pressure, viscosity, heat capacity and thermal conductivity than air (Driesner, 2007; Driesner and Heinrich, 2007; Sharqawy et al., 2010; Cas and Giordano, 2014).

Table 1.2. Physical and chemical bulk properties of tropospheric air and standard seawater. Values given as an approximation and have some variability (Dreisner, 2007; Driesner and Heinrich, 2007).

Physical medium	Density (kg m^{-3})	Temperature (°C)	Pressure (MPa)	Viscosity (Pa s)	Pressure gradient (Pa m^{-1})	Specific heat capacity (J kg^{-1} $°C^{-1}$)	Thermal conductivity (W m^{-1} $°C^{-1}$)	Thermal diffusivity (m^2 s^{-1})	Water content
Air	~1	-60 – 50	~0.1	~10^{-5}	~10	~1200	~0.025	~10^{-5}	~1%
Seawater	~1000	2 – 30	0.1 – 50	~10^{-3}	~10^{4}	~4200	~0.6	~10^{-7}	~97%

The density of seawater is a primary control on the ascent and transportation of pumice in the water column and at the ocean surface. At 56 – 62% porosity (dependent on the bulk magma density and gas pressure–temperature conditions), gas-filled pumice becomes positively buoyant and will ascend through the water column without any momentum required. In the subaerial environment, clast ascent is driven by a combination of ejecta momentum and buoyancy within a hot, eruptive plume (Cashman and Fiske, 1991; Head and Wilson, 2003). Submarine pumice

transportation and deposition is governed by the timescales of saturation/waterlogging and permeable outgassing, connectivity of the pore network and its ability to retain vapor, and the strength of ocean currents (Fiske et al., 2001; Jokiel and Cox, 2003; Allen et al., 2008; Jutzeler et al., 2014; Fauria et al., 2017; Fauria and Manga, 2018).

The ocean is heavily stratified with many layers and currents with variable directions and speeds (Rossby, 1936; Stommel, 1948; Price et al., 1987). The interaction of submarine pyroclasts with these currents can result in very complex transportation and dispersal patterns; for example, larger pyroclasts from smaller *submarine* eruptions can potentially disperse farther than comparatively large *subaerial* eruptions (Coombs and Landis, 1966; Bryan et al., 2012; Jutzeler et al., 2014; Carey et al., 2018). Tephra fallout on the ocean surface from large subaerial eruptions can add further complexity to the interpretation of submarine volcaniclastic stratigraphy through the introduction of settled "foreign" material.

Hydrostatic ocean pressure can influence the *style* of submarine volcanic activity, particularly in volatile-rich magmas with high explosive potential; hydrostatic pressure increases linearly with ocean depth (Head and Wilson, 2003; Allen et al., 2010; Manga et al., 2018). Explosive volcanic activity is thought to be rarer in the deep sea; however, our understanding is limited due to a lack of observations in the deeper parts of our oceans (Kelley, 2017). In theory, the greater pressure experienced at deep volcanic vents suppresses volatile degassing and decompressive bubble growth in magma and hence the ability of a magma to erupt explosively (Head and Wilson, 2003; Rotella et al., 2014; White et al., 2015). However, the discovery of volcanic tephra (pyroclasts) at very deep locations (>2 km) challenges this notion (Sohn et al., 2008; Clague et al., 2009; Helo et al., 2011; Pontbriand et al., 2012).

An understanding of the pressure controls on submarine volcanism can be translated to volcanism in other inaccessible environments of variable pressure relative to subaerial conditions, for example, subglacial volcanism, and extra-terrestrial volcanism on the surfaces of Venus (higher ambient pressure), Enceladus, Mars and Io (all lower/negligible ambient pressure) (Stevenson, 1982; Head et al., 1992; McEwen et al., 1998; Hartmann et al., 1999; Wilson and Head, 2002; Hynek et al., 2003; Meyer and Wisdom, 2008; Owen et al., 2013a; Airey et al., 2015). Observations, sample analysis and computational modelling of submarine systems can assist us in modelling these other volcanic systems while allowing for contrasts in primary physical controls,

for example, ambient temperature and density, gravitational acceleration, crustal structure, planetary volatile content and primary melt composition (Tuffen et al., 2010; Airey et al., 2015).

1.4.2. Caveats in studying silicic submarine volcanism

Silicic submarine volcanism is most common on volcanic arcs where volatile- and sediment-rich subducted crustal material provides a geochemical component to mix with asthenospheric-derived melts (Schmidt and Poli, 1998; Stern, 2002; Wallace, 2005; van Keken et al., 2011). These settings produce a range of primary mafic to more evolved and differentiated silicic magmas at depth (Coats, 1962; Ewart et al., 1977; Wright and Gamble, 1999; Smith and Price, 2006; Wright et al., 2006a). There are fewer documented silicic eruptions on the seafloor, and their eruptive repose interval may be larger than that of their mafic seafloor counterparts (Langmuir et al., 1992; Rubin et al., 2012), but silicic eruptions on volcanic arcs can present greater risks (Manville et al., 2009; Tani et al., 2013; Nomikou et al., 2014).

With few recent examples of silicic explosive volcanism on the seafloor, volcanologists have relied primarily on the sampling of ancient submarine volcaniclastic sequences to understand these types of eruptions (Kato, 1987; Fiske et al., 2001; Gifkins et al., 2002; Wright et al., 2003; Yuasa and Kano, 2003; Barker et al., 2012b; Rotella et al., 2015). Sequences of older, uplifted submarine stratigraphy also offer environments more conducive to accessible, cost-effective fieldwork, e.g., ancient volcanism in Greece, Tasmania and Japan (Allen and McPhie, 2000; McPhie and Allen, 2003; Allen and McPhie, 2009). These ancient sequences offer their own limitations, for example, lack of knowledge of the original vent depth, duration and mass eruption rate, and overprinting of glass alteration by external meteoric water.

Ocean currents and pumice-raft dispersal have been shown to deliver large volumes of tephra from submarine silicic explosive eruptions away from their source and associated areas of proximal deposition (Coombs and Landis, 1966; Bryan et al., 2012; Carey et al., 2018). The remobilization and/or removal of pumice from the volcaniclastic record makes this archive unreliable, particularly when interpreting eruptive volumes and clast size distributions (Allen and McPhie, 2009; Carey et al., 2018). Complex pyroclast transportation and settling further complicates temporal reconstruction of submarine eruption dynamics, as clasts may not settle in

accordance with their eruptive sequence due to the effects of variable clast saturation, raft residence time, ocean density, and ocean currents (Cashman and Fiske, 1991; Allen and McPhie, 2000; Allen et al., 2008).

Grain size distributions, and textural and morphological analysis of ash from explosive *subaerial* eruptions are inherently useful for assessing the efficiency, depth and mechanism of magma fragmentation (Woheltz, 1983; Barberi et al., 1989; Kueppers et al., 2006; Rust and Cashman, 2011; Liu et al., 2015a). In the *submarine* environment, ash is easily suspended, remobilized or removed from stratigraphy altogether. In the eventuality that ash *is* preserved, grain size distributions and textures may reflect a bias in ash source, preservation and settling mechanisms. Submarine volcanic ash (and lapilli) can also be attributed to multiple sources including secondary pyroclast fragmentation, abrasion processes or ash venting from lava flow carapaces (Cashman and Fiske, 1991; Murch, 2018). Common subaerial field practices, e.g., isopach, isomass and isopleth mapping, and subsequent deposit volume calculations and total grain size distribution analysis, cannot be easily applied to submarine stratigraphy because of these limitations.

One of the primary difficulties in interpreting ancient stratigraphy is a lack of knowledge of eruptive vent depths, and hence the hydrostatic pressure at which eruptions took place. To prevent bias and misinterpretation of silicic submarine volcanic successions and their associated eruptive styles, exploring and sampling *recent* eruptions with known vent locations and eruptive durations is inherently useful (Allen et al., 2010). While is it common, and reasonable, to draw on existing knowledge of subaerial eruptions to improve our understanding of less familiar, deep submarine systems, we can also learn more about well-studied volcanic systems by interpreting more complex processes in unusual eruptive environments. The 2012 Havre eruption gives us the opportunity to study a recent eruption with clear proximal stratigraphy, known vent depths and locations, and a range of eruptive products with distinguishable timing relationships.

1.5. Volcanic degassing in silicic magmas

Silicic magmas saturated in volatiles (H_2O, CO_2, S, F, Cl) have the potential to erupt explosively (Eichelberger and Westrich, 1981). As magma is driven out of storage regions and into the volcanic conduit by the magma overpressure, the decrease in confining lithostatic pressure drives the exsolution of volatiles dissolved in the melt (Sparks, 1978; Cashman and Sparks, 2013). The nucleation and subsequent growth of bubbles in the melt increases the buoyant gas fraction (vesicularity) of the magma, further driving the ascent of magma through the conduit. Upon eruption, quenched magmas preserve their textural histories and residual volatile contents (Eichelberger and Westrich, 1981).

By studying the textures of vesicles and crystals, and analyzing the concentrations of volatiles in matrix glass, volcanologists gain significant insight into quenching pressure conditions, magma decompression rates, and bubble and crystal nucleation and growth histories (Sparks, 1978; Eichelberger and Westrich, 1981; Ferguson et al., 2016). Small pockets of melt trapped in phenocrysts during crystal growth (melt inclusions) also record volatile contents of magma at depth, and can be used to interpret magma storage pressures and styles of volatile degassing (Gardner et al., 1995; Wallace, 2005; Collins et al., 2009).

1.5.1. H_2O solubility, speciation and analysis

Water is the most abundant volatile in silicic magmas and is found in high concentrations in forearc magmas at subduction zones (up to 7 wt. % H_2O; Wallace, 2005; Wysoczanski et al., 2006; Plank et al., 2013) (**Figure 1.6**). Dissolved water is a primary modulator of magma viscosity, where a several wt. % change can result in a viscosity shift of several orders of magnitude (Bottinga and Weill, 1972; Giordano et al., 2004; Giordano et al., 2008). Water also influences the glass transition temperature (T_g) – the temperature at which melt is effectively "quenched" to a brittle state. Increasing H_2O content in the melt can reduce T_g by over 200°C, but T_g is also controlled by the magma cooling rate and geochemical composition (Deubner et al., 2003; Giordano et al., 2005; Del Gaudio et al., 2007).

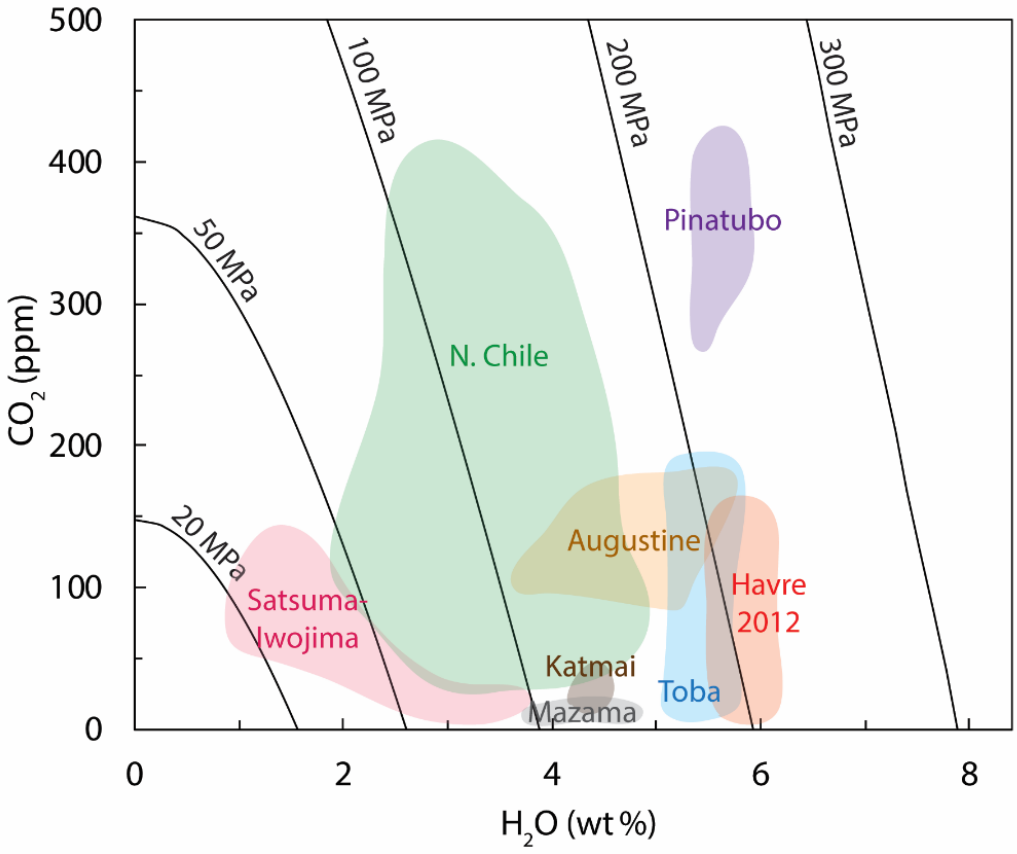

Figure 1.6. Volatile content of dacitic – rhyolitic arc magmas at subduction zones (subaerial and submarine eruptions) and respective magma storage pressures based on H_2O-CO_2 solubility isobaric calculations at 850°C (Newman and Lowenstern, 2002). Fields of volatile contents from Wallace (2005) and for the 2012 Havre eruption from Manga et al. (2018).

The solubility of water in melt – the maximum concentration of H_2O able to remain dissolved within the melt – is well established as a function of pressure from numerous experimental studies and theoretical models (Dixon et al., 1995; Newman and Lowenstern, 2002; Liu et al., 2005). As magma ascends, pressure decreases, and so does the solubility of H_2O. To equilibrate at lower pressure, H_2O exsolves from the melt lowering the dissolved water content remnant in melt (H_2O_t), a process known as volcanic degassing (with H_2O used here as an example). In volatile-saturated magmas, a valid assumption for hydrous arc melts (**Figure 1.6**), H_2O_t can be used to determine the pressure at which magma quenched (Burgisser et al., 2010; Owen et al., 2013b; Schipper et al.,

2013). These pressures can be converted into depths when applying a lithostatic (subaerial) or hydrostatic (submarine) model.

H_2O_t in matrix glass can be complicated by the late addition of molecular water (H_2O_m) *not* associated with degassing, but from external sources such as seawater or meteoric water (in subaerial settings). This is a process known as rehydration (Bonatti, 1965; Giachetti and Gonnermann, 2013; Seligman et al., 2016). By increasing H_2O_t, the quenching signatures are masked, which thus leads to misinterpretation of quenching depth. Accounting for rehydration is paramount when analyzing water in subaqueous products due to the exposure of glass to a dense water-abundant medium over long residence times. Addition of H_2O_m to the matrix glass can be assessed using water speciation (OH and H_2O_m), and used subsequently to reconstruct pre-rehydration H_2O_t (McIntosh et al., 2014; Dingwell et al., 2016). Accurately measuring and interpreting water in volcanic glass remains one of the cornerstones of physical volcanology (Devine et al., 1995; von Aulock et al., 2014).

1.5.2. Other volatile phases: CO_2, S, F and Cl solubility

Other volatile phases in silicic magmas may contribute over one wt. % of total volatile content, but water remains the most abundant phase (Wallace, 2005). CO_2 and S are very low in abundance in rhyolitic arc magmas (<0.1 wt. % and commonly less than a few hundred ppm), but can affect the solubility of H_2O in magma (**Figure 1.6;** Wallace, 2005). The addition of these phases effectively lowers the H_2O saturation potential in magma (Zhang, 1999; Newman and Lowenstern, 2002; Liu et al., 2005). CO_2 exsolves much deeper in the volcanic conduit or region of magma storage, hence, the majority of CO_2 is expected to have exsolved prior to eruption. CO_2 degassing in silicic magmas is not controlled by speciation, and CO_2 solubility scales linearly with pressure (Behrens et al., 2004; Liu et al., 2005). S exsolves much shallower than CO_2 (more similar to H_2O), but S degassing is more complex and highly dependent on the redox state of the magma (Scaillet et al., 1998; Wallace, 2005). Relative proportions of H_2O, CO_2, and S provide insights into styles of degassing in silicic volcanic conduits and volatile exsolution rates, but the low abundances of CO_2 and S have limited effect on magma rheology and vesiculation in water-rich rhyolites (Carroll and Webster, 1994; Gardner and Webster, 2016).

F and Cl have greater abundance in silicic forearc magmas, on the order of 0.02 – 1 wt. % each (Wallace, 2005). F, like H_2O, can modulate magma viscosity, albeit to a lesser extent than H_2O (Dingwell et al., 1985; Giordano et al., 2008). F has also been found to have an impact on bubble nucleation in rhyolitic melts, where greater F contents can reduce the surface tension of bubbles, which results in faster bubble nucleation rates (Gardner et al., 2018). Cl can also affect the solubility of H_2O in magma, but is found to have less of an effect on vesiculation and rheology (Webster et al., 1997; Webster et al., 2015; Webster et al., 2017). Determining Cl and F contents in volcanic glass can prove useful for assessing the possible effects of seawater rehydrating submarine volcanic glass, and halogen fluxes into the ocean. Although less abundant than H_2O, I consider CO_2, S, F and Cl concentrations in volcanic glass and the effects on conduit and post-eruptive processes during the 2012 Havre eruption within this dissertation.

1.5.3. Bubble nucleation, growth, coalescence and collapse

Bubbles can nucleate and grow at various depths within the volcanic conduit. Bubble nucleation and growth rates depend on the pressure conditions, magma composition, rheology and ascent, decompression rate and volatile content available in the magma to exsolve into the vapor phase (Sparks, 1978; Toramaru, 1995; Gonnermann and Gardner, 2013; Shea 2017). Quenching of erupting magma preserves the shape and size distribution of bubbles and crystals as pumice and lava microtextures (Eichelberger and Westrich, 1981). Vesicle textures record the state of magma at one moment in time (quenching), but quantitative analysis of vesicle number densities, vesicle volume distributions, vesicle connectivity and permeability can be used to interpret the history of bubble nucleation and growth throughout the volcanic conduit (**Figure 1.7**; Cashman and Sparks, 2013).

In the submarine environment, vesicle connectivity is also a primary control on the ability of pumice to retain vapor in isolated or poorly coalesced vesicles. This has significant implications on the ability of pumice to ascend (or sink) in the water column and, potentially, float on the ocean surface (Cashman and Fiske, 1991; Allen et al., 2008; Fauria et al., 2017). 3D analysis of vesicle textures can reveal further information regarding the elongation and shearing of vesicles due to the accumulation of strain within the volcanic conduit (Rust and Cashman, 2011; Dingwell et al.,

2016). In high viscosity rhyolitic magmas, significant strain accumulation and shear within the volcanic conduit can induce magma fragmentation (Papale, 1999). However, termination of deeper submarine conduits at higher "ambient" pressure may inhibit this accumulation of strain (Head and Wilson, 2003; Cas and Giordano, 2014; Manga et al., 2018).

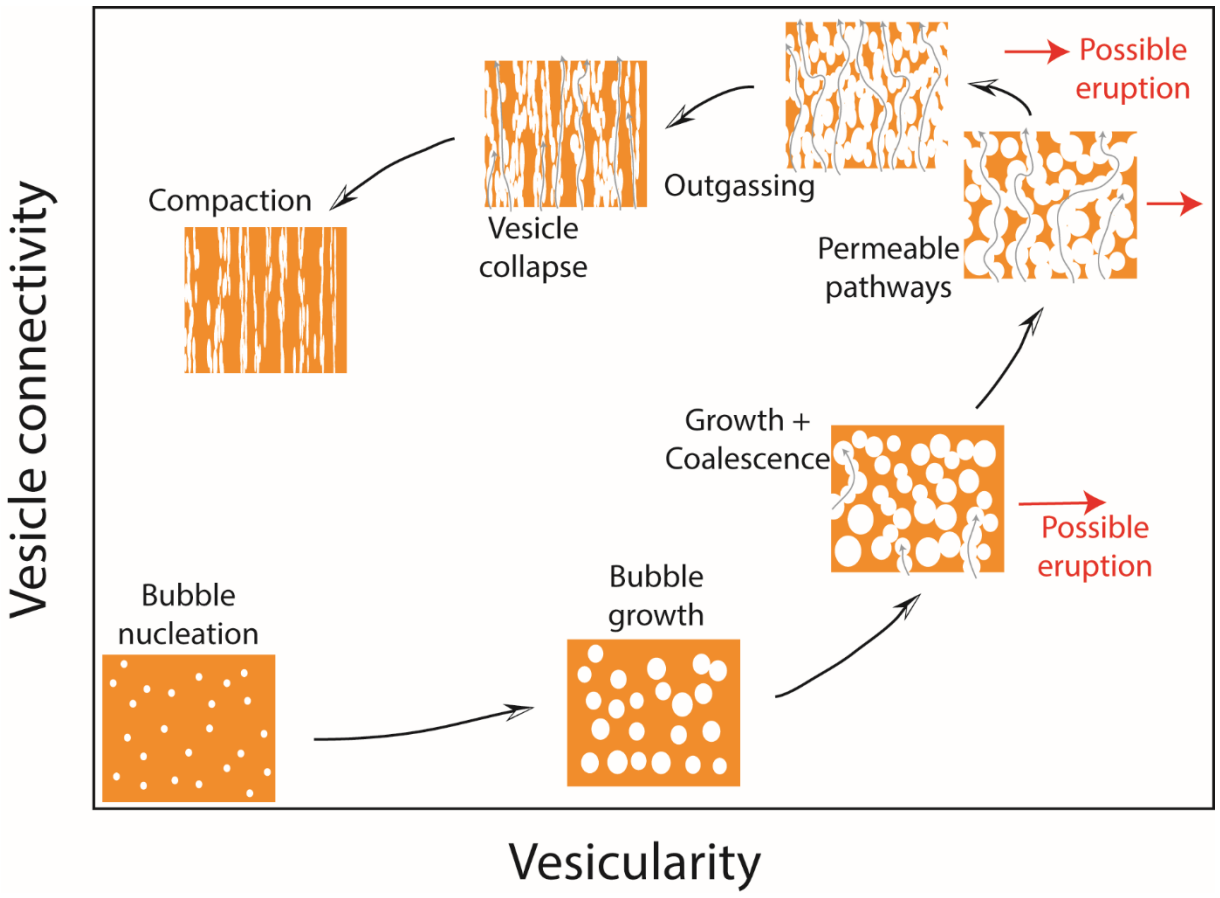

Figure 1.7. Schematic path of bubble nucleation, growth, coalescence, permeable pathway development, magma outgassing, and eventual vesicle collapse and compaction in a space of vesicularity (% pore volume of total volume) vs. connectivity (% of pore volume that is connected to exterior) for a single magma parcel. Magma outgassing pathways are given by grey arrows. Red arrows denote the possible textures found in the production of pumice during explosive eruptions.

By combining quantitative analysis of vesicular microtextures, measurements of volatile concentrations in matrix glass and melt inclusions, and conduit ascent modeling, volcanologists can interpret the degassing and vesiculation of magma from storage to surface. The following chapters apply a number of microanalytical methods to submarine volcaniclastic deposits to assess the degassing and vesiculation history of magma during the 2012 Havre eruption.

Dissertation disclosure:

With a number of scientists with varying expertise involved in the Havre research group, the dissertation presents several studies in collaboration with a number of researchers. Likewise, the dissertation draws from several recently published, and in-progress, studies addressing other scientific questions regarding the 2012 Havre eruption and submarine volcanism; the student has been a research contributor and co-author to these works (Carey et al., 2018; Manga et al., 2018; Manga et al., In Press). Chapter 1 presents an overview of the volcanology and chronology of Havre and the 2012 eruption respectively mostly derived from published papers by other authors (Carey et al., 2018; Murch, 2018; Ikegami et al., 2018). Chapters 2 and 3 are derived from published (Mitchell et al., 2018) and currently in-review (Mitchell et al., In Rev.) manuscripts, respectively and thus present original work. Chapter 4 is a manuscript that is currently in preparation for submission to a peer-reviewed journal and also contains original work. Supplemental methods, data and interpretations for each chapter can be found within the appendices following the main dissertation chapters.

2. DYNAMICS OF A POWERFUL DEEP SUBMARINE ERUPTION RECORDED IN H_2O CONTENTS AND SPECIATION IN RHYOLITIC GLASS: THE 2012 HAVRE ERUPTION

As published in: *Mitchell, S.J., McIntosh, I.M., Houghton, B.F., Carey, R.J. and Shea, T., 2018. Dynamics of a powerful deep submarine eruption recorded in H_2O contents and speciation in rhyolitic glass: The 2012 Havre eruption. Earth and Planetary Science Letters, 494, pp. 135-147.*

ABSTRACT

Constraining the syn-eruptive volatile contents of magmatic melt is critical to understanding the intensities and styles of deep submarine volcanic eruptions, for which direct observations are scarce. Quantifying residual magmatic water contents in volcanic glass is complicated by rehydration, i.e., late-stage addition of molecular water. The 2012 deep submarine silicic eruption of Havre volcano provides an unusual opportunity to quantify glass water contents from a recent, well-sampled stratigraphic sequence. Fourier-transform infrared and microRaman spectroscopy measurements of water concentration and water speciation across the Havre 2012 eruptive sequence reveal an unanticipated range of excess molecular water within pumice. This excess water requires rapid timescales of diffusion that are inconsistent with our current understanding of low temperature secondary rehydration in both subaerial and subaqueous eruptive products. Diffusion models applied to enrichment profiles at vesicle edges confirm that low temperature rehydration is an unlikely cause. We instead support higher temperature, syn-eruptive pumice rehydration by condensed magmatic water and seawater in a submarine plume. Hydroxyl concentrations suggest shallow quenching depths of Havre pumice hundreds of meters above the 900-meter-deep main vent. Our data also support the presence of a vapor-rich plume and consequent modification of ocean pressure above the vent. We combine this novel volatile data with textural information and cooling rate calculations to explore the conditions that would cause slower, shallow cooling of clasts from a deep submarine eruption. By exploring the physical

conditions for the interaction between pumice and submarine plumes, we emphasize fundamental differences between subaerial and submarine clast-producing eruptions.

2.1. Introduction

Volcanic eruptions are driven by exsolution of volatiles such as H_2O and CO_2, whose solubility in magma is controlled by pressure and temperature conditions. Volatile exsolution into a vapor phase during magma ascent increases magma buoyancy, and the dynamics of subsequent bubble growth and magmatic degassing are fundamental controls on eruption style (Sparks et al., 1978; Zhang et al., 2007; Cashman and Sparks, 2013). If erupted melt is quenched to glass sufficiently quickly, residual volatile contents can be used to infer pressure and temperature conditions relating to quench and pre-eruptive degassing processes (Eichelberger and Westrich, 1981; Giachetti and Gonnermann, 2013). The volatile record is particularly useful in settings such as deep submarine volcanoes, where direct observations of eruptions are extremely challenging and have been limited primarily to low intensity mafic volcanism (Schipper et al., 2010; Rubin et al., 2012; Soule et al., 2012; Gardner et al., 2016).

Along submarine volcanic arcs, silicic magmas are volatile-rich and their degassing during ascent is dominated by H_2O after CO_2 exsolves at depth (Newman and Lowenstern, 2002; Stern, 2002; Liu et al., 2005; Wallace, 2005). Consequently, reconstructing depths and pressures of silicic submarine eruptive processes will rely primarily on quantifying residual H_2O in matrix glasses. Variations in hydrostatic pressure and ocean temperature and density (attributed to the presence of submarine eruption plumes) may complicate interpretations of pyroclast H_2O contents. However, this also means that H_2O data provide an opportunity to investigate plume dynamics and models of submarine pyroclast formation and dispersal. The following study presents the first detailed H_2O data for clasts from a deep submarine silicic eruption in order to determine quenching depths and cooling histories within submarine plumes.

2.1.1. H_2O speciation and diffusion

Water is present in silicate melts and glasses as two species: hydroxyl ions (OH) that are bound to the aluminosilicate framework and diffusive water molecules (H_2O_m) that can exsolve into the

vapor phase at volatile saturation (Stolper, 1982; Newman et al., 1986; Zhang et al., 1991). The total water content (H_2O_t) is the sum of these two species (**Eq. 1.1**). The two species are related via an equilibrium reaction (**Eq. 1.2**) in which H_2O_m reacts with bridging oxygen atoms (O^o) in the silicate melt structure (Stolper, 1982). The equilibrium constant K_{eq} of this interconversion reaction determines the relative proportions of the H_2O_m and OH species, i.e., the 'water speciation' (**Eq. 1.3**; the square brackets indicate mole fractions).

(1.1) $$H_2O_m + OH = H_2O_t$$

(1.2) $$H_2O_m + O^o \rightleftharpoons 2OH$$

(1.3) $$K_{eq} = [OH]^2/([O^o][H_2O_m])$$

As K_{eq} varies with temperature, so does the water speciation (Stolper, 1982; Zhang et al., 1997; Nowak and Behrens, 2001; see Appendix **A1**). For a given H_2O_t content, higher temperatures give higher K_{eq} thus lower H_2O_m/OH ratios. Lower temperatures give lower K_{eq} and thus higher H_2O_m/OH ratios. Importantly, the *speed* of the interconversion reaction decreases with decreasing temperature (Zhang et al., 1991; Zhang et al., 2007). The time required to maintain equilibrium speciation thus increases dramatically during cooling until interconversion becomes negligible and speciation is effectively frozen-in at a temperature of apparent equilibrium (T_{ae}). T_{ae} is equivalent to the temperature of the glass transition (T_g), which varies with H_2O_t content and cooling rate (Dingwell and Webb, 1990; Zhang et al 1997; Xu and Zhang, 2002; Giordano et al., 2005; Del Gaudio et al., 2007; Giordano et al., 2008). Measuring H_2O speciation and calculating T_{ae} is therefore a useful method for finding T_g and cooling histories of silicate glasses (e.g., Giordano et al., 2005).

Disequilibrium speciation occurs when species proportions differ from those expected under equilibrium conditions for a given temperature (hence K_{eq} value) and H_2O_t content. In such cases, measured T_{ae} does not equal T_g. Disequilibrium speciation is often associated with alteration of H_2O_t content, which would prevent the use of H_2O_t to infer quench pressures. An important cause of such alteration, especially in silicic glasses, is secondary rehydration, i.e., the low-temperature addition of ambient water after deposition (Giachetti and Gonnermann, 2013; Giachetti et al., 2015; Dingwell et al., 2016; Martin et al., 2017; Shea et al., 2017). Interconversion is negligible at low temperatures, so diffusive addition of H_2O_m increases both H_2O_t and the H_2O_m/OH ratio,

resulting in lower T_{ae} values (Denton et al., 2009; McIntosh et al., 2017). This is a problem when analyzing subaqueous silicic glasses as extended exposure to water can result in significant rehydration (Bonatti, 1965; Denton et al., 2009).

Other processes that can alter H_2O_t and H_2O speciation include solubility-driven bubble resorption due to pressure increase or temperature decrease (Watkins et al., 2012; Carey et al., 2013; McIntosh et al., 2014; Watkins et al., 2017), and sub-T_g rehydration during cooling over temperatures and timescales that enable significant H_2O diffusion (McIntosh et al., 2014; Bindeman and Lowenstern, 2016). In these cases, disequilibrium speciation can provide insights into the pressure and temperature histories of clasts prior to and following eruption.

2.1.2. The 2012 Havre eruption

The volatile record of submarine pyroclasts has the potential to reveal a number of eruptive processes occurring in deep submarine environments where direct observations are not possible. However, the known vulnerability of silicic glasses to secondary rehydration means that the clearest insights will be gained for pyroclasts sampled from well-constrained deposits soon after a known eruption. Over the past decade, first-time subaerial observations of features from submarine eruptions (e.g., pumice rafts) have presented exciting opportunities to study deep submarine systems (Kelley, 2017). The eruption of Havre volcano, Kermadec Arc, on 17th July 2012 was the largest deep-submarine silicic eruption recorded in modern history (Carey et al., 2014). The eruption produced a bulk volume of 1.5 km^3 of rhyolite (SiO_2 = 70–72 wt. %), with the majority (1.2 km^3) forming a floating pumice raft. Other erupted material included 14 submarine lava flows and domes, and pumiceous seafloor deposits (**Figure 2.1**, **Table 2.1** and Carey et al., 2018).

The clastic units identified include a seafloor bed of giant pumiceous blocks (GP), the floating pumice raft (RP) that subsequently washed ashore in Australia, Fiji and New Zealand (Jutzeler et al., 2014), a ~0.01 km^3 multi-lobate ash, lapilli and block pumiceous clastic deposit (ALB), a thin (10–50 cm thick) layer of ash and fine lapilli that covers the entire caldera (AL), a <<0.001 km^3 clastic unit at 950 m depth of texturally-distinct, higher density, tube pumice adjacent to a lava flow (Lava G) with a texturally similar pumiceous carapace (LGL), and a tongue of broken, dense dome fragments on the eastern flank of Dome OP (DB). Volumetrically, the majority of the

pumiceous units originated from a vent on the southern caldera rim at 900 m depth, i.e., hydrostatic equivalence to 9.2 MPa (assuming seawater density of 1027 kg m^{-3}, Millero and Huang, 2009). This vent is now covered by the main lava dome (Dome OP) with a summit at 650 m depth or 6.5 MPa of hydrostatic pressure (**Figure 2.1b**).

The range of clastic and effusive products is a strong indicator of variable eruptive styles during the 2012 event (Carey et al., 2018). Assessing the volatile record within these deposits can therefore further our understanding of a variety of deep submarine eruptive styles.

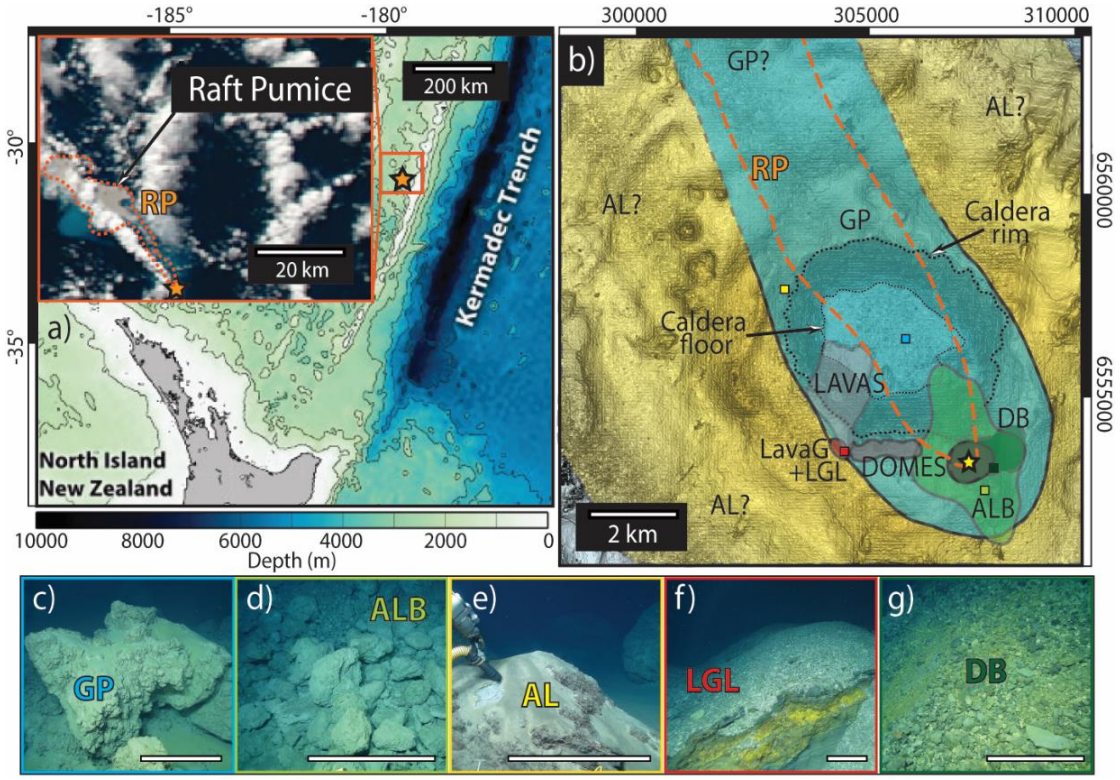

Figure 2.1. Overview of the 2012 Havre eruption. **(a)** Location of the Havre caldera at 1000 – 2000 m depth in the Kermadec rear-arc. Inset shows MODIS imagery from July 18 2012 highlighting the distribution of the pumice raft (RP) on the first day of the eruption (Carey et al., 2014). **(b)** Spatial distribution of 2012 eruptive units (for descriptions see **Table 2.1**). The dashed orange line marks initial subaerial distribution of the pumice raft. The Giant Pumice (GP) unit has a defined boundary until just outside the caldera rim, beyond which it is inferred (Carey et al., 2018).The proposed vent location at 900 m depth for the Giant Pumice, Raft Pumice and Ash-Lapilli-Block units is marked with a star; it is now overlain by a large dome. Representative images of each sampled seafloor units are shown in **(c-g)**, with photo location marked by colored boxes in **(b)**. Scale bars correspond to 1 m. In **(e)**, the thin Ash-Lapilli unit is being sampled from the top of a giant pumice block. In **(f)**, Lava-G-Lapilli is the clastic layer on top of dense lava.

Table 2.1. Descriptions of the 2012 clastic units from which products were analyzed within this study with approximate unit volumes from Carey et al. (2018). Abbreviations correspond to those used in the subsequent figures and text.

Stratigraphic Unit	Abbreviation	Unit description	Erupted volume (km^3 bulk)
Giant Pumice	GP	Extensive >35 km^2 field of gently-settled, mostly irregularly-shaped giant pumices with 1–9 m diameters. Some clasts have breadcrusting and curviplanar features on exteriors.	0.1
Raft Pumice	RP	Raft pumice resident on the ocean surface for up to 4 years post eruption and counting. This unit makes up the majority of the total eruptive volume. Clast size mostly in the decimeter range when found on beaches.	>1.2
Ash-Lapilli-Block	ALB	Ash, lapilli and block apron of pumice clasts around, and stratigraphically beneath, dome OP. Deposit thins and average clast size decreases with distance from dome.	0.01
Ash-Lapilli	AL	10-50 cm thick ash and fine lapilli layer dispersed across the caldera and further afield. Stratigraphically above all pumiceous units, above and below DB and proximal to Dome OP.	0.1
Lava-G-Lapilli	LGL	Small localised clastic deposit of tubular pumice proximal to, and considered to be genetically related to lava flow G.	<<0.001
Dome fragments	DB	Aprons of dome collapse talus east and north-east of the Dome OP, and stratigraphically above the GP and ALB units. (Block to lapilli).	<0.01

2.2. Materials and Methods

2.2.1. Sampling and preparation

Pumiceous lapilli were sampled from all seafloor units by an ROV during a research cruise to Havre in April 2015, ~1000 days after the eruption. For the Giant Pumice unit, samples included interiors and exteriors of clasts as well as sections of light and dark banding. Raft Pumice was sampled on the shores of New South Wales, Australia in July 2013 (~300 days after eruption). The density of every 8–32 mm lapilli or fragment was measured following Houghton and Wilson (1989). Representative clasts were then selected and prepared for volatile analysis (see Appendices **A2** and **A3**).

2.2.2. Volatile measurements

H_2O_t, H_2O speciation (OH and H_2O_m), and CO_2 contents within matrix glasses were measured by high spatial resolution Fourier-transform infrared (FTIR) spectroscopic imaging in the mid-IR range using a Varian Inc. Lancer Focal Plane Array camera at JAMSTEC, Yokosuka, Japan (e.g., McIntosh et al., 2014; **Figure 2.2**). H_2O_t and OH concentrations were obtained using the method of McIntosh et al. (2017), which accounts for the species-dependence of the 3500 cm^{-1} H_2O_t molar absorptivity coefficient. For further details of FTIR methodology, see Appendices **A2** and **A4**.

H_2O_t contents were also analyzed by microRaman (μRaman) spectroscopy at University of Hawai′i at Mānoa, using a Witec Alpha300R microscope with a ~1 μm analytical spot size. H_2O_t concentrations were determined using the Matlab-based program SpeCTRa (Spectral Correction Tools for Raman – Shea et al., 2014; Shea et al., 2017). For further details, see Appendix **A5**. H_2O_t profiles were acquired within the densest dome fragment (DB) and Lava-G-Lapilli to look for H_2O_t vesicle-edge variation.

2.2.3. Calculating equivalent quench pressures

Calculated ascent rates for the 2012 Havre eruption infer that the magma underwent equilibrium degassing (Gonnermann and Manga, 2005; Manga et al., 2018). Clast H_2O_t contents are therefore converted into equivalent quench pressures based on the pressure-dependence of H_2O_t solubility (Burgisser et al., 2010; Owen et al., 2013b; Schipper et al., 2013). For this, we use the VolatileCalc solubility model with an eruption temperature of 800°C (Newman and Lowenstern, 2002). If disequilibrium degassing did occur, equivalent quench pressures would be lower than reported here.

To assess whether H_2O_t contents have been altered by post-eruption processes, we examine our data for evidence of disequilibrium speciation (see Section **2.1.1**). Speciation data output by the VolatileCalc model do not account for the temperature dependence of K_{eq} (**Eq. 3**), so we apply the speciation models of Zhang et al. (1997) and Nowak and Behrens (2001) to the VolatileCalc H_2O_t output. The range of expected equilibrium H_2O_m and OH contents and H_2O_m/OH ratios were thus calculated for assumed T_g between 800°C (i.e., instant quench) and 400°C (i.e., the experimental lower T_g limit found for water-rich rhyolite with cooling <1 K min^{-1}; Giordano et al.,

2005). T_{ae} values calculated from measured H_2O speciation are also compared with expected T_g values for rhyolite. See Appendix **A1** for full details of equilibrium speciation and T_{ae} calculations.

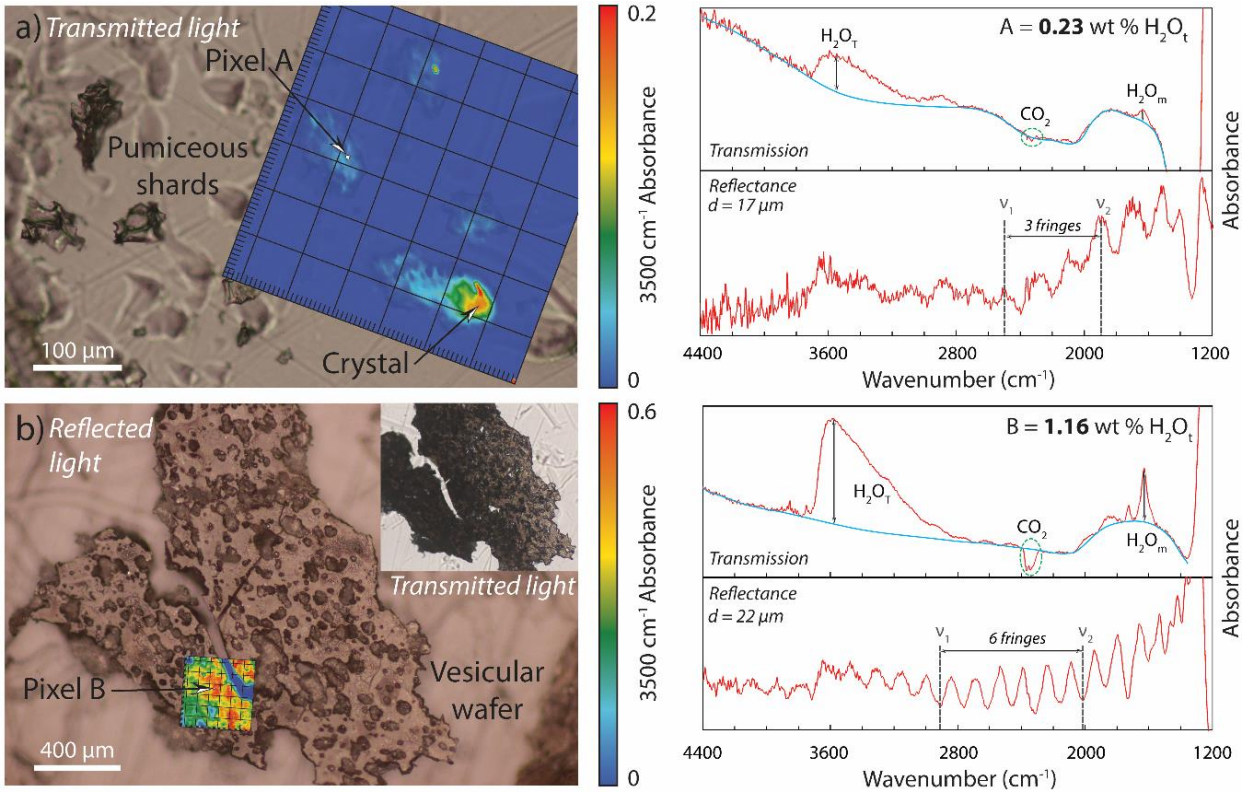

Figure 2.2. FTIR imaging technique for **(a)** vesicular shards and **(b)** denser doubly-polished wafers. 350 x 350 µm FTIR images of IR absorbance were acquired in both transmission and reflectance mode, from which individual spectra can be extracted for every ~5.5 x 5.5 µm pixel. Example spectra are shown for pixels A **(a)** and B **(b)**. Absorbance of the 3500 cm^{-1} H_2O_t, 1630 cm^{-1} H_2O_m and 2349 cm^{-1} CO_{2m} peaks is obtained from transmission spectra. Glass thickness (d) at each location is found from the wavelength of interference fringes in reflectance spectra. See Appendix **A4** for detailed methodology. Note that no dissolved CO_{2m} was detected in any analysis; noise in spectra around 2350 cm^{-1} is due to interference from atmospheric CO_2.

2.3. Results

The ranges in H_2O_t concentrations obtained by FTIR for each unit were: Giant Pumice (**GP**: 0.1–0.6 wt. %), Raft Pumice (**RP**: 0.3–0.8 wt. %), Ash-Lapilli-Block (**ALB**: 0.05–0.5 wt. %), Ash-Lapilli (**AL**: 0.15–1.0 wt. %), Lava-G-Lapilli (**LGL**: 0.5–1.2 wt. %), and dense dome fragments (**DB**: 0.3–1.6 wt. %). Full data are given in Appendix **A6**. There is good agreement between FTIR and Raman H_2O_t data for related clasts despite the difference in analytical volume (FTIR = ~900 μm^3 and µRaman <4 μm^3) (Appendices **A7** and **A8**). CO_2 content was below detection limits in all samples, and melt inclusions from Havre Giant Pumice detect very little CO_2 at depth (<150 ppm), implying that most CO_2 will have exsolved prior to eruption (Liu et al., 2005; Wallace, 2005; Manga et al., 2018). We therefore do not expect any significant effect of CO_2 on H_2O solubility and equivalent quench pressures (see Appendix **A9**).

The large range in clast average H_2O_t of 0.05–1.6 wt. % (**Figure 2.3**) corresponds to quenching pressures of 0.1–20 MPa at 800°C (Newman and Lowenstern, 2002) (Appendix **A9**). The majority of these data are equivalent to pressures ranging from the top to the bottom of the water column at Havre. However, clast average H_2O_t data from two dome fragments erupted at 650-900 m depth are equivalent to pressures up to 450 m deep into the volcanic conduit (1350 m depth) (Appendices **A6** and **A9**). H_2O_t contents alone thus do very little to differentiate eruption processes of different units. Examination of the H_2O speciation data, however, enables a more nuanced interpretation.

2.3.1. Water speciation in 2012 Havre clasts

OH and H_2O_m concentrations were determined for 28 representative clasts covering all sampled units (**Figure 2.3** and Appendix **A10**). Comparison with the two equilibrium speciation models suggests H_2O_m values are higher than the equilibrium speciation field expected for even the broad range of T_g = 400–800°C in rhyolite (Zhang et al., 1997; Nowak and Behrens, 2001). Giant Pumice (including banding) and Ash-Lapilli-Block display the highest excess H_2O_m relative to equilibrium speciation as seen in the H_2O_m/OH ratio (**Figure 2.3c, d**).

Speciation data from Giant Pumice, Ash-Lapilli-Block, and Ash-Lapilli units lie entirely outside of equilibrium speciation due to excess H_2O_m. Raft Pumice lies just outside of equilibrium speciation for T_g = 400°C with excess H_2O_m of 0–0.2 wt. %, while Lava-G-Lapilli exhibits

equilibrium speciation for T_g = 400–600°C. Dome fragments display variable speciation, with two clasts in apparent equilibrium for T_g of ~400 and 550°C, one clast just outside the expected range with ~0.1 wt. % excess H_2O_m, and two with high H_2O_m/OH ratios and up to 1 wt. % excess H_2O_m (**Figure 2.3**).

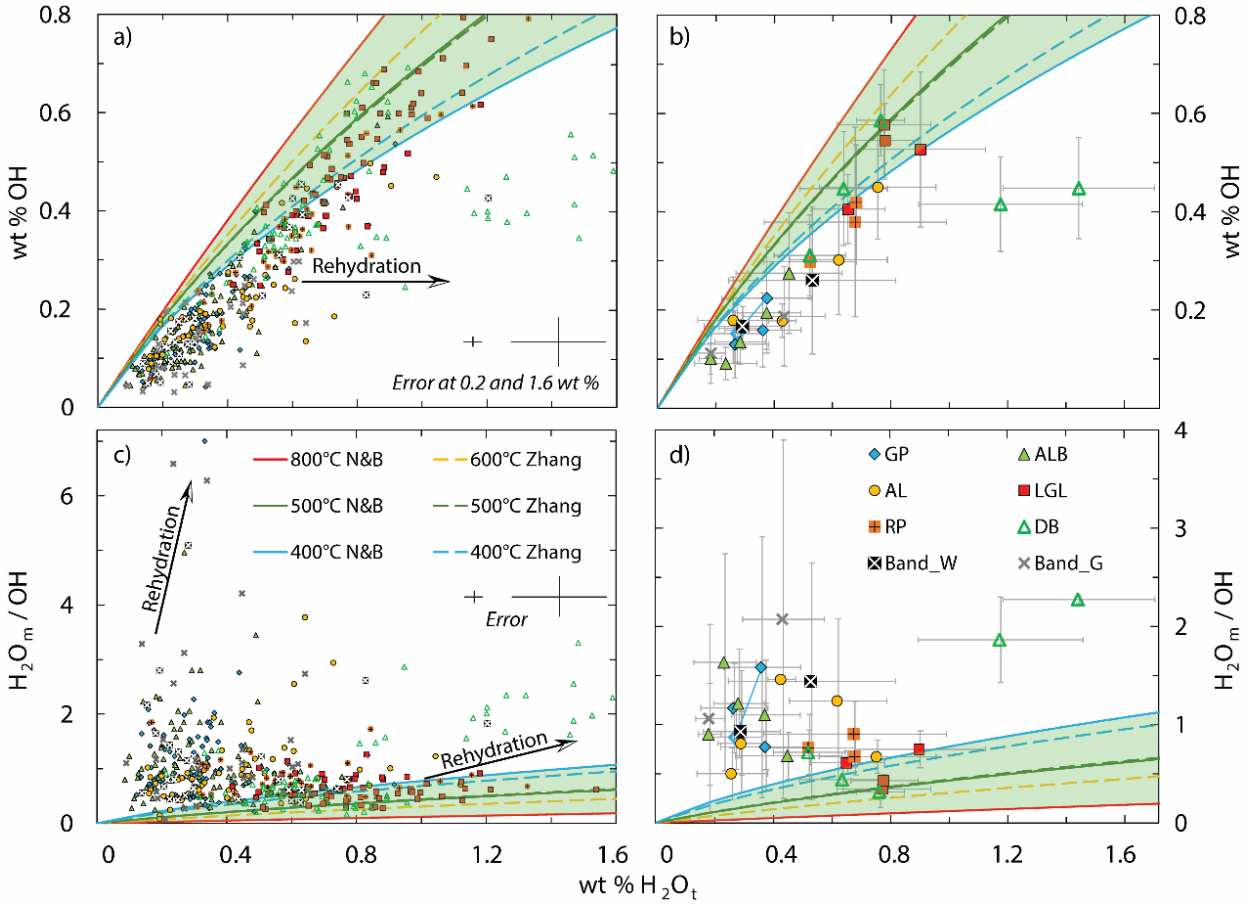

Figure 2.3. FTIR water speciation data from Havre pumice units, including gray (Band_G) and white (Band_W) banding from the interior and exterior of a Giant Pumice clast. Plots show **(a, b)** OH vs. H_2O_t, and **(c, d)** H_2O_m/OH vs. H_2O_t. **(a)** and **(c)** show all 463 individual pixel analyses. Black crosses show representative errors derived from the ±3 µm error on glass thickness, which is the major source of analytical error for thin samples. **(b)** and **(d)** show average data for each clast; error bars represent ±1 standard deviation from the mean. The green area marks the region of equilibrium speciation in rhyolite for glass transition temperatures (T_g) ranging from 400 to 800 °C, derived from the water speciation models of Nowak and Behrens (2001) and Zhang et al. (1997). The arrow identifies the direction of excess of H_2O_m addition, i.e., rehydration. The hollow blue diamond gives the analyzed GP clast interior, with a blue line connecting it to its exterior analysis.

2.3.1.1. Apparent equilibrium temperatures

Clast T_{ae} calculated from measured speciation are shown in **Figure 2.4**. Highly vesicular clasts (>60%) typically have lower T_{ae} values of 200–400°C and T_{ae} increases with decreasing vesicularity (R^2 = 0.66) down to ~45 %. At lower vesicularities, which includes three dome fragments and one Lava-G-Lapilli clast, T_{ae} then appears to decrease with decreasing vesicularity (**Figure 2.4a**).

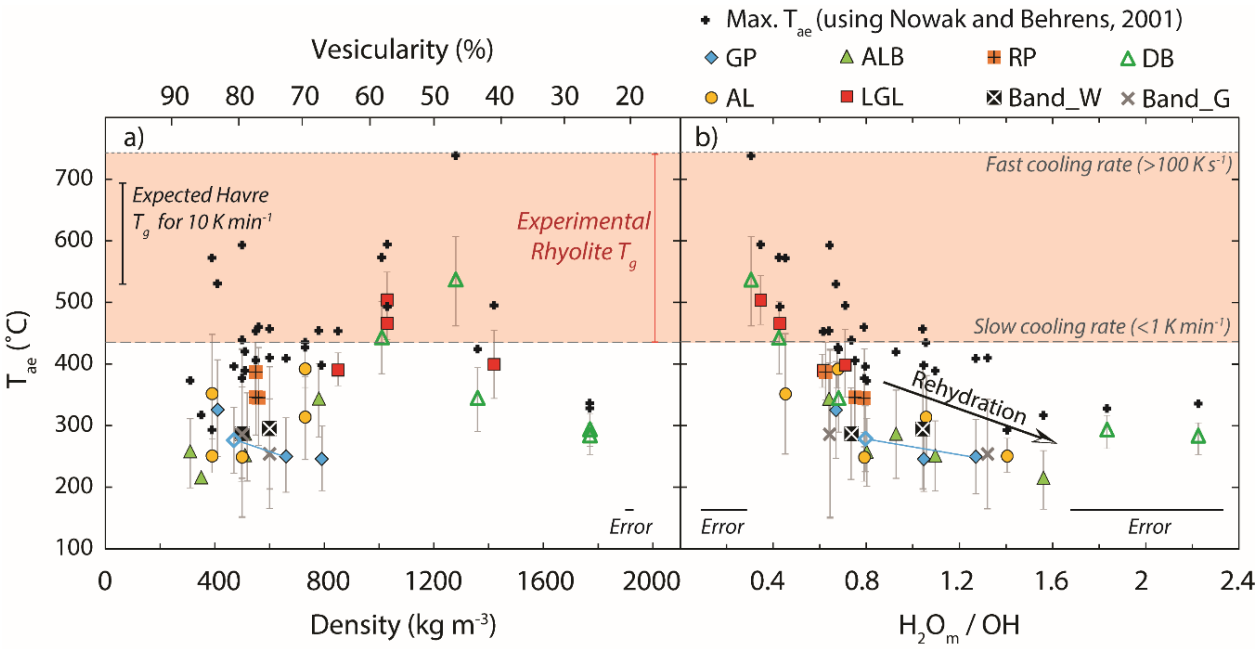

Figure 2.4. Average apparent equilibrium temperature (T_{ae}) calculated for each clast with ±1 standard deviation error bars is plotted against **(a)** clast density and equivalent vesicularity (assuming dense rock equivalent of 2400 kg m^{-3}) and **(b)** average clast H_2O_m/OH. Both plots show the experimental T_g range from dry rhyolite at fast cooling rates (>100 K s^{-1}) to hydrous (> 2 wt. % H_2O_t) rhyolite at slow cooling rates (< 1 K min^{-1}) (Dingwell and Webb, 1990; Giordano et al., 2005); and the T_g range calculated for Havre clasts using measured H_2O_t and assuming cooling of 10 K min^{-1} (Giordano et al., 2008). Black crosses indicate maximum T_{ae} of individual pixel analyses within each clast. Analytical uncertainty in density is given as 30 kg m^{-3}.

The expected T_g range in **Figure 2.4** is derived from experimental and theoretical studies of how T_g varies with melt composition, H_2O_t content, and cooling rate. Dry rhyolite quenched at >>20 K min^{-1} can have T_g close to 800 °C, whereas rhyolite with >>2 wt. % H_2O_t and cooled

slowly at ~1 K min^{-1} may have T_g as low as 420°C (Dingwell and Webb, 1990; Deubner et al., 2003; Giordano et al., 2005). We input our measured H_2O_t and whole rock XRF data (Carey et al., 2018) into the Giordano et al. (2008) viscosity model, which assumes a cooling rate of ~10 K min^{-1}, to evaluate the likely T_g range of the Havre clasts based on their water content. For our H_2O_t range of 0.1–1.6 wt. % we calculate a T_g range of 700–520°C for Havre clasts, where T_g is lower at higher H_2O_t.

For all but two dome fragments and two Lava-G-Lapilli clasts, clast average T_{ae} is too low to be a true record of T_g, even if cooling was <<10 K min^{-1}. Instead, low apparent T_{ae} values reflect addition of H_2O_m without re-equilibration of species concentrations (McIntosh et al., 2017). However, for several samples, the maximum T_{ae} within each clast falls within the T_g range calculated for the Havre clasts (black crosses, **Figure 2.4**). This variation within clasts indicates that the addition of H_2O_m affects clasts in a heterogeneous way (also seen in **Figure 2.3a, c**). The excess H_2O_m and T_{ae} less than expected T_g in most 2012 Havre clasts are characteristically consistent with some form of rehydration (**Figure 2.4b**). The exceptions are one Lava-G-Lapilli clast and one dome fragment that have the lowest H_2O_m/OH ratios. These clasts contain ~0.8 wt. % H_2O_t, corresponding to predicted T_g of ~580°C for cooling of 10 K min^{-1} (Giordano et al., 2008). Their average T_{ae} values of >500°C are therefore consistent with these clasts experiencing only minor rehydration, especially if they experienced cooling slower than 10 K min^{-1} and hence lower T_g.

2.3.2. H_2O_t enrichment profiles

µRaman H_2O_t profiles were acquired in the densest dome fragment and a Lava-G-Lapilli clast (26 and 57% vesicularity respectively) to look for spatial variations in H_2O_t around vesicles (**Figure 2.5**). Lava-G-Lapilli profiles show no significant enrichment or depletion in H_2O_t (**Figure 2.5b**); these observations are consistent with the limited rehydration of these clasts revealed by FTIR (**Figure 2.3**). Enrichment at vesicle margins was however observed in the dome fragment and five profiles were chosen to model H_2O_t diffusion (**Figure 2.5a**). In these profiles, H_2O_t concentrations increase towards vesicle margins up to 3.1–4.7 wt. %, three times higher than the far-field plateaus of 1.2–1.6 wt. % H_2O_t. The length scale of enrichment (5 – 15 µm) is similar

amongst the five profiles; minor differences could be attributed to 2D cross-sectioning effects (McIntosh et al., 2014).

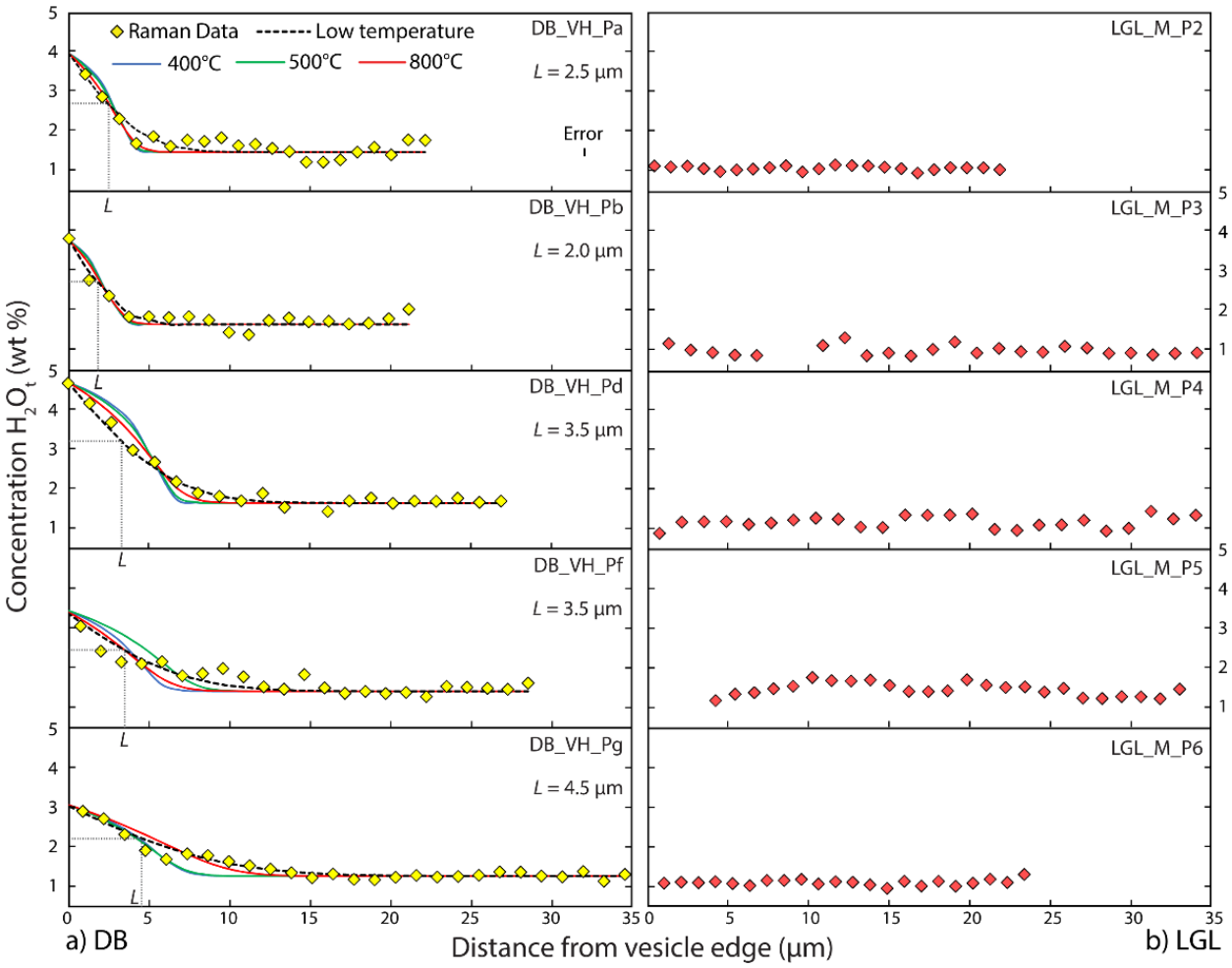

Figure 2.5. µRaman H_2O_t vesicle-edge profiles from dense samples of **(a)** dome fragments (DB) and **(b)** Lava-G-Lapilli. H_2O_t enrichments at DB vesicle edges were modelled using diffusion models for low temperature (Giachetti and Gonnermann 2013) and 400, 500 and 800°C (Ni and Zhang, 2008) scenarios. Best fit timescales calculated for each profile at each temperature are given in **Table 2.2**. *L* marks the profile half-fall distance from the vesicle edge. No systematic H_2O_t variation was found in Lava-G-Lapilli profiles. H_2O_t error is smaller than the symbol; variability in profile plateaus implies some spatial heterogeneity in glass H_2O_t.

A 1D diffusion model was applied to these enrichment profiles to estimate the necessary H_2O diffusion timescales assuming different scenarios of low temperature (5–40°C), 400°C, 500°C and 800°C (**Table 2.2**). The model was developed based on Ficks 2nd law and the elevated temperature scenarios account for known temperature and H_2O concentration-dependence of H_2O diffusivity (Ni and Zhang, 2008). See Appendix **A11** for full model outline and input parameters.

Table 2.2. 1D diffusion model input parameters, output timescales, and best-fit Σ_{RMS} values for the five DB μRaman H_2O_t profiles in **Figure 2.5a**. For low temperature, log*D* is taken as the maximum, average, and minimum H_2O diffusivity values reported for obsidian hydration in Giachetti and Gonnermann (2013). *Log*D* = -19 is an extrapolation of the Ni and Zhang (2008) H_2O diffusivity model to low temperature, assuming 4 wt. % H_2O_t. At high temperatures (400 – 800°C), *D* is calculated using the input temperature with the H_2O-dependent Ni and Zhang (2008) diffusivity model. *D* therefore varies with concentration along the diffusion profile. For these runs, a characteristic diffusivity (D_{ch}) is derived from the best-fit time and half-fall distance. See Appendix **A11** for model details.

Profile name	**Low temperature best-fit time (years)**				**Lowest Σ_{RMS} values**	**Initial C_0 (wt. %)**	**Initial C_I (wt. %)**	**Half-fall distance C (wt. %)**	**Half-fall distance *L* (μm)**
	Log*D* = **-24**	Log*D* = **-21.6**	Log*D* = **-20.7**	Log*D* = **-19***					
DB_VH_Pa	178 ka	1116	89	1.8	3.36	4.0	1.50	2.75	2.5
DB_VH_Pb	70 ka	437	35	0.7	2.35	3.8	1.67	2.735	2.0
DB_VH_Pd	225 ka	1408	113	2.2	1.68	4.7	1.65	3.175	3.5
DB_VH_Pf	334 ka	2087	167	3.3	3.33	3.5	1.40	2.45	3.5
DB_VH_Pg	551 ka	3446	276	5.5	1.98	3.1	1.25	2.175	4.5
	High temperature best-fit time (seconds)			**Lowest Σ_{RMS} values**			**Characteristic diffusivity LogD_{ch}**		
	400°C	*500°C*	*800°C*	*400°C*	*500°C*	*800°C*	*400°C*	*500°C*	*800°C*
DB_VH_Pa	26	6	0.4	4.15	3.99	3.67	-12.6	-12.0	-10.8
DB_VH_Pb	14	3	0.2	2.80	2.74	2.61	-12.5	-11.9	-10.7
DB_VH_Pd	20	6	0.5	3.40	3.11	2.35	-12.2	-11.7	-10.6
DB_VH_Pf	74	27	1.0	5.16	4.92	4.56	-12.8	-12.3	-10.9
DB_VH_Pg	150	30	2.5	3.15	3.00	2.75	-12.9	-12.2	-11.1

C is the concentration in wt. %.
D is the diffusion coefficient in $m^2\ s^{-1}$.
Σ_{RMS} is the sum of the root mean square of residuals.

Best-fit diffusion profiles and corresponding timescales were calculated based on the lowest calculated Σ_{RMS} values (sum of root mean square residuals) relative to the μRaman data (**Table 2.2**). From these, we calculated the half-fall distance (L) from the vesicle edge, i.e., the distance at which concentration is halfway between the maximum and minimum H_2O_t concentration, and a characteristic diffusivity (D_{ch}) (Anovitz et al., 2006; McIntosh et al., 2014). We find that for vesicle-edge enrichments in the dome fragment, L = 2.0–4.5 μm (**Figure 2.5a**). In highly vesicular samples, e.g., from the Giant Pumice and Ash-Lapilli-Block units, bubble wall thicknesses are always <10 μm and, in many cases, <3 μm (Appendix **A7**). For these samples, we note that similar diffusion half-fall distances would be sufficient to enrich an entire bubble wall so that no clear diffusion profile would be observable and bulk H_2O_t would be elevated across the entire wall relative to the original H_2O_t (see ALB image in Appendix **A7**).

2.4. Discussion

Both FTIR and μRaman data from Havre 2012 clasts challenge current notions for submarine clast-producing eruptions. We first use OH concentrations to find clast quenching pressures, and examine their implications and underlying assumptions. We then discuss the timescales needed for observed glass rehydration to occur using the outputs of the 1D diffusion model. Finally, we present the physical processes and conditions required to explain syn-eruptive rehydration.

2.4.1. Clast quenching pressures

Havre clasts have been affected by rehydration, so their H_2O_t contents cannot be used to reveal their equilibrium quenching pressure (P_Q). Instead, we use OH contents to determine P_Q because the concentration of this non-diffusing species becomes fixed at T_g and is unaffected by disequilibrium addition of H_2O_m (Zhang et al., 2017; Ni and Zhang, 2018). It is known from speciation models how OH content varies with H_2O_t under equilibrium conditions at a given temperature (e.g., **Figure 2.3a, b**). By assuming a value for T_g, i.e., the temperature at which OH concentration became fixed, we can translate measured OH contents into corresponding H_2O_t contents (McIntosh et al., 2017). These H_2O_t contents can then be converted into equivalent equilibrium quenching pressures (P_Q) based on the known pressure-dependence of H_2O_t solubility.

Given that cooling rates in large submarine plumes are not known, and will likely vary, we assume endmember T_g values of 400°C and 800°C when converting our OH data to P_Q values. These T_g values span the full range reported in the literature for rhyolites of varying H_2O_t contents and quench rates (see Section **2.3.1.1**). For a given OH content, lower assumed T_g gives higher reconstructed H_2O_t and higher equivalent P_Q; higher assumed T_g gives lower reconstructed H_2O_t and lower equivalent P_Q. The variation in reconstructed H_2O_t and P_Q with choice of T_g value is smallest for low OH contents, because temperature curves of speciation models all converge at low OH and H_2O_t (see **Figures 2.3a, b** and **2.6**).

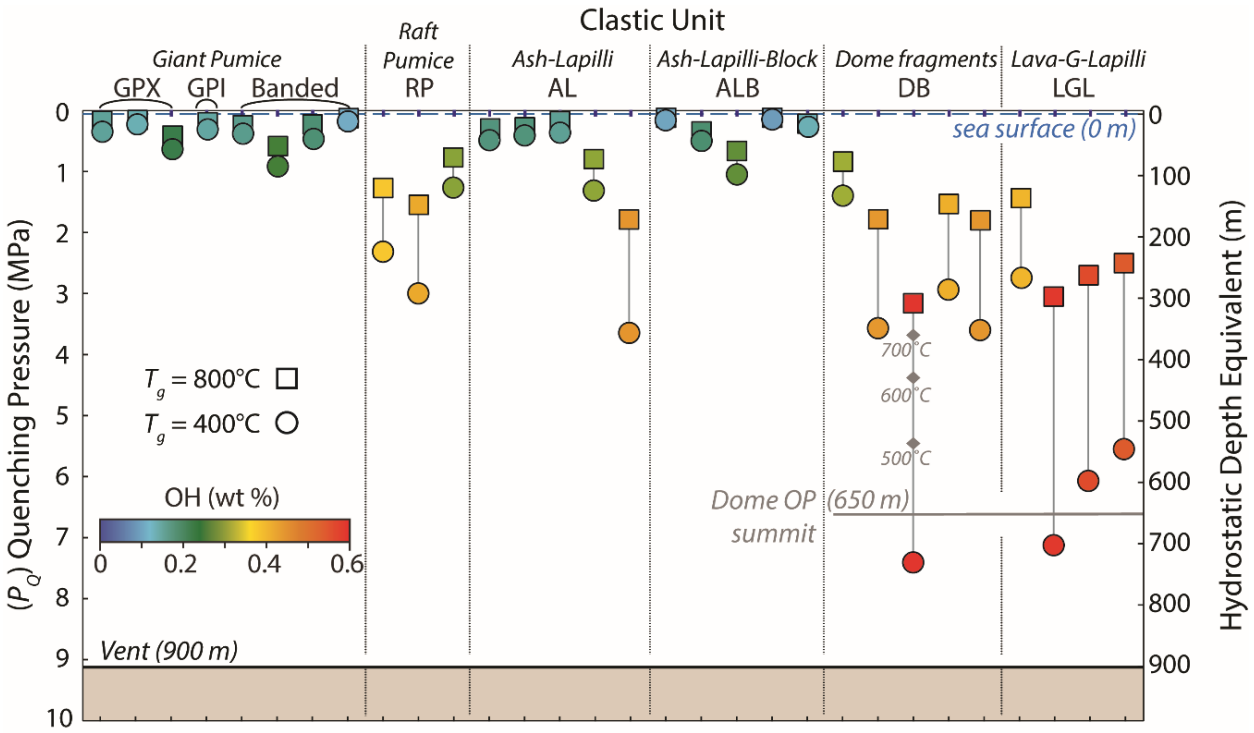

Figure 2.6. Average OH concentrations for each clast plotted against their equivalent quench pressures (P_Q), assuming T_g values between 800 °C (squares) and 400 °C (circles). One example (clast DB_VH) is shown for 100 °C increments in assumed T_g value; this highlights the greater sensitivity of P_Q to choice of T_g for low T_g values. Clast OH wt. % corresponds to the color bar. Banded Giant Pumice samples (white_GP_{in}, white_GP_{ex}, gray_GP_{ex} and gray_GP_{in}) are plotted from left to right, respectively. The 900 m vent and Dome OP summit depths (Carey et al., 2018) are plotted assuming hydrostatic pressure conditions in the water column. Sea surface (0 m) is plotted at 0.1 MPa absolute pressure.

Figure 2.6 shows P_Q values for Havre clasts calculated from clast average OH contents using our combined solubility-speciation relationships and T_g values of 400 to 800°C (see Appendix **A1** for further details). These P_Q values are converted to quench depths assuming hydrostatic equivalence. Matrix glasses of Havre clasts have significantly less OH than expected for quench at the pressure of the 900 m deep vent (where 0.6 to 0.95 wt. % OH would be expected for T_g of 400 to 800°C, respectively – see Appendix **A9**).

This is particularly the case for the Giant Pumice, Ash-Lapilli and Ash-Lapilli-Block clasts (**Figure 2.6**). The high vesicularity of these units (>65 %, **Figure 2.4a,** Appendix **A10**) indicates that the magma was saturated with volatiles, so low residual OH and H_2O_t concentrations cannot be a function of initial volatile undersaturation. Neither can they be explained by some theoretical amount of undetected CO_2 in the melt (Appendix **A9**). Low OH thus indicates that either 1) clasts were mostly quenching at very shallow depths (<300 mbsl); or 2) the assumption of hydrostatic pressure is not applicable due to reduced bulk density in the submarine plume.

2.4.1.1. Cooling rates

The data for the dome fragment lapilli and Lava-G-Lapilli present an immediate conundrum, because these are inferred to have erupted effusively at the vent (Carey et al., 2018) yet have lower OH contents than expected for vent depth (**Figure 2.6**). Using the highest average H_2O_t recorded in these clasts in the model of Giordano et al (2008) gives a predicted T_g value of ~550°C for cooling of 10 K min^{-1}. Subaerial rhyolite domes can have cooling rates of <<1 K min^{-1} (Gottsmann and Dingwell, 2001; Befus et al., 2015). It is therefore possible that these inferred effusive deposits did experience slower cooling, leading to T_g <550 °C. This could potentially explain the one DB sample that has an OH content that is consistent with quench at the depth of the overlying Dome OP. However, it is not possible for any cooling rate to create the T_g values of <400°C necessary to make the measured OH contents of the other clasts consistent with quench at vent depth. This therefore has implications for the assumption of hydrostatic pressure (see Section **2.4.1.3**).

The clasts that make up the rest of the Havre eruption sequence were mobile in the water column and should have experienced faster cooling than the dome and lava deposits. Subaerial pyroclasts quenched in air can have cooling rates of 10-100 K s^{-1}, whereas pyroclasts quenched in

water can cool at rates >100 K s^{-1} (Xu and Zhang, 2002; Wallace et al., 2003; Allen et al., 2008). However, the low OH and H_2O_t contents indicate that most Havre clasts did not quench instantaneously upon entry into the water column at vent depth. As speciation curves converge at low H_2O_t content <0.3 wt. %, the choice of assumed T_g also does not alter the low P_Q values for these clasts (**Figures 2.3** and **2.6**). Clasts therefore cooled slowly enough to allow degassing to lower pressures prior to quench. This contrasts with the near-instantaneous quench inferred for small shards from other submarine clastic eruptions (Potuzak et al., 2008; Schipper et al., 2010). The exteriors of larger clasts like those erupted at Havre are still likely to experience rapid cooling of >>10 K min^{-1} when in contact with water (Allen and McPhie, 2009; Fauria and Manga, 2018). However, clast interiors, and clast exteriors insulated by a warm submarine plume or surrounding vapor, may cool more slowly. Furthermore, submarine clasts will experience multiple stages of cooling due to competing effects of water ingestion, steam condensation and conductive cooling (Fauria and Manga, 2018). For cooling on the order of 10 K min^{-1}, even clasts with as little as 0.1 wt. % H_2O_t could spend time above the glass transition before quenching at T_g of ~700°C (Giordano et al., 2008).

Provided that upward transport through the water column occurred on the order of minutes, such cooling rates would enable Giant Pumice, Raft Pumice, Ash-Lapilli and Ash-Lapilli-Block clasts to continue degassing during decompressive ascent. Heat retention and continued degassing within larger silicic submarine clasts during ascent has been suggested previously based on expanded clast interiors in dredge samples elsewhere along the Kermadec Arc (Barker et al., 2012b; Rotella et al., 2013). With volatile speciation data, we can now further constrain the eruptive mechanisms and thermal histories of pyroclasts that cannot be distinguished from textural observations alone.

2.4.1.2. Raft and Giant Pumice segregation

OH concentrations and calculated P_Q for Raft Pumice are significantly higher than for Giant Pumice (**Figure 2.6**), which is remarkable considering that the raft pumice definitely reached the ocean surface yet giant pumice blocks are found on the seafloor proximal to the vent (**Figure 2.7a**). Raft Pumice is currently considered to be genetically linked to the seafloor Giant Pumice (>0.1

km^3) and to originate from the same vent (Carey et al., 2018). However, the distinctly higher OH content of the Raft Pumice implies differences in quenching or ascent timescales between these two units.

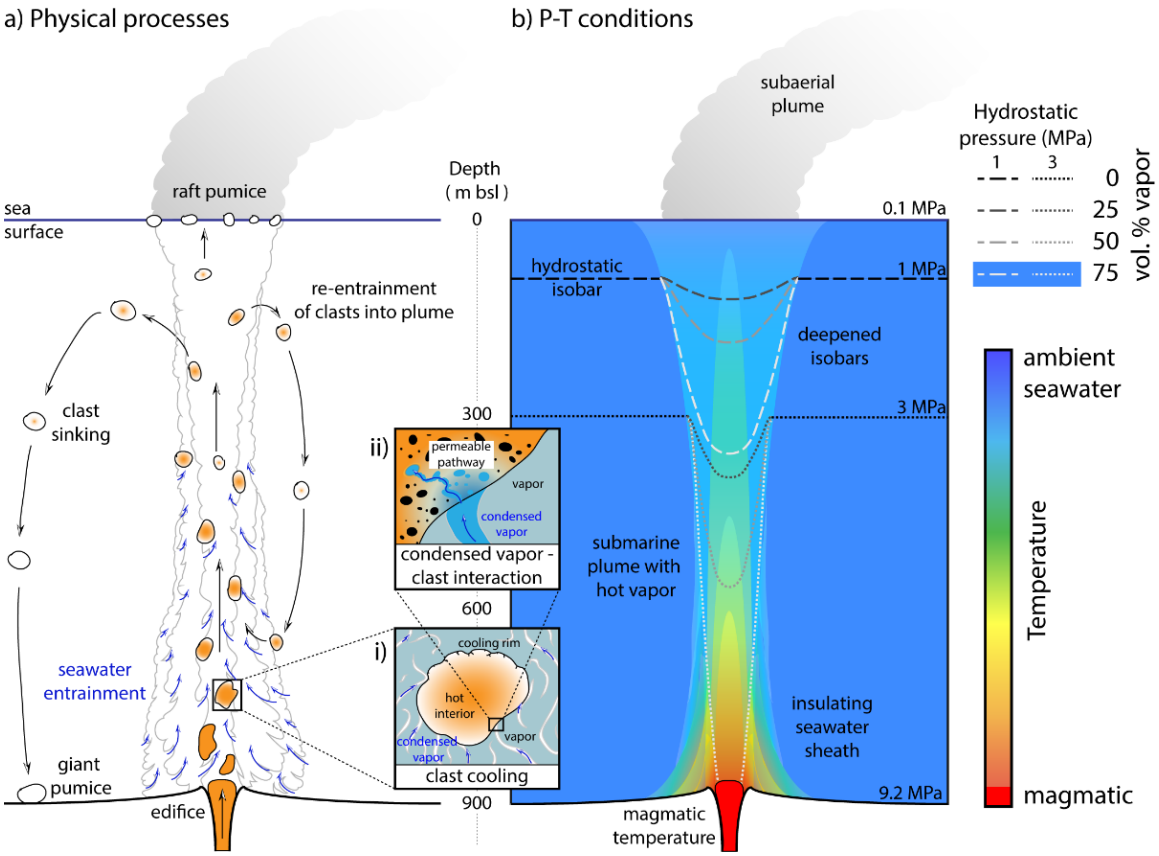

Figure 2.7. Schematic model of **(a)** physical eruption processes and **(b)** pressure-temperature conditions within the submarine volcanic plume occurring during the 2012 Havre eruption. **(a)** Clasts cool within a vapor-rich plume over timescales of seconds to minutes, enabling ongoing degassing during ascent to shallow depths. Segregation of raft and giant pumice occurs here according to influence of clast size; clasts that become waterlogged sink and may become re-entrained in the plume. Insets show **i)** interaction of hot condensed vapor with the exterior of a cooling clast, where quench fractures are beginning to develop on the upper clast rim, and **ii)** the diffusion of water through permeable bubble pathways in a hot clast, resulting in vesicle-edge H_2O_t enrichment and clast rehydration. The process of entraining seawater into a vapor-rich plume is more efficient at depth (blue arrows). **(b)** The potential for deviation from hydrostatic pressure conditions within the plume is illustrated by calculated depths of isobars at 1 and 3 MPa for varying vapor contents within the plume (0, 25, 50 and 75% by volume), assuming a simple vapor with constant density 10 kg m^{-3}. Near the vent, an insulating sheath of warm seawater may form in which higher temperature diffusion can occur on short timescales.

One possibility is that smaller clasts cooled faster, hence deeper, than larger clasts, preserving higher OH contents (Allen and McPhie, 2009). Larger clasts (e.g., giant pumice blocks) would have cooled more slowly and remained above T_g for longer, allowing for continued exsolution of volatiles and interconversion of OH to H_2O_m, resulting in lower OH concentrations upon quenching (Stolper, 1982; Zhang, 1997; Allen and McPhie, 2009; Rotella et al., 2013; Rotella et al., 2015). Alternatively, the difference in OH with clast size may occur if faster ascent of larger clasts enabled them to degas to shallower depths before quenching. The faster ascent (up to 15 m s^{-1}) of larger clasts (>1 m diameter) during the 2012 eruption has been proposed by Manga et al. (2018) due to the scaling of buoyant clast ascent velocity with clast diameter.

Another possibility is that smaller clasts were more readily transported in the eruption column than the larger clasts (**Figure 2.7a**). If smaller clasts were transported into the raft quickly enough to prevent full equilibrium exsolution and subsequently quenched rapidly in contact with air, they may preserve higher OH contents and float more readily due to the trapping of air by water ingestion (Fauria, 2017; Fauria et al., 2017). Larger, slower-cooling clasts that were less easily transported by the eruption column would spend longer in the water column than smaller clasts (Allen et al., 2008; Allen and McPhie, 2009). Ongoing degassing and slow cooling would favor lower OH, while outgassing of exsolved vapor and subsequent waterlogging would promote their settling to the seafloor. This scenario contradicts the suggestion of faster rise of giant clasts, and requires consideration of how smaller clasts could be more readily entrained and transported to the surface.

We favor the faster ascent of larger clasts as the explanation for the different OH contents of Raft Pumice and Giant Pumice. This is based on the assumption that the size distribution of the initial pumice raft was indeed finer than that of Giant Pumice (Manga et al., 2018). However, the comminution of blocks within the raft immediately after the eruption may have masked the original size distribution; there was no ocean-based observation of the raft until three weeks after the eruption. The alternative possibility is that Raft Pumice and Giant Pumice were not genetically linked, and were instead two separate eruptive phases with differences in magma ascent rates, degassing conditions, eruptive style, and/or submarine jet and plume properties. Consequently, two microtexturally-similar pumiceous units would be produced but with different degassing histories and quenching pressures. Future microtextural studies will seek to constrain any

permeability, vesicularity and vesicle size distribution distinctions between Giant Pumice and Raft Pumice that could account for observed OH variations.

2.4.1.3. The hydrostatic pressure assumption

The second possible explanation for the low OH contents of the Havre clasts is deviation from hydrostatic pressure within the submarine plume. Depth-equivalent P_Q calculations assume a hydrostatic pressure based on cold seawater with density 1027 kg m^{-3} (Millero and Huang, 2009). This may be reduced due to the presence of vapor within a submarine jet and plume. For simplicity, we consider a non-condensable magmatic vapor phase of density 10 kg m^{-3} across all water depths. By calculating pressure within the plume for a given set of vapor-liquid volume proportions, we assess the extent to which vapor addition could depress isobars in the plume (**Figure 2.7b**). If the submarine plume consists of 25, 50, or 75% vapor, the depth of the 1 MPa isobar would increase from 89 m to 118, 176, or 346 m, respectively. Likewise, the depth of the 3 MPa would increase from 287 m to 382, 570, or 900 m, respectively; the final calculation terminates at conduit depth. In reality, these phase proportions vary due to competing effects of condensation and thermal expansion of vapor. However, these simple assumptions enable us to assess the implications of non-hydrostatic pressure conditions.

The effect of vapor addition on isobar depth is weakest at shallow depths (**Figure 2.7b**), so shallow quenching (with its implications for cooling timescales and ascent rates) is still required for low OH units with apparent P_Q <<1 MPa (i.e., Giant Pumice, Ash-Lapilli-Block and Ash-Lapilli – **Figure 2.6**). Equivalent quench depths for clasts with higher OH contents corresponding to P_Q of ~1 to 3 MPa would be more affected by isobaric deepening in a vapor-rich plume, but are still likely to have quenched above the vent (**Figure 2.7b**). However, for the dome fragment and Lava-G-Lapilli clasts with higher OH contents, a combination of low T_g and deepening of isobars would be enough to make these OH concentrations consistent with quenching at vent depth (**Figure 2.6, 2.7b**). A large volume of vapor may be expected to be present with efficiently outgassing lava domes during the eruption. The influence of a vapor-rich plume would thus resolve the apparent conundrum of the relatively low OH contents of these deposits that are inferred to have erupted effusively at the seafloor (**Section 2.4.1.1**).

Modifying the bulk density of the overlying water column by vapor addition also has implications for the buoyancy of pumice within a submarine plume. Continuing with the simple assumption of a vapor phase density of 10 kg m^{-3} and bulk magma density of 2400 kg m^{-3}, clasts would need to have a minimum vesicularity of 57% in order to rise buoyantly and unassisted by momentum in hydrostatic-equivalent seawater (Allen and McPhie, 2009; Manga et al., 2018). Vapor addition, which reduces the bulk density of the overlying water column, increases the minimum vesicularity required for such buoyancy-driven ascent. For a submarine plume containing 25, 50, or 75% vapor, the minimum vesicularity for buoyant rise would increase to 68, 78, and 89%, respectively. On the other hand, decreasing overlying pressure at the vent via vapor addition would also drive higher decompression rates and subsequently greater magma ascent rates upon eruption. Magma ascent rates of >10 m s^{-1} calculated for Havre assuming normal hydrostatic pressure at the vent are sufficient to provide additional momentum to all erupted clasts (Manga et al., 2018). Increased magma ascent rates due to reduced vent pressure and the associated additional momentum would enable even those clasts below the vesicularity threshold for buoyant rise to ascend within a vapor-rich plume, and potentially to reach the surface raft (Fauria, 2017).

Complications arise when considering the stability of an "underpressured" plume due to induced lateral pressure gradients from the vapor plume into seawater. A sustained, high mass eruption rate (MER) of vapor, such as that calculated for the raft pumice phase (Carey et al., 2018), may inhibit such a collapse. Determining accurate P_Q and buoyancy thresholds requires precise knowledge of water content and speciation, CO_2 concentration, T_g, and the physical conditions within a submarine plume (**Figure 2.7b**). A complex computational model is required to assess the effects of vapor addition into the water column. Nevertheless, FTIR and µRaman data advocate for shallow, non-instantaneous quenching of pumiceous clasts in a complex, vapor-rich, deep submarine plume during the 2012 Havre eruption.

2.4.2. Timescales of rehydration

Excess H_2O_m and H_2O_t enrichment around vesicle-edges provides evidence for submarine rehydration, but does not permit direct determination of how fast rehydration occurred (**Figures 2.3** and **2.5**). Vesicular silicic pyroclasts with high connected porosity and permeable pathways

are particularly vulnerable to secondary rehydration (Giachetti and Gonnermann, 2013; Giachetti et al., 2015; Dingwell et al., 2016; Seligman et al., 2016). Accordingly, the pumiceous Havre samples (Giant Pumice and Ash-Lapilli-Block) exhibit the greatest relative extent of rehydration (**Figure 2.4,** Appendix **A10**). This is consistent with the thin bubble walls within these pumices (Appendix **A7**). However, the relative lack of rehydration characteristics in Lava-G-Lapilli and the large range of rehydration characteristics in dense dome fragments, despite all samples being the same young age, suggests simple secondary rehydration cannot be the sole contributor of excess disequilibrium H_2O_m.

The rate of rehydration depends heavily on the diffusivity coefficient (D_{H2O}), which covers a broad range of 10^{-24} to 10^{-21} (m^2 s^{-1}) at ambient temperature, to 10^{-14} to 10^{-11} for 400–800°C (Ni and Zhang, 2008; Giachetti and Gonnermann, 2013; Seligman et al., 2016). The calculated half-fall distances (L) of dome fragment profiles enable us to explore possible rehydration mechanisms and timescales. For low temperature diffusion, we use L and the maximum timescale (τ_{max}) for rehydration to occur (i.e., the 1000 days between eruption and sampling) to calculate a characteristic diffusivity (D_{ch}) where $D_{ch} = L^2/\tau_{max}$ (Appendix **A11**). We find that resulting D_{ch} values of $10^{-19.3}$ to $10^{-18.6}$ are too high to be consistent with secondary rehydration up to 100°C, which would require anything from 40 to 500,000 years to form the observed profiles (**Table 2.2**, **Figure 2.8**) (Giachetti and Gonnermann, 2013; Bindeman and Lowenstern, 2016). For Raft Pumice collected only 300 days after the eruption, logD_{ch} values would be even higher (-18.8 to -18.1). The diffusion model proves that, whilst ambient seawater provides a dense medium with abundant H_2O molecules to diffuse across a liquid-glass interface, its temperature is too low create the observed profiles by simple secondary rehydration.

Assuming instead that dome fragment rehydration profiles formed at higher temperatures, we find that their best-fit timescales are 13–151 seconds for T = 400°C, 3–30 seconds for 500°C, and <3 seconds at 800°C (**Figure 2.8**, **Table 2.2,** Appendix **A11**). These correspond to logD_{ch} values of -12.9 to -10.6 (**Table 2.2**). Although diffusion modelling assumed a constant temperature, in reality, profiles will have formed over a temperature range during cooling. The relatively high logD_{ch} values suggest, however, that time spent at high temperature may be the dominant control on rehydration (McIntosh et al 2014; Bindeman and Lowenstern, 2016). Together these results

imply rehydration occurred at temperatures above or near the glass transition on timescales of seconds to minutes, consistent with our inferred clast cooling and ascent rates (Manga et al., 2018).

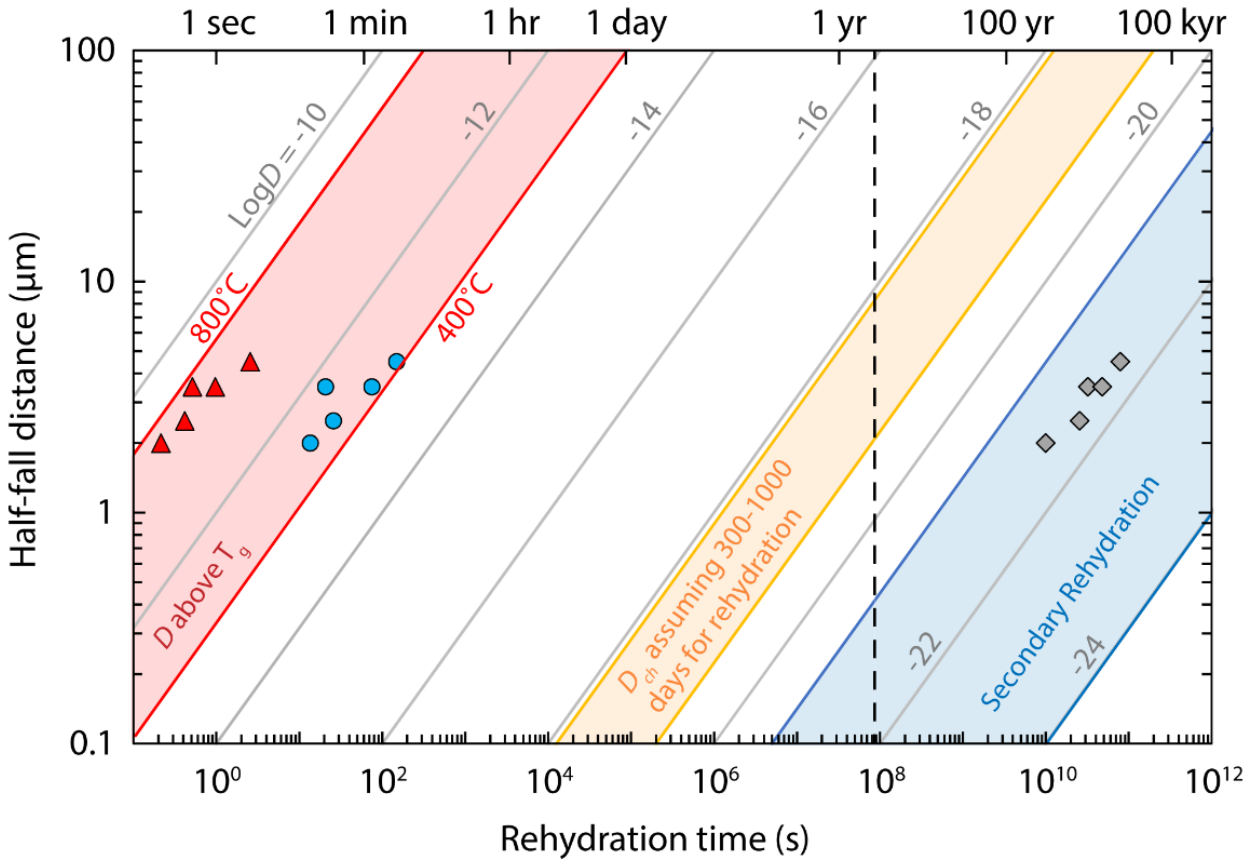

Figure 2.8. Relationship between rehydration length scale, time, and H_2O diffusivity, based on $L = \sqrt{Dt}$. Red area covers H_2O diffusivity in rhyolite melt/glass at 400 – 800 °C (Ni and Zhang, 2008). Blue area covers H_2O diffusivity during low temperature secondary rehydration (Giachetti and Gonnermann, 2013). Half-fall distances (L) from DB profiles (**Figure 2.5**) are plotted against their best-fit timescale for diffusion at low T (gray diamonds), 400 °C (blue circles) and 800 °C (red triangles). Yellow area covers the characteristic diffusivity (D_{ch}) values required for the DB profiles to form in the time between eruption and sampling (300 – 1000 days; dashed line).

2.4.3. Potential rapid rehydration mechanisms

Given the timescales and temperatures of rehydration suggested by our diffusion modelling, we now explore the physical mechanisms and H_2O sources that could produce rapid rehydration signatures. The dome fragments that contain the modelled H_2O_t enrichments are inferred to have cooled within an effusive dome carapace at < 10 K min^{-1}. The enrichment profiles are similar to those in experiments showing cooling-induced resorption of magmatic vapor from vesicles into melt/glass (McIntosh et al., 2014). The low vesicularity (<30%) and presence of isolated bubbles within these dome fragments may indicate that vapor resorption was accompanied by reduction in bubble volume, as outgassing cannot occur at such low porosity (Watkins et al., 2012). This would suggest that the rehydration source was magmatic H_2O within bubbles. Bubble resorption can also be caused by pressure increase (Watkins et al., 2012), as might be experienced by sinking clasts, but it would only create the observed disequilibrium speciation if temperature was also decreasing and preventing interconversion of resorbed H_2O_m. Vapor resorption can continue at temperatures below T_g, provided that there is sufficient time for significant diffusion (McIntosh et al 2014; Bindeman and Lowenstern, 2016). Vapor resorption from isolated bubbles in a slowly cooling dome deposit would therefore account for why these dense dome fragments with high H_2O_t and H_2O_m/OH deviate from the overall trend in T_{ae} vs. vesicularity (**Figure 2.3d, 2.4a,** Appendix **A10**).

Clasts from other units are inferred to have cooled more rapidly in the water column. Based on the observed trends in higher H_2O_m/OH and lower T_{ae} with increasing vesicularity and decreasing quench pressure, we suggest that residence time within the plume was a key control on the extent of rehydration (**Figure 2.7a**). Temperatures between 300°C and T_g would produce observed disequilibrium speciation on the order of minutes to hours, consistent with inferred cooling timescales (**Table 2.2; Figure 2.8**). Syn-eruptive rehydration at intermediate temperatures within the plume can therefore account for the short timescales, range of excess H_2O_m, and $T_{ae} << T_g$ values in Havre pumice (**Figures 2.3** and **2.8**).

Young vesicular pyroclasts from subaerial eruptions where cooling rates are rapid (Xu and Zhang, 2002) do not exhibit disequilibrium speciation and rehydration signatures, and hence vapor resorption is unlikely (e.g., Pinatubo, 1991; Soufrière Hills, 1997 – Giachetti and Gonnermann,

2013). This is likely similar for vesicular submarine clasts. Instead, rapid diffusion from an external water source is required to explain the syn-eruptive rehydration of vesicular Havre clasts.

One possible rehydration source is heated seawater, as a turbulent plume will entrain surrounding seawater (**Figure 2.7a**). However, the high specific heat capacity of seawater, which increases above 100°C (Driesner, 2007), would make it challenging for erupted clasts and exsolved gases to heat large parcels of water entrained within the plume. The more likely scenario is rehydration by hot, condensed magmatic H_2O within the submarine plume (**Figure 2.7**). H_2O is not supercritical at 1–10 MPa and condenses at 180–307°C (Bischoff and Rosenbauer, 1984). Exsolved magmatic water present at temperatures >100°C in both the water column and erupted clasts would therefore exist as a liquid, in contrast to subaerial plumes where it would be vapor. As it is more kinetically-favorable to diffuse a liquid across an interface than a vapor, this would provide an efficient rehydration source. The presence of liquid H_2O at temperatures up to 300°C means that clasts erupted into a superheated liquid-vapor mixture that cooled more slowly during decompressive ascent (**Figure 2.7**). Diffusion can occur both above and below T_g on timescales that are orders of magnitude faster than secondary rehydration (**Figure 2.8**), so rehydration is likely to continue even as clasts continue to cool below T_g (Bindeman and Lowenstern, 2016). This is particularly so for larger clasts where the interiors cool slowly (GP_{in} – **Figure 2.7a**).

The nature of the rehydration source (heated seawater or condensed magmatic vapor) will be investigated in subsequent isotopic analyses and geochemical modelling. With our existing data, we here provide evidence for a potentially novel syn-eruptive rehydration mechanism of volcanic clasts during a deep submarine eruption, which may be unique to high-pressure eruptive environments.

2.5. Concluding Remarks

Volatile data and speciation data are critical evidence for evaluating syn- and post-eruptive processes and conditions, particularly in deep submarine environments where eruptive styles are unwitnessed. Our volatile analysis from clastic products of the 2012 deep submarine Havre eruption offers several major findings:

1) Hot, buoyant clasts quenched hundreds of meters above the vent, as evidenced by low OH concentrations of matrix glasses.
2) Pumiceous clasts erupted into large, thermally-insulating submarine plumes may experience similar cooling rates to pyroclasts in subaerial plumes, as opposed to rapid quenching rates in cold seawater.
3) Addition of vapor to the water column may reduce ocean density and therefore pressure, and consequently have a profound effect on pumice buoyancy, clast quenching, and eruptive vent dynamics in the deep submarine environment.
4) Extensive rehydration identified within the recently erupted products suggests a more rapid and complex rehydration mechanism than slow secondary rehydration by cold seawater. Instead, rehydration is caused by either hot seawater or condensed magmatic vapor.

Our study develops the current paradigms of deep submarine eruptive processes and the extent of interaction of clasts with ambient fluids during large submarine eruptions. Our interpretations of volatile contents from analyses of glass samples provide an analytically robust foundation for future, heavily quantitative studies and inputs for computational modelling. By understanding fully the physical and chemical processes occurring within a submarine eruptive plume and linking these to measureable volatile contents of erupted glasses, we can significantly improve interpretation of large submarine volcaniclastic eruptions and their products.

3. SUBMARINE GIANT PUMICE: A WINDOW INTO THE SHALLOW CONDUIT DYNAMICS OF A RECENT SILICIC ERUPTION

Currently in review as: *Mitchell, S. J., Houghton, B. F., Carey, R. J., Manga, M., Fauria, K., Jones, M. R., Conway, C. E., Soule, A. S., Wei, Z., & Giachetti, T., Submarine giant pumice: A window into the shallow conduit dynamics of a recent silicic eruption. Bulletin of Volcanology.*

ABSTRACT

Meter-scale vesicular blocks, termed "giant pumice", are characteristic primary products of many subaqueous silicic eruptions. The size of giant pumice allows us to describe meter-scale variations in textures and geochemistry with implications for shearing processes, ascent dynamics and thermal histories within submarine conduits prior to eruption. The submarine eruption of Havre volcano in 2012 produced at least 0.1 km^3 of rhyolitic giant pumice from a single 900-meter-deep vent, with blocks up to 10 meters in size transported to at least 6 km from source. We sampled and analyzed 29 giant pumice from the 2012 Havre eruption. Geochemical analyses of whole rock and matrix glass show no evidence for geochemical heterogeneities in parental magma; any textural variations can be attributed to equilibrium crystallization of phenocrysts and microlites, and degassing. Meter- to micron-scale textural analyses of giant pumice identify textural diversity throughout an individual block and between the exteriors of individual blocks. Extensive growth of microlites occurred near conduit walls where magma was then mingled with ascending microlite-poor, low viscosity rhyolite. We identify evidence for post-disruption vesicle growth during pumice ascent in the water column above the submarine vent. A 2D cumulative strain model with a flared shallow conduit may explain observed vesicularity contrasts (elongate tube vesicles vs spherical vesicles). Low vesicle number densities in these pumice from this high-intensity silicic eruption demonstrate the effect of hydrostatic pressure above a deep submarine

vent in suppressing rapid late-stage bubble nucleation and inhibiting explosive fragmentation in the shallow conduit.

3.1. Introduction: Submarine giant pumice

Voluminous deposits of giant pumiceous blocks up to meters across ("giant pumice") are more commonly associated with submarine silicic eruptions than subaerial eruptions and can be found throughout the subaqueous volcaniclastic record (Kano et al., 1996; Risso et al., 2002; Kano, 2003; Allen and McPhie, 2009; Allen et al., 2010; Von Lichtan et al., 2016; Manga et al., 2018). They are observed (1) in uplifted ancient sequences with interpreted subaqueous provenance, (2) on the modern seafloor, or (3) on fossil lake shores from sublacustrine volcanic eruptions (Risso et al., 2002; Allen and McPhie, 2009; Houghton et al., 2010; Barker et al., 2012b; Carey et al., 2018). Subaqueous giant pumice have been studied in detail at Lake Taupo, New Zealand from the 1.8 ka Taupo eruption (White et al., 2001; Houghton et al., 2010; von Lichtan et al., 2016), the Sumisu Domes on the Izu-Bonin arc (Allen et al., 2010) and in other locations of various water depths, although in less detail (Risso et al., 2002; Kano, 2003).

Multidisciplinary analytical studies have been conducted for decades on pumice from *subaerial* silicic eruptions to infer shallow conduit dynamics and processes of volatile exsolution from the host melt (Whitham and Sparks, 1986; Klug et al., 2002; Polacci et al., 2004; Wright et al., 2006b; Giachetti et al., 2010; Houghton et al., 2010; Shea et al., 2010). Quantitative information, such as vesicle number densities, vesicle volume distributions, permeability and vesicle connectivity, is commonly extracted from studies of vesicular microtextures. In combination with geochemical data and models for magma ascent, these data can be used to understand bubble nucleation, bubble coalescence, magma decompression rates and outgassing from the conduit.

Similar techniques can be applied to deposits in submarine settings to reveal the effects of high hydrostatic pressure from the overlying ocean, which provides a fundamental control on the production of pumiceous clasts (Head and Wilson, 2003; Cas and Giordano, 2014; Murch, 2018). Explosive fragmentation of magma in conduits is thought to occur at very shallow vents or at sufficiently high decompression and strain rates (Cashman and Scheu, 2015; Manga et al., 2018).

Non-explosive mechanisms include the spalling of hot, vesicular subaqueous dome carapaces (Houghton et al., 2010; Allen et al., 2010), slow, buoyant detachment of hot, vesicular magma bodies (Rotella et al., 2013), or the rapid propagation of cooling joints through a rapidly ascending magma body in the water column (van Otterloo et al., 2015; Manga et al., 2018). Limited understanding of the fragmentation mechanisms results from the lack of direct observations of submarine silicic eruptions.

One benefit of analyzing giant pumice is their preservation of meter-scale variations in texture, providing a larger, intact window into the dynamics of magma ascent and fragmentation than smaller lapilli. Giant pumice from the 2012 eruption of Havre submarine volcano have a moderately well constrained mass eruption rate and vent depth (Carey et al., 2018; Manga et al., 2018). This study presents detailed textural and geochemical analyses of giant pumice and provides a quantitative bridge between observations and inferred physical processes within a submarine silicic conduit. Characterizing giant pumice at sub-meter- to micron-scale resolution allows us to assess the role of hydrostatic pressure control on magma decompression and fragmentation.

3.2. Giant pumice from the 2012 Havre eruption

The 2012 eruption of Havre volcano on the Kermadec Arc, NZ, is the largest recorded deep submarine silicic eruption in the last 360 years. More than 1.5 km^3 of rhyolite (70–72 wt. % SiO_2) erupted at vent depths of 650–1220 m with the majority of the volume from one 900 m deep vent (Carey et al., 2014; Carey et al., 2018). A deposit of giant pumiceous blocks (GP unit) up to five clasts thick covers >36 km^2 of the caldera floor to at least six km from the vent. The calculated volume in this sector is 0.1 km^3, which is a minimum as the deposit extends further than six km in the unmapped region down-current from the vent. The seafloor giant pumice deposit is inferred to be genetically related to the production of a pumice raft that formed over a 21.5 hour period on July 18, 2012 from their similar dispersal patterns (Jutzeler et al., 2014; Carey et al., 2018). Assuming a synchronous, linked origin, the time-averaged mass eruption rate estimated for this eruptive phase is ~10^7 kg s^{-1} (Carey et al., 2018). Clast diameters, based on remotely operated vehicle (ROV) observation, average 1–2 m and increase with distance from the vent; the largest

observed clasts are 9 m in diameter (Carey et al., 2018). Works is in progress to determine the full size distribution of giant pumice has not yet been determined. A 0.11 km^3 rhyolitic dome – named Dome OP – now overlies the vent responsible for the pumice raft and GP deposit (**Figure 3.1**).

A 1D conduit ascent model for Havre 2012 conditions and magma is compatible with fragmentation *above*, and not below, the vent (Manga et al., 2018). The inferred dissolved magmatic water concentration at 900 m depth (9.2 MPa hydrostatic pressure) would have kept the melt viscosity low enough that the strain rate fragmentation threshold (Papale, 1999; Gonnermann and Manga, 2003) was not reached before extrusion into the ocean. Giant pumice blocks display a range of clast-scale textures: sub-rounded to angular shapes, exterior fabrics within preferred lineation of textures, angular curvi-planar exteriors, deep fractures within entire clasts, and rare breadcrusted exteriors (**Figure 3.1**).

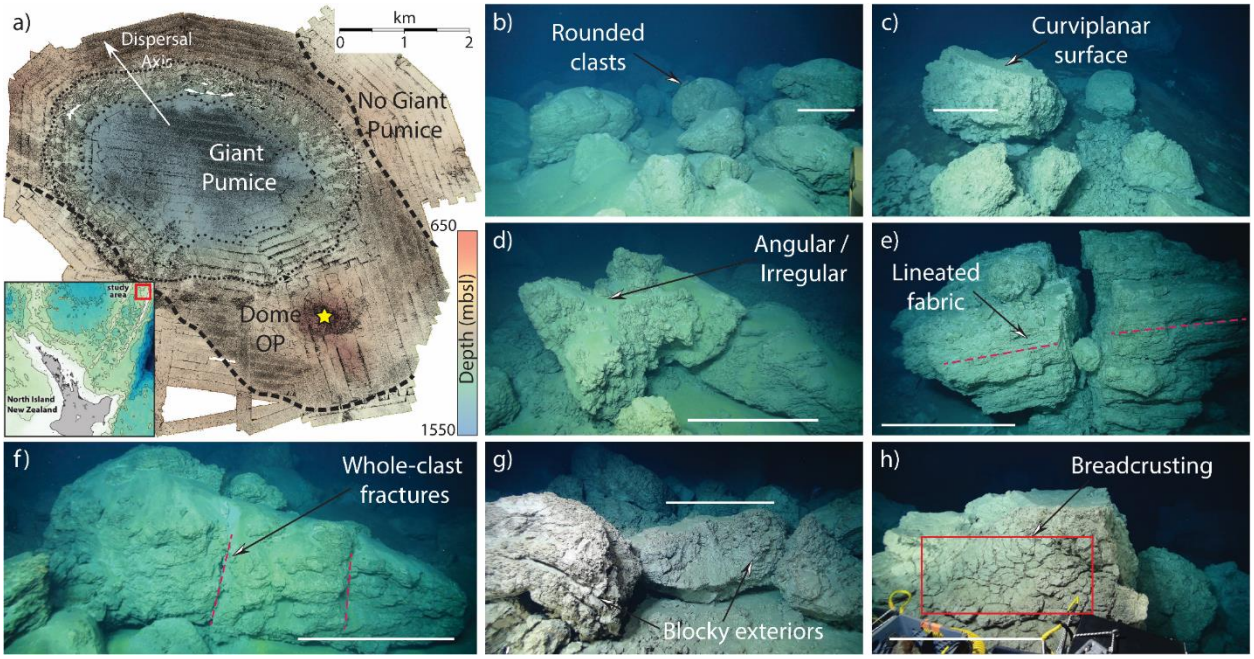

Figure 3.1. Characteristics of GP from the 2012 Havre eruption. (a) Distribution of GP across the Havre caldera illustrated as seafloor roughness from AUV bathymetry. A clear interface between rough and smooth outlines the extent of GP (dashed line); the proposed vent locality under Dome OP is starred (Carey et al., 2018). The location of the Havre caldera along the Kermadec Arc is given in the inset. Examples of GP blocks are given in (b) through (f) highlighting a variety of morphological and textural characteristics, a 1 m scale bar is given in each image for the relevant clast.

3.3. Analytical methods

The pumiceous exteriors of 29 individual giant pumice, and one intact 1.5x1x1m giant pumice (GP290), were collected with a remotely operated vehicle, *Jason*, in 2015 (Carey et al., 2018). In this study, we use 'exterior fragments' to refer to broken pieces of individual GP exteriors, including the GP290 exterior. Exterior fragments up to 30 cm across were examined and classified by their dominant macrotextural characteristics from a subset of 26 individual GP clasts; 10 were then selected for more detailed density, microtextural and geochemical analysis. GP exterior fragments were classified either as *banded*, *regular* (lack of banding or significant vesicle shearing) or *tube* (pumice with dominantly tube vesicles – Kato, 1987; Dingwell et al., 2016) (see Appendix **B1** for details).

3.3.1. Density and 2D microtextural analysis

For the 10 analyzed giant pumice, we measured density/vesicularity from 10 – 100 exterior fragments 8–32 mm in diameter following the methods of Houghton and Wilson (1989). Clasts selected for thin section and geochemical analysis represented the modal density, i.e., close to mean vesicularity, of each distribution. Backscattered electron (BSE) images of thin sections were acquired at 50x, 250x and 500x magnification for vesicles and at 250x, 500x and 1000x for microlites using a JEOL JXA-8500F microprobe analyzer at 15 keV accelerating voltage with an 8 nA beam current at the University of Hawai'i at Mānoa (see Appendix **B2** for image processing).

Vesicle number densities (N_V) and volume distributions (VVDs) of vesicles 2.4 µm to 3.78 mm in diameter were acquired from binary-processed BSE images and scans following Shea et al. (2010), assuming spherical vesicle geometries as per the methods of Sahagian and Proussevitch (1998) (see Appendix **B2** for stereo-conversion details). The stereo-conversion of elongate, tube and sheared vesicles uses a modification of the Sahagian and Proussevitch (1998) method (see Appendix **B3**). Microlite number densities (mN_A) were determined from counting microlites in BSE images where mN_A values were corrected for image vesicularity to obtain microlites per melt area (mN_{Am}).

3.3.2. 3D textural analysis

A 0.8x0.4x0.4 m fragment taken from one half of the intact 1.5 m-wide giant pumice clast (GP290) was scanned at 0.165 mm/voxel resolution using X-ray computed tomography at the University of Texas Austin micro-CT facility. Small cores (<10 mm^3) from GP290 and other Havre pumice were imaged at 0.61 and 1.22 µm/voxel resolution using X-ray computed microtomography (XRT) on beamline 8.3.2 at the Lawrence Berkeley National Laboratory's Advanced Light Source synchrotron facility. Scans were used to obtain vesicle aspect ratios and vesicle orientation in samples with either spherical or elongate vesicles (see Appendix **B4** for method details).

Cylindrical cores (2–10 cm^3) were extracted from 26 GP exteriors to determine connected vesicle porosity and permeability (k); 27 GP290 cores were used to assess textural diversity within a single giant pumice. Cores with tube vesicles were acquired in orientations parallel and perpendicular to the elongation axis. The Darcian (k_1) and inertial (k_2) permeability of cylindrical cores were determined using a PMI CFP-34RUE8A-3-6 Capillary Flow Porometer at the University of Oregon. k_1 and k_2 values were fit to the Forchheimer equation over a range of flow rates (Degruyter et al., 2012):

$$\frac{\Delta P}{L} = \frac{\mu_g}{k_1} U + \frac{\rho_g}{k_2} U^2 \qquad \text{(Eq. 1)}$$

where ΔP is pressure difference over the core, L is core length, U is flow rate determined from the outgassing velocity and core cross-sectional area, ρ_g is air density = 1.2 kg m^{-3}, and μ_g is gas viscosity = 10^{-5} Pa s.

Vesicle connectivity was determined for cores and non-cylindrical fragments of samples that were too fragile to core. We measured the porosity of 61 fragments, 52 of which had cylindrical geometries suitable for permeability analysis. Total porosity (ϕ_t) and connected porosity (ϕ_c) of cores/fragments were determined using an AccuPyc II 1340 Gas Pycnometer at the University of Oregon. Connectivity (c) was quantified as the ratio ϕ_c/ϕ_t.

3.3.3. Whole rock and glass geochemistry

X-ray fluorescence analyses (XRF) of crushed whole-rock samples determined the major, minor and trace element concentrations of the bulk magma composition of 10 pumice clasts, as

well as grey and white bands from GP290. XRF analyses used a Rigaku RIX1000 at the National Museum of Nature and Science in Tsukuba, Japan (see Appendix **B5** for XRF analysis details). Matrix glass and phenocrysts (plagioclase, orthopyroxene and titanomagnetite – Carey et al., 2018) were analyzed using the UH Mānoa microprobe at 15 keV with a 10 nA current. The microprobe obtained major and minor element concentrations.

3.4. Geochemistry of Havre giant pumice

The whole-rock major element compositions of giant pumice samples determined in this study are consistent with those previously reported for the pumice raft and Dome OP from the 2012 Havre eruption (Rotella et al., 2015; Carey et al., 2018) (**Figure 3.2**). Giant pumice samples analyzed have a narrow SiO_2 range of 71.9–72.3 wt. % (normalized to 100 wt. %) where all elements are within 8% relative standard deviation (RSD) and with no variation between individual samples (see Appendix **B5** for all analyses). Similarly, there is little variation in trace element geochemistry with statistical differences only for S and Cu, though there is no statistical correlation between the two. There is no bulk geochemical variation between adjacent white and grey bands from GP290 (see Appendix **B5**).

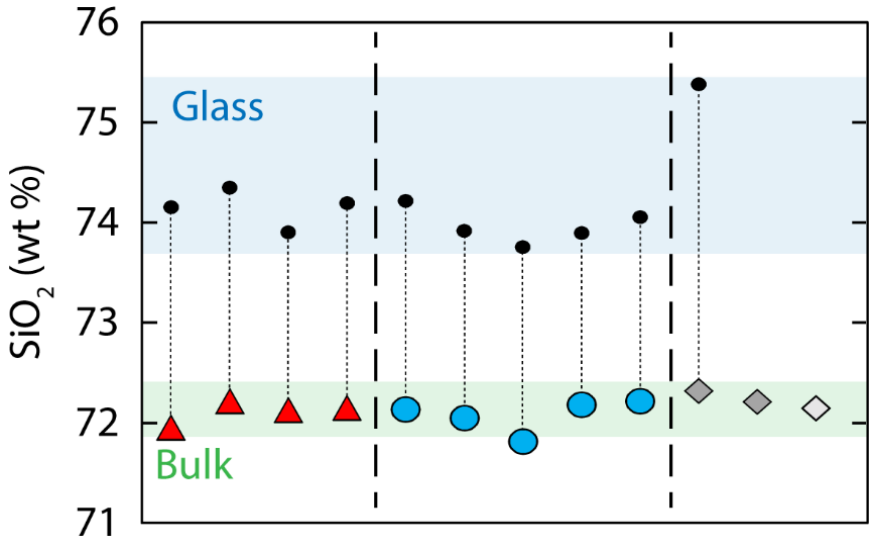

Figure 3.2. Major element SiO_2 variation between whole rock and matrix glass for each sample in every textural classification: Tube (red triangle), Regular (Blue circle), Banded (grey and white diamonds). The green box gives the whole rock range of raft pumice and Dome OP from Rotella et al. (2015) and Carey et al. (2018).

There are greater geochemical variations within matrix glasses between giant pumice than bulk composition. The SiO_2 range increases to 74.1–75.5 wt. % where the more evolved glass compositions are found within grey banding (GP290), even when directly adjacent to white bands (**Figure 3.2**). We can attribute major element variations in glass to the equilbrium crystallization of the expected phenocryst and microlite phases (see Appendices **B5** & **B6**). The lack of significant or consistent variation in major and/or incompatible trace elements between giant pumice and previous XRF analyses indicates a chemically homogeneous GP magma source with no evidence for mixing with a second, geochemically-distinct magma.

3.5. Textural results

GP clast exteriors (including GP290) were classified into three main groups: regular, tube and banded based on macro-scale observations (**Figure 3.3**). Regular giant pumice fragments have average vesicularities of 68–89%, tube giant pumice fragments =62–88% and banded giant pumice fragments =64–84%. There is no observable variation in giant pumice vesicularity with distance from source, although full assessment is limited by the number and spatial distribution of samples (see Appendix **B1**). There are two forms of banding in giant pumice. First, we observe thin (mm-scale) sinuous banding with slight color variation. Thin banding is defined by localized regions that appear slightly darker in hand samples with inferred higher density. A second type of banding contains cm-wide darker grey bands with sharp boundaries with adjacent white bands of similar density (**Figure 3.3**). Out of 29 giant pumice analyzed, only GP290 displays the second form of banding (**Figure 3.3i-k**).

Elongate vesicles with near circular cross sections dominate tube pumice (e.g., **Figure 3.3**). Banded pumice display a similar macrovesicular texture to the regular samples and lack tube vesicles, although some stretched vesicles are present. There is also variability between individual regular giant pumice where large, cm-size vesicle populations dominate some samples but not others (**Figure 3.3a-d**). There is little evidence from macroscale observations for collapsed degassing pathways or magma compaction in any of the giant pumice samples (Saar and Manga, 1999; Rust and Cashman, 2004; Burgisser et al., 2017).

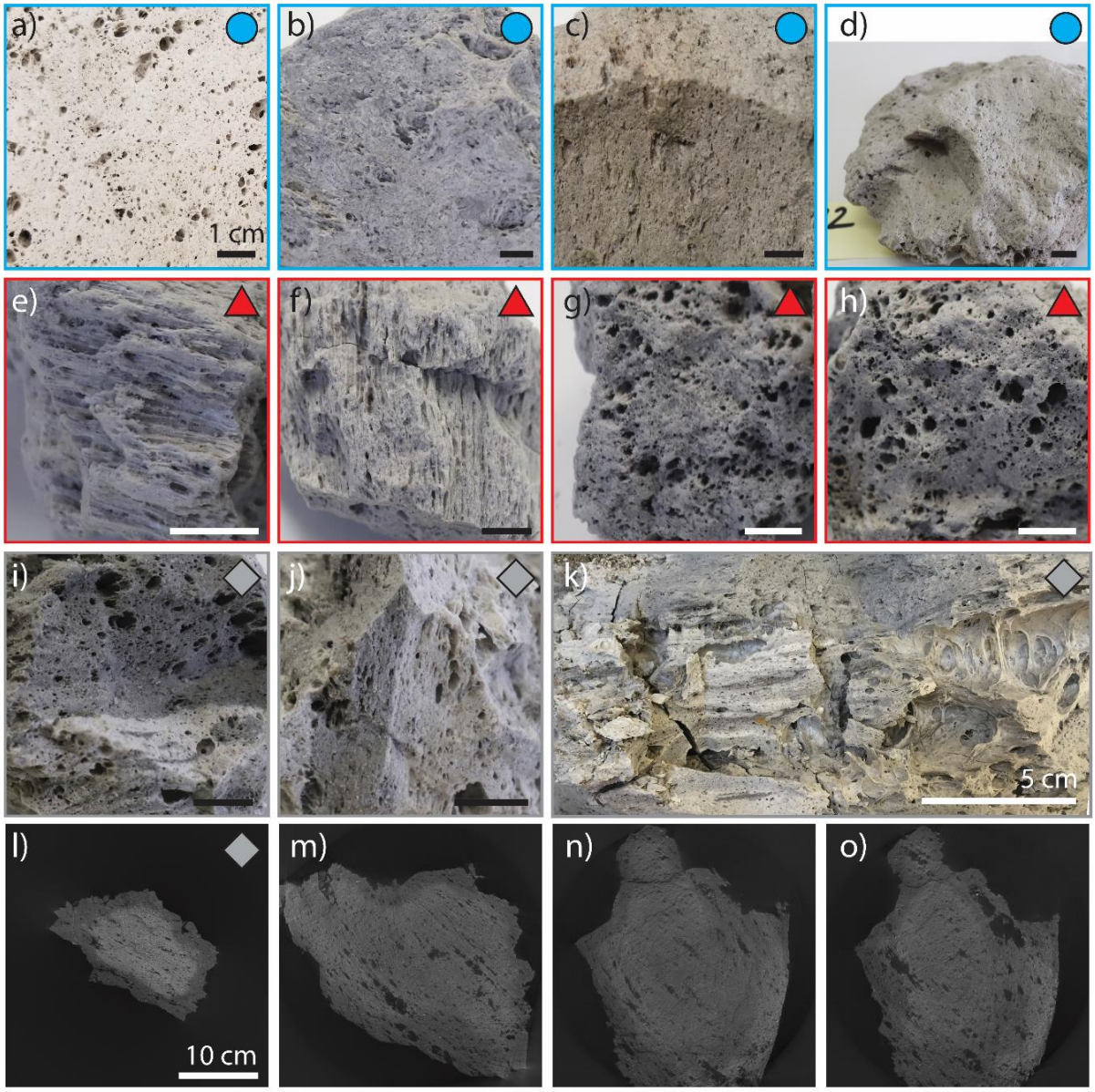

Figure 3.3. Macrotextural classification of giant pumice fragments and large scan images. 'Regular' pumice given in (a) though (d). 'Tube' pumice are given both normal (e and f) and parallel (g and h) to the elongate vesicle orientation. Grey and white bands in giant pumice (GP290) have sharp interfaces between bands (i-k). Images (a) through (j) are given with a 1 cm scale bar and corresponding symbology to Figure 2. Images (l) to (o) show 2D slices through the large GP290 scan; images are the same size. Note the darker edges in (l). Thin fractures crosscut the GP290 fragment with multiple jointing directions.

3.5.1. Whole-clast textural heterogeneity in GP290

GP290, the 1.5 m^3 intact giant pumice recovered from the seafloor 1.4 km from the main vent, serves as our meter-scale window into magma textural diversity. The 3D CT scan of a large fragment from GP290 shows variations in the abundance of mm to cm-size vesicles, and reveals large, 5-10 cm vesicles that we cannot see in thin section or small fragments (**Figure 3.3l - o**). Vesicle with diameters <500 µm (~3 pixel resolution) are not resolved in the coarse-resolution CT scan. There is a darker, lower density rind (85-90% vesicularity and <4 cm thick) on the exterior portions of the pumice fragment enclosing a heterogeneously vesicular interior (**Figure 3.3l**).

Permeable pathways are a few cm across and run throughout the fragment, but have no preferred orientation relative to the exterior, e.g., radial from the center. There is no visible change in abundance of large 1-5 cm diameter vesicles away from the exterior. There are also small, randomly oriented zones of shearing up to 5 cm across, but adjacent non-sheared regions are not marked by sharp textural interfaces. Banding is difficult to distinguish with the CT scan due to a lack of density contrast between grey and white bands, but visual observations suggest that even though bands may run parallel through the clast, there is little preferred orientation relative to the clast exterior.

These observations (reflected in other fragments of GP290) reveal the textural heterogeneity captured within a single meter-sized giant pumice clast (Carey et al., 2018). GP290 appears to show greater textural diversity (banding and vesicle size distributions) compared to the other 28 GP block exteriors sampled. However, the largest of these exterior pieces was <40 cm across so we are not able to observe the full textural diversity in other giant pumice.

3.5.2. Permeability and vesicle connectivity

There is no systematic distinction in permeability between the pumice textural types (banded, tube, regular) (**Figure 3.4a, b**). Darcian permeability (k_1) varies across all GP exteriors (5×10^{-13} to 2×10^{-9} m^2); GP290 k_1 values span a narrower range (5×10^{-13} to 10^{-11} m^2). The broad range is expected for pumice with high vesicularity and coalesced vesicles where the highest k_1 values reflect large vesicles within cores (Degruyter et al., 2012). There is no correlation between connected porosity and permeability, and all k_1 and k_2 (inertial) values for GP lie within the region

defined as "explosive" for subaerial magma (Degruyter et al., 2012) despite the inferred "non-explosive" fragmentation of GP (Manga et al., 2018). Permeability in tube pumice does not depend on vesicle orientation, probably because of the very high connected porosity (**Figure 3.4**).

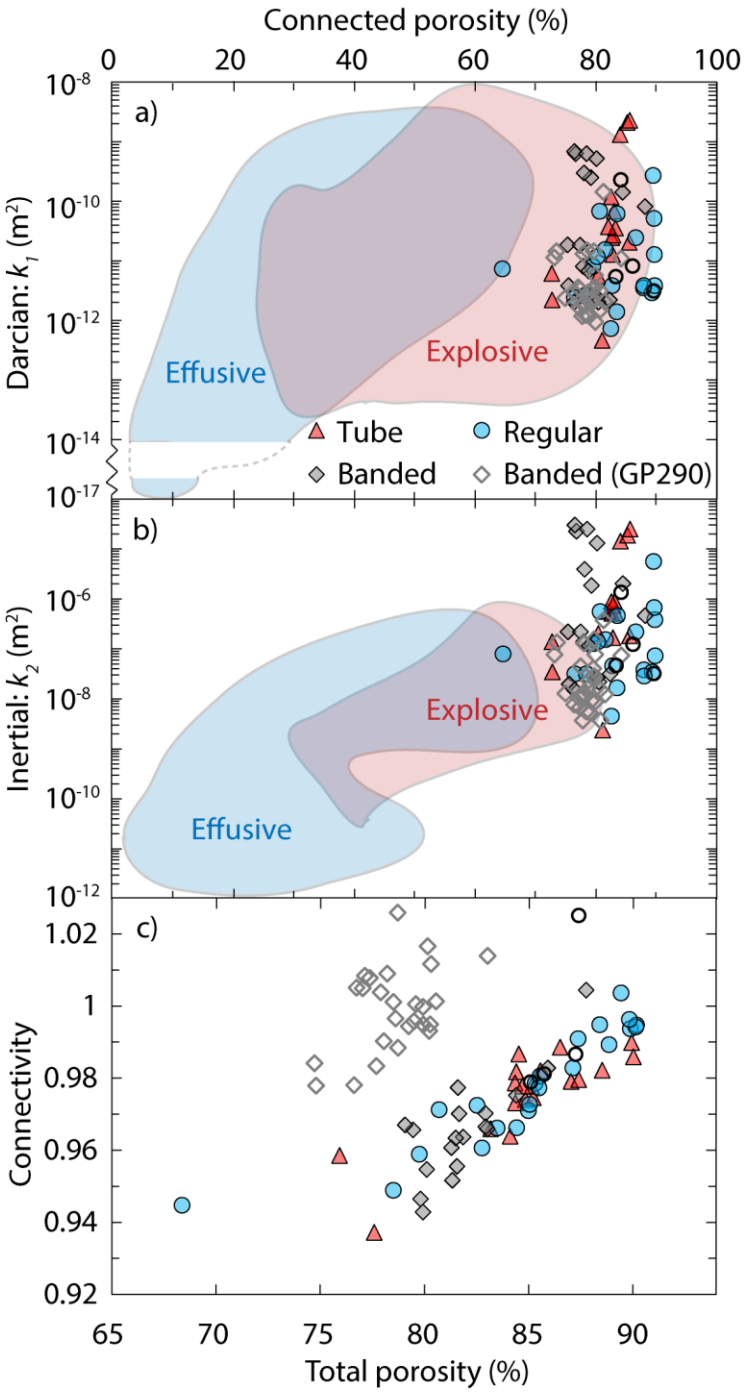

Figure 3.4. Permeability vs. connected porosity (a and b), and total porosity vs. connectivity (c). Connected porosity is compared against both the Darcian (k_1) and inertial (k_2) permeability (a, b). The regions defined by "effusive" and "explosive" are determined from multiple datasets of subaerial pumice (Degruyter et al., 2012). Empty symbols (primarily GP290) are data from Manga et al. (2018). Connectivity values > 1 are unrealistic (a result of analytical error) and should be assumed to be ~1.

There *is* a clear increase in connectivity (*c*) with total porosity in most giant pumices (**Figure 3.4c**). Banded GP290 fragments have only 0–2% isolated porosity at 75–82% total porosity where *c*~1; the GP290 vesicle network is almost *fully* connected. GP290 also does not show systematic changes in vesicularity with distance from the outer margin. All other GP clast exteriors sit on a different trend where there is up to 5% isolated porosity at total porosity=75%. Connectivity only approaches 1 where total porosity is >87% (**Figure 3.4c**). Other finely-banded giant pumice exteriors exhibit lower connectivity than the rest of the regular and tube samples, but these samples do not sit on the same trend as GP290 (see **B7** for all data).

3.5.3. Microlite and vesicle microtextures

Microlites of pyroxene and feldspar are generally 5–20 µm long and consistently smaller than 50 µm. Habits are mostly acicular (pyroxene) and swallow-tail to tabular (feldspar) (**Figure 3.5**). Vesicularity-corrected microlite number density (mN_{Am}) varies over two orders of magnitude; tube and regular giant pumice have mN_{Am} values of 2×10^5 to 3×10^6 cm^{-2}. White and grey pumice bands in GP290 are an order of magnitude higher than regular and tube pumice (8×10^6 to 2×10^7 cm^{-2}) (**Figure 3.5b**). Grey pumice bands display higher average microlite sizes than regular pumice and white bands. An extensive study of microlite shape and size distributions is deserving of it's own study and outside of the scope of this project. The higher number densities in banded pumice are attributed to primarily feldspar nucleation and an increase in pyroxene nucleation (Appendix **B8**); very few feldspar microlites are identified within tube and regular pumice (**Figure 3.5a**). There are well-defined, sharp interfaces in mN_{Am} between adjacent grey and white bands where grey bands have up to 10x more microlites (**Figure 3.5c**). In banded clasts, the elongate edges of microlites with acicular-tabular habits commonly align to the edges of sub-rounded vesicles (**Figure 3.5d**).

Vesicle sizes, shapes, connectivity and abundances were examined in both 2D and 3D for GP290, to provide a 3D understanding of the relationship between vesicle shape and connectedness (**Figure 3.3-5**). Vesicles analyzed in 2D display a range of shapes and textural maturity (extent of bubble coalescence and deformation) although most giant pumice exteriors are dominated by vesicles 10–100 µm in diameter with well-rounded shapes and little evidence of

collapsed degassing pathways (**Figure 3.5e-h**). In exteriors of regular pumice, some circular vesicles are observed between vesicles with more convoluted perimeters and irregular shapes (**Figure 3.5e**, Appendix **B9**). Banded GP290 exterior and interior samples have similar vesicularities and vesicle sizes to regular pumice, but the vesicle shapes conform to the shapes of adjacent microlites (**Figure 3.5h**). Cross sections of vesicles in tube samples are nearly circular when not affected by coalescence (**Figure 3.5g**). See Appendix **B2** for vesicle shape analysis.

3.5.3.1. Vesicle number densities (N_{Vm}) and vesicle volume distributions (VVDs)

Vesicle number densities for all GP clast exteriors analyzed by 2D image analysis span almost an order of magnitude (2.6×10^8 to 1.3×10^9 cm^{-3}) when assuming spherical vesicle geometry following Sahagian and Proussevitch (1998) (**Figure 3.6a**). Tube pumice exteriors have consistently higher apparent N_{Vm} values (1.1×10^9 cm^{-3} to 1.3×10^9 cm^{-3}), but the extreme elongation of vesicles in tube pumice means that the assumption of sphericity is *not* valid, and their actual N_{Vm} is lower. Here we apply an alternative formula for stereo-conversion assuming a prolate, rather than spherical, vesicle geometry used by Sahagian and Proussevitch (1998), of 1:3:10, where 1 and 3 are the measured vesicle diameters and 10 is the prolate axis (see Appendix **B3** for full stereo-conversion details). The range of aspect ratios was determined by XRT analysis for pumice cores. Of the conversion factors in Sahagian and Proussevitch (1998), the non-spherical assumption of 1:3:10 is the best available approximation for the tube samples where the majority of vesicle sizes in question (10–100 µm) have aspect ratios of 10–50 (see Appendix **B4**).

By applying the tube-vesicle stereo-conversion, number densities of tube pumice exteriors are reduced ($1.9–2.6\times10^8$ cm^{-3}) and now closely match the GP290 exterior banded values of $2.5–3.6\times10^8$ cm^{-3}. An interior fragment of GP290 with 80% vesicularity has similar N_{Vm} (3.1×10^8 cm^{-3}) to the GP290 exterior. Some stretched bubbles in regular giant pumice exteriors necessitate the use of a smaller aspect ratio geometry (1:1:2) (**Figure 3.6**).

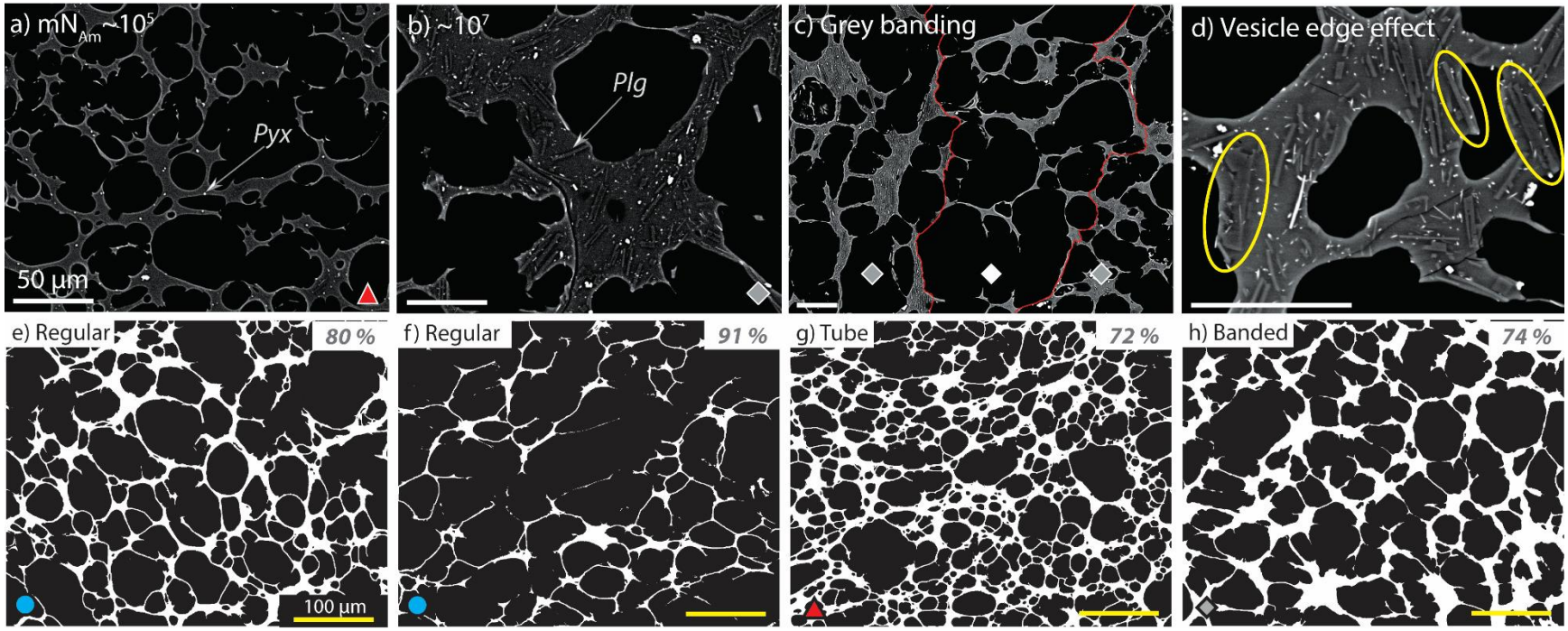

Figure 3.5. BSE images of microlite phases, habits and number densities and vesicles. a) and b) identify the crystal phases of pyroxene (Pyx) and plagioclase (Plg) over varying orders of magnitude of microlite number density (mN_{Am}). c) shows the sharp interface (red line) and number density difference between grey and white bands. d) shows how the growth of plagioclase microlites impedes vesicle edge relaxation (circled in yellow); Each image (a to d) is given a 50 µm scale bar and mN_{Am} values in (a) and (b) are in cm^{-2}. Processed binary BSE images (e) through (h) are acquired at 250x magnification. Black is vesicle pore space and white is glass, phenocrysts and microlites. Each image gives the textural classification, the 2D image vesicularity (%) and a 100 µm scale bar. All images are given prior to separation of coalesced vesicles. Tube vesicles (c) are viewed as a normal cut of the elongate vesicle axis (i.e., shortest diameter).

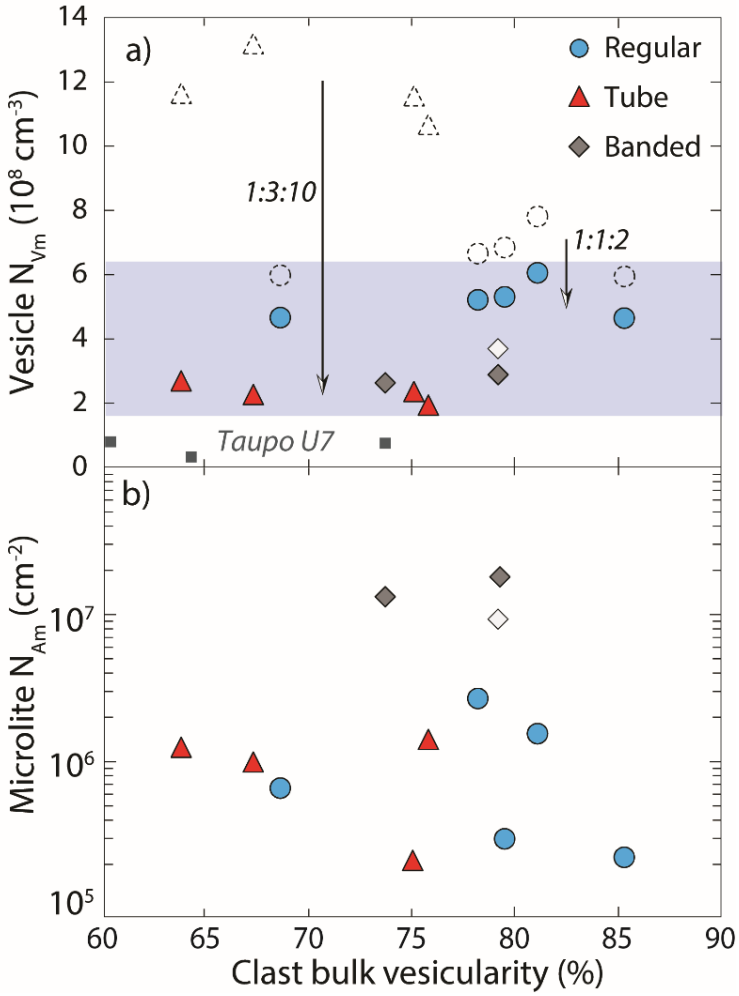

Figure 3.6. a) Corrected vesicle number density per volume (N_{Vm}) vs clast vesicularity for all analyzed samples when applying a non-spherical 3D stereo-conversion for defined aspect ratios appropriate to the whole-clast macrotextural and 3D-XRT microtextural observations; banded pumice does not require a non-spherical assumption. The blue box highlights the resulting small range of N_{Vm} values from the adjustment. Number densities are also given for the 1.8 ka Taupo Unit 7 giant pumiceous blocks from Houghton et al. (2010). b) Melt-corrected microlite number density per area (mN_{Am}) vs clast vesicularity for all analyzed samples.

With a 1:1:2 correction, regular pumice N_{Vm} values are reduced from 5.9–7.8×10^8 cm^{-3} to 4.6–6.0×10^8 cm^{-3}. With or without correction, regular pumice exteriors have higher N_{Vm} values than GP290 exteriors where smaller vesicles (< 20 µm) are sparse (**Figures 3.5** and **3.6**) (see Appendix **B4**) and there is negligible isolated porosity (**Figure 3.4c**). Correcting for elongate vesicles narrows the total range of vesicle number densities identified in all giant pumice exteriors (1.9–

6.0×10^8 cm^{-3}). We expect some natural variation in N_{Vm} in a single magma source, but generally N_{Vm} lie well within an order of magnitude (e.g., Houghton et al., 2010; Shea et al., 2010).

The modal vesicle diameter by volume is relatively consistent through all GP fragment exteriors (30–48 µm) with the exception of HVR_192 (60 µm) (**Figure 3.7, Table 3.1**). The modal vesicle diameter by number density is similar (16–37 µm) showing that total porosity is dominated by the most numerous vesicle size. Vesicle volume distributions cannot be accurately determined for tube pumice after the extreme stereo-conversion (see Appendix **B3**); the calculations are only valid for a spherical assumption (see Appendix **B2**). Comparison of adjacent white and grey bands show an increase in small, circular vesicles (<60 µm) in white bands (**Figure 3.7l**). Some regular pumice display subtle bimodal distributions with a consistent primary mode at 30–60 µm and a variable secondary mode at 100–600 µm (**Figure 3.7c-e**). **Table 3.1** compiles all 2D microtextural data for each giant pumice exterior.

3.6. Magma decompression rates and textural interpretations

Similar vesicle number densities among GP clasts imply a common early ascent history of GP magma where N_{Vm} values of 10^8 cm^{-3} are associated with dominantly heterogeneous bubble nucleation at crystals edges or at melt impurities (Shea, 2017). Despite the low crystallinity of GP (~5 vol. %; Carey et al., 2018), bubble growth at free crystal surfaces produces vesicles 100 – 200 µm in diameter; these contribute towards the coarser mode in the VVDs (**Figure 3.7**). Silicic Plinian eruptions commonly produce pumice with N_{Vm} of 10^9–10^{10} cm^{-3} (e.g., Novarupta, Askja, Taupo, Mt. St. Helens; Houghton et al., 2010). The highest values are attributed to late-stage, very high decompression rates (dP/dt ~10–100 MPa s^{-1}) and non-linear, rapid vesicle nucleation in the very shallow conduit (<10 MPa) prior to fragmentation (Toramaru, 2006; Cluzel et al., 2008; Shea, 2017). For the GP phase, we calculate maximum dP/dt of 0.9–5.0 MPa s^{-1} at the vent using our corrected N_{Vm} range (**Figure 3.6**) and the Shea (2017) dP/dt equation for a rhyolite. These decompression rates are very unlikely to produce bubble number densities of 10^9–10^{10} cm^{-3} through inferred heterogeneous bubble nucleation (Gonnermann and Manga, 2005; Toramaru, 2006). The termination of the Havre conduit at 9.2 MPa inhibits processes such as late-stage

vesicle nucleation, disequilibrium degassing and explosive magma fragmentation (Manga et al., 2018).

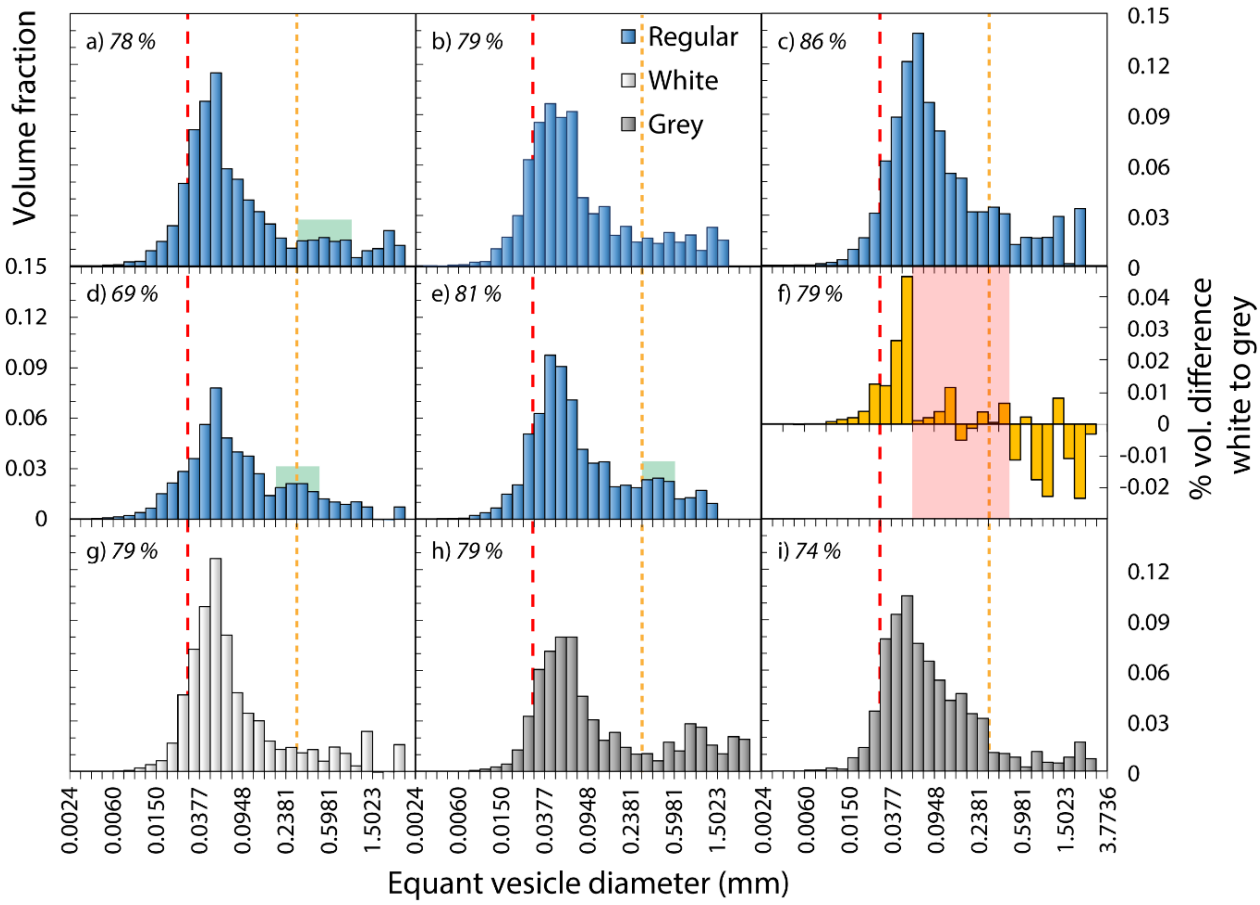

Figure 3.7. Vesicle volume distributions (VVDs) for all samples except for tube pumice (see Appendix A). Equant vesicle diameters are given across 32 geometric bins ($\times 10^{0.1}$ from Sahagian and Proussevitch (1998)) from 2.4 µm to 3.78 mm. Absolute volume fractions are given as opposed to fractions adjusted to 100% volume. Whole clast vesicularity is given for all samples. The red dashed and yellow dotted lines correspond to reference vesicle sizes of 30 µm and 300 µm to compare volume contributions of the smallest, modal and largest vesicle diameters. Plot (f) displays the % volume difference between the %-adjusted VVDs of (g) and (h) – adjacent white and grey bands in GP290. The red box shows a region of inconsistent variation in volume in (f). Coarser modes qualitatively identified by pale green box.

Table 3.1. Vesicle and microlite parameters and outputs from 2D image analysis and 3D stereoconversions.

Group	Sample #:HVR_	Vent distance (km)	*Clast vesic. (%)	Mean Image vesic. (%)	Clast V_g/V_l	Vesicles analyzed	Vesicles included	N_V (cm^{-3})	N_{Vm} (cm^{-3})	**Adjusted N_{Vm} (cm^{-3})	mN_{Am} (cm^{-2})	***Modal 3D EqD (µm)	+Modal Volume EqD (µm)
Regular	041	3.12	78.1	66.9	3.57	14966	3622	6.3E+07	6.6E+08	5.1E+08	2.7E+06	25.7	47.5
	096	1.65	79.4	73.1	3.85	13780	3080	6.0E+07	6.8E+08	5.3E+08	3.3E+05	25.7	37.7
	192	1.19	85.2	82.5	5.76	9873	1916	3.7E+07	6.0E+08	4.6E+08	2.6E+05	32.4	59.8
	221	4.65	68.5	60.8	2.17	16769	3835	7.9E+07	5.9E+08	4.6E+08	7.0E+05	32.4	47.5
	231	5.81	81.0	69.3	4.26	11038	3390	6.0E+07	7.8E+08	6.0E+08	1.6E+06	16.2	37.7
Tube	003	1.03	75.0	74.2	3.00	14275	4676	5.7E+07	1.2E+09	2.3E+08	2.3E+05	37.1	47.5
	022	1.20	63.7	61.0	1.75	25356	6447	9.5E+07	1.2E+09	2.6E+08	1.3E+06	37.1	30.0
	115	0.42	75.7	75.7	3.12	18088	3935	4.5E+07	1.1E+09	1.9E+08	1.5E+06	29.5	47.5
	270	4.92	67.2	67.4	2.05	14882	5244	7.3E+07	1.3E+09	2.2E+08	1.0E+06	29.5	30.0
Banded	290	1.43	73.6	65.7	2.79	9542	3119	6.7E+07	2.6E+08	n/a	1.3E+07	30.0	47.5
	290_G	1.43	79.1	68.9	3.78	11078	1936	5.9E+07	2.8E+08	n/a	1.8E+07	23.8	47.5
	290_W	1.43	79.1	76.1	3.78	16564	2323	7.5E+07	3.6E+08	n/a	9.3E+06	23.8	59.8
	290(int)	1.43	79.3	70.4	3.83	9435	2775	6.4E+07	3.1E+08	n/a	4.8E+06	23.8	37.7

** Selected clast vesicularity (vesic.) is equal to the mean giant pumice vesicularity from each density distribution analysis (see Appendix B1)*

*** Bubble number density (N_{Vm}) adjusted with the most appropriate non-spherical vesicle geometry stereoconversion*

**** Modal vesicle diameter from number density per size bin after 3D stereoconversion. Value take from size bin median*

+Modal vesicle diameter by total vesicle volume, i.e., histogram mode from Figure 10. Note that tube values may be inaccurate due to non-prolate stereoconversion included here.

Tube and regular giant pumice have microlite number densities (10^5–10^6 cm^{-2}) that are consistent with dP/dt =0.1–1 MPa s^{-1}, but higher dP/dt is required to produce GP290 microlite number densities (up to 10^7 cm^{-2}) (Toramaru et al., 2008). We can exclude rapid microlite nucleation as a result of undercooling as vesicle number densities are too low (Toramaru, 2014). This implies that extended microlite nucleation and growth seen in GP290 was either controlled by slower cooling rate or by reduced dP/dt <<0.01 MPa s^{-1} (similar to vesicle-poor rhyolite lava effusion; Brugger and Hammer, 2010) in a localized region of the conduit.

3.6.1. Evidence for post-fragmentation vesicle expansion

Subtle bimodal VVDs with varying coarse modal size and volume demonstrate that there are variable vesiculation controls after an early common ascent despite similar N_{Vm}. Bimodal VVD signatures are observed in many subaerial rhyolite pumice eruptions, but these coarser modes are usually broader and attributed to bubble coalescence (Giachetti et al., 2010; Shea et al., 2010). Coalescence *is* observed in GP clast exterior vesicles, however these can be successfully separate to reconstruct the pre-eruptive VVD (**Figure 3.5,** Appendix **B2**). The coarser modes (100–600µm) vary in volume and modal size more than the primary vesicle modes at 30–60 µm and display highly heterogeneous textures. We attribute these to a variable extent of heterogeneous bubble growth around vesicles and some post-disruption vesicle expansion.

Some giant pumice exteriors appear to show the secondary expansion of vesicles post-disruption (e.g., Houghton et al., 2010; Mitchell et al., 2018b). This is implied from some bred-crusted exteriors, and evident from the presence of circular vesicles deforming proximal vesicles in microtextures (**Figures 3.1h, 3.5e**, Appendix **B9**). The difference in adjacent vesicle shapes suggests two distinct stages of vesicle growth. The deformed vesicles do not share the expected vesicle convolution and breakdown seen for "collapsing" vesicles (Rust and Cashman, 2004).

Secondary vesicle growth is not widely recorded in subaerial rhyolite due to an ambient environment that limits post-disruption decompressive expansion. Tropospheric dP/dt are ~10^{-5}–10^{-4} MPa s^{-1} whereas submarine dP/dt are ~ 0.01–0.1 MPa s^{-1} for pyroclasts ascending at 1 to 10 m s^{-1} respectively. Greater dP/dt and permeable outgassing during submarine clast ascent would allow continued expansion of vesicles; dP/dt of this range, however, are insufficient for late-stage

nucleation in the water column. This likely explains the greater measured vesicularities (up to 92%) relative to those predicted at seafloor vent pressures by Manga et al. (2018) (i.e., 75–80%). The irregular shape of surrounding vesicles also suggests that secondary vesicle growth occurs whilst magma is still ductile and bubbles can still deform. Many of these vesicles appear isolated in the 2D images; isolated vesicles would permit expansion of vapor within the bubble without outgassing (see Appendix **B9**). Late-stage vesicle expansion supports previous hypotheses that giant pumice cool slowly in the water column (Fauria and Manga, 2018; Mitchell et al., 2018a). Residence time of giant pumice within a possible thermal plume before settling in cold seawater will be a dominant control on clast cooling rates (Mitchell et al., 2018a).

3.7. Discussion

Geochemical homogeneity throughout Havre GP suggests that observed textural diversity arises from a combination of processes above and below the vent. The following discussion develops a 2D strain model and a conceptual shallow conduit model to explain the observed textures. We then explore processes that accompany ascent of hot giant pumice blocks within the water column, and the underlying controls on production of giant pumice in the submarine environment.

3.7.1. Eruptive shallow conduit model

We propose that: 1) a velocity gradient across the conduit created spatially variable shear that is reflected in the textural differences between regular and tube pumice; and 2) that cooling near the conduit walls produces magma with lower ascent velocity that permits microlite growth and subsequent banding.

3.7.1.1. Strain and bubble deformation

We use a 2D conduit strain model to assess how textures observed in both tube and regular giant pumice could be produced simultaneously, prior to eruption into the water column. The results of the 1D conduit ascent model by Manga et al. (2018) (gas fraction, magma pressure, mean melt velocity, magma viscosity and bubble radius based on vesicle number density – see Appendix

B10), provide input parameters for the 2D model that terminates at 9 MPa (hydrostatic-equivalent vent depth), and assumes constant conduit radii (25 and 50 m) and a laminar velocity profile (also assumed in the 1D model).

We calculate cumulative strain (γ_t), expected maximum bubble aspect ratios (AR), and decompression rates (dP/dt) throughout the conduit focusing on the results from the shallow conduit from Manga et al. (2018) (200 m below the vent). Cumulative strain calculations only initiate when the Capillary number (Ca) is > 1 in the conduit, i.e., when the timescale of bubble relaxation exceeds the timescale of bubble shearing. Below this, vesicle deformation will be small. We use equations from Canedo et al. (1993) and Rust and Manga (2002) for Ca and AR calculations. In this instance, vesicles – and subsequent AR calculations – are assumed to undergo "simple" shear due to the velocity profile as opposed to "pure" shear prior to conduit fragmentation (Dingwell et al., 2016). Details of the model are explained in Appendix **B10**.

The 25 m radius conduit leads to significant cumulative strain (γ_t >>10) in the shallow conduit (**Figure 3.8**). γ_t approaches 10^4 at the conduit walls, but strain rates remain insufficient to fragment magma in the conduit, even at the walls. Decompression rates vary from 5 to 0.1 MPa s^{-1} with distance from the conduit center – matching those predicted by Shea (2017) – and modal vesicle size AR are >>10 throughout the shallow conduit (**Figure 3.8**). There is only a very narrow region (<1.5 m across) in the conduit where Ca<1 and little strain has accumulated. A conduit with a 25 m radius would not be able to produce the non-sheared vesicle textures observed in regular and banded giant pumice; textures would be dominated by elongate tube vesicles (Dingwell et al., 2016).

We increase the conduit radius to 50 m and maintain mass eruption rate (MER) by reducing velocity to explore the lower strain conditions required to produce m-scale regions with very little vesicle shear, as in regular giant pumice. For this 50 m radius model, most of the conduit experiences low strain rates (Ca<1) until the top 1000 m, and total strain at the vent is then significantly lower than the 25 m case (**Figure 3.8**). The conduit edges still experience high strain (γ_t>100), but there is a 20 m wide region in the center of the shallow conduit where γ_t<1. Lower velocities also result in lower dP/dt of 0.7 to 0.01 MPa s^{-1}. The Ca<1 region is larger than in the 25 m model and would allow for the production of both sheared and non-sheared vesicles at the eruptive vent (**Figure 3.9a**).

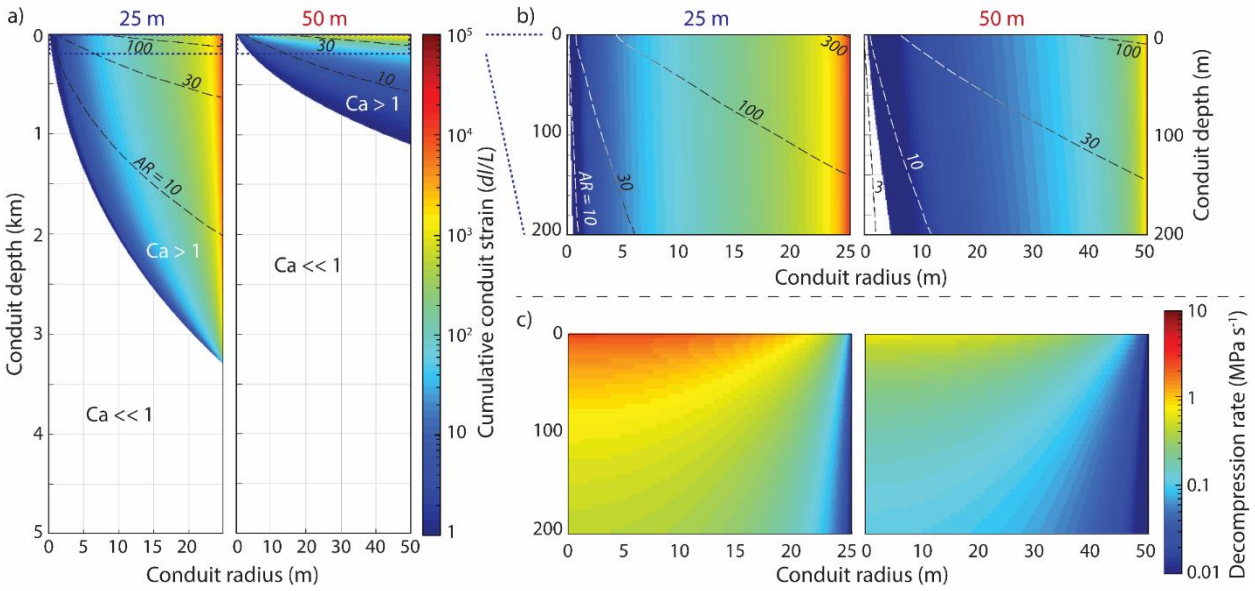

Figure 3.8. 2D strain modeling of the two conduit radii (25 and 50 m) assuming constant mass eruption rate (10^7 kg s^{-1}; Carey et al., 2018). The model shows the cumulative conduit strain (γ_t) when Ca >1 in both conduits with expected vesicle aspect ratios (AR) given by dashed lines. Plots with the same strain color bar for a) 5 km of the conduit, b) the top 200 m of the conduit. Conduit depth of 0 m = 10 MPa. c) Shows the difference in decompression rates (dP/dt) across the same region of the shallow conduit.

Manga et al. (2018) inferred a conduit radius of 21 m to match the MER determined by Carey et al. (2018). We suggest that a flared conduit with radius 50 m or greater would be sufficient to generate shallow regions with low accumulated strain and spherical vesicles. Mechanical erosion near the surface (seafloor) can widen conduits to create a flared vent, with models predicting widening by a factor of a few (Aravena et al., 2018). If GP was produced at lower MER than the pumice raft (<<10^7 kg s^{-1}) then it is also possible to generate the required conditions in a narrower conduit. Either way, the model suggests that elongate vesicles are likely to be dominant within giant pumice clasts, even when the conduit is flared, although tube vesicles may only be present at AR>100. The higher dP/dt in the conduit center (**Figure 3.8**) may be partially responsible for the higher N_{Vm} values in regular giant pumice (**Figure 3.6**). By fixing the vent pressure (9 MPa) we also limit the possibility that gas addition above the vent may reduce apparent hydrostatic pressure and drive higher dP/dt (Mitchell et al., 2018a).

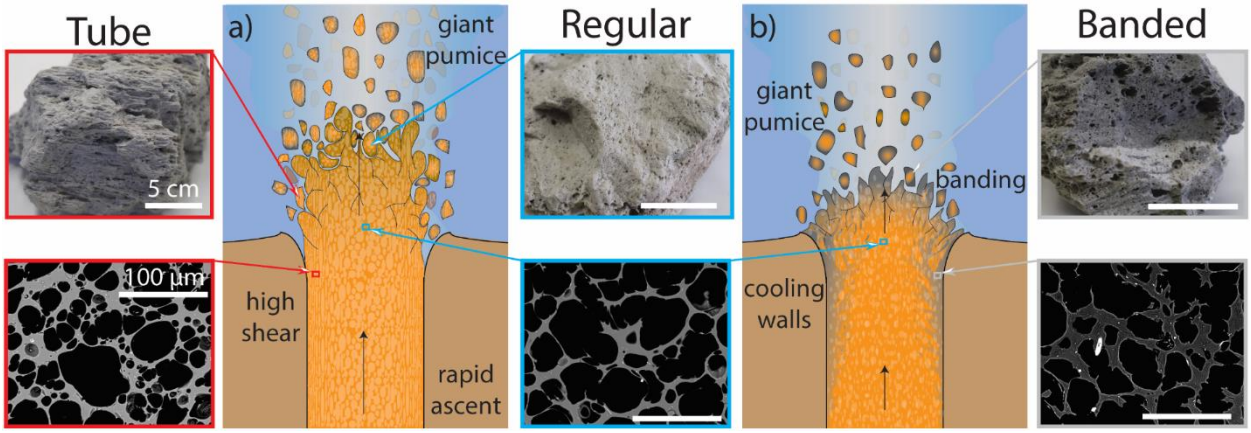

Figure 3.9. Schematic model of shallow conduit dynamics leading to the macro- and microtextures observed in: a) synchronous production of tube and regular giant pumice, and b) banded giant pumice from cooling conduit wall and subsequent microlite-rich magma assimilation in the latter stages of the GP-phase. The gradient of orange to grey gives an arbitrary temperature scale from fresh magma at 800°C to ambient rock temperature in the ocean. The conduit width, size of eruptive products and vesicle sizes are not given to scale. All images have a 5 cm scale bar in macrotextures and 100 µm in BSE images. Shorter arrows in b) suggest possible slower ascent rates as a result of gas loss.

Our sampling of only 29 giant pumice exteriors means we are unable to state explicitly that there are more tube giant pumice than regular giant pumice. We also cannot demonstrate the textural diversity throughout all of these pumice as only GP290 was analyzed as a whole block. However, there is observable mm-scale textural heterogeneity in most pumice seen as either thin, sinuous denser bands, small regions of shear, or areas with spatially-variable vesicle size distributions. Complex conduit geometry may generate local textural heterogeneity, for example, cm-scale regions of sheared and non-sheared vesicles from some mingling during ascent. This may produce textures like those observed in GP290 (**Figure 3.3l-o**).

3.7.1.2. Source of textural banding in GP290

Grey bands in GP290 have higher microlite number densities, and increased microlite size with respect to adjacent white bands and other pumice (**Figures 3.5** and **3.6**). GP290 also has complete

connectivity at lower porosity than other giant pumice samples (**Figure 3.4c**). The juxtaposition of mm to cm-size bands in pumice with distinctly different cooling and crystallization histories suggests mingling of different magma regions with variable cooling rates (**Figure 3.9b**). This has implications for our use of an isothermal conduit model when considering temperature controls on viscosity and consequent strain accumulation.

We propose that the microlite-rich regions are derived from cooler magma at conduit edges or localized shear zones where dP/dt is <0.1 MPa s^{-1} and magma is cooling (**Figure 3.9b;** Sano and Toramaru, 2017). The complete connectivity of GP290 relative to all other giant pumice in **Figure 3.4** suggests greater textural maturity, i.e., continued bubble coalescence and lack of any isolated vesicles. We infer that permeable outgassing and a breakdown of coupled gas and magma velocity (Manga et al., 2018) reduced the magma velocity (**Figure 3.4**). It is also possible that GP290, and other clasts that display textural banding, were generated during a later stage of the GP-forming phase as the eruption waned. Lower upward velocities at the conduit wall, gas loss, cooler magma would allow for extended microlite crystallization as seen throughout GP290 (Sano and Toramaru, 2017). Higher velocity and dP/dt in the conduit center, and low melt viscosities <10^7 Pa s (due to limited volatile exsolution under hydrostatic pressure) could still allow for melt domains to mingle in the shallow conduit where slow-cooling, microlite-rich magma was assimilated into the microlite-poor central magma body resulting in textural banding (**Figure 3.9b**). Magma mingling may also have occurred above the vent prior to non-explosive fragmentation (Manga et al., 2018). Interactions with seawater could create a spatially-complex thermal gradient within the erupted magma; experiments, cooling models and quench depths show that GP magma did not quench instantly (Fauria and Manga, 2018; Mitchell et al., 2018a).

The sharp interfaces in microlite number density between adjacent microlite-poor and microlite-rich bands (**Figures 3.5** and **3.6**), and a lack of changes in vesicle size distribution and vesicle shape between bands does not suggest microlite crystallization as a result of shear-localized degassing. Degassing and induced microlite crystallization has been shown to occur in small regions of high strain within the conduit (Kushnir et al., 2017). However, we observe no consistent elongation of vesicles exclusive to the grey bands as we do within the tube pumice samples. The complex framework and frequency of grey bands throughout GP290 implies the mingling of two different magma textures as opposed to the *in situ* development of shear localization bands.

3.7.2. Giant pumice in the water column: Fragmentation and ascent

Fragmentation by cooling-joint propagation has been suggested to generate large pumice clasts that separate, rise and settle through the water column, preserving meter-scale textural diversity (Manga et al., 2018). A lack of destructive fragmentation in the conduit permits large regions of tube vesicles to be preserved in giant pumice with lineated fabrics throughout the clast (**Figure 3.1e, 3.3**). Giant tube pumice are rare in subaerial explosive eruptions as strain rates in regions of high vesicle shear usually fragment magma efficiently with tube vesicles and elongate permeable pathways (Wright et al. 2006b; Dingwell et al., 2016). Greater length scales of observations of magma heterogeneity in the shallow conduit at Havre could be an analogue for the deeper conduit dynamics in subaerial silicic systems at equivalent pressures. It is possible that textural analysis of deep submarine pumice could provide a secondary window into deeper regions of subaerial silicic conduits and the distribution of large vesicles in pumice.

The presence of a large, vapor-rich submarine plume or hot seawater sheath at Havre was speculated to control the cooling rates of giant pumice in the water column (Mitchell et al., 2018a). Many clasts from the 2012 Havre eruption are found to have cooled through the glass transition at very shallow depths (Rotella et al., 2013; Mitchell et al., 2018a). Models from Manga et al. (2018) and Fauria and Manga (2018) demonstrate that rise time to the ocean surface is rapid (<10 min) for clasts larger than 10-20 cm. Thus, continued decompression during ascent through the water column would have promoted post-disruption vesicle growth that we observe in giant pumice exteriors (Rotella et al., 2013). The high permeability of some giant pumice (**Figure 3.4**) may reduce the effects of thermal expansion within vesicles, as gas may escape quickly and ingested water can accelerate pumice cooling (Rust and Cashman, 2011; Fauria and Manga, 2018; Manga et al., 2018). Observations of bread-crusted exteriors in some giant pumice, however, imply that some clast interiors were able to expand faster than permeable gas loss (**Figure 3.1h**).

A lack of rapidly quenched, dense rinds in *all* 29 giant pumice could also suggest that the "exteriors" sampled were not in fact original brittle fragmentation surfaces, but instead surfaces ensuing from secondary fragmentation and breakup of clasts (Mitchell et al., 2018b) in the water column. Large fractures that transgress entire clasts demonstrate the fragility of some of these blocks (**Figure 3.1e, f** and **3.3k, o**). Thus, the GP exteriors we sample are not necessarily

representative of surfaces generated by brittle fragmentation (Manga et al., 2018). Examples such as the breadcrusted exterior (**Figure 3.1h**) may be more representative of *original* fragmentation surfaces.

Giant pumice from the 2012 Havre eruption share some textural similarities with the giant pumice from Taupo and, the Sumisu Domes. The subaqueous-derived Taupo blocks from shallow depths (<200 m) have lower vesicularities than GP (58–73%), denser rinds and inferred mass eruption rates of only ~10^3 kg s^{-1} (Houghton et al., 2010). While the inferred mechanism of autobrecciation of a vesicular dome carapace at Taupo shares similarities with the brittle fragmentation mechanism suggested for Havre, MER differs by up to four orders of magnitude (Von Lichtan et al., 2016; Manga et al., 2018). Giant pumice from The Sumisu Dome Complex share many textural (~77% vesicularity, tube fabrics on the associated dome carapace) and morphological characteristics (slabby, polyhedral blocks with internal cracks and jointing) with Havre GP (Allen et al., 2010). The pumice are interpreted to have erupted from depths of 900–1100 m implying similar hydrostatic effects on conduit dynamics and fragmentation to Havre GP. However a lack of vesicles >3 mm across and texturally uniform interiors of Sumisu giant pumice signifies that additional processes are required to explain the textural heterogeneity in GP.

The analyses presented here increase the number of detailed studies of subaqueous giant pumice textures, of which there are only a few at present. However, we note that the microtextures observed in GP exhibit few key characteristics (e.g., vesicle connectivity, vesicle number density) that would define them as deep submarine rather than subaerial. Only the enhanced presence of tube pumice and dominant preservation of meter scale clasts may fingerprint a deep submarine eruptive source.

3.8. Summary and implications for further study

The well-preserved deposits of the 2012 Havre eruption provide one of the best-known field sites for studying silicic volcanic activity on the seafloor. GP provides meter-scale windows into complex shallow conduit dynamics below the main eruptive vent (900 mbsl) and processes in the water column affecting vesiculation. Quantitative analysis of geochemistry and microtextures,

coupled with whole-clast observations and a model for magma flow, lead to several conclusions about the GP-phase of the 2012 eruption.

1) A compositionally homogenous magma supply prevailed throughout the GP-phase; no new, geochemically distinct magma was introduced or entrained into the conduit. Instead, textural banding in GP290 was the result of mingling microlite-rich and microlite-poor melt. We find evidence that microlites were generated by cooling near conduit walls.
2) Producing a region with low cumulative strain at the vent – required to keep bubbles from becoming highly deformed – is possible by incorporating a flared shallow conduit or by decreasing GP mass eruption rate. Incorporating thermal gradients, and changes in bubble size distribution and crystallinity into 2D conduit models may also resolve uncertainty.
3) Bread-crusted exteriors, the overprint and deformation of earlier-formed vesicles by later-stage vesicles imply some giant pumice exteriors experienced post-fragmentation vesicle growth as the clasts continued to decompress in the water column. This supports previous models of slow cooling and continued degassing of large pumice blocks to shallow water depths.
4) Textural analysis across a single meter-scale clast shows that: (1) clasts contain vesicles that span six orders of magnitude, and (2) clasts vesicle textures are spatially homogeneous. Large vesicles may be preserved because of the absence of explosive fragmentation and permit efficient permeable outgassing and subsequent water ingestion.

Our study offers new insight into deep submarine conduit dynamics during the 2012 Havre eruption where a number of findings suggest directions for further research. We emphasize the need to establish the physical and temporal relationships between units derived from the same vent, such as the voluminous pumice raft and Dome OP with GP, to assessing changing conduit dynamics throughout the entire 2012 eruption. Detailed study of microlite nucleation and growth rates could enhance our understanding of late-stage decompression, strain and cooling rates in the shallow conduit, and during buoyant ascent in the deep submarine environment. This study highlights the importance of determining submarine vent depths to assess hydrostatic pressure controls on the melt properties within the shallow conduit and the consequent textural diversity and maturity of erupted deep-sea pumice.

4. TEXTURAL, DEGASSING AND TIMING RELATIONSHIPS BETWEEN PUMICEOUS UNITS FROM THE 2012 SUBMARINE HAVRE ERUPTION

In preparation as: *Mitchell, S.J., Houghton, B.F. and Carey, R.J. Textural, degassing and timing relationships between pumiceous units from the 2012 submarine Havre eruption*.

ABSTRACT

The 2012 eruption of Havre submarine volcano produced at least six clastic units and 15 rhyolitic lava flows and domes. Observations of the units on the seafloor established a basic eruptive stratigraphy that has subsequently been re-examined and tested (Ikegami et al., 2018; Murch, 2018). Textural and microanalytical data provide further constraints on relationships between eruptive units. Further, these data can be used to interpret conduit dynamics and infer eruptive styles for each unit. In this study, we analyze the density, componentry, vesicle microtextures and connectivity, and volatile concentrations of lapilli and lapilli-sized fragments from diverse volcanic products of the 2012 eruption including the pumice raft, seafloor giant pumice blocks, ash-lapilli-block deposit, ash-lapilli layer, lava-G-lapilli, and the largest lava dome (Dome OP). The giant pumice and pumice raft have previously been inferred to have erupted from the same vent at the same time.

We offer evidence, from vesicle number densities and isolated porosity data, that the pumice raft phase may have preceded the giant pumice phase of the eruption. This counters the previously suggested synchronous eruption of the two units. Textural data supports a transition from raft-forming to giant-pumice-forming to dome-forming behaviors from the 900 meter deep vent due to changes in shallow conduit geometry and rates of magma decompression. We also propose a more detailed explanation for the ash-lapilli-block deposit supported by textural data and volatile contents, which accounts for its complex position within the main stratigraphy and its density-current-like deposit morphology. There is little distinction between volatile concentrations in matrix glasses between units; however, there is a notable contrast in H_2O contents in quartz- and plagioclase-hosted melt inclusions between banded giant pumice, and the pumice raft and other

giant pumice. We revise the conduit ascent model of Manga et al. (2018) utilizing new melt inclusion data that imply lower magma ascent and decompression rates in the shallow conduit. Pumice from the raft-forming phase of the eruption have similar vesicle number densities to shallow-erupted submarine pumice or pumice from large subaerial silicic explosive eruptions. All other units were highly influenced by the influence of 9.2 MPa of hydrostatic pressure on the 900m deep vent. This resulted in pumice and lava textures more representative of the deeper submarine environment.

4.1. Background

The eruption of Havre submarine volcano in July 2012 was the largest silicic submarine eruption of the past 360 years, and produced over 1.5 km^3 of rhyolite (70 – 72 wt. % SiO_2; Carey et al., 2018). The eruption produced 15 lavas and 6 pumiceous clastic deposits with complex dispersal and stratigraphic relationships. These recent seafloor deposits present an ideal field site to study the pumiceous deposits of a large silicic submarine eruption because there has been little remobilization by ocean currents, burial by sediment, or alteration by seawater.

Pumiceous low-density clastic material erupted into water experiences complex transport and deposition processes (Cashman and Fiske, 1991; Allen and McPhie, 2000; Allen et al., 2008). Interpretations of submarine stratigraphy are challenging if there is a lack of exposures of bedding below the most recent surface; these deposits cannot be analyzed *in situ* by submersibles with the same precision and delicacy that is common in subaerial fieldwork. Nevertheless, with a range of deposits with inferred effusive and explosive styles, complex fragmentation mechanisms, known vent depths, an established stratigraphic framework, and some constraints on eruptive phase duration (Carey et al., 2018; Manga et al., 2018, Murch, 2018), the Havre 2012 eruption presents an opportunity to study deep silicic submarine volcanism in detail.

Hydrostatic pressure is a modulating factor of submarine eruptive mechanisms (Head and Wilson, 2003; Allen et al., 2010; Cas and Giordano et al., 2014; Manga et al., 2018). At deep volcanic centers, such as Havre (900 – 1500 m deep), overlying pressure on eruptive vents inhibits late stage exsolution of volatiles dissolved in melt, subsequent bubble growth, and the rapid decompression of magma (Manga et al., 2018; Section **3.6**). With increasing hydrostatic pressure,

the explosivity potential will decrease, assuming all other factors remain the same, which theoretically results in lower-intensity, effusive eruptive styles under greater influence of overlying pressure (Head and Wilson, 2003; Degruyter et al., 2012; White et al., 2015; Cassidy et al., 2018). However, the initial volatile content and composition of magma in storage, and geometry and wall-permeability of conduits are also factors that affect degassing, vesiculation and outgassing of magma regardless of subaerial or subaqueous origin (Sparks, 1978; Sparks and Cashman, 2013; Cassidy et al., 2018). In this chapter, I consider how changes in magma composition and conduit conditions control different eruptive styles at a fixed vent depth of 900 m during the 2012 Havre eruption.

By analyzing the vesicle microtextures and volatile contents in crystal-hosted melt inclusions and matrix glass of pumiceous deposits, we can interpret the degassing, vesiculation, and strain history of magma ascending from regions of storage, through a conduit, and erupting on the seafloor (Sparks, 1978; Eichelberger and Westrich, 1981; Cashman and Sparks, 2013; Cassidy et al., 2018). The same methods can also assess changes in these processes throughout different phases of eruption from a single vent. With known vent depths and estimates of eruptive phase duration, the comparison of deep submarine silicic pumice microtextures with pumice from shallow submarine, sublacustrine, and subaerial silicic explosive eruptions can broaden our understanding of hydrostatic pressure effects.

Within this study, I analyze the textures and volatile contents of the identified major clastic units of the 2012 eruption (GP – giant pumice blocks, RP – raft pumice, ALB – ash-lapilli-block deposit, AL – ash and lapilli layer and LGL – lava-G-lapilli) and the largest dome (Dome OP) to extend previous stratigraphic interpretations and to determine the causes behind changes in eruptive style, pumice transportation, and deposit morphologies. This knowledge can subsequently be translated to other environments of contrasting confining pressure, e.g., subglacial and extraterrestrial volcanism (Wilson and Head, 1992; Owen et al., 2013a; Airey et al., 2015), and to ancient silicic submarine deposits where there are very few eruptive constraints (Wright et al., 2006a; Allen et al., 2010; Tani et al., 2013).

4.2. Stratigraphy of the 2012 Havre eruption

An expedition to Havre volcano in 2015 (MESH) used an ROV (remotely operated vehicle) to observe, map and sample the 2012 volcanic products, thus establishing a stratigraphic framework of the 2012 eruption (**Figures 4.1-4.3**) (Carey et al., 2014; Carey et al., 2018). The lava flows and domes produced during the 2012 eruption act as useful stratigraphic markers due to the presence (or lack) of overlying clastic units (Ikegami et al., 2018; Murch, 2018). The giant pumice block deposit (GP) is another useful stratigraphic marker that has helped to constrain the sequences of subunits within the ash and fine-lapilli deposit (AL) (**Figure 4.3**).

Previous studies (Carey et al., 2018; Ikegami et al., 2018; Murch, 2018) interpreted the stratigraphic relationships via the following stages:

1) Firstly, the eruption and emplacement of Lavas A-E from five vents with depths of 1280 – 1140 mbsl on the southwestern caldera walls (**Figure 4.3**). Further details of the timing relationship between individual lavas were studied in detail by Ikegami et al. (2018).
2) Synchronous production of the pumice raft (RP) and giant pumice unit (GP) from a single vent 900 mbsl on the SE rim of the caldera (**Figure 4.2a-d**; Jutzeler et al., 2014; Carey et al., 2018). The synchronous production of these units was inferred based on dispersal direction and macrotextural similarity (Carey et al., 2018). RP has a well-constrained mass eruption rate of ~10^7 kg s^{-1}; GP is unconstrained. This phase was the most voluminous of the eruption (Carey et al., 2018).
3) The eruption of the first ash and lapilli (AL) subunit (S1). S1 is interpreted to have erupted following RP and GP as the generation of ash from explosive magma fragmentation within the conduit due to magma-water interactions. S1 is interpreted to have erupted from the same vent as RP and GP and was subsequently deposited on top of GP (**Figure 4.3**; Murch, 2018).
4) The effusion of lava domes K through N on the S rim of the caldera. Neither S1 nor GP were found on these domes (**Figure 4.3**). Lavas F-I are assumed to have erupted sometime prior to or during the time; these lavas lie outside of the GP dispersal area where GP cannot be used as a stratigraphic marker (Ikegami et al., 2018).

5) The ash-lapilli-block deposit (ALB) is inferred to have erupted after GP and prior to Dome OP based on stratigraphy (Carey et al., 2018). The relationship between S1 and ALB is unknown (Murch, 2018). AL subunit S2 is inferred to be the distal deposit of ALB, the result of a density current fed by a collapsing plume centered around the main vent (**Figure 4.1**). S2 was deposited via dilute suspension flows in the caldera (Murch, 2018).

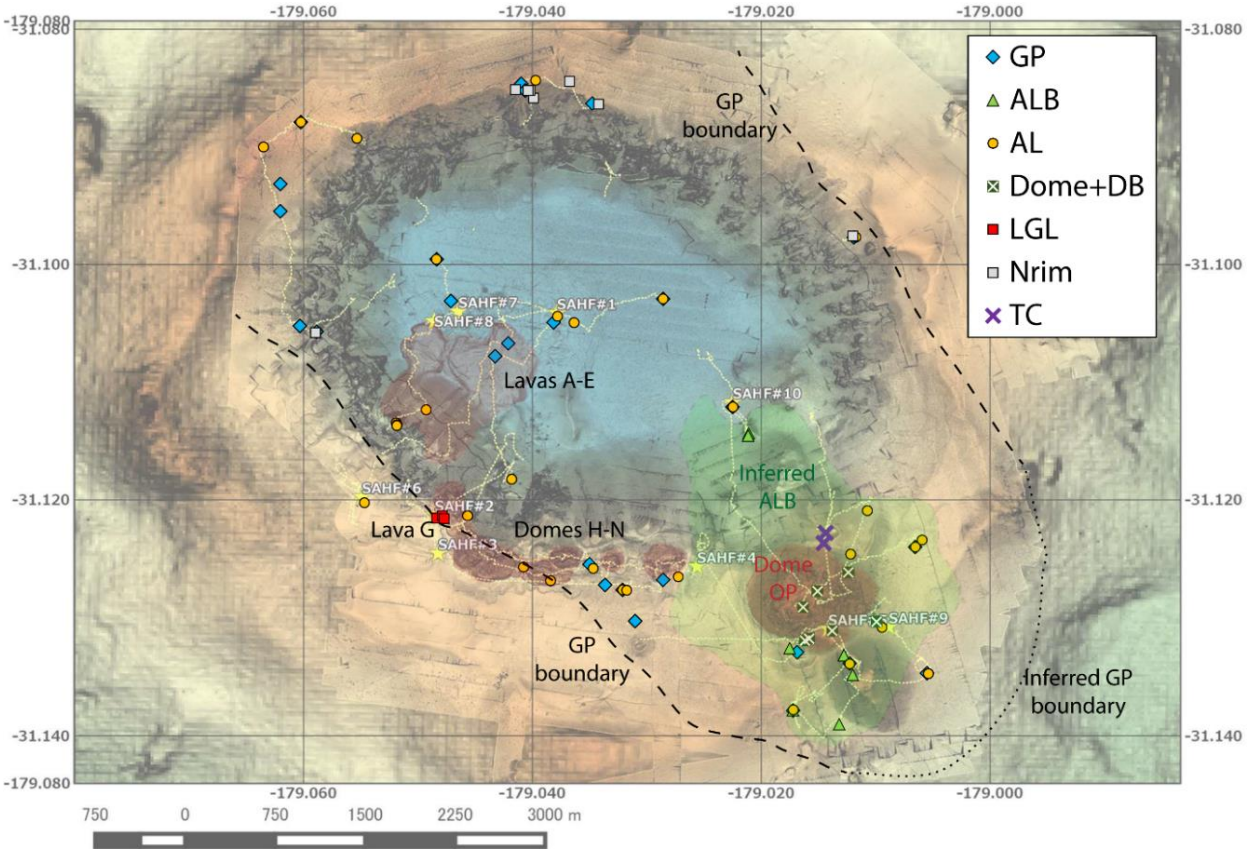

Figure 4.1. Sample locations (with the corresponding unit) collected during the MESH 2015 expedition across the Havre caldera. Locations are overlain onto the AUV *Sentry* high-resolution bathymetry data; RP (raft pumice) was sampled on the ocean surface and far away shorelines but is derived from the vent beneath Dome OP. Roughness of the bathymetry is used to infer the boundary of the GP (giant pumice) unit. Smooth regions around Dome OP and within the GP deposit are inferred to correspond to the ALB (ash-lapilli-block) unit (green). AL (ash and fine lapilli) is assumed to cover the entire caldera and extend many km further. Effusive 2012 deposits (lava flows and domes) are highlighted in red. TC samples can be seen on top of a cone-like feature not associated with the new 2012 edifices. Dotted yellow lines mark the dive paths of the ROV *Jason* during the MESH expedition. The caldera floor (blue) is ~1500-1540 mbsl and the caldera rims range from 850-1000 mbsl.

6) The effusion of lava domes O and P is inferred to have occurred sometime within stage 4 and a long while after (P is the later phase of Dome OP which forms a single edifice with O) (**Figure 4.3**; Ikegami et al., 2018). AL subunit S4b is found around and on the flanks of Dome OP (an ash venting deposit from lava effusion) (Murch, 2018).

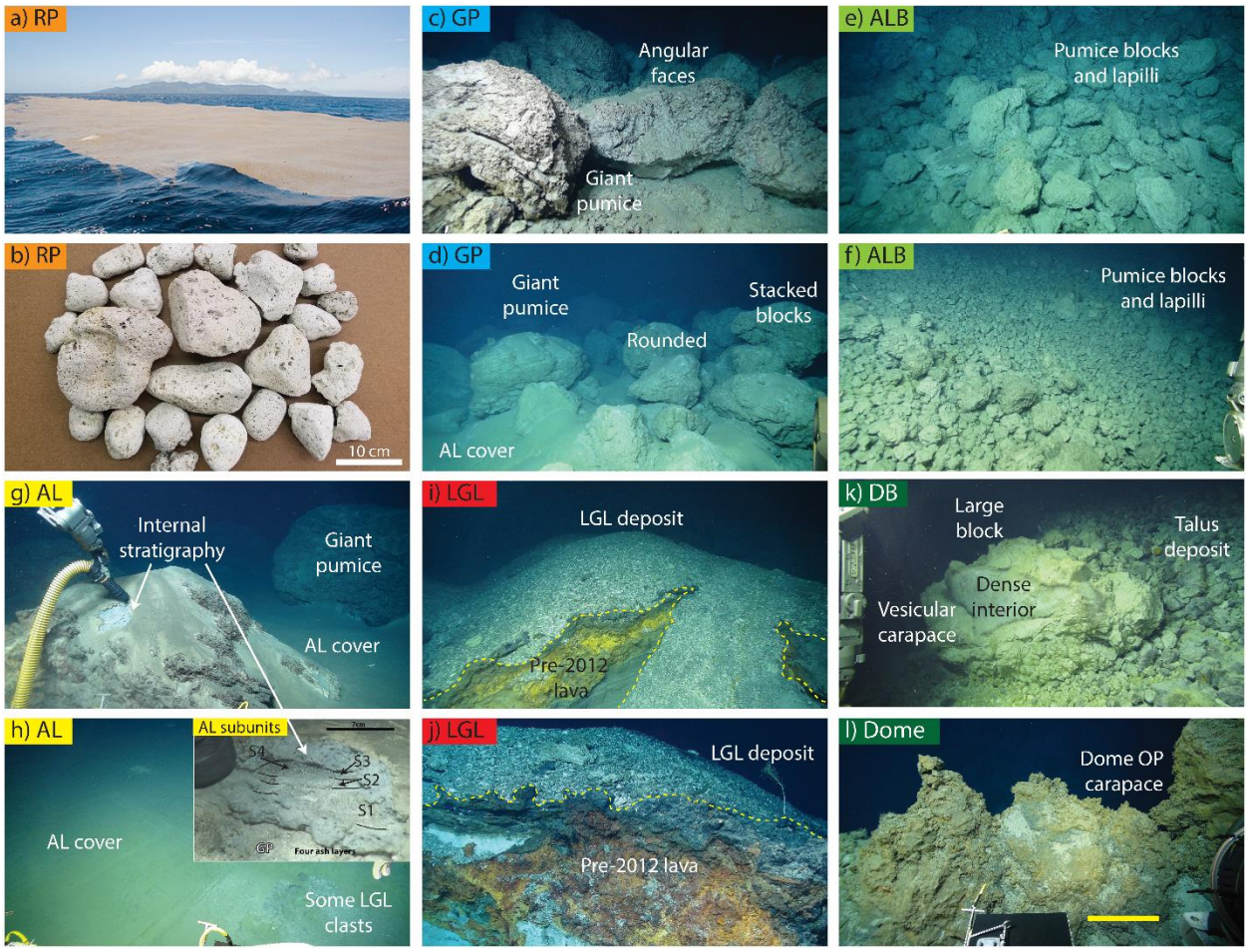

Figure 4.2. Photographs of the main pumiceous units of the 2012 eruption taken by the ROV *Jason* in 2015 or land-based photos of the pumice raft. a) The coherent pumice raft observed 8 weeks after the eruption from the HMS Canterbury; b) Raft pumice washed ashore in Fiji in summer 2013; c) meter-scale giant pumice blocks; d) and g) – giant pumice blocks covered by AL; e) and f) – a mixture of vesicular blocks and lapilli from ALB surrounding Dome OP; i) and j) – Lava-G-Lapilli deposited on top of pre-2012 lava flows at Havre; k) Talus (including large blocks) on the NE flank of Dome OP (also classified earlier as DB); l) *in situ* Dome OP carapace.

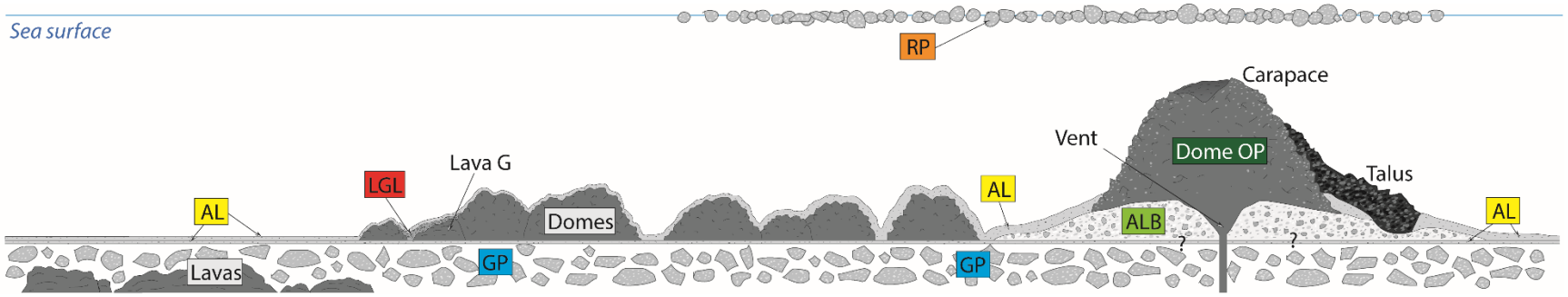

Figure 4.3. Schematic stratigraphy of Havre 2012 eruption as seen across the southern rim of the caldera from Lava A to Dome OP. A breakdown of the AL inner stratigraphy is given within the stratigraphic description in the text. AL is not the primary focus of this study, and hence I do not breakdown the complex stratigraphy within as shown in Murch, (2018). Clast sizes represent the meter-scale giant pumices (GP), inferred-as-smaller raft pumice (RP), block- to lapilli-size clasts of ALB, and finer lapilli and ash in LGL and AL. Dome O has a vesicular spiny carapace while Dome P has a regular blocky morphology. The dome talus extends east of Dome O. ? denotes uncertainty in stratigraphy below Dome OP.

7) Deposits with difficult timings to constrain are LGL and S3, both inferred to have erupted passively from ash-venting of the Lava G carapace that erupted sometime between 2) and 4) (Mitchell et al., 2018a; Murch, 2018). S3 is thought to be the finer grain size member of the lava-G-lapilli deposit (LGL); S3 ash was transported via suspension in a thermal plume from the lava flow surface. AL subunit S4a has a sharp contact with the underlying S3 layer and is thought to be the result of fallout of crystal-rich ash derived from cores of lavas F-I exposed through mass wasting events sometime after S3.
8) One of the latest stages of the eruption was the mass wasting of the eastern flank of Dome OP resulting in a talus deposit of blocks and lapilli-sized dome fragments (**Figure 4.3**). This deposit is mixed with the underlying ALB deposit (DB).

This study aims to provide a textural and volatile geochemical framework to support (or challenge) the inferred temporal relationships between individual units, particularly those derived from the main 900 mbsl vent: RP, GP, ALB, DB and Dome OP. As DB clasts are derived from Dome OP, we refer herein to all these samples (talus and carapace) as Dome. The LGL unit is also assessed in detail to support the origins of clastic material proximal to Lava G proposed by Ikegami et al. (2018) and Murch (2018). I also analyze pumiceous clasts from a lapilli and block deposit on the northern rim of the caldera (Nrim) that are inferred to be 2012 deposits, but that have no definitive origin; and four samples acquired from the top of a pre-2012 small cone feature 100 m across (samples collectively known as TC, but that lie within the area of the ALB deposit).

4.3. Methodology

Of the 290 samples collected during the 2015 MESH expedition, 82 contained lapilli and fragments of pumiceous material 8 – 32 mm in diameter (the commonly used size range for density and microtextural studies). Details on the collection and initial processing of seafloor samples can be found in Section **1.2.2**, and Appendices **A2** and **B1**. Pumice raft (RP) samples were collected from the shores of Fiji and New South Wales, Australia, after washing ashore ~1 year after the July 2012 eruption (Jutzeler et al., 2014); we also compare our RP data with microtextural data of

raft samples collected just three weeks after the eruption (Rotella et al., 2015). Sample locations and the corresponding seafloor units can be found in **Figure 4.1**.

Due to ROV sampling techniques, samples from different clastic units did not always contain 100 (or ideally 200) clasts for analysis, which is typical of subaerial pumice studies (Houghton and Wilson, 1989; Mitchell et al., 2018b). For each sample, we measured the density of all material 8 – 32 mm in diameter following Houghton and Wilson (1989); measurements have ± 30 kg m^{-3} error. Vesicularity is determined using a whole rock density of 2380 kg m^{-3} as determined in Chapter 3; this is similar to values used for other Kermadec silicic systems (2400 kg m^{-3} – Barker et al., 2012a; Rotella et al., 2015).

Clasts selected for 2D thin section microtextural analysis were taken from the modal density of each unit (RP, ALB, DB and LGL), and then from the lower and higher tail ends of each distribution to cover the range of vesicularities observed within each unit (Shea et al., 2010). Giant pumice fragments analyzed in Chapter 3 use only the modal density from each GP sample. Samples from TC and Nrim were not analyzed in microtextural detail based on poor constraints on eruptive origin and time constraints, and Murch (2018) analyzed the microtextures and volatiles of AL ash in detail. Due to issues with sampling, it was difficult to place constraints on the subunit(s) that were the source of the sparse lapilli collected in acquired AL samples, the more vesicular clasts we infer to have been sampled from either subunits S1 or S2.

Backscattered 2D electron (BSE) images of microtextures were acquired at 50x, 250x and either 500x, 750x or 1000x magnification (depending on the apparent number of vesicles <10 µm in diameter), and at the scan level (47 pixel/mm resolution). BSE images were acquired using a JEOL JXA-8500F microprobe analyzer at 15 keV accelerating voltage with an 8 nA beam current. The methods of 2D microtextural analysis (vesicle number density, vesicle volume distributions, and spherical and tubular stereoconversions (Sahagian and Proussevitch, 1998)) are given in Appendix **B3**.

We used a AccuPyc II 1340 Gas Pycnometer to determine the total ($\emptyset_t$) and isolated porosity volume ($\emptyset_i$) of cylindrical cores and fragments of cm-size pumice clasts from RP, GP, ALB and Dome. Vesicle connectivity is given as $(\emptyset_t - \emptyset_i)/\emptyset_t$. We used a PMI CFP-34RUE8A-3-6 Capillary Flow Porometer to measure the permeability of samples from RP and Dome. Further method details of pycnometry and capillary flow porometry given in **Chapter 3**.

The concentrations of H_2O, CO_2, S, Cl and F in matrix glass and phenocryst-hosted melt inclusions were measured using a CAMECA IMS 1280 ion microprobe at the Woods Hole Oceanographic Institution (WHOI). Concentrations were determined using a calibration of standards with known volatile contents from previous Fourier transform infrared (FTIR) measurements, as following the methods of Hauri et al. (2002). See Appendix **C1** for standard analyses, the calibration curves used to determine unknown concentrations, and SIMS analysis sample preparation methods. MicroRaman was used as an alternative method for H_2O_t acquisition in melt inclusions (see methods in section **2.2.2** and Appendix **A5**). We also acquired Cl, F, Na and K concentrations of quartz-polymorph crystals found in Dome vesicles using the JEOL JXA-8500F microprobe analyzer at 15 keV accelerating voltage with 15 nA beam current and a spot size of 10 µm.

4.4. Density distributions and componentry

Figure 4.4 shows (a) the density distributions for all the units analyzed and (b) the density/vesicularity of every individual 8 – 32 mm clast within each sample with linear distance from the main vent (see Appendix **C2** for full breakdown). The average vesicularity of 3352 clasts from the 2012 Havre eruption is 70%; this is lower than the vesicularity of 75 – 80% calculated by the Manga et al. (2018) model. However, units LGL, DB, TC and outliers from other units skew the overall distribution to lower vesicularity (**Figure 4.4a**). Total vesicularity ranges from 0 to 92%, there are no clasts more vesicular than this. Vesicularities of 65 – 85% are observed in the majority of samples analyzed where there is no identifiable change with distance from the vent (**Figure 4.4b**).

The breakdown of individual units attributed to the main vent (GP, ALB, RP and AL) give mean and median vesicularities of 72 – 77% and 75 – 79%, respectively (**Figure 4.4a**). LGL, DB and TC have very different distributions; Nrim is similar to the main vent units with high mean vesicularity, but is significantly skewed by denser clasts. LGL and DB have mean vesicularity of ~ 55%, although DB has a very broad, even spread of density, and LGL has a much narrower interquartile range; TC (mean vesicularity = 65%) sits somewhere between the Dome OP-vent-

derived units, and LGL and DB. Differences in the distribution spreads are better assessed using the componentry of each unit (**Figure 4.5**; Appendix **C3**).

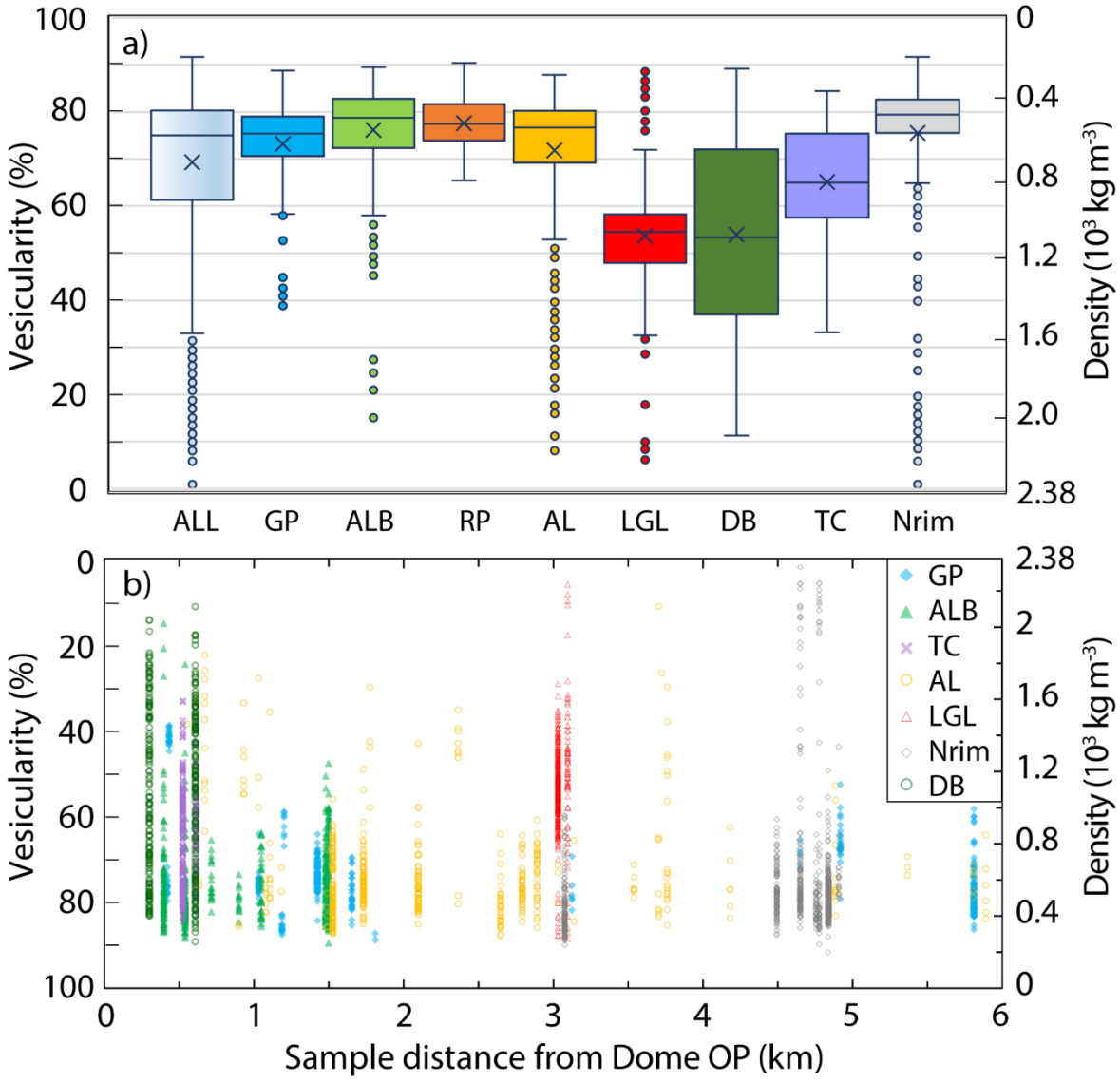

Figure 4.4. a) Box and whisker plots of density and corresponding vesicularity (DRE = 2380 kg m^{-3}) for all 8 – 32 mm clasts/fragments from pumiceous units identified in the 2012 eruption and the entire eruption (ALL). Each plot gives the mean (×), median (—), interquartile range (box), 5th to 95th percentiles (whiskers) and outliers outside of the latter range (°). b) The density / vesicularity of every clast analyzed by the Houghton and Wilson (1989) method with distance of the sample from the main vent (beneath Dome OP). Note that LGL, TC and some of AL samples are interpreted to have different vent origins.

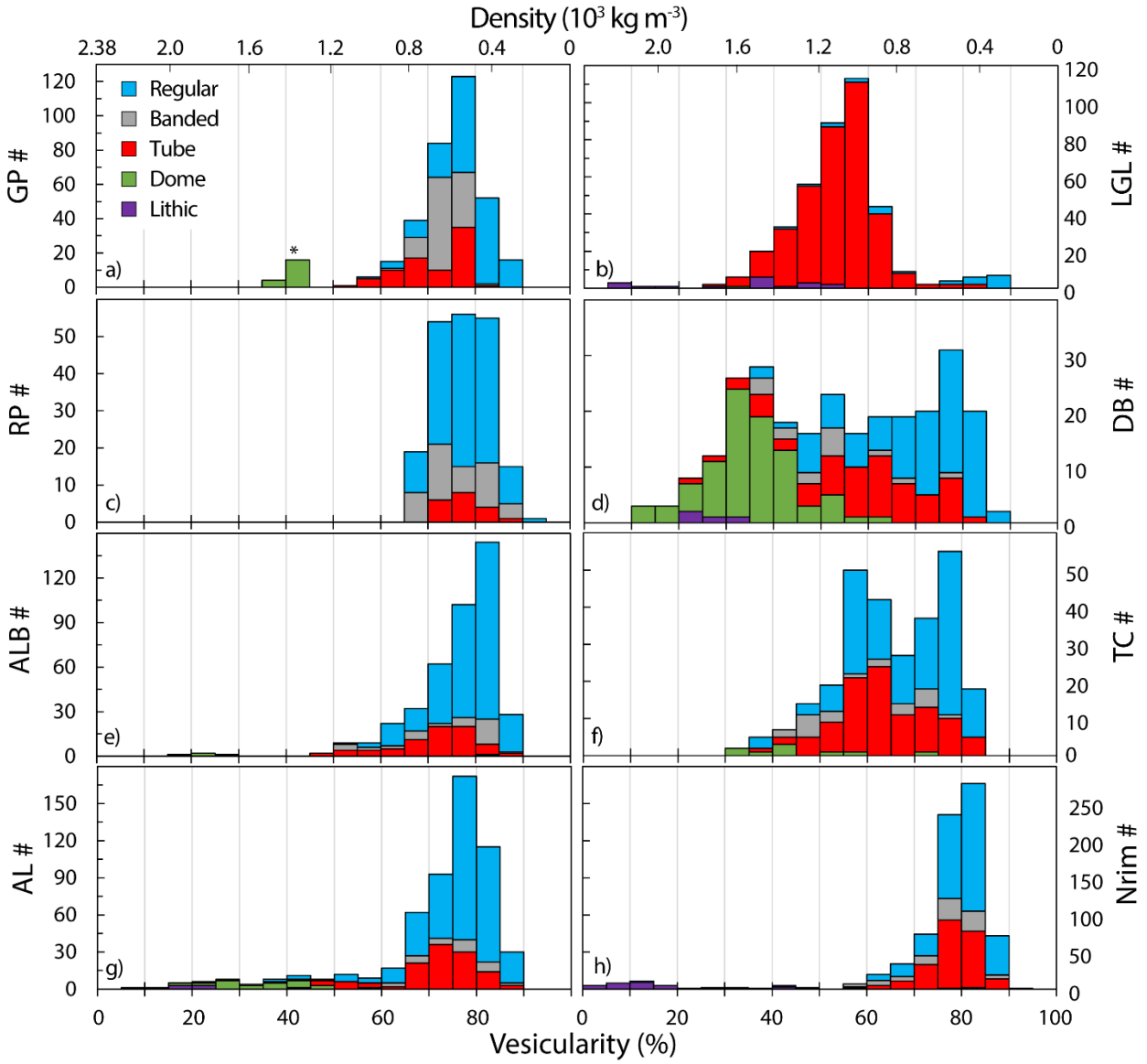

Figure 4.5. Textural componentry of all 8 – 32 mm diameter clasts/fragments from each pumiceous unit. # is the number of clasts analyzed within each pumiceous unit (GP, RP, etc.). Regular, Tube and Banded are defined by the textural classifications in Chapter 3; Dome is any low vesicularity 2012 lava; Lithic is any pre-2012, hydrothermally altered, or non-magmatic material. Note that the "Tube" pumice in the raft contain strictly elongate vesicles and not fully tubular. * denotes the dense exteriors of a giant vesicular block from the flanks of Dome OP (lower vesicularity that most GP).

For clastic componentry we identify five distinct textural categories similar to those used for GP (Chapter 3): 1) *Regular* pumice clasts are uniform and show no textural banding, brecciation or extensive vesicle shearing; 2) *Banded* pumice clasts have banding that is observed at the macro- and micro-scale as in Chapter 3; 3) *Tube* pumice clasts are dominated by elongate vesicles that can stretch the entire clast (tube vesicles), these clasts can have a "woody" fabric (Kato, 1987); 4) *Dome* material, i.e., high density rhyolite derived from the 2012 eruption, presumably from Dome OP; and 5) *Lithic* material not formed during the 2012 magma, this includes ash/lapilli aggregates, hydrothermal aggregates and old, altered dense lava.

The clastic units derived from the main vent (GP, RP, ALB and AL) are dominated by regular pumice and have similar modal vesicularities, although banding is observed in GP (as studied in detail in Chapter 3) and RP. ALB contains a few dome fragments, and AL has a tail of dense dome and lithic material, which can be attributed to those AL subunits with identified denser clastic components (subunit S4 as identified within Murch (2018)). DB, the Dome OP flank collapse mixed with ALB deposits, exhibits a broad, polymodal density distribution where the componentry changes with vesicularity: regular pumice dominates between 65 – 85%, tube pumice between 50 – 65% vesicularity, and dome material for lower vesicularity (<50%). LGL is almost ubiquitously tube and woody pumice with a single vesicularity mode (~55%). This mode is considerably lower than the mean vesicularity of tube pumice identified in other deposits (~75% in GP, ALB and Nrim). There are no banded pumice or dome fragments found in LGL, and the tails of the distribution are exclusively regular pumice (high vesicularity) and lithic material (low vesicularity). Nrim shows a componentry similar to that of GP, ALB and AL, although it has a significant tail of dense lithic material (sampling of fragments of pre-2012 lava with altered surfaces) and a very sharp modal vesicularity of 80 – 85% (the most vesicular mode). There is a significant population of tube pumice with high vesicularity similar to GP, RP and ALB. TC deposits have an even split of regular and tube pumice, although there is a bimodal distribution in both components.

4.5. Microtextural analysis of Havre products

4.5.1. Vesicle connectivity and permeability

There is a significant separation between the vesicle connectivity (c) of RP and GP (**Figure 4.6**). RP clasts have lower vesicle connectivity (i.e., higher isolated porosity) than GP fragments despite the similar total porosity ($\emptyset_t$) range (72 – 91%). RP clasts have values of c = 0.35 – 0.95, whereas GP has c = 0.92 to 1.0; the low connectivity of some raft pumice is very surprising for highly vesicular pumice. Banded giant pumice (GP290) has narrower $\emptyset_t$ (74 – 82%) but is almost fully connected (0.97 – 1.0) as shown in Chapter 3. ALB pumice are most similar to GP being, mostly, completely connected at high $\emptyset_t$ (>85%); ALB pumice has a greater textural affinity to giant pumice than raft pumice. There are clearly three distinct populations of connectivity at high $\emptyset_t$ (GP+ALB, Banded GP, and RP). Dome c values = 0.9 – 1.0 (c >1 error removed) at 20 – 51% total porosity. In all units, connectivity increases with $\emptyset_t$, but to a different extent (**Figure 4.6**); see Appendix **C4** for all pycnometry data.

We apply a threshold to assess whether clasts sink or float as a function of vesicle saturation by seawater (s) and vesicle connectivity (the determined isopycnal is equal to seawater density – 1027 kg m^{-3}; Driesner and Heinrich, 2007). s = 1 when all connected porosity is filled with water and isolated vesicles are filled with vapor of 1 kg m^{-3}. The threshold for a clast sinking is calculated for connectivity as:

$$c > \frac{2379\emptyset_t - 1026}{1026s\emptyset_t}$$

Lower porosity (>85%) RP clasts with low c sit above the threshold, i.e., the pumice floats. RP clasts with high connectivity at higher $\emptyset_t$ require greater trapped gas content to be able to float, so s is adjusted to 0.86. A threshold where s = 0.86 is the best fit to divide RP from GP and ALB pumice (**Figure 4.6**). This implies that some vapor remains trapped within RP connected porosity (>14% of connected porosity volume), as experimentally proven by Fauria et al. (2017).

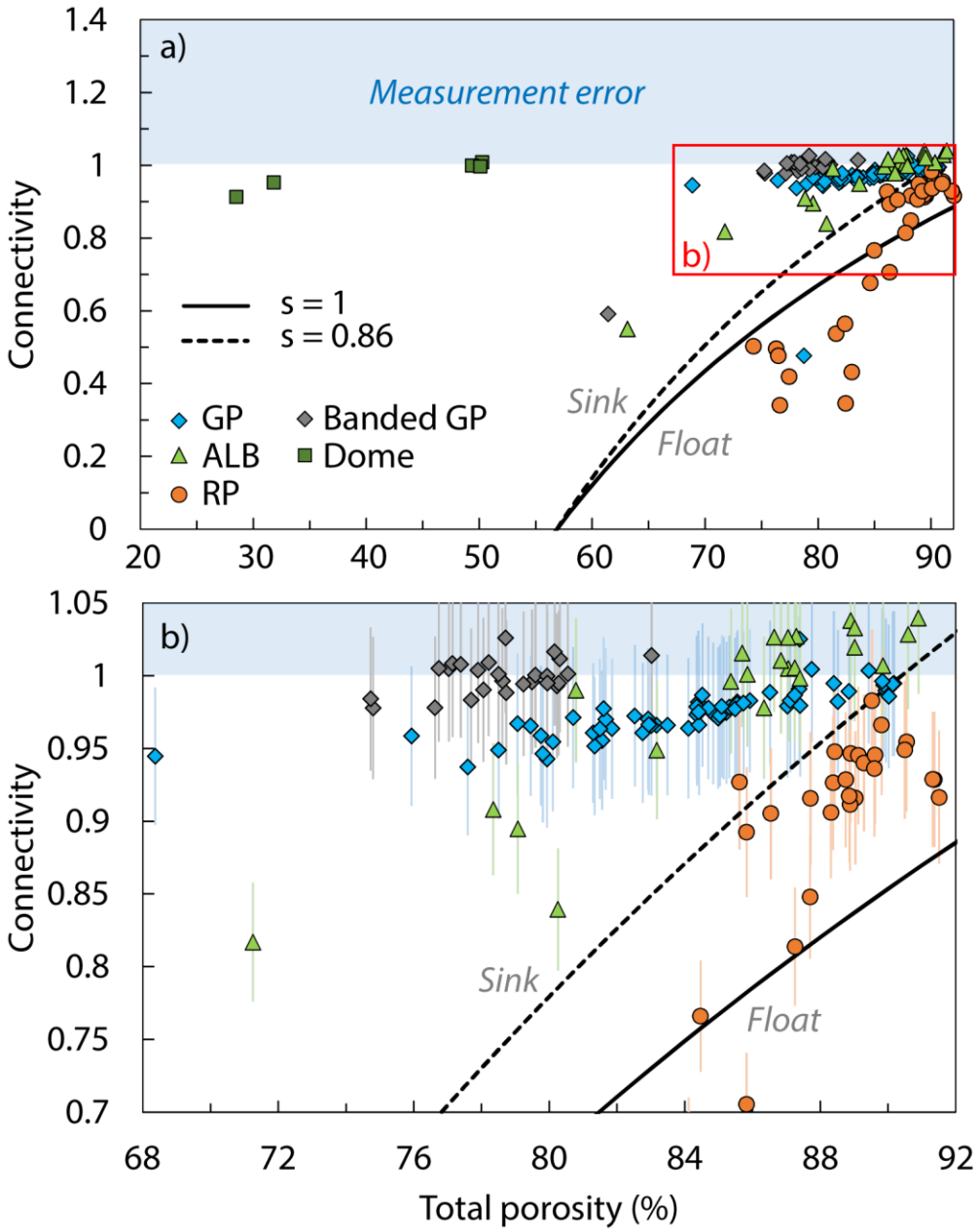

Figure 4.6. Total porosity vs. vesicle connectivity from pycnometry analysis of cores and fragments from RP, GP, ALB and Dome OP; b) is an inset from plot a) with analytical error added. GP, Banded GP and some RP data published previously by Manga et al. (2018) and Chapter 3. Analytical errors are given in the expanded inset. Connectivity values >1 are likely 1.00 in reality due to measurement error and analytical precision. *s* lines represent a constant density of 1027 kg m^{-3} – the threshold for floating vs. sinking in seawater. *s* = the saturation volume proportion of the connected porosity.

Darcian permeability (k_1) spans 3.5 orders of magnitude (5×10^{-13} – 10^{-9} m^2) throughout GP whereas RP has a tighter range from 7×10^{-13} – 9×10^{-12} m^2 despite the range in vesicle connectivity (see Appendix **C4**). There is no correlation of k_1 with $\emptyset_t$ or connected porosity within GP. The banded GP (GP290) shows a similar range to RP at lower $\emptyset_t$ (Appendix **C4**). Dome fragments, despite the low $\emptyset_t$ again have a similar k_1 range from 6×10^{-13} – 2×10^{-12} m^2; dome permeability values are new data. GP data was given in Chapter 3 and RP data acquired by Jones (unpublished),

4.5.2. Vesicle size distributions and number densities

Pumices and pumiceous fragments from units associated with the 900-meter-deep vent (now beneath Dome OP) show textural variability between units (**Figure 4.7**); there is also variability within the Dome samples themselves (**Figure 4.7j-l**). RP clasts display a broader size distribution of vesicles than GP or ALB, particularly in the finer vesicle sizes (<30 μm). RP vesicles are mostly circular, show a lack of preferred orientation, and most of the coalesced vesicles have very narrow bubble throats. The degree of coalescence decreases with decreasing vesicularity (**Figure 4.7a-c**). GP fragments have many larger vesicles and very few fully circular vesicles. Some vesicles in GP290 have irregular edges (this is due to the presence of microlites impeding late-stage vesicle expansion – Chapter 3). The degree of coalescence is greater in GP than RP, and there are considerably fewer isolated vesicles, as also observed in the He-pycnometry analysis (**Figure 4.6**). ALB pumice are similar to GP fragments, although vesicle shapes in ALB can be more irregular due to high degrees of coalescence (**Figure 4.7g-i**).

Dome clasts display two types of texture: 1) microlite-poor fragments collected from flank talus with low vesicularity, relaxed vesicles and smooth vesicle edges (**Figure 4.7j**); and 2) microlite-rich fragments collected from the exterior of a large talus block and the *in situ* carapace with deformed vesicles and with some preferred vesicle orientation and connected pathways (**Figures 4.7k** and **l** respectively). There are also small crystals of the quartz-polymorph cristobalite in some vesicles of the latter type of Dome samples (discussed in Section **4.5.3**). Dome samples lack the larger vesicles observed in GP and ALB, and coalescence is more sporadic; many smaller vesicles remain isolated.

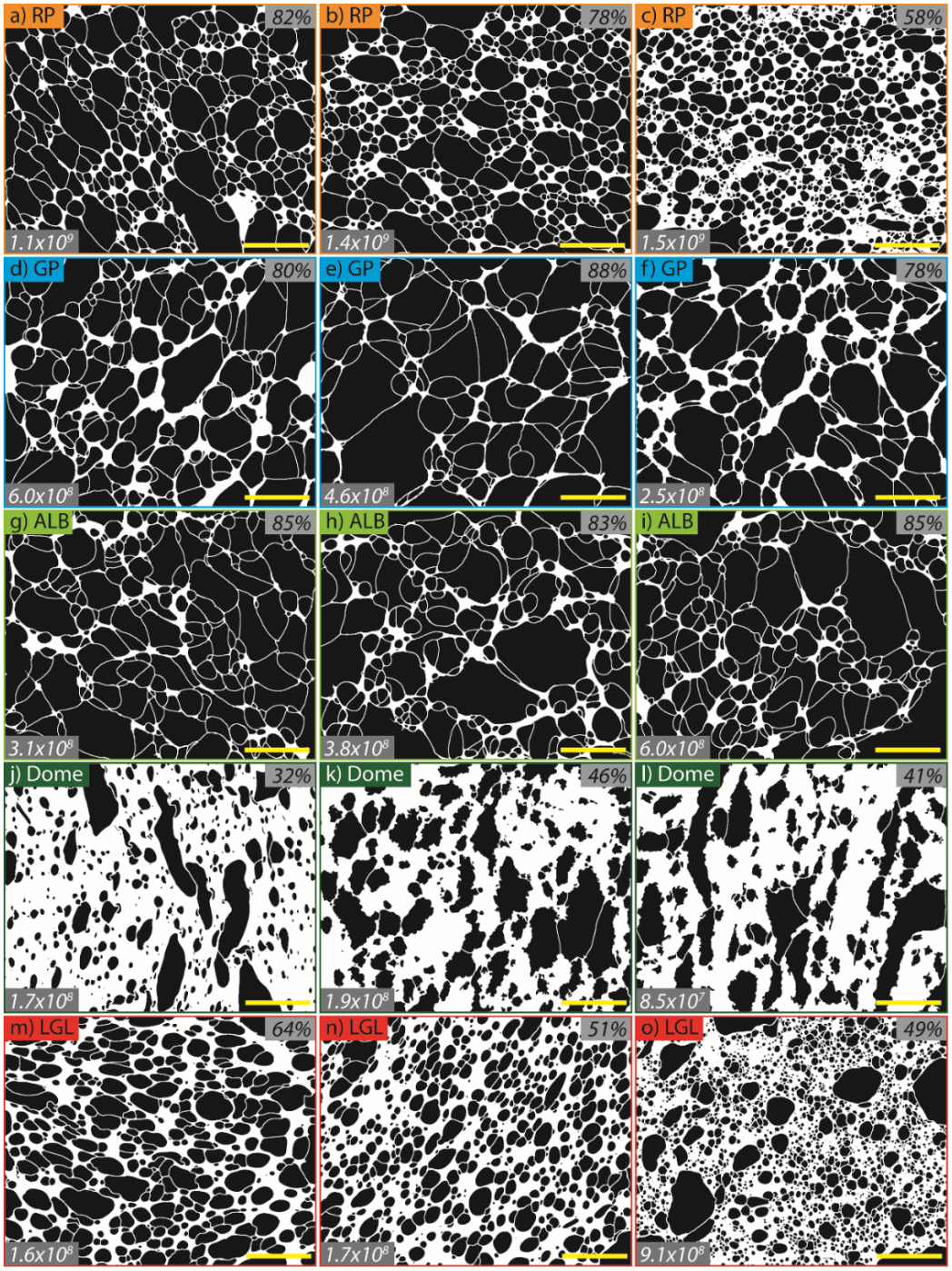

Figure 4.7. Example binary BSE images for each of the pumice units taken at 250x magnification with 2.67 pxl/µm resolution; scale bar = 100 µm. Vesicles are in black, and crystals and glass in white. All vesicles are decoalesced for number density analysis. Each image gives the unit, image vesicularity (%), and whole clast corrected vesicle number density (in cm^{-3}). Note that LGL images are tube vesicles cut perpendicular to the elongate vesicle axis. Images j) and k) were acquired from Dome OP talus, and l) from the *in situ* lava dome O carapace

LGL clasts have lower vesicularity and (apparently) very high vesicle number densities where there is significantly less vesicle coalescence (**Figure 4.7m-o**); as vesicularity decreases the vesicle number density increases and mean bubble size rapidly decreases. However, LGL clasts are dominated by extremely elongate vesicles as observed in the macrotextures. RP vesicles that show similar number densities and size distributions to LGL are mostly rounded, non-elongate and regular as shown by componentry analysis (**Figure 4.5**). Low vesicularity LGL clasts exhibit a very large number of 1 – 10 µm vesicles, although all LGL thin sections were acquired perpendicular to the elongate tube axis (**Figure 4.7o**). A compilation of all vesicle microtextural data from each unit (vesicle number densities, modal vesicle size, tubular stereo-conversions, volume fractions etc.) can be found in **Table 4.1**.

Vesicle number densities (N_{Vm}) are determined through the spherical or tubular stereo-conversion of 2D vesicle area distributions to 3D vesicle volume distributions (Sahagian and Proussevitch, 1998; Chapter 3); see Appendix **C5** for raw 2D vesicle number density distributions. N_{Vm} for Havre 2012 units range from 8.5×10^{7} to 1.5×10^{9} cm^{-3} after corrections are applied for prolate vesicle geometry (**Figure 4.8; Table 4.1**). RP clasts show consistently higher N_{Vm} values than the rest of the units (9.7×10^{8} to 1.5×10^{9} cm^{-3}) that match closely with pumice raft data from Rotella et al. (2015), despite using different image nesting structures. ALB vesicle number densities sit between RP and GP and within the higher end of GP N_{Vm} values (3.1×10^{8} to 7.5×10^{8} cm^{-3}); these are the regular GP from **Figure 4.5**. Dome talus N_{Vm} values are similar to lower N_{Vm} GP and banded GP, except for the Dome O carapace at 8.5×10^{7} cm^{-3}. We also compare the Havre 2012 data to data for other subaqueous silicic pumice-producing eruptions (**Figure 4.8**; Houghton et al., 2010; Rotella et al., 2015).

Table 4.1. Compilation of all vesicle microtextural data from every unit, including data from *Chapter 3 and +Rotella et al. (2015).

Unit	Group	Sample	[a]Distance (km)	[b]Clast density (gcc)	[c]Clast Ves (%)	[d]Img Ves (%)	[e]Vg_ Vl	D_Mod2 D (µm) [f]	D_Mod3 D (µm) [g]	D_Nv3 D (µm) [h]	[i]Abs. vol frac (<30)	[j]Abs. vol frac (>300)	[k]Vol % (<30 µm)	[l]Vol % (>300 µm)	[m]Nv (cm-3)	[n]Nvm (cm-3)	[o]Nvm adjust (cm-3)	[p]Prolate conversion applied	Vesicles analyzed	Vesicles used in analysis
GP*	Sph	41	3.12	0.526	78.1	66.89	3.57	23.8	47.5	25.7	0.185	0.120	0.241	0.157	1.4E+08	**6.6E+08**	5.1E+08	1.1.2	14966	3622
GP*	Sph	96	1.65	0.494	79.4	73.06	3.85	23.8	37.7	25.7	0.213	0.114	0.272	0.145	1.4E+08	**6.7E+08**	5.3E+08	1.1.2	13780	3080
GP*	Sph	192	1.19	0.355	85.2	82.5	5.76	30.0	59.8	32.4	0.128	0.158	0.126	0.155	8.8E+07	**6.0E+08**	4.6E+08	1.1.2	9873	1916
GP*	Sph	221	4.65	0.756	68.5	60.8	2.17	15.0	47.5	32.4	0.116	0.071	0.211	0.129	1.9E+08	**5.9E+08**	4.6E+08	1.1.2	16769	3835
GP*	Sph	231	5.81	0.456	81	69.28	4.26	23.8	37.7	16.2	0.163	0.098	0.229	0.138	1.5E+08	**7.8E+08**	6.0E+08	1.1.2	11038	3390
GP*	Tub	3	1.03	0.600	75	74.16	3.00	15.0	47.5	37.1	-	-	-	-	2.9E+08	**1.2E+09**	2.3E+08	1.3.10	14275	4676
GP*	Tub	22	1.20	0.871	63.7	61.02	1.75	11.9	30.0	37.1	-	-	-	-	4.2E+08	**1.2E+09**	2.6E+08	1.3.10	25356	6447
GP*	Tub	115	0.42	0.583	75.7	75.69	3.12	18.9	47.5	29.5	-	-	-	-	2.6E+08	**1.1E+09**	1.9E+08	1.3.10	18088	3935
GP*	Tub	270	4.92	0.787	67.2	67.42	2.05	11.9	30.0	29.5	-	-	-	-	4.3E+08	**1.3E+09**	2.2E+08	1.3.10	14882	5244
Band_GP*	Bulk	290	1.43	0.634	73.6	65.7	2.79	30.0	47.5	30.0	0.141	0.076	0.182	0.098	6.4E+07	2.5E+08	-	-	9542	3119
Band_GP*	Grey	290	1.43	0.502	79.1	68.94	3.78	30.0	59.8	23.8	0.116	0.156	0.176	0.239	5.9E+07	2.8E+08	-	-	11078	1936
Band_GP*	White	290	1.43	0.502	79.1	76.09	3.78	23.8	47.5	23.8	0.149	0.084	0.211	0.119	7.5E+07	3.6E+08	-	-	16564	2323
Dome	Talus	7	0.43	1.394	41.9	39.3	0.72	7.5	94.8	6.0	0.040	0.034	0.191	0.162	1.4E+08	**2.4E+08**	1.9E+08	1.1.2	9687	3935
Dome	Talus	118	0.33	1.109	53.8	34.52	1.16	9.5	94.8	11.9	0.066	0.061	0.248	0.230	1.7E+08	**3.6E+08**	2.8E+08	1.1.2	12117	3736
Dome	Carapace	10	0.05	1.786	25.6	34.56	0.34	9.5	59.8	9.5	0.038	0.001	0.263	0.008	5.3E+07	8.5E+07	-	-	9912	3544
ALB (DB)	VH	189	0.303	1.719	28.4	26.2	0.40	9.4	23.6	4.7	-	-	-	-	3.7E+08	**5.2E+08**	1.7E+08	1.2.5	8047	4145
ALB	L	184	0.399	0.343	85.4	81.2	5.85	23.8	37.7	15	0.188	0.153	0.194	0.158	8.8E+07	6.0E+08	-	-	15223	2584
ALB	L	189	0.30	0.593	74.7	76.74	2.95	18.9	47.5	11.9	0.255	0.056	0.284	0.063	1.9E+08	7.5E+08	-	-	13348	4036
ALB	VL	189	0.30	0.423	82.4	83.9	4.68	23.8	47.5	23.8	0.144	0.185	0.148	0.190	6.7E+07	3.8E+08	-	-	9997	2100
ALB	M	120	0.54	0.423	82	76.9	4.56	30.0	75.3	18.9	0.116	0.090	0.343	0.104	5.7E+07	3.1E+08	-	-	9350	2208
ALB	H	184	0.40	0.93	61.2	47.2	1.58	18.6	46.8	11.8	0.218	0.046	0.367	0.077	5.5E+08	6.0E+08	-	-	16604	2955
RP	L	FJ	-	0.38	84.2	76.87	5.33	15.0	30	15	0.293	0.174	0.307	0.182	2.2E+08	1.4E+09	-	-	18382	4553
RP	M	FJ	-	0.477	80.1	77.3	4.03	11.9	37.7	11.9	0.213	0.067	0.303	0.096	2.1E+08	1.1E+09	-	-	17737	5770
RP	M	FJ	-	0.487	79.7	76.1	3.93	11.9	37.7	11.9	0.229	0.126	0.295	0.162	2.4E+08	1.2E+09	-	-	22613	4084
RP	H	FJ	-	0.696	71	61.9	2.45	15	23.8	7.5	0.245	0.109	0.405	0.181	2.8E+08	9.7E+08	-	-	26677	5856
RP	M_band	FJ	-	0.474	80.2	62	4.05	11.9	23.8	11.9	0.262	0.143	0.373	0.203	2.9E+08	1.5E+09	-	-	27060	5262
RP_Rot+	*L*	-	-	*0.274*	*88.6*	-	7.76	-	*52*	-	-	-	-	-	*1.1E+08*	*9.8E+08*	-	-	-	*818*
RP_Rot+	*M*	-	-	*0.554*	*76.9*	-	3.33	-	-	-	-	-	-	-	*1.5E+08*	*6.6E+08*	-	-	-	*553*
RP_Rot+	*H*	-	-	*0.672*	*72.0*	-	2.57	-	-	-	-	-	-	-	*3.4E+08*	*1.2E+09*	-	-	-	*717*
LGL	L	70	0	0.829	64.7	59.8	1.83	23.8	30	23.8	-	-	-	-	1.4E+08	**4.0E+08**	1.6E+08	1.2.5	15294	2708
LGL	M	70	0	1.004	58.1	52.1	1.39	14.8	23.5	11.8	-	-	-	-	3.5E+08	**8.3E+08**	1.7E+08	1.3.10	11468	7058
LGL	H	70	0	1.294	*46.1*	41.8	0.86	5.9	11.8	5.9	-	-	-	-	2.7E+09	**5.0E+09**	9.1E+08	1.3.10	18510	4983

a = distance from derived vent; b = whole clast density in 10^3 kg m^{-3}; c = corresponding clast vesicularity (DRE = 2380 kg m^{-3}); d = mean vesicularity of all 250x mag. BSE images; e = pore space fraction / glass fraction; f = modal vesicle circular diameter prior to stereo-conversion; g = modal vesicle spherical diameter after stereo-conversion; h = middle spherical diameter of modal vesicle number density bin; i = absolute total volume fraction of all vesicles smaller than 30 µm; j = absolute total volume fraction of all vesicles larger than 300 µm; k = % volume fraction of all vesicles smaller than 30 µm; l = % volume fraction of all vesicles larger than 300 µm; m = vesicle number density prior to density correction; n = vesicle number density after density correction; o = vesicle number density if a non-spherical stereo-conversion is applied; p = vesicle aspect ratio used from Sahagian and Proussevitch (1998) if a non-spherical stereo-conversion is applied. Talus samples are equivalent to DB.

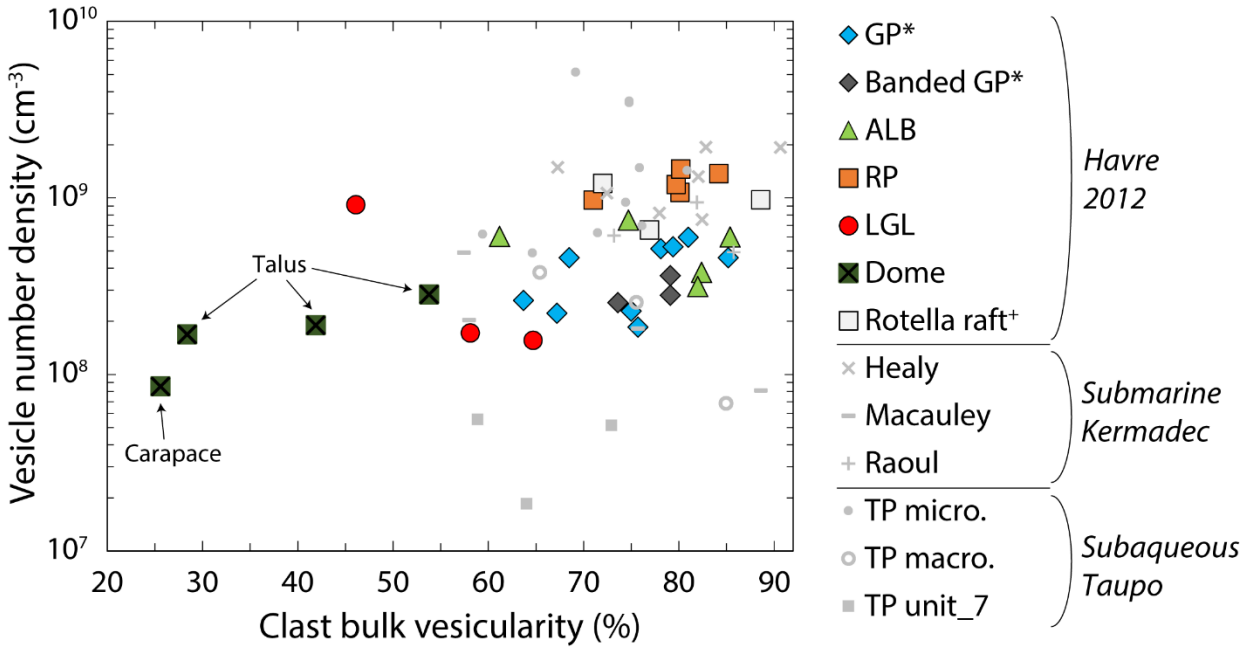

Figure 4.8. Vesicle number density (after density correction and possible prolate stereo-conversions; see **Table 4.1**) vs. whole clast vesicularity for each pumiceous unit from Havre 2012, and other subaqueous silicic eruptions. *Data acquired from Chapter 3. Rotella raft, Healy, Macauley and Raoul (SW) data from Rotella et al. (2015). TP data are from the 1.8 ka Taupo eruption where micro. and macro. are microvesicular and macrovesicular pumice from Unit 2 – The Hatepe Plinian (Houghton et al., 2010). Talus and carapace samples are identified within Dome.

The higher vesicle number densities in RP clasts are attributed to a greater number of vesicles <20 µm in diameter (**Figure 4.9**). GP, RP and ALB have similar vesicle size distributions for vesicles between 20 and 1000 µm, but ALB shows similarities with both RP and GP that deviate at the smaller vesicle sizes. All Dome samples have very few vesicles between 15 and 40 µm in comparison to the higher vesicularity pumice units. Despite that, they show similar vesicle size distributions between 50 and 1000 µm with the exception of the Dome O carapace (lowest bulk vesicularity) that is depleted in vesicles <6 µm and >100 µm in diameter (**Figure 4.9**). We observe similar relationships in **Figure 4.10**, particularly when comparing the modal vesicle diameter by number density and volume fraction of vesicles <30 µm with bulk vesicularity. RP clasts have consistently lower modal vesicle number density than GP, and ALB pumice show textural

similarities with both RP and GP (**Figure 4.10b, c**). We note that for lower vesicularity LGL, the tubular stereo-conversion may be insufficient to assess fully the microtextural differences with other units, a vesicle aspect ratio assumption of 1:10 (**Table 4.1**) may be too small to capture the tube vesicle nature of LGL pumice where aspect ratios can reach 1:>100 (**Figure 4.7m-o**).

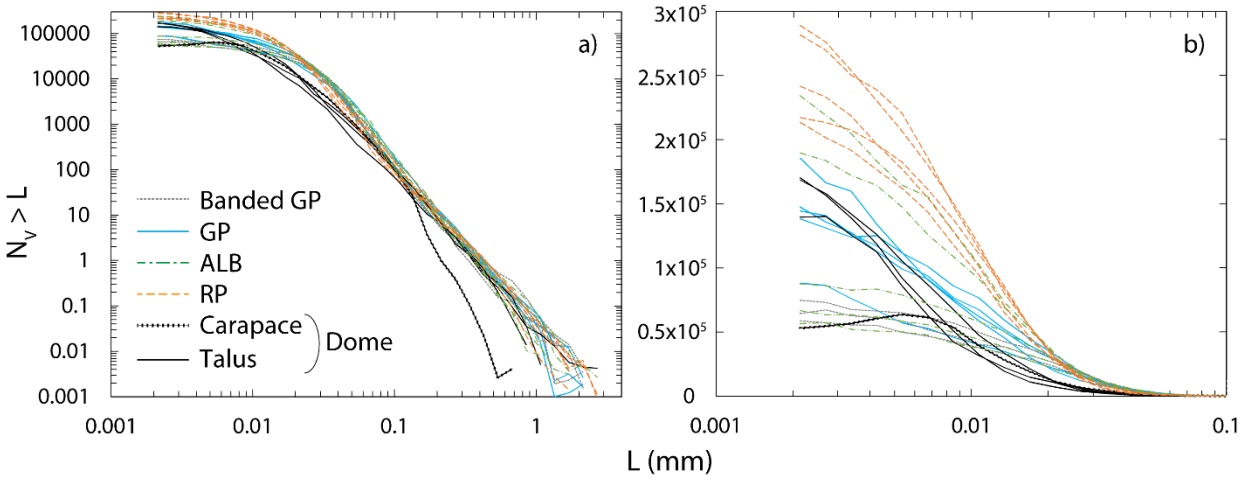

Figure 4.9. Cumulative number density of each size fraction (N_V) greater than the next largest size fraction (L) from stereo-conversion analysis. Vesicle diameter (circular equivalent) ranges from 2.1 – 2780 µm. Note that samples with the elongate stereo-conversions (LGL, tube giant pumice) are not included within this comparison. The same plot is given at both the logarithmic (a) and linear (b) scale.

Averaged minimum wall thicknesses between vesicles are calculated using an algorithm that determines the wall thickness between two adjacent vesicles (see Appendix **C6** for details). Dome samples display the highest minimum wall thicknesses (mean = 2.9 – 4.1 µm), as expected for low vesicularity material, higher than LGL clasts at the same vesicularity that only have 1.5 – 1.7 µm mean wall thicknesses. There is no clear difference between the mean, maximum and range of wall thicknesses in GP, RP and ALB (Appendix **C6**). At high vesicularity (60 – 85%) all pumice clasts are expected to have very thin bubble walls (~1 µm) that will rupture during bubble coalescence.

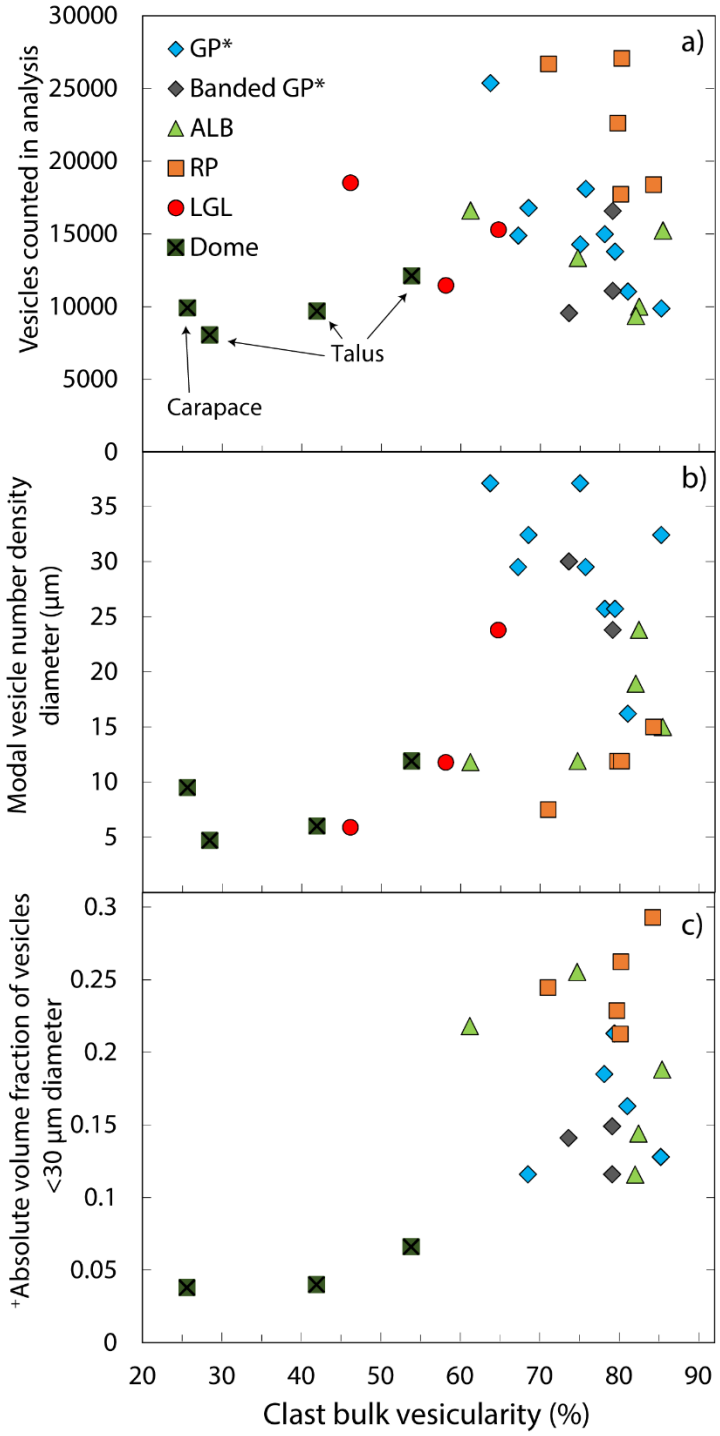

Figure 4.10. Vesicle properties from each clast analyzed in greater microtextural detail vs. whole clast vesicularity. *Data acquired from Chapter 3. [+]Samples with the elongate stereo-conversions applied are not included in c). See **Table 4.1** for further data. a) is the number of vesicles analyzed within the entire image nest for each sample; b) is vesicle diameter of the size bin with the greatest vesicle number density; c) is the total volume fraction of all vesicles that are <30 µm in diameter.

4.5.3. Vapor-phase cristobalite in dome vesicles

Cristobalite is identified within dome carapace and talus vesicles (**Figure 4.11**); this was verified through acquiring Raman spectra of the crystals (see Appendix **C7**). In its stable form, this silica polymorph forms at temperatures far exceeding that of rhyolitic magma (>1450°C; Richet, 1982). The crystals seen here are a meta-stable form of cristobalite that precipitates out of silica-rich fluids within vesicles where there is a high rate of outgassing; this is relatively common in large, warm silicic domes (Baxter et al., 1999; Horwell et al., 2013; Schipper et al., 2015; Kendrick et al., 2016; Schipper et al., 2017; Ikegami et al., 2018).

Vapor-phase cristobalite crystals grow into pre-existing vesicles from the vesicle edge. The exsolution of Cl and F from the melt results in the outgassing of HCl and HF (Schipper et al., 2017). These highly acidic vapors can dissolve glass and remove large amounts of SiO_2; these regions of dissolution appear darker in BSE images, i.e., regions of lower mean atomic density (**Figure 4.11**). Exsolved SiO_2 reacts with the acidic vapors in pore space forming fluids rich in SiF_4 and $SiCl_4$. Experimental studies show that temperatures around 200 – 270°C are sufficient to cause precipitation of the SiO_2 phase as cristobalite (Riker et al., 2015; Schipper et al., 2015). Vapor-phase cristobalite crystals can be identified from their euhedral crystal habits, presence *inside* vesicles, internal "fish-scale" micro-cracking (**Figure 4.11d**), and association with glass dissolution textures and diktytaxitic void space between microlites (Horwell et al., 2013; Kushnir et al., 2016).

It is important to consider vapor-phase cristobalite for several reasons: 1) the implications for permeability, vesicle connectivity and dome outgassing (Kendrick et al., 2016; Kushnir et al., 2016); 2) the nature and initial concentrations of halogens (Cl and F) degassing from the magma (Wallace, 2005; Riker et al., 2015; Schipper et al., 2017); 3) the internal cooling rates of submarine silicic domes (Horwell et al., 2013); and 4) the need to remove these crystals from 2D BSE images to calculate accurate vesicle number densities and size distributions for Dome samples (see Appendix **C7**). I acquired size distributions of cristobalite within three Dome samples: two from the talus (DB_007 and DB_118) and one from the *in situ* Dome O carapace (**Figure 4.12**). The talus samples have similar mean crystal circular-equivalent diameters (10 – 12 μm), size distributions, and % of vesicle area taken up by cristobalite (5 – 8%).

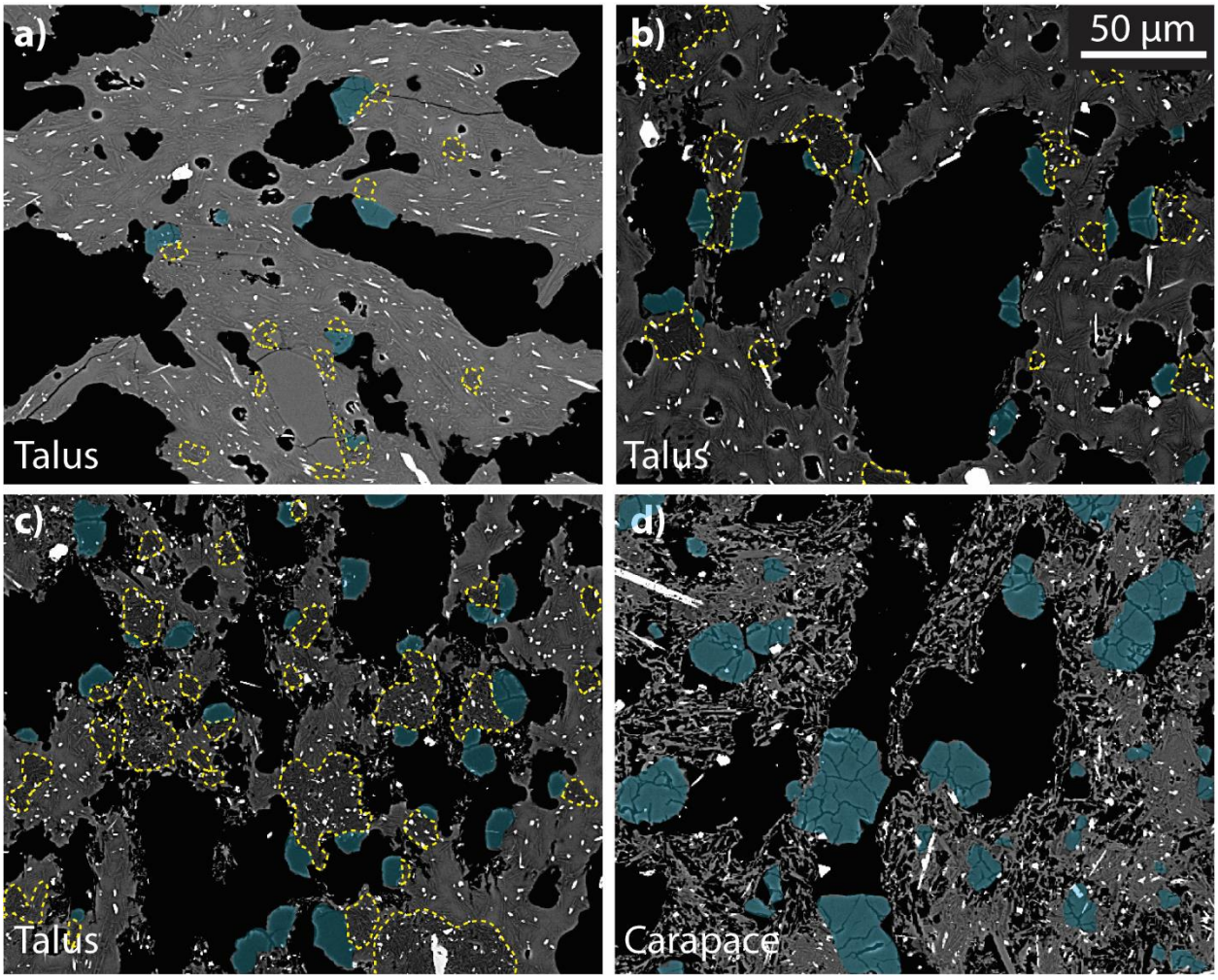

Figure 4.11. Vapor-phase cristobalite crystals in Dome OP talus (a-c) and *in situ* carapace (d) in unprocessed BSE images at 250x magnification. Vesicles are in black, pyroxene and Fe-Ti oxide microlites are seen as bright white, and glass and acicular plagioclase microlites are observed in grey. Cristobalite crystals (highlighted in blue) are characterized by angular habits, internal "fish-scale" fractures and darker BSE color than glass (due to lower average atomic mass). Regions of silica depletion from the glass are outlined (yellow dashed line). No areas are highlighted in (d) as most of the glass has undergone full dissolution.

The crystal size distributions are comparable to those from Horwell et al. (2013) and Schipper et al. (2017). Carapace crystals are generally larger, with maximum diameters up to 52 µm; they have extensive fish-scale fractures and euhedral habits (**Figure 4.11d**), and take up 43% of total vesicle area (**Figure 4.12**). In many cases, carapace crystals appear to have grown to fill the pre-

existing vesicles. We observe here the evolution of cristobalite within a submarine silicic dome by analyzing crystals from older, rapidly-quenched dome material, to the freshest *in situ* summit material where there was significant outgassing (**Figure 4.11**). Almost all glass has been removed from the carapace sample leaving behind only a framework of microlites, cristobalite, vesicles and diktytaxitic pore space between crystals (**Figure 4.11d**).

Compositional data of cristobalite from the three samples show that these crystals take up residual concentrations of Cl, Na and K; F content is negligible (<10 ppm). As mean crystal size increases, cristobalite crystals contain lower amounts of all residual elements, (see Appendix **C7** for compositional data).

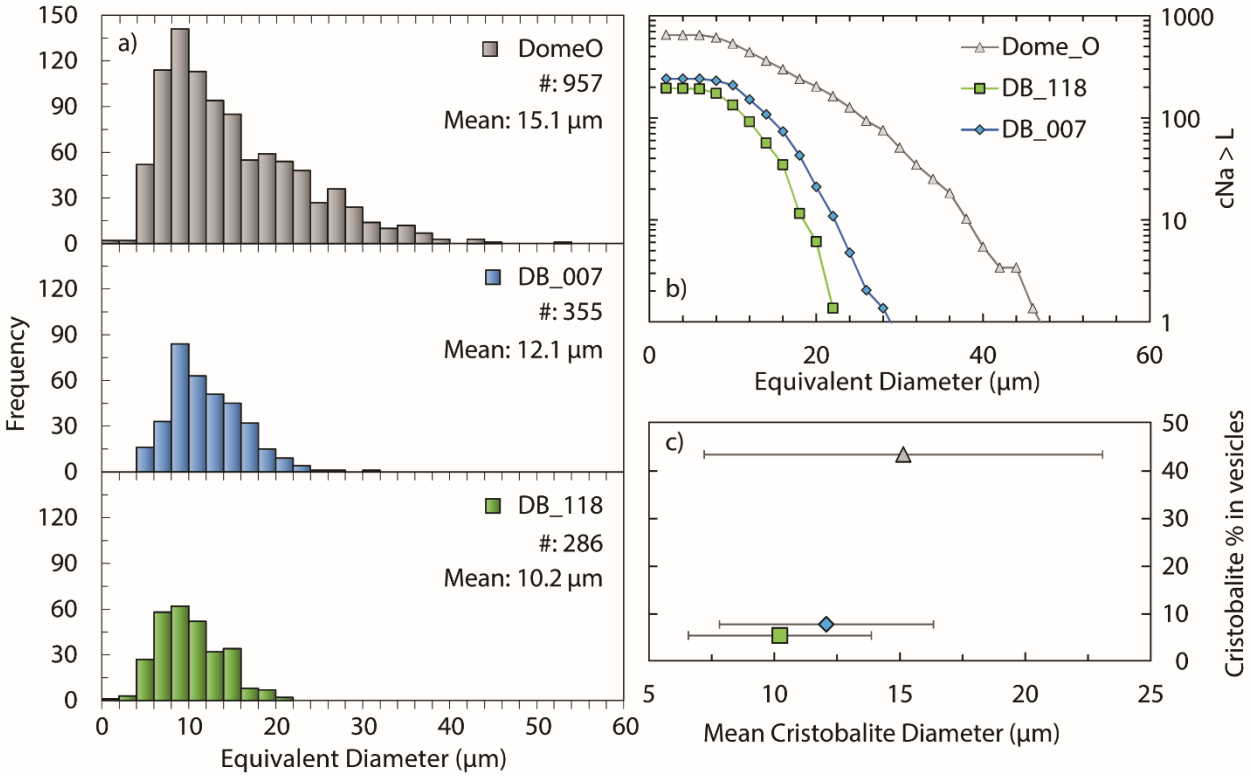

Figure 4.12. Cristobalite size distributions (a), crystal number density per unit area (cNa) (b), and mean crystal size vs. % area of vesicularity taken up by cristobalite (c). Samples are from the Dome O carapace and two talus samples (DB_007 and DB_118). Cristobalite diameters given as diameters of the equivalent circular area.

4.6. Volatile concentrations in matrix glass and melt inclusions

Matrix glasses reveal similar volatile contents within and between different units, particularly in the lower abundance volatiles (CO_2, S and F) (**Figure 4.13; Table 4.2**). H_2O_t varies between 0.2 and 1.7 wt. % in all samples with no consistent increase with other volatile phases. LGL has consistently higher H_2O_t than GP and Dome; RP and ALB span this range.

As SIMS cannot distinguish speciation within H_2O_t as FTIR does, and we do not measure H isotopes within this study, we cannot distinguish rehydration sources or excess of H_2O_m in the matrix glass as identified in Chapter 2. The Cl/F ratio vs. H_2O_t (**Figure 4.13**) can be used to possibly identify rehydration by seawater (diffusion of dissolved Cl^- ions into the glass), but we see no significant relationship between the two. However, the extensive study of H_2O and rehydration in Mitchell et al. (2018a) (Chapter 2) allows us to focus on the other volatile phases within this study. We note that the H_2O_t range from SIMS is similar to the range from FTIR (0.05 – 1.4 wt. %), although inconsistent within the individual unit ranges.

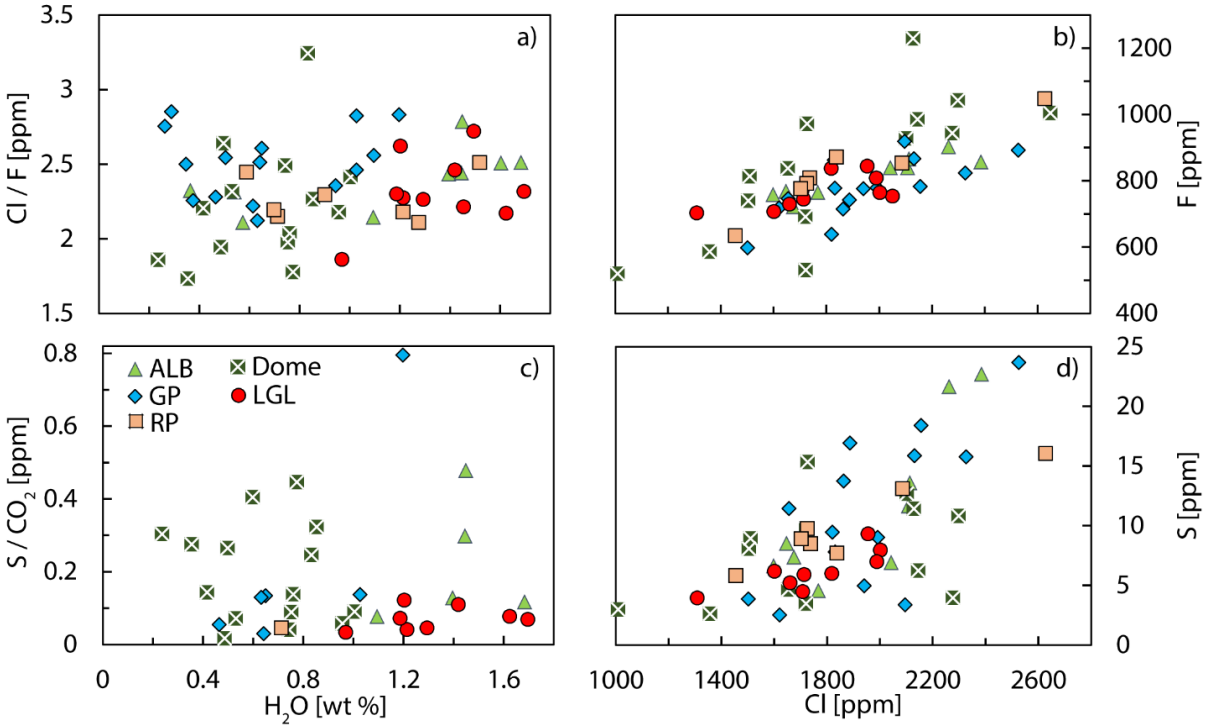

Figure 4.13. Matrix glass volatile concentrations and ratios from SIMS analysis for all major pumiceous units. Plots are the halogen ratio (Cl/F) vs. H_2O (a), Cl vs. F (b), the S/CO_2 ratio vs. H_2O (c) and S vs. Cl (d).

Table 4.2. Matrix glass volatile concentrations from SIMS analysis with ±1 standard deviation error.

Unit	Mode	H_2O (wt. %)	±1σ	CO_2 (ppm)	±1σ	F (ppm)	±1σ	S (ppm)	±1σ	Cl (ppm)	±1σ
ALB	H	1.68	-	100.1	*10.6*	839	*2.6*	11.6	*0.26*	2108	*5.2*
		1.45	-	47.5	*9.4*	856	*5.1*	22.7	*0.42*	2385	*18.5*
		1.60	-	-	-	902	*2.8*	21.6	*0.17*	2262	*17.6*
		1.40	-	53.8	*19.1*	839	*8.2*	6.9	*0.33*	2042	*27.1*
		1.44	-	45.6	*13.8*	866	*7.4*	13.6	*0.19*	2113	*11.6*
ALB	M	1.09	-	111.0	*3.8*	768	*5.6*	8.5	*0.24*	1646	*14.2*
		0.54	-	-	-	764	*11.7*	4.6	*0.21*	1767	*17.8*
		0.36	-	-	-	721	*8.1*	7.4	*0.55*	1675	*17.1*
		0.57	-	-	-	758	*6.8*	6.6	*0.62*	1597	*10.2*
		2.13	-	-	-	781	*6.6*	-	-	-	-
DB	7	0.24	-	29.4	*6.7*	813	*6.9*	8.9	*0.08*	1510	*10.1*
		0.35	-	41.4	*11.1*	1229	*11.2*	11.4	*0.61*	2128	*39.2*
		0.50	-	23.2	*2.6*	1004	*3.5*	-	-	2649	*97.0*
		0.60	-	26.4	*2.3*	1284	*67.0*	10.7	*0.64*	-	-
		0.50	-	37.2	*5.6*	1064	*60.3*	9.8	*0.40*	-	-
		0.42	-	75.5	*12.5*	1042	*21.4*	10.8	*0.31*	2298	*47.1*
DB	H	0.85	-	39.3	*7.9*	928	*5.5*	12.7	*0.24*	2102	*8.5*
		0.76	-	58.7	*4.6*	739	*22.2*	8.1	*0.39*	1504	*52.8*
		0.83	-	39.6	*2.5*	531	*31.0*	9.7	*0.29*	1722	*19.4*
		0.77	-	34.3	*5.8*	972	*12.1*	15.3	*0.44*	1726	*31.1*
DB	VH	1.00	-	43.8	*3.5*	943	*8.1*	4.0	*0.14*	2277	*34.0*
		0.75	-	52.2	*8.4*	837	*42.2*	4.6	*0.22*	1654	*108.6*
		0.74	-	86.2	*6.9*	691	*11.5*	3.5	*0.05*	1721	*49.7*
		0.49	-	178.1	*10.8*	520	*42.5*	3.0	*0.21*	1010	*61.8*
		0.96	-	108.3	*16.8*	985	*29.7*	6.2	*0.23*	2145	*63.5*
		0.53	-	36.6	*4.2*	586	*19.7*	2.6	*0.27*	1358	*56.8*
GP	22	0.94	-	-	-	778	*14.2*	-	-	1832	*17.1*
		1.10	-	-	-	778	*6.3*	9.0	*0.16*	1992	*15.3*
		0.64	-	129.7	*14.2*	598	*4.8*	3.9	*0.14*	1502	*17.7*
		1.20	-	29.8	*4.4*	892	*8.0*	23.7	*0.19*	2526	*26.9*
		1.03	-	115.3	*8.2*	824	*8.0*	15.8	*0.31*	2326	*21.9*
		1.03	-	-	-	866	*2.1*	15.9	*0.19*	2131	*8.1*
GP	231	0.61	-	-	-	746	*4.6*	11.4	*0.23*	1656	*16.1*
		0.50	-	-	-	742	*3.5*	16.9	*0.24*	1887	*8.1*
		0.65	-	102.4	*1.0*	715	*3.6*	13.7	*0.37*	1863	*6.0*
		0.29	-	-	-	638	*4.3*	9.5	*0.22*	1820	*23.8*
		0.26	-	-	-	783	*13.6*	18.4	*1.61*	2155	*57.6*
GP	290G	1.14	-	-	-	721	*4.3*	-	-	-	-
		0.78	-	-	-	-	-	-	-	-	-
		0.35	-	-	-	776	*11.9*	5.0	*0.51*	1940	*44.7*
		0.46	-	61.5	*4.5*	919	*16.2*	3.4	*0.14*	2096	*27.6*
		0.38	-	-	-	718	*5.6*	2.5	*0.10*	1621	*20.6*
GP	290W	0.63	-	60.4	*2.7*	862	*13.6*	7.8	*0.29*	1830	*46.2*
LGL	H	1.49	-	94.0	*16.4*	753	*5.5*	-	-	2050	*10.8*
		1.45	-	-	-	772	*6.1*	4.5	*0.26*	1708	*15.5*
		1.29	-	134.6	*13.5*	707	*6.9*	6.2	*0.18*	1601	*8.0*
LGL	L	0.97	-	118.3	*15.6*	703	*14.8*	4.0	*0.48*	1309	*32.5*
		1.20	-	65.4	*8.1*	764	*9.9*	8.0	*0.23*	2002	*10.5*
		1.21	-	127.4	*17.4*	730	*5.0*	5.2	*0.42*	1660	*13.8*
		1.19	-	81.7	*10.8*	745	*1.6*	5.9	*0.55*	1713	*7.3*
LGL	M	1.62	-	77.5	*9.2*	837	*9.7*	6.0	*0.36*	1818	*26.4*
		1.42	-	63.9	*3.8*	808	*8.9*	7.0	*0.26*	1988	*22.6*
		1.70	-	134.8	*5.8*	844	*6.0*	9.3	*0.28*	1955	*27.2*
RP	band	0.71	-	185.0	*32.0*	808	*5.2*	8.5	*0.30*	1738	*18.5*
		1.21	-	-	-	792	*16.3*	9.8	*0.42*	1726	*32.3*
		0.70	-	-	-	776	*9.7*	8.9	*0.30*	1703	*32.0*
		0.90	-	-	-	634	*9.3*	5.8	*0.17*	1455	*14.9*
		1.28	-	-	-	872	*5.7*	7.7	*0.47*	1838	*20.5*
RP	H	1.52	-	-	-	1047	*23.4*	16.0	*1.19*	2628	*107.2*
		1.55	-	-	-	799	*13.4*	-	-	-	-
		0.59	-	-	-	853	*11.9*	13.1	*0.39*	2087	*51.6*

CO_2 is low in abundance throughout all samples (<50 ppm), although there is the possibility of some vesicle edge contamination causing heterogeneous ^{12}C signals (**Figure 4.13**). Nevertheless, the low CO_2 content supports the results from Mitchell et al. (2018) where the CO_2 peak was not identifiable in any FTIR spectra. S contents are comparably very low and consistent (<25 ppm) throughout all units. This verifies XRF and EPMA analyses of S in giant pumice (Chapter 3); SIMS analysis provides the most accurate and highest resolution data compared with previous techniques used (Hauri et al., 2002). F, Cl and S concentrations correlate well with each other (**Figure 4.13**). F concentrations range from 500 – 1100 ppm and Cl from 1000 – 2600 ppm.

Melt inclusions from quartz and some plagioclase phenocrysts 1 – 2 mm in diameter from RP and GP samples reveal a range of H_2O = 4.3 – 5.2 wt. % with some outlying values (**Figure 4.14**). The H_2O ranges for melt inclusions within quartz and within plagioclase fully overlap; there is no distinction between the two. However, there is an identifiable decrease in CO_2 and S content in plagioclase-hosted melt inclusions. A selection of melt inclusions from the white bands of GP290 (giant pumice with banding) show an overlapping range from 5.1 – 6.5 wt. % H_2O; other volatile ranges (CO_2, S, Cl, F) are fully consistent with RP and other GP data (**Figure 4.14**). Some melt inclusions from RP and GP290 show increased H_2O *and* Cl, but consistent F; this is possibly due to seawater rehydration (**Table 4.3**).

Repeat measurements of GP290 melt inclusions using µRaman spectroscopy revealed a much lower range (~2 – 3 wt. % H_2O_t) than that acquired from SIMS analysis (Appendix **C8**). It is possible that the SIMS analyses altered the surface H_2O content, which was subsequently analyzed by µRaman spectroscopy. The additional RP and GP melt inclusion data advocate strongly for higher H_2O (**Figure 4.14**). Exposed melt inclusions in smaller crystals (<0.5 mm) from thin sections of RP and GP samples reveal lower H_2O_t ranges of 2.2 – 3.1 wt. % using µRaman analysis; CO_2 is unknown here and so cannot be used to establish singular data points in **Figure 4.14a**.

All melt inclusions from SIMS analysis have ranges of 20 – 230 ppm CO_2, 40 – 155 ppm S, 750 – 1100 ppm F, and 2400 – 3800 ppm Cl, without considering outliers (**Figure 4.14**). There are systematic increases in Cl and F with H_2O in the main H_2O range from melt inclusions, and likewise between both halogens (**Figure 4.14b, e** & **f**). The low abundance of CO_2 and S in melt inclusions (<230 ppm) results in a weaker, but positive relationship.

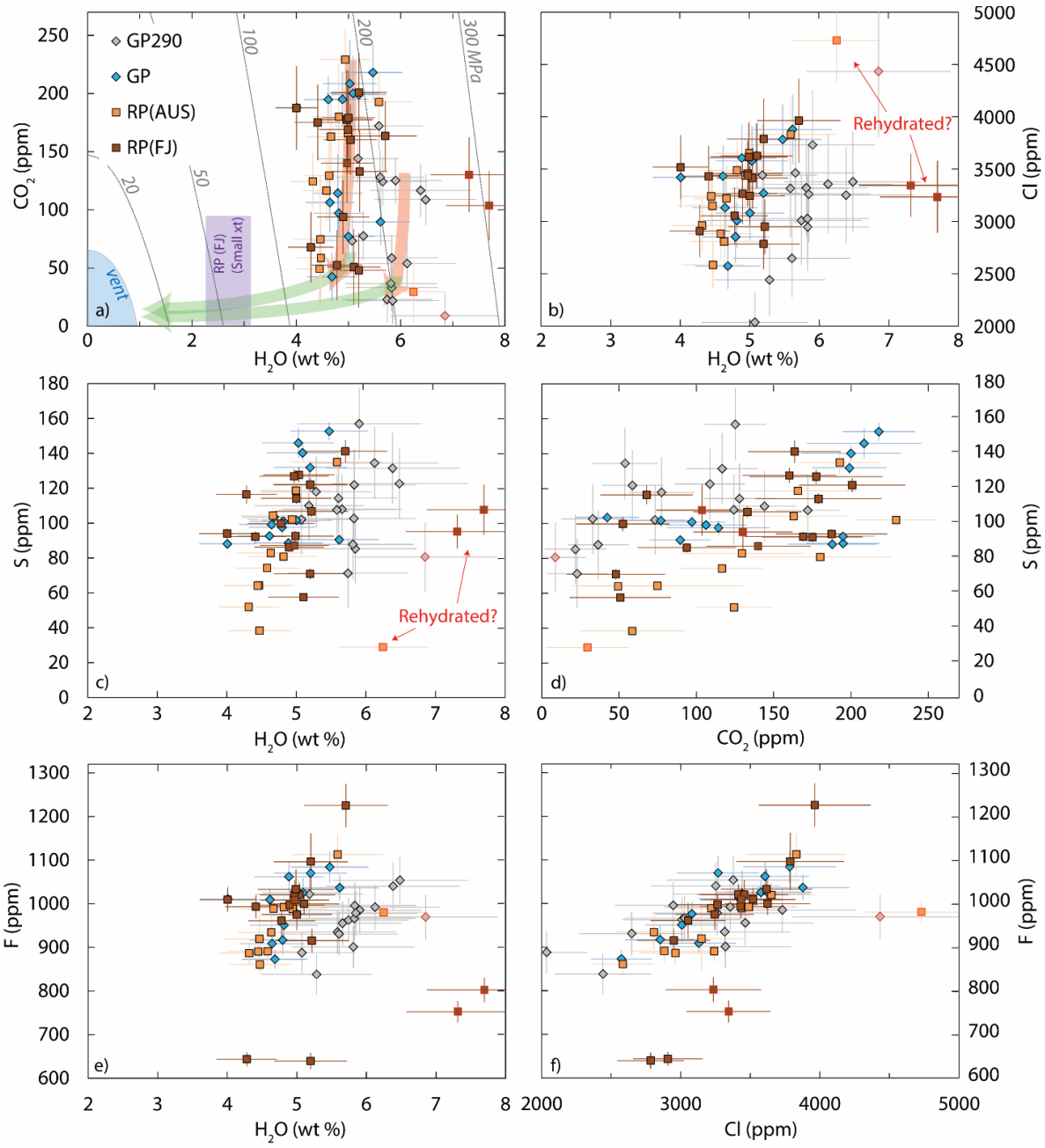

Figure 4.14. Melt inclusion volatile concentrations with ±2σ error bars for GP, GP290 and RP (AUS = collected in Australia, FJ = collected in Fiji). Solubility isobars in (a) calculated using VolatileCalc (Newman and Lowenstern, 2002) using a melt temperature of 850°C (Manga et al., 2018); vent depth isobar at 9 MPa. Range of H_2O_t concentrations from microRaman analysis of small RP phenocrysts in purple box (a). Open equilibrium degassing trend given by red arrows, closed equilibrium degassing given by green arrows. Melt inclusions outlined in red represent melt inclusion with excess H_2O (rehydration?). b) through f) plot other volatile phases against each other.

Table 4.3. Melt inclusion volatile concentrations from SIMS analysis of RP (RPFJ + AUS), GP (GP_) and Banded GP (HVR290) samples with ±2 standard deviation error.

Melt inclusion	H_2O (wt. %)	±2σ	CO_2 (ppm)	±2σ	F (ppm)	±2σ	S (ppm)	±2σ	Cl (ppm)	±2σ
GP290-1b@154	5.74	*0.86*	23	*19.5*	963	*51.3*	71	*19.8*	3009	*426*
GP290a@156	6.12	*0.92*	54	*20.7*	992	*52.4*	134	*20.6*	3356	*474*
GP290b@157	5.66	*0.85*	124	*21.2*	955	*50.7*	108	*20.1*	3464	*489*
GP290_QLh@180	5.07	*0.76*	73	*20.1*	888	*48.2*	102	*20.0*	2036	*288*
GP290e@187	6.85	*1.03*	8.9	*19.5*	970	*51.4*	81	*19.8*	4433	*626*
GP290i@199	5.29	*0.79*	78	*20.9*	838	*46.4*	118	*20.2*	2441	*345*
GP290o@203	5.83	*0.87*	59	*19.7*	996	*52.8*	122	*20.2*	2946	*416*
GP290s@206	5.90	*0.89*	125	*19.8*	985	*51.8*	157	*20.7*	3731	*527*
GP290-1b@155	5.83	*0.87*	33	*20.1*	966	*51.1*	103	*20.0*	3027	*427*
GP290_QLb@174	6.38	*0.96*	117	*22.8*	1040	*54.1*	131	*20.4*	3252	*459*
GP290_QLb@175	6.48	*0.97*	109	*22.3*	1054	*54.6*	123	*20.3*	3378	*478*
GP290h@198	5.58	*0.84*	172	*20.1*	935	*50.0*	108	*20.1*	3317	*468*
GP290_QLh@179	5.61	*0.84*	128	*22.9*	931	*50.0*	114	*20.2*	2648	*374*
GP290fe@188	5.85	*0.88*	22	*19.5*	978	*51.9*	85	*19.9*	3262	*461*
GP290h@197	5.81	*0.87*	37	*19.6*	901	*48.9*	88	*19.9*	3322	*469*
GP290u@207	5.18	*0.78*	144	*20.5*	1022	*53.7*	110	*20.1*	3441	*487*
GP_A@188	4.82	*0.48*	97.0	*21.7*	951	28.8	100.9	3.24	3008	262.0
GP_H@204	4.68	*0.47*	42.4	*20.6*	873	21.2	103.5	3.24	2574	218.1
GP_K@210	4.80	*0.48*	114.3	*33.2*	917	32.4	97.6	4.22	2852	249.1
GP_G@214	4.01	*0.40*	188.0	*28.6*	1011	29.2	88.2	2.61	3421	292.4
GP_G@215	4.89	*0.50*	195.0	*23.7*	1062	35.2	88.6	2.49	3606	317.7
GP_B@187	5.62	*0.56*	89.6	*19.8*	1037	28.6	90.5	2.46	3878	332.8
GP_A@190	5.47	*0.56*	218.0	*23.5*	1084	35.9	152.7	5.12	3783	332.2
GP_A@192	4.61	*0.46*	194.8	*20.4*	1009	27.1	92.7	2.71	3434	293.9
GP_J@194	4.65	*0.46*	106.3	*25.9*	909	22.6	99.2	2.92	3130	266.6
GP_H@203	5.00	*0.50*	77.1	*21.0*	976	27.0	101.7	2.96	3081	264.0
GP_G@213	5.20	*0.52*	199.0	*24.0*	1070	38.3	131.9	3.72	3269	294.6
GP_D@201	5.03	*0.52*	208.6	*37.2*	1025	26.5	146.0	8.72	3577	331.3
GP_D@202	5.09	*0.52*	200.1	*32.2*	1026	33.4	140.3	4.32	3627	313.4
RPFJ_F@242	5.04	*0.51*	160.2	*30.3*	1021	24.9	127.7	4.36	3414	293.2
RPFJ_F@243	4.97	*0.50*	177.5	*42.9*	1020	34.2	126.9	3.95	3457	313.8
RPFJ_D@250	4.28	*0.44*	67.8	*30.0*	643	15.8	116.4	5.31	2908	249.1
RPFJ_R@252	5.10	*0.51*	50.8	*32.7*	1000	25.7	57.6	2.03	3625	307.5
RPFJ_E@253	4.99	*0.55*	169.1	*37.8*	1033	45.6	92.5	2.79	3617	327.7
RPFJ_N@257	7.31	*0.74*	130.1	*32.2*	752	25.0	95.2	9.69	3345	302.4
RPFJ_O@234	4.78	*0.48*	52.4	*30.1*	961	40.8	99.8	3.91	3053	270.7
RPFJ_O@235	4.90	*0.50*	93.8	*31.7*	997	24.6	86.2	2.73	3265	289.4
RPFJ_I@238	5.20	*0.52*	47.9	*31.9*	640	18.7	70.9	3.03	2784	240.1
RPFJ_J@239	7.70	*0.82*	103.6	*29.7*	802	28.0	107.7	14.48	3235	343.4
RPFJ_Q@240	5.71	*0.60*	163.5	*29.9*	1226	49.9	141.2	6.50	3963	401.9
RPFJ_F@241	5.00	*0.51*	179.0	*40.8*	975	35.7	114.2	3.07	3245	282.9
RPFJ_F@245	5.20	*0.53*	200.9	*34.3*	1096	65.7	122.1	3.94	3788	387.3
RPFJ_S@254	5.22	*0.53*	133.0	*35.2*	915	27.1	106.7	3.13	2950	261.9
RPFJ_S@255	4.01	*0.40*	187.5	*36.1*	1009	26.9	94.1	2.72	3520	304.4
RPFJ_K@236	4.41	*0.44*	175.1	*32.5*	993	26.4	92.3	2.96	3431	291.7
RPFJ_R@251	4.97	*0.50*	140.1	*33.7*	1009	27.5	87.1	2.57	3438	292.3
RPAUS_F@156	4.63	*0.48*	129.5	*39.3*	934	39.3	82.9	2.98	2808	273.3
RPAUS_F@157	4.58	*0.46*	116.6	*26.3*	891	24.6	74.3	2.05	2883	247.2
RPAUS_C@162	4.32	*0.44*	124.4	*24.7*	886	24.6	52.0	1.58	2962	258.9
RPAUS_K@167	4.47	*0.45*	58.5	*34.0*	861	21.7	38.4	1.19	2585	219.8
RPAUS_G@169	6.25	*0.64*	29.5	*27.0*	980	24.4	29.0	0.98	4730	404.6
RPAUS_A@173	4.66	*0.47*	163.0	*35.2*	989	25.8	104.3	4.90	3220	312.2
RPAUS_H@175	4.94	*0.50*	229.2	*26.0*	989	25.4	102.1	2.84	3439	295.0
RPAUS_C@163	4.46	*0.51*	74.7	*55.4*	919	72.6	64.4	2.17	3150	326.8
RPAUS_C@164	4.45	*0.45*	49.2	*26.0*	891	24.1	64.1	1.73	3241	278.3
RPAUS_L@170	5.59	*0.65*	192.8	*26.2*	1113	47.6	135.0	6.61	3832	354.9
RPAUS_A@172	4.99	*0.51*	165.8	*37.9*	1020	28.6	118.8	3.19	3651	313.8
RPAUS_L@171	4.82	*0.49*	180.1	*46.0*	992	27.9	80.8	2.48	3489	301.8

Without a much larger dataset, it is difficult to distinguish definitively the differences in volatile contents between different RP and GP samples; interpretations based on weak qualitative assessment may not represent the actual dynamics of the system. On average, GP290 has higher H_2O and lower CO_2 than RP and other GP samples (**Figure 4.14a**).

4.7. Interpretations and discussion

The following discussion brings together the microtextural and volatile datasets to establish temporal and degassing relationships between different units of the 2012 Havre eruption. I interpret stratigraphic observations, textural data and componentry to suggest eruptive dynamics and emplacement mechanisms for the minor units. I then discuss the storage regions of the major clastic units prior to eruption, and the subsequent conduit dynamics that resulted in the textures analyzed by refining the Manga et al. (2018) model.

4.7.1. A transition of eruptive style: Textural evidence and conceptual models

A primary aim of this study was to establish textural similarities or differences between the units derived from the OP vent (GP, RP, ALB and Dome), which could aid in the establishment of the timing of these phases. There is geochemical homogeneity between all of these units, thus we do not attribute changes in eruptive mechanism and intensity to shifts in major element geochemistry or introduction of a second magma (Carey et al., 2018; Chapter 3). Manga et al. (In Press) suggest that the transition from a high mass eruption rate (MER), pumice-producing eruption to low-intensity, effusive, dome-producing eruption was the result of onset of significant lateral gas loss from the conduit into the surrounding oceanic crust. This was the result of high-viscosity magma stagnating at the conduit walls, effectively narrowing the conduit (Chapter 3).

Based on similar bulk magma composition, initial volatile content and vesicularity range, I suggest that RP, GP and ALB underwent the same early vesiculation history (**Figures 4.4, 4.5** and **4.14**). Differences in the shallow conduit conditions (vent geometry and conduit outgassing) and the pressure-temperature conditions within the plume/water column resulted in the observed microtextural differences and vesicle connectivity (**Figures 4.6**–**4.10** and **4.15**). The greater vesicle number density and lower modal vesicle size in RP clasts are inferred to result from continued

bubble nucleation in the shallow conduit due to higher decompression rates (dP/dt) than GP magma (Toramaru, 2006; Hamada et al., 2010; Gonnermann and Gardner, 2013; Toramaru, 2014; Shea, 2017). Calculated dP/dt for GP in Chapter 3 was ~0.1 – 5 MPa s^{-1} across the width of the conduit. By increasing (dP/dt) to >10 MPa s^{-1} for the RP magma, more bubbles could have nucleated in the shallow conduit (Toramaru, 2014). Differences in the observed vesicle microtextures suggest either that RP and GP were not erupted at the same time as hypothesized by Carey et al. (2018) and Manga et al. (2018), or that the two units represent further complexity in the shallow conduit.

There are four possible conceptual models needed to explain the observed microtextures and difference in inferred decompression rates between RP and GP: 1) changing vent geometry and conduit width at a fixed mass eruption rate, 2) an overall reduction in MER from RP to GP, and 3) lower apparent vent pressure during RP from a high flux of vapor into the water column. It is possible that the real explanation is a combination of the above; however, I will explain each model as individual scenarios to emphasize the individual mechanisms and effects of each. A fourth model is needed to explain synchronous RP and GP production from the same vent.

In scenario 1), an overlapping range of H_2O in RP and GP melt inclusions implies similar early vesiculation history, magma viscosity and therefore ascent rates for both units (**Figure 4.14**). However, greater decompression rates can be achieved for RP by increasing the magma ascent velocity in the shallow conduit. This can be achieved by reducing the conduit radius, and thus conserving mass and momentum through the conduit into the ocean at a fixed MER. However, this would require higher magma overpressure during the RP phase to combat frictional effects slowing magma ascent velocity within a narrow conduit. If RP were the products of the ascent during the initial opening of a narrow vent, subsequent erosion of the conduit walls and widening of the vent (Aravena et al., 2018) would result in a decrease in magma ascent velocity and decompression, and consequently, the formation of GP blocks. The subsequent transition to the dome-forming phase would follow the model of Manga et al. (In Press), whereby the loss of volatiles to the conduit walls from the reduction of magma overpressure decreased the MER, dP/dt and therefore, vesicularity (**Figure 4.15**).

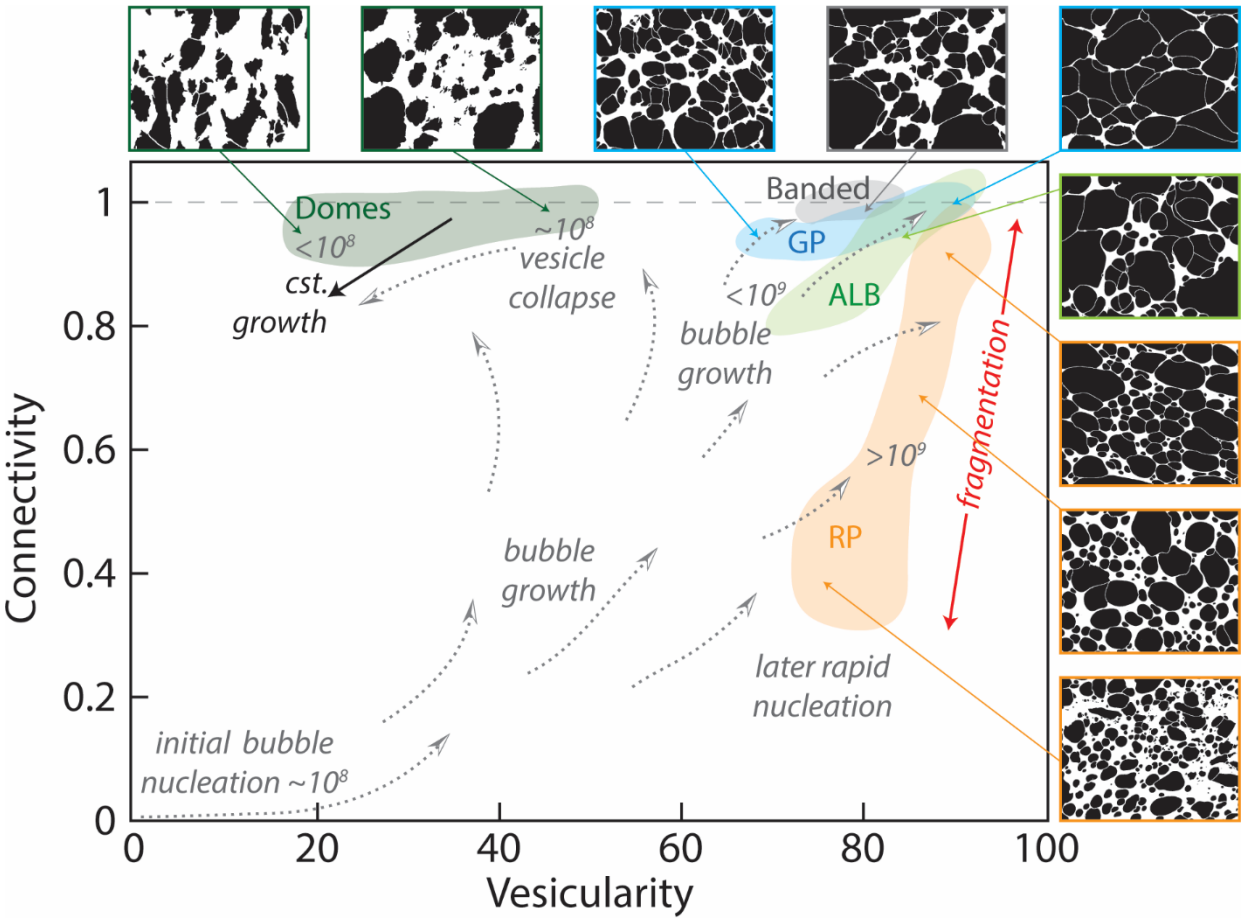

Figure 4.15. Degassing evolution during the pumiceous phases of the 2012 Havre eruption with unit regions bound by the data from Figure 4.6. Example textures are given to represent the various stages of textural maturity placed at the corresponding whole clast vesicularity. The plot illustrates paths of vesiculation attributed to each unit highlighting processes of: initial bubble nucleation, later bubble growth, continued bubble nucleation in RP resulting in higher vesicle number density (given in cm^{-3}), vesicle collapse during outgassing, and growth of vapor-phase cristobalite in vesicles. Fragmentation of RP magma can take place anywhere along the trend shown. The giant pumice vesiculation path diverges to produce GP, Banded GP, and ALB pumice. The time arrow implies a temporal change from RP to GP to Dome-forming phases. Binary BSE images were acquired at 500x magnification; each image is 240 µm across.

Scenario 2), the reduction of MER from RP to GP, requires some decrease in magma overpressure or the initial volatile budget available for degassing. There is no observable change in the initial volatile content and thus, this scenario relies on the outgassing of volatiles while still relatively deep in the conduit. The limited range of permeability in RP (Appendix **C4**) and lower vesicle connectivity than GP (**Figure 4.15**) implies that permeable outgassing was limited during

the RP phase and thus, high mass eruption rates were maintained. In this scenario, the changes do not require modification of the vent geometry. In both scenarios 1) and 2), there is no required modification of confining – and therefore non-hydrostatic – pressure at the vent (Section **2.4.1.3**).

Scenario 3) draws on the conceptual model presented in Chapter 2 where mixing of magmatic vapor in the water column reduces the bulk ocean density above the vent, and therefore, the apparent confining pressure (**Figure 2.7**). Decreasing the pressure at the vent would increase dP/dt in the shallowest regions of the conduit, enough so to allow RP magma to possibly fragment prior to eruption into the ocean; however, the magnitude of this confining pressure reduction is currently unknown (**Figure 4.16**). Following from scenarios 1) and 2), waning mass eruption rate and increased outgassing (Manga et al., In Press) during the GP phase would restore vent pressure to hydrostatic equivalence (~9 MPa). The transition to the dome-forming phase would occur at complete hydrostatic equivalence (**Figure 4.16**). As explained in Chapter 2, the presence of such a vapor plume requires sufficient stability to prevent collapse and vapor condensation. Until the plausibility of a stable vapor plume can be verified (or discounted) through computational modeling, this scenario remains only a possibility.

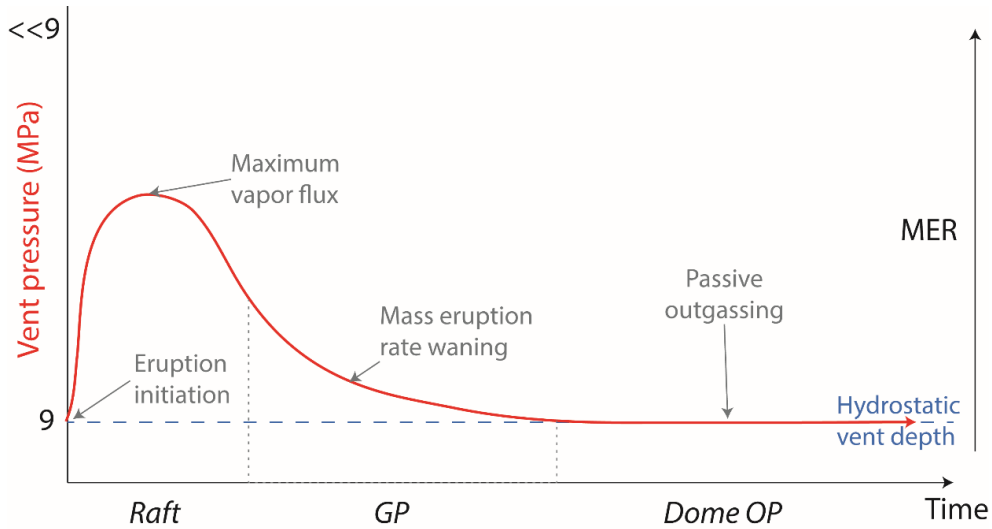

Figure 4.16. The reduction in the 900 m deep vent pressure as a result of overlying vapor in the water column and the inferred change in mass eruption rate (MER). Vent pressure decreases during the RP phase from a high vapor flux; the transition to the GP phase results in a lower MER. The dome forming phase experience negligible change in vent pressure. Time is schematic on the plot; RP duration is observed as 21.5 hours (Carey et al., 2018) and the maximum possible duration of Dome OP effusion is ~1000 days. There are fewer constraints on the duration of the GP phase.

In scenario 4), RP and GP were produced during the same time interval, but the difference in vesicle number density reflects the position of magma within the conduit prior to eruption. Assuming a laminar velocity profile, magma in the conduit center can decompress faster than at the conduit margins. This would imply that RP was sourced from the conduit center, whereas GP was sourced from the margins. However, this does not fully account for the presence of some banding in raft pumice, the common shallow quenching depths, and differences in textural maturity (permeability and vesicle connectivity) between the two units. More work is required to resolve fully the timing between RP and GP.

4.7.1.1. Banded pumice and dome effusion

The slowing, cooling and crystallization of magma adjacent to the conduit walls is inferred to have produced microlite-rich magma during the GP phase resulting in banded GP clasts (such as GP290) (**Figure 4.15**; Chapter 3). Increased outgassing through the conduit walls (Manga et al., In Press) explains why banded GP vesicles are completely connected at lower vesicularity than other GP (**Figure 4.6**). We suggest that banded GP formed during the latter stages of the GP phase and the transition to the dome-forming phase. This was the result of continued lateral outgassing and narrowing of the conduit from magma adjacent to the conduit walls (**Figure 4.15**). Even though some banding is identified within the pumice raft (**Figure 4.5**; Carey et al., 2018), it is possible that some banded fragments were able to float despite high vesicle connectivity, as observed by reducing the saturated volume proportion in **Figure 4.6**. The possible transition from RP to GP may not reflect an *instant* change in eruptive style, but rather a gradual, diffuse transition due to changes in the shallow conduit or confining pressure (**Figure 4.16**).

The dome material (that we identify as Talus (DB); **Figure 4.3** and **4.7**) was moderately vesicular (40 – 50%), but porosity was completely connected and with the same vesicle number density as GP (**Figures 4.8** and **4.15**). This suggests a similar early vesiculation history for GP and Dome OP but greater outgassing during the slower dome effusion and therefore, the collapse of permeable vesicle pathways. A combination of lateral gas loss, permeable outgassing and narrowing of the conduit is inferred to have greatly reduced MER to ~10^3 – 10^4 kg s^{-1} during the dome-forming phase (Carey et al., 2018; Manga et al., In Press).

As vesiculation diminished with time from volatile undersaturation, magma vesicularity and ascent rate decreased, eventually resulting in the slow effusion of Dome OP. The precipitation and growth of cristobalite within dome vesicles decreased the vesicle connectivity and porosity with time (**Figure 4.15**; Kendrick et al., 2016; Kushnir et al., 2016). Textural observations of cristobalite size distributions further support the suggestion that the talus is material from early dome effusion that quenched faster than the sampled Dome OP carapace, which was collected *in situ* (**Figure 4.11**). The implied reduction in chemical impurities in cristobalite with time (Appendix **C7**) is attributed to initial fluids being rich in components exsolved from the glass (Schipper et al., 2017). When little glass remained (as in **Figure 4.11d**), only the SiO_2 component was utilized for crystal growth, i.e., the pore space fluids contained a greater proportion of silica.

4.7.1.2. Origin and timing of ALB with respect to GP and RP

The ash-lapilli-block deposit (ALB) pumices have many textural similarities with GP fragments and some with RP clasts. **Figures 4.8 – 4.10** demonstrate how vesicle number densities, Nv distributions and modal vesicle diameters of ALB pumice are similar to GP and RP. All units exhibit a similar range of whole clast vesicularities and componentry; however, the ALB deposit geometry is very different. GP extends many kilometers from the source vent with a single dispersal axis, whereas ALB is confined to lobes that extend in all directions no further than 1.5 km from Dome OP, and is found on top of GP (**Figure 4.1**; Carey et al., 2018). The ALB deposit thickness and mean clast size decreases with distance from Dome OP on the western lobe (**Figures 4.1** and **4.3e, f**).

Carey et al. (2018) suggest a density current from a collapsing plume resulted in the proximal deposition of lapilli- to block-size pumice clasts after synchronous RP and GP production. Murch (2018) infers that the AL subunit (S2) was the distal ash component of these flows, transported across the caldera floor by a lateral, dilute suspension flow on the seafloor. However, Chapter 2 demonstrated that ALB pumice was transported hundreds of meters above the vent prior to settling, the same as GP and RP. The similarity of ALB textures with GP and RP, and shallow quenching depths, make it challenging to infer that ALB pumice were rapidly deposited in a density current after the entirety of the GP phase. The very small difference in density between seawater and

water-saturated, high vesicularity lapilli (>80%) would make it challenging to generate the submarine density currents required for rapid ALB deposition. Computational modeling is required to support fully the previous model of Carey et al. (2018) and Murch (2018). I propose here an alternative scenario where water saturation and clast settling timescales were the main control on the proximal deposition of ALB, and the stratigraphic positioning above GP despite synchronous production of the two. The lobe-like geometry of the ALB deposit was the result of changing ocean current directions on the seafloor that controlled lateral clast transportation.

Pumice lapilli produced at a deep vent (900 mbsl for Havre) will saturate quickly with seawater after outgassing, and thus cannot ascend far through the water column. These clasts will settle close to source, and cannot remain afloat for long periods of time (Allen et al., 2008; Fauria et al., 2017; Manga et al., 2018; Fauria and Manga, 2018). Clasts of only a few cm across should not reach the sea surface unless assisted by initial ejecta momentum (Fauria and Manga, 2018; Manga et al., 2018); substantial additional momentum is unlikely in the submarine environment considering the suppression of magma decompression rates by hydrostatic pressure (Chapter 3). However, large pumice blocks that rise rapidly to the surface (at ~1 – 10 m s^{-1}) can break up in the water column due to the propagation of cooling joints, fractures from clast expansion and decompression, or collision with surrounding clasts (secondary fragmentation; Mitchell et al., 2018b). Broken fragments will then rapidly saturate and subsequently settle to the seafloor close to the vent. A broad range of sub-rounded to angular and irregular ALB clast morphologies (**Figure 4.2e, f**), lack of exterior alteration or rapidly quenched rinds, and high vesicularity clasts with large vesicles similar to those in GP (**Figure 4.7**), all imply that ALB clasts are fragments of larger pumice clasts that underwent continued degassing in the water column (see Section **3.6.1**). This accounts for the speciation interpretations, quenching depths and textural characteristics of both GP and RP in ALB (Mitchell et al., 2018; Chapter 3); however, it does not account for the stratigraphic position of ALB.

Even though ALB sits stratigraphically above GP, fully saturated ALB-sized clasts will sink at settling velocities up to three orders of magnitude slower than meter-sized giant pumice blocks; the settling velocity of pumice in water scales linearly with clast diameter at higher Reynolds number (Re >100) for particles >1 cm in diameter (Cashman and Fiske, 1991; Bonadonna and Houghton, 2005). The timescale of ALB clasts settling relative to GP clasts may be sufficient to

reverse the stratigraphy. The very high vesicularity of ALB fragments would result in slower settling velocities due to the very small density difference between seawater and a high-vesicularity pumice fully saturated by seawater.

We do note that smaller clasts will saturate with seawater faster than larger clasts assuming that seawater infiltrates vesicle networks at a constant rate with distance from the clast exterior (Cashman and Fiske, 1991; Fauria and Manga, 2018). However, the presence of large cracks, cm-sized vesicles, and highly permeable pathways identified in GP blocks (Section **3.5.1**) could result in rapid block saturation on a decimeter-, rather than, meter-predicted timescale. This means that GP blocks may reach saturation and terminal ascent velocity faster than anticipated, thus allowing for a delay of settling of ALB relative to GP (Carey et al., 2018; Chapter 3). The timescales of waterlogging, buoyancy reversal and settling of clasts with variable shapes and diameters affected by lateral ocean currents require more detailed modeling to verify this hypothesis (Fauria and Manga, 2018).

4.7.2. Textural interpretations of other 2012 clastic units

Other clastic units (and subunits) from the 2012 Havre eruption are not directly related to the conduit dynamics and eruptive style transitions at the main vent beneath Dome OP. I assess the differences in origin and eruptive mechanisms of these units, drawing on interpretations from previous studies, and textural and volatile data within this study.

4.7.2.1. LGL: Ash venting from of a pumiceous lava carapace

The pumice within Lava-G-Lapilli (LGL) is almost ubiquitously tubular and woody (**Figure 4.5**) at lower mean vesicularity than the rest of the pumice within other clastic units (**Figure 4.4**). Both of these characteristics match observations of the Lava G carapace and subunit S3 of the AL unit that contain large volumes of ash with tube vesicles and woody fabrics (**Figure 4.17b;** Murch, 2018). Previous studies conclude that the LGL deposit was the result of ash venting and spalling of the vesicular carapace of Lava G during active outgassing (**Figure 4.17a;** Ikegami et al., 2018; Murch, 2018). Lava G is the only 2012 effusive feature (aside from Dome OP) to display very low volatile loss on ignition values from XRF analyses (**Table 1.1**; Carey et al., 2018) implying the

continued degassing of an extruded lava during emplacement and cooling. Other lavas with no associated clastic units retained a large wt. % of volatiles dissolved within the melt (**Table 1.1**).

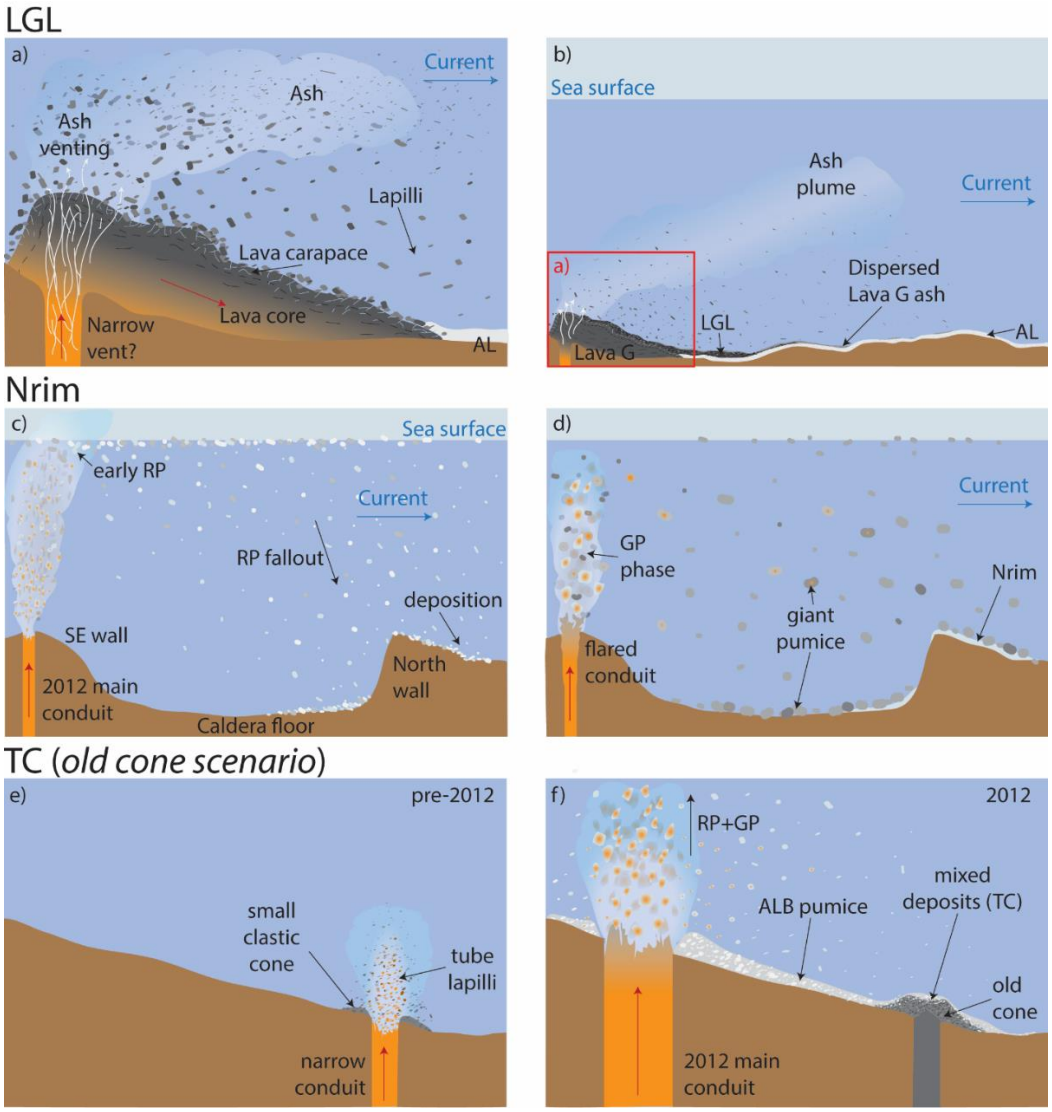

Figure 4.17. Schematic of eruption and depositional mechanisms for various units identified within the 2012 Havre eruption stratigraphy: Lava-G-Lapilli (LGL) (a,b), North Rim Pumice (Nrim) (c,d), and old cone deposits (TC) (e,f). Orange represents magmatic temperatures; clasts can be seen cooling. White clasts are generally vesicular, darker clasts are comparatively denser. Clasts, conduit and spatial extent are not to scale. a) shows the generation of LGL clasts from the surface of lava flow G; b) shows the dispersal of finer LGL clasts and ash shards from the flow and deposition within AL; c) shows the breakup, saturation and current-driven deposition of pumice from the pumice raft on the northern caldera rim; d) shows how GP blocks are found on top of the Nrim pumice; e) shows the formation of a small clastic cone prior to 2012 eruption and the subsequent burial of the cone from ALB pumice in 2012 (f).

Volatile datasets for LGL have the narrowest spread of all units (**Figure 4.13**) and calculations from OH concentrations suggest that LGL clasts quenched very close to the eruptive vent at 950 mbsl (Mitchell et al., 2018a). The H_2O speciation data for LGL closely matches speciation for the Lava G carapace and AL ash (subunit S3), but infers a range of glass transition temperatures (T_g) reflecting differences in cooling rates attributed to variable clast size. Temperatures for Lava G carapace T_g of ~450 – 500°C (Mundana and Carey, 2017) and LGL T_g of ~500 – 600°C (Mitchell et al., 2018a) are lower than for AL-S3 tube shards that exhibit T_g closer to magmatic temperatures (700 – 800°C; Murch, 2018).

LGL clasts have similar vesicle number densities to the rest of the 2012 Havre units, only if the tube vesicle geometry correction was applied (**Figure 4.8**). Lava G has a similar bulk composition to the main vent units (**Table 1.1**; Carey et al., 2018; Ikegami et al., 2018), which suggests that the magma producing Lava G, and therefore LGL, derives from the same source as the main conduit magma. However, the lower vesicularity of LGL in comparison to, for example, RP, GP and ALB (**Figures 4.4** and **4.5**) magma suggests that Lava G magma outgassed prior to eruption. Nevertheless, Lava G magma ascended rapidly enough to induce significant strain, and thus vesicle elongation, within the Lava G conduit. We cannot rule out the possibility of some vesicle elongation occurring during flow propagation; however, the smaller dimensions of the flow and relatively thin carapace (2 m thick) infer that the majority of strain occurred within the conduit. It would be very difficult to produce extreme vesicle shearing and tube development in an *in situ* lava carapace that quenched rapidly in contact with seawater. A lack of spherical vesicles in LGL pumices and the Lava G carapace implies that most of the conduit experienced very high strain, similar to that identified for GP tube pumice within Chapter 3. Microtextural observations of the AL-S3 ash grains and samples from the exposed Lava G core show that tube vesicles dominate the vesicle textures from the core to the carapace (Ikegami et al., 2018; Murch, 2018). Therefore, I suggest that the conduit was significantly narrower than the Dome OP vent (perhaps <20 m in diameter; **Figure 4.17a**) to induce significant cumulative strain throughout the entire conduit.

4.7.2.2. Nrim: The fallout of pumice from the early stages of the pumice raft

Nrim samples were collected on the northern rim of the caldera over 4 km from the main 2012 vent down the GP and RP dispersal axis (**Figures 4.1** and **4.4**). The lapilli to small-block distribution differs substantially from the giant pumice blocks observed in the same location. Similarities in the macrotextures, vesicularity range and componentry of Nrim pumice with RP and GP, suggest a common magma source. GP is found on top of the lapilli-rich deposit and, due to the presence of lapilli on the top of the caldera rim, I do not advocate for deposition of Nrim by density currents as suggested for ALB and AL-S2 by Carey et al. (2018) and Murch (2018).

The clast size distributions of Nrim samples from ROV images are similar to the ALB deposits; however, the interpreted origin of ALB suggests that material of this size should saturate rapidly and deposit close to the main vent (**Figures 4.1–4.3**). Despite this, the fresh pumice surfaces and textural similarities with ALB, GP and RP discount the possibility that they are derived from a pre-2012 Havre eruption from a vent located elsewhere on the Havre volcanic summit.

I propose that Nrim represents the breakup and fallout of large pumice blocks from the bottom of the coherent pumice raft prior to dispersal (**Figure 4.17c**). Large volumes of pumice submerged in the shallow water column (identified in MODIS imagery during the raft-forming phase of the eruption) would eventually have to settle if unable to retain vapor in isolated vesicles (Carey et al., 2014). The position of Nrim samples along the RP dispersal axis would imply a likely source was the pumice raft (Jutzeler et al., 2014; Carey et al., 2018).

Nrim also contained a large number of tube-vesicle lapilli that RP was lacking (even just a few weeks after the eruption; **Figure 4.5**; Rotella et al., 2015). Tube pumice within the pumice raft would saturate rapidly (due to poor vapor trapping from wider vesicle throats as result of lower water surface tension effects) and fall out close to the main caldera. Only a few RP samples collected from beach shores thousands of km away show elongate vesicles, but nowhere near the elongation required to be classified as "tube" vesicles; most RP vesicles have near-spherical geometries. In summary, Nrim is the fallout of very permeable, vesicular pumice fragmented / abraded during the early hours of the pumice raft when clast packing density was very high (**Figure 4.17c**); a large volume of the raft remained initially submerged due to the overlying pumice mass

on the ocean surface. GP blocks erupted during and after the RP phase, and then settled on top of the lapilli-rich deposit on the northern rim of the Havre caldera (**Figure 4.17d**).

4.7.2.3. TC: A mixture of 2012 and pre-2012 deposits

Four samples collected from the rim and flanks of a pre-existing cone within the ALB dispersal area (TC) had broader density distributions and more mixed componentry than other units derived from the main 900 m deep vent, e.g., ALB, RP and GP (**Figures 4.1** and **4.5**). TC samples were a mixture of higher vesicularity ALB-like pumice with large vesicles, including some high-vesicularity tube pumice, and lower vesicularity tube pumice very similar to the LGL tube pumice, but with more surface alteration; these two distinct pumice populations correspond to the two density modes identified in the componentry distribution (**Figure 4.5f**).

Observations of the deposit via the ROV suggest that TC is a mixture of ALB pumice and darker clastic material (higher density tube pumice) from the pre-existing cone. The similarity of this denser tube pumice to LGL clasts suggest that a conduit with high strain produced a comparatively small, clastic eruption resulting in the formation of a clastic cone prior to 2012 (**Figure 4.17e**). The deposition of ALB proximal to Dome OP (<500 m from TC) covered the pre-2012 deposit, with the possibility of deposit mixing upon sampling (**Figure 4.17f**). The other possible origin of the denser tube pumice is lateral blasts of early Dome OP material during the transition from pumice production to dome effusion (Manga et al., In Press); potentially similar to subaerial Vulcanian explosions (Isgett et al., 2017). The vesicularity of this tube pumice (mostly 50 – 70%; **Figure 4.5f**) fits in the vesicularity range missing between Dome OP and GP, ALB or RP (**Figure 4.15**). If this is true, these deposits may offer a useful insight into the inferred transition of eruptive style (**Figure 4.16**). Targeted microtextural and geochemical work on TC tube pumice could verify their origin (pre-2012 or 2012) and offer insight into either eruptive style transitions, or older Havre volcanism and smaller silicic clast-producing eruptions.

4.7.3. Magma storage, degassing and conduit ascent

Isobars applied to melt inclusion H_2O-CO_2 data using the VolatileCalc solubility model (Newman and Lowenstern, 2002) determine an interpreted storage region of Havre 2012 magma

from 130 – 210 MPa (**Figure 4.14a**). This broadens a previous estimate of ~200 MPa identified from previous melt inclusion data from just GP290 (Manga et al., 2018). Assuming lithostatic pressure (DRE = 2500 kg m^{-3}; a combination of crustal basalt and silicic lava) and 9.2 MPa of hydrostatic pressure, this corresponds to 4.9 – 8.1 km beneath the seafloor (5800 – 9200 mbsl). The revised range of H_2O (4.3 – 5.2 wt. %) is closer to the global average of initial H_2O for arc magmas of around 4 wt. % (Stern, 2002; Wallace, 2005; Shaw et al., 2008; Plank et al., 2013). The melt inclusions from smaller crystals analyzed using µRaman correspond to depths below the seafloor of 1.3 – 2.9 km; uncertainty within this range is due to a lack of CO_2 information from µRaman analysis (**Figure 4.14a**). The likely storage pressure of these smaller crystals was 40 – 50 MPa for CO_2 <50 ppm. Previous modeling of conduit ascent for Havre magma shows that velocity, decompression rate, and viscosity do not increase significantly until the last kilometer of ascent. Below this, decompression rates would be sufficient for the growth of smaller phenocrysts outside of the magmatic storage region during magma ascent (Toramaru et al., 2008).

The range of CO_2, with a relatively consistent H_2O range (**Figure 4.14a**), suggests open degassing of CO_2 within magma storage and during the early stages of conduit ascent. The loss of CO_2 then resulted in closed degassing of H_2O from the melt reflected by the decrease in H_2O in smaller melt inclusions (**Figure 4.14a**). These degassing trends are consistent with equilibrium degassing rather than disequilibrium degassing (Newman and Lowenstern, 2002; Gonnermann and Manga, 2005); decompression rates are insufficient for disequilibrium degassing of H_2O (Manga et al., 2018). GP290 magma is interpreted to have evacuated deeper parts of the storage region after the eruption of RP magma and most of GP magma because GP290 H_2O concentrations are 1 wt. % higher than the rest of RP and GP (**Figure 4.14a**). The bulk magma composition remained the same as shown in Chapter 3 (**Figure 3.2**). The lower average CO_2 in GP290 melt inclusions suggest that this magma underwent continued open exsolution of CO_2 prior to loss of H_2O during later magma ascent.

Most H_2O (~4 wt. % down to ~0.4 wt. %; Mitchell et al., 2018a) and nearly all S (<150 ppm down to <25 ppm) had degassed upon eruption (**Figure 4.13;** Appendix **C9**). The lack of S within the system is unlikely to have had as significant an effect on H_2O solubility as CO_2 (Carroll and Webster, 1994). Cl and F have much lower diffusivity than H_2O and so partition primarily into the melt rather than vapor phase (Webster et al., 1997; Schipper et al., 2017). Cl and F are also highly

incompatible in crystal phases and so melt in crystal-rich magma can be enriched in halogens relative to the melt inclusions (Carroll and Webster, 1994; Schipper et al., 2017); this is not the case for the crystal-poor Havre magma. However, F and Cl have not completely degassed from the melt upon eruption, as seen in matrix glass (**Figure 4.13**). Some loss of Cl and F to the vapor phase earlier in the shallow conduit can provide the HCl and HF vapor required to remove SiO_2 from glass to form cristobalite (**Figure 4.11;** Schipper et al., 2017). We detect no F in the vapor-phase cristobalite, however there is up to 90 ppm Cl in cristobalite (see Appendix **C7**). To produce $SiCl_4$-enriched fluids suggests that either Cl exsolved more readily than F in the shallow conduit, or that heated seawater within water-saturated vesicles permitted the diffusion of Cl ions from seawater into the $SiCl_4$ fluid phase.

The incomplete loss of F and Cl from the melt also means that, upon quenching, most Havre pumice have up to 0.3 wt. % halogens in the glass (up to 50% of the total volatiles in matrix glass). F and Cl at these concentrations are unlikely to control degassing and bubble nucleation at depth due to the great abundance of dissolved H_2O (an order of magnitude greater wt. %). However, closer to the vent, the halogens may have some effect on modulating magma viscosity (Giordano et al., 2008) or late stage bubble nucleation; F has been experimentally shown to reduce surface tension thus resulting in greater nucleation rates (Gardner et al., 2018). Cl does not exist in high enough quantities to generate brines in shallow magma, and is far below computed Cl solubility at the determined storage pressures (Webster et al., 2015).

The loss of Cl from melt to vapor could have implications for considering fluxes of acidic Cl complexes and HCl vapor into the open ocean and shallow crust during large silicic submarine eruptions (Hedenquist and Lowenstern, 1994; Gruen et al., 2014). Assuming that all unaccounted-for Cl in matrix glass has outgassed into either the ocean or shallow conduit walls through lateral outgassing (Manga et al., In Press), we calculate that $0.75 – 2.1 \times 10^9$ kg of Cl was theoretically lost throughout the duration of the RP-GP-Dome phase from the main vent. For the time-constrained RP phase, this equates to potentially 220 – 780 ton s^{-1} Cl into the ocean or crust. Within the shallow crust, Cl-enriched fluids (potentially twice as saline as seawater (6 wt. % Cl vapor)) have the potential to form altered zones around the shallow conduit containing veins of mineral deposits (Gruen et al., 2014; Manga et al., In Press).

The identified decrease in halogen content from the melt inclusions to the matrix glass may also have implications for magma ascent rates (see Appendix **C9**). The relatively low diffusivity of Cl and F, in comparison to H_2O, CO_2 and S, commonly results in little change in melt halogen content during rapid magma ascent. Increases in the relative halogen proportion in the melt can be the result of fractionation of these melt-compatible volatiles during crystallization (Carroll and Webster, 1994; Schipper et al., 2017). It is possible that the exsolution of Cl and F indicates slower magma ascent than previously anticipated; modeling of halogen exsolution in the Havre system would verify this.

4.7.3.1. Revising the conduit ascent model

New melt inclusion data refines previous estimates of average initial H_2O content from 5.8 to 4.8 wt. % for the volume majority of the 2012 eruption (**Figure 4.14a**); 5.8 wt. % is inferred to represent the late stage (GP290) magma. Therefore, I update the results of the Manga et al. (2018) 1D conduit ascent model by applying a range 4.3 – 5.2 wt. % H_2O and a bottom storage pressure of 200 MPa to the existing model. I fix the mass eruption rate to equate to that observed from RP production (10^7 kg s^{-1}; Carey et al., 2018). We find that mean velocity at the vent decreases from ~30 – 35 m s^{-1} to 10 – 15 m s^{-1} (**Figure 4.18**). There is a decrease in mean vesicularity from 86% to ~80% and consequently in the mean decompression rates (dP/dt) from ~2 MPa s^{-1} to 0.3 – 0.7 MPa s^{-1} (**Figure 4.18**). Maximum dP/dt doubles in the conduit center when assuming a parabolic laminar velocity profile (Llewelin and Manga, 2005; Chapter 3). These lower dP/dt values are much closer to the calculated ocean decompression rates in Chapter 3. This implies that pumice can continue to decompress and vesiculate in the water column, as shown in GP textures in comparison to RP textures (**Figures 4.7** and **4.15**). However, without a significant reduction in dP/dt; only the extent of clast cooling and quenching could potentially terminate vesicle growth (Mitchell et al., 2018a).

This reduction in ascent and decompression rates suggests that the eruption of RP and GP magma was more influenced by the effect of hydrostatic pressure. Textural evidence suggests that banded GP was erupted after RP and GP as eruption intensity began to wane (**Figure 4.15**); the previous model results counter this. However, we suggest that greater open degassing fluxes and

gas loss from the conduit substantially reduced shallow conduit ascent velocity (Manga et al., In Press), despite the higher initial water content. The lower vesicularity (80%) at the vent also better matches the mean and modal values identified through density and pycnometry analysis and allows for reasonable continued vesiculation (**Figures 4.4 – 4.6**). The reduction in velocity would also reduce the cumulative strain within the conduit determined in **Figure 3.8** for GP textural conditions. The resulting effect would be a larger proportion of the shallow conduit able to produce bubbles with little or no elongation; a more plausible scenario based on macro- and microtextural observations.

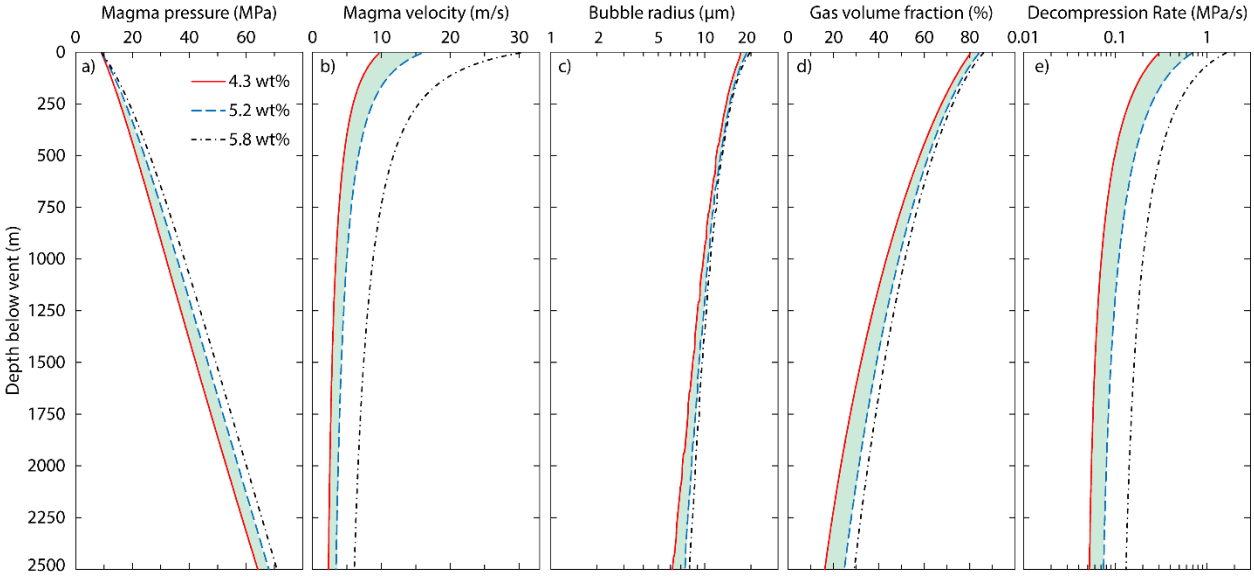

Figure 4.18. Revised conduit ascent model results using new melt inclusion data (4.3 – 5.2 wt. % initial H_2O) in comparison to previous results using 5.8 wt. % H_2O (Manga et al., 2018). a) is the internal magma pressure; b) is the bulk velocity of the magma taking into account crystal and bubble suspension (Llewellin and Manga, 2005); c) is the bubble radius calculated from the bubble number density and gas volume fraction (d); e) is the decompression rate calculated as the product of (b) and the gradient of (a). The region of interpreted ascent conditions is given in green. Initial starting pressure of magma from 200 MPa using a fixed conduit mass eruption rate of 10^7 kg s^{-1} and initial bubble number density of 2×10^8 cm^{-3} (**Figure 4.8**). All values are given as the mean across the conduit; maximum magma velocity in the conduit is double the values shown. Magma velocity assumes coupling of melt and gas velocity as shown by Manga et al. (2018).

The model results shown in **Figure 4.18** use an initial bubble number density of 2×10^8 cm^{-3}, as found within most GP (**Figure 4.8**). However, I also ran the same model using an initial bubble number density of 1.5×10^9 cm^{-3} to better represent the determined RP textures; this change had very little effect on magma ascent. Therefore, even if the higher N_{Vm} values from RP magma were the true initial conditions, we observe no real change in ascent conditions (**Figure 4.6**). The similar ranges of melt inclusion H_2O concentrations for RP and GP magma suggest that there was very little difference in the original volatile content. Differences in vesicle size and number distribution between the two units are attributed to changes in *only* the very shallow conduit, such as changing vent geometry and extent of permeable outgassing (Manga et al., In Press), or even the modification of hydrostatic pressure above the vent (Section **2.4.1.3**).

4.7.4. Study implications

This chapter presented a number of findings that further our understanding of the stratigraphic relationships between units erupted during the 2012 Havre eruption. In the units studied, we identify a range of eruptive styles, clast emplacement and depositional mechanisms, and significant textural diversity despite the geochemical homogeneity and relatively constant hydrostatic pressure effect (~9 – 10 MPa). We emphasize that hydrostatic pressure is not the only primary control on eruptive style in deep submarine silicic eruptions. Changes in conduit conditions will significantly alter the eruption dynamics throughout the eruption.

The detailed assessment of clast textures and volatile concentrations has allowed us to draw the following main conclusions:

1) For high vesicularity (>80%) pumice to remain afloat for many months and even years, the connected vesicle network must trap at least 14 volume % vapor within vesicles to maintain positive buoyancy. This supports previous experimental work that showed that this process can occur (Fauria et al., 2017).
2) Differences in vesicle number density, connectivity and volume contribution of very small vesicles (<10 μm in diameter) between RP and GP clasts further support that the two units experienced different decompression histories reflecting changes in the conduit conditions with time. GP may post-date most of the pumice raft production, with banded GP magma

arriving in the latter stages of GP and prior to Dome OP effusion. Some banded raft clasts reflect some latter stage magma being able to float rather than sink.

3) The deposition of the ALB deposit on top of GP does *not* represent the actual eruptive timing between the two units. ALB is now interpreted as the result of RP and GP clast breakup in the eruptive plume throughout both phases. The much smaller ALB clasts settled slowly through the water column and were deposited proximal to the main vent in localized lobe deposits from ocean-bottom currents.
4) Initial storage regions of Havre magma are shallower than previously estimated, and initial H_2O content is lower for the majority of magma erupted. The microlite-poor GP290 magma originated at a deeper, more hydrous part of the storage system, and the microlite-rich grey bands originated adjacent to the shallow conduit walls and mingled with the microlite-poor melt at very shallow depths.
5) The initial 2012 Havre in-storage magma was rich in halogens and resulted in the significant outgassing of Cl into the conduit walls and ocean. During the effusion of Dome OP, these fluxes of $SiCl_4$-rich fluids permitted the extended growth of vapor-phase cristobalite.
6) Changes in conduit conditions, geometry and outgassing may be just as critical controls on large submarine eruption styles as hydrostatic pressure; eruptive mechanisms can vary within a single vent at a fixed ocean depth.

5. CONCLUSIONS

Deep submarine silicic volcanism is one of the least well-studied research areas within volcanology today. With few documented eruptions, even fewer observed eruptions, difficulty of access, and the high costs of submarine exploration, understanding of deep-sea eruptions has been a significant challenge in comparison to subaerial and even planetary volcanism. The 2012 eruption from Havre volcano offered an ideal chance to study deep submarine silicic volcanism in fine detail. With over 290 samples collected during a 2015 expedition that span the entire 2012 stratigraphy, there is a great deal to learn about this eruption and the processes unique to the deep submarine environment. This chapter summarizes the previous chapters, and assesses the broader implications for research within silicic submarine volcanism, in particular one of the major aims of the dissertation: how does hydrostatic pressure modulate explosive vs. effusive volcanism? The chapter concludes by identifying avenues for further research and exploration based on these findings.

5.1. Synopsis

Chapter 2 presented total water content (H_2O_t) and water speciation data (OH and H_2O_m) within matrix glass in samples for all clastic 2012 units at Havre. The data show that recent deep submarine eruptions may have products with excess H_2O_m indicating diffusion and addition of H_2O_m sometime after eruption, i.e., rehydration. The timescales and diffusivity coefficients of rehydration by cold seawater are insufficient for the very young deposits from the 2012 eruption, as determined by a 1D diffusion model applied to the vesicle-edge H_2O_t enrichments. An implication is that an alternative process of rapid, higher-temperature rehydration (above 100ºC, but well below 800ºC – magmatic temperature) is required to explain the data. It is very possible that pumice from many large submarine silicic eruptions experience such a rehydration prior to deposition. The potential sources of excess H_2O_m were either 1) seawater entrained into, and heated within, submarine eruptive plumes, or 2) exsolved magmatic vapor that condensed into the water column at temperatures of 100 – 300ºC with increasing hydrostatic pressure. The OH concentrations from FTIR analysis imply that clasts in large submarine eruptions may quench

hundreds of meters *above* the inferred vents if there is an adequate source of insulation within the water column, i.e., an eruptive plume. These results suggest that, most of the giant pumice blocks may have made It to the surface prior to waterlogging and sinking.

Chapter 3 presented a detailed textural assessment of clasts from the giant pumice unit (GP), from the meter- to micron-scale, to assess conduit and post-conduit dynamics, and the effect of hydrostatic pressure on pumice generation at a deep submarine vent. The conclusion is that textural diversity observed within GP was not due to any changes in magma geochemistry (complete magma homogeneity), but instead to changes in the geometry and thermodynamic conditions within the shallow volcanic conduit. Mingling of microlite-rich and microlite-poor magma can occur, derived, respectively, from slower ascending, crystallizing magma at the conduit walls and magma ascending rapidly along the axis of the conduit; this was observed in clasts as textural banding. Domains of tube vesicles in some GP blocks implies that significant strain accumulation occurred in the shallow conduit without fragmentation prior to eruption. Modeling of strain in the shallow conduit supported this, but required a flared shallow conduit to produce regions of little strain accumulation to explain the presence of *non*-tube vesicles in many of the GP blocks. Chapter 3 also explored the process of post-eruption vesicle expansion due to high decompression rates during pumice ascent in the water column. Textural evidence and whole-clast observations, such as juxtaposed regions of vesicle growth and deformation, and bread-crusted block exteriors, supported the occurrence of this process in deep silicic eruptions.

Microtextural evidence in Chapter 4 (vesicle number density and connectivity) may suggest that the pumice raft and giant pumice were not necessarily erupted simultaneously, and builds on previous models that assessed a potentially gradual transition, rather than abrupt change, in eruptive style from high-intensity raft pumice production to low-intensity dome effusion, with giant pumice representing this transition. I presented three conceptual models to explain the eruptive transition based on macro- and micro-textural observations and volatile content, and a fourth model that supports the previous interpretations of synchronous raft and giant pumice eruption; further computational modeling is required to verify the correct hypothesis. Textural evidence further supports the implication in previous experimental work that vesicle networks must “trap” pockets of vapor, allowing pumice to remain float for many years on the ocean surface. The identification and growth of vapor-phase cristobalite within vesicles of the main dome has

implications for considering the cooling rates and permeability of submarine silicic domes, and fluxes of outgassing volatiles – particularly for magmas initially rich in halogens. An assessment of melt inclusions, from both GP blocks and the pumice raft, was used to refine initial magma storage conditions and inputs for the existing conduit ascent model, which has implications for considering the decompression rates of magma during the 2012 eruption.

5.2. Broader implications from the dissertation

This study provides one of few quantitative textural and chemical assessments of pumice from a recent, deep-submarine silicic volcanic eruption. Even though the deposits analyzed are from one eruption (Havre 2012), there are fundamental interpretations that have broader implications to field of submarine volcanology.

5.2.1. Role of hydrostatic pressure in modulating explosive vs. effusive volcanism

From the work undertaken, I conclude that ~9 MPa of hydrostatic pressure was sufficient to modulate magma ascent velocities and decompression rates, and fully inhibits magmatic volatile-driven fragmentation during the 2012 event. Hydrostatic pressure does play a significant role in pumice production and the shallow conduit conditions in comparison to subaerial silicic conduits, where there is negligible vent pressure. However, observations and analysis of pumice from multiple deposits exhibiting a variety of textural characteristics (from a vent at a fixed depth), imply that hydrostatic pressure does not fundamentally control a specific eruptive style.

As with any volcanic system, a number of integrating physical processes control conduit and eruptive dynamics such as: initial magma storage conditions, initial magma composition and volatile content, conduit geometry, the onset of permeability, and permeable gas loss from a conduit. The range of pumice vesicularity, textural maturity, inferred mass eruption rates, and eruptive mechanisms during the 2012 Havre eruption from the same ocean depth highlights how the role of hydrostatic pressure can be overruled depending on pre-eruptive conditions such as vent geometry. The effect of hydrostatic pressure exerts a greater control on lower mass eruption rate events – such as lava effusion – where morphologies of erupted lavas and domes are similar, unless affected by the substrate slope. At this point in time, there is no suite of conditions that can be used

as a signature of explosive or effusive silicic volcanism. Better constrained submarine eruptions and more sophisticated computational models are required; however, our Havre constraints provide a critical component in the development of such models and the understanding of samples from future field studies. It is important for us not to categorize silicic submarine eruptions within a particular style or classification purely by calculating the overlying hydrostatic pressure; submarine eruption styles can vary even if produced at similar vent depths.

5.2.2. Deep submarine conduits: A window into the depths of subaerial conduits?

Analytical studies of pumice, and lava flow and dome microtextures rely on the assumption that the textures observed are representative of the magma at the time of fragmentation or quenching below the glass transition temperature. This inherently limits our ability to interpret the conditions and state of magma deeper within the conduit from natural samples, which is critical, and essential for understanding the evolution of magma and processes prior to eruption, e.g., the onset of magma permeability, gas loss from the conduit, and microlite crystallization. Assessing deposits from deep submarine eruptions may present a solution to this.

The termination of deep submarine volcanic conduits at high pressure (e.g., 9.2 MPa for the Havre vent) can provide a window into magma at lithostatic pressure-equivalent depths within a subaerial volcanic conduit (e.g., 9.2 MPa is equivalent to ~350 – 390 m below the surface depending on crustal density). Studying submarine eruptions from vents significantly deeper than Havre could provide insight into the state of magma at even deeper conditions within a subaerial volcanic conduit (e.g., 2500 mbsl is equivalent to 25.3 MPa, which has lithostatic-equivalence to ~950 – 1070 m deep in the crust). A direct inference of magma erupted in deep submarine eruptions to deep conditions within a subaerial conduit would require the comparison of geochemically-similar systems and eruptions with comparable mass eruption rates and total eruptive volumes. Nevertheless, this could present a unique opportunity to study the transient evolution of bubble and crystal textures during magma ascent in *subaerial* eruptions by analyzing natural samples from *submarine* eruptions.

5.2.3. Sources and timescales of rehydration in submarine pumice

The identification of rapid rehydration of submarine pumice is a finding of great importance within this dissertation. Further research of H_2O in the matrix glass of submarine pumice must consider the possibility that interactions of magma and seawater can drive the rapid, syn-eruptive diffusion of water and or vapor into melt and/or glass at a variety of temperatures. Assessing H_2O in glass remains a critical tool in interpreting fragmentation and quenching depths, but it should approached carefully when analyzing pumice from large submarine eruptions surrounded by an abundance of external H_2O. It is highly likely that old pumice no longer express these hot, rapid rehydration signatures due to masking by cold seawater rehydration signatures over much longer timescales. The very recent Havre deposits provide a unique insight into this rapid process. Identifying the exact source of the excess H_2O_m in Havre pumice can be resolved by subsequent geochemical studies focusing on the H and O isotopes of H_2O within volcanic glass.

5.3. Future directions

Although this dissertation is a significant contribution to understanding the dynamics of the 2012 Havre eruption, it also highlights many areas for potential further study in the broader field of submarine volcanism.

5.3.1. Microtextural analysis

In particular, I stress the importance of quantifying size, shape, and compositional distributions of microlites in submarine pumice and domes, to assess late-stage decompression, strain, cooling, and crystal nucleation histories within the shallow conduit. Experimentally constraining rates of microlite growth and nucleation in conditions specific to Havre will aid our understanding of the role of pre-eruptive magma rheology on eruption style. Understanding the physical nature of magma entering the water column will allow us to evaluate the proposed rapid propagation of cooling joints, thermal gradients through the magma body, and glass transition temperatures.

The growth of cristobalite in dome vesicles causes decreases in vesicularity, permeability and vesicle connectivity that can increase dome strength, but inhibits the outgassing of vapor. Further analysis of cristobalite abundance, growth rates and composition will constrain rates of cooling of

submarine silicic dome and outgassing fluxes. On a broader scale, there is a need to assess fully the microtextures of *all* lavas and domes erupted during the 2012 Havre eruption, not just Dome OP and Lava G. Lava and dome textures can help us to understand submarine lava flow cooling rates, the insulation efficiency of silicic lava crusts, and the resulting effect on lava rheology. Continued research into lava composition, rheology and petrology from the 2012 lavas and domes will allow us to interpret the sub-surface architecture that assisted the transportation of magma along the S and SW rim of the Havre caldera during 2012.

5.3.2. Computational modeling

Through detailed microanalytical research, the dissertation highlights many processes unique to the submarine eruptive environment that require computational modeling, *now* with well-constrained inputs. Here, I highlight the need for more detailed modeling of seawater and vapor interactions with pumice, and the timescales of clast ascent and settling when accounting for processes of waterlogging and permeable outgassing.

The stratigraphic superposition of units, such as ALB and AL, show that there were complex relationships between clast size and processes and rates of transportation through the water column. This is the case for interpreting all submarine pumice deposits, not just the 2012 Havre eruption. Modeling clast ascent and settling velocities *separately* is computationally simple, and has been achieved in previous studies. However, the timescales of water infiltration and saturation, and permeable outgassing, which depend highly on vesicle connectivity and size distribution, are key processes that need to be quantified *together* in subsequent clast transportation models. An achievable first step would be to combine timescales of clast ascent and settling, incorporating the timescale and rate of clast saturation. Quantifying these absolute timescales of clast transportation for a range of clast sizes provides the framework for future models and fieldwork assessing the deposition of pumice in the ocean.

Another area of computational modeling to pursue is that of the physical conditions (pressure-temperature-density-phase) within submarine eruption plumes. Assuming mass eruption rates and vapor fluxes from a vent, modeling submarine eruption plumes will allow us to constrain further the cooling rates of pumice, the entrainment and heating of seawater, and possible modification of

hydrostatic pressure above the vent. Waterlogging of clasts and plume-edge cooling can also theoretically lead to column instabilities and subsequent density currents driving lateral particle transport. This complex, larger scale modeling will provide the grounding environmental conditions required to assess the previously discussed clast transportation dynamics.

On a finer scale, to constrain rehydration timescales accurately requires the development of a diffusion model that incorporates time-dependent clast cooling, phase changes in the ambient environment, water speciation changes with temperature, and the changes in melt–glass rheology and structure around the glass transition. The potential presence of a vapor-rich plume and identification of multiple rehydration sources during the Havre 2012 eruption necessitates assessment of rehydration by seawater and/or magmatic-derived vapor over a range of pressures and temperatures.

Finally, I highlight the need to incorporate natural complexities into the current conduit ascent models for the 2012 Havre eruption. Previous research identifies a lack of fragmentation within the conduit, but high mass eruption rate. This presents a situation where the rheology of magma exiting the vent rapidly is a critical control on subsequent brittle fragmentation processes during rise through the water column. By incorporating more complex parameters and processes into conduit models (for example, microlite crystallinity and growth rates, cooling of magma at conduit walls, variable conduit geometry (e.g., erosion and flaring), and variable bubble size distributions), we can reduce areas of uncertainty, and more critically assess the role of hydrostatic pressure on submarine eruption and conduit dynamics.

5.3.3. Interpreting ancient eruptions and potential fieldwork

This dissertation explored only the pumice lapilli-bearing deposits of the 2012 volcanic eruption at the Havre caldera, which was limited by the sampling from the 2015 expedition. Nevertheless, we now have quantitative constraints for Havre that do not exist in such detail for any other submarine silicic eruption. Older deposits observed in the caldera walls at Havre present further opportunities to study larger caldera-forming eruptions, and thus, deep submarine silicic eruptions on a much larger scale. Deep submarine silicic calderas are very common along the Kermadec and Izu-Bonin forearcs and so Havre will now be an essential field site to answer further

questions. Future exploration and research at Havre can address both broader questions such as the role of hydrostatic pressure on much larger silicic eruptions, and questions more specific to the 2012 eruption. Primarily, I emphasize the need to observe and understand deposit relationships further away from the caldera in order to verify the hypothesized unit relationships, e.g., between the pumice raft and giant pumiceous blocks, or the extent of deposits such as AL. As well as furthering our understanding of the dynamics of deep submarine silicic eruptions, subsequent expeditions to the Havre caldera can explore the hydrothermal field and unexpected abundance of life identified on the seafloor. This biologically rich field site can be used to understand the rapid recovery of ecosystems following large volcanic eruptions of the seafloor.

5.4. Concluding statement

The research in this dissertation aimed to further understanding of large silicic submarine volcanic eruptions, utilizing deposits from the unusually well constrained 2012 Havre eruption. With multiple research themes and avenues of scientific interest, it is my hope that this work has provided motivation for others to study such unique, natural phenomena in some of the most remote locations on our planet. It has been both a challenge and a privilege to undertake this research and to contribute to the fascinating and exciting field of silicic submarine volcanology.

APPENDICES

APPENDIX A – SUPPLEMENTARY MATERIAL FOR CHAPTER 2

Appendix A1: ***Equilibrium speciation and temperature of apparent equilibrium***

Equilibrium speciation was calculated based on two models of how the constant K_{eq} varies with temperature (°C) (Eq. **A1**: Nowak and Behrens, 2001, and Eq. **A2**: Zhang et al., 1997).

$$K_{eq} = 27.98 \exp\left(\frac{-4210}{T+273.15}\right) \quad \text{(Eq. A1)}$$

$$K_{eq} = \exp\left(1.876 - \left(\frac{3110}{T+273.15}\right)\right) \quad \text{(Eq. A2)}$$

The Nowak and Behrens (2001) model (Eq. **A1**) was derived for haplogranite composition in the temperature range 500 – 800°C; the Zhang et al. (1997) model (Eq. **A2**) was derived for rhyolite composition in the temperature range 400 – 600°C. There is good agreement between the models in the low temperature range (see also **Figure 2.3**) but divergence increases when Eq. **A2** is extrapolated to >600 °C; Eq. **A1** is therefore preferred for determining K_{eq} in the high temperature range and subsequently, the Nowak and Behrens (2001) model was extrapolated down to T_g = 400°C

To calculate how species concentrations vary with K_{eq}, we use the system of equations laid out in Zhang and Ni (2010):

$$K_{eq} = \frac{[OH]^2}{[H_2O_m][O]} \quad \text{(Eq. A3)}$$

$$[H_2O_t] = \frac{\frac{C_w}{18.015}}{\frac{C_w}{18.015} + \frac{(100 - C_w)}{W}} \quad \text{(Eq. A4)}$$

$$[H_2O_m] = \frac{C_1}{C_w}\,[H_2O_t] \quad \text{(Eq. A5)}$$

$$[OH] = 2([H_2O_t] - [H_2O_m]) \quad \text{(Eq. A6)}$$

$$[O] = 1 - [H_2O_m] - [OH] \quad \text{(Eq. A7)}$$

where square brackets denote mole fractions, C_w is the wt. % of H_2O_t, C_1 is the wt. % of H_2O_m, and W is the weight of the dry melt per mole of oxygen, assuming all Fe is ferrous. We calculate W = 32.6 g mol^{-1} for Havre clasts based on XRF data published in Carey et al. (2018).

For simplicity, Eq. **A3** can be rewritten in terms of $[H_2O_t]$ (**A4**), giving:

$$K_{eq} = \frac{4[H_2O_t](C_1 - C_w)^2}{C_1(C_1[H_2O_t] - 2C_w[H_2O_t] + C_w)} \quad \text{(Eq. A8)}$$

To calculate how species concentrations vary for a given value of K_{eq} and H_2O_t wt. % (i.e., C_w), we solve Eq. **A8** for the unknown value C_1, i.e., H_2O_m in wt. %, according to:

$$C_1 = \frac{C_w\left(K(2[H_2O_t]-1) + \sqrt{K}\sqrt{K(1-2[H_2O_t])^2 - 16([H_2O_t]-1)[H_2O_t]} - 8[H_2O_t]\right)}{2(K-4)[H_2O_t]} \quad \text{(Eq. A9)}$$

Equilibrium OH wt. % at a given H_2O_t wt. % and K_{eq} value is then simply $C_{OH} = C_w - C_1$. With this method, variation in equilibrium OH and H_2O_m contents with H_2O_t was calculated for 400, 500, 600, and 800 °C (**Figure 2.3**).

To find T_{ae} of samples analyzed by FTIR (**Figure 2.4**), we solve Eq. **A8** using measured values of H_2O_t wt. % (C_w) and H_2O_m wt. % (C_1). With this value of K_{eq} (or K_{ae}), T_{ae} is then obtained by solving Eq. **A1** or Eq. **A2** for *T*. T_{ae} values are similar for both speciation models so we present only the Nowak and Behrens (2001) model data in **Figure 2.4**.

Appendix A2: *Sample selection and preparation*

In March-April 2015, an expedition aboard the R/V Roger Revelle spent three weeks mapping, exploring and sampling the 2012 Havre eruption using the ROV *Jason* and AUV *Sentry.* A total of 290 samples were collected across the stratigraphic sequences, using the ROV manipulator, push cores, a vacuum pipe and scoops to effectively sample all lava and clastic deposit types. Collected seafloor samples were immediately washed thoroughly and dried at 80°C for over 24 hours. Seventy-three samples from all pumiceous units (Giant Pumice, Raft Pumice, Ash-Lapilli-Block, Ash-Lapilli, Lava-G-Lapilli and Dome fragments) were sieved and lapilli-sized pumiceous clasts or fragments 8 – 32 mm in diameter selected for density analysis. One giant pumice clast

with dimensions of 1.5 x 1 x 1 m (HVR_290) was collected intact from the seafloor (Carey et al., 2018). For this clast, samples were taken from both the interior and exterior.

Clast density was analyzed following the method of Houghton and Wilson (1989). Clasts were cleaned again to remove any fine ash from exterior vesicles and then their exteriors were finely coated in hydrophobic silicon spray with negligible mass addition. Clasts were numbered in descending size order for every sample, their dry weight measured, and then their submerged wet weight measured relative to a ballast. Using Archimedes principle (**Eq. A10**) the density for each clast was acquired.

$$density = \frac{dry\ mass}{dry\ mass - wet\ mass} \quad \text{(Eq. } \mathbf{A10}\text{)}$$

Every clast within a specific stratigraphic unit was placed into a single density distribution. Clasts at the modal density (M) and a selected lower (L) and higher (H) density representative of each unit were then selected for volatile analysis (Shea et al., 2010). The density distribution of the DB unit was broad without a single mode so clasts were instead selected from five density bins. Another sample included within DB is the exterior fragment of a dense block several meters in diameter (HVR_007). For giant pumice HVR_290 exterior and interior clasts, only the modal densities were chosen for a direct comparison of the average / modal density. Analytical uncertainty in density measurements is given by the precision of the mass measurements where ± 2 standard deviations = 30 kg m^{-3}.

For FTIR imaging analysis, clasts with < 60% vesicularity (> 930 kg m^{-3}) were prepared at UH Mānoa as doubly polished < 30 µm wafers using Crystalbond resin. Prepared wafers were placed in an acetone bath for 24 hours to dissolve the Crystalbond. If the resin is not fully removed, a contamination peak can be seen at ~1730 cm^{-1}. For clasts with higher vesicularities, thin wafers tend to break up once the resin is removed, and it also becomes difficult to fully remove resin from vesicle walls. Clasts with >60% vesicularity were therefore fragmented into thin glass shards ~10–30 µm thick using the SELFRAG facility at the National Museum of Nature and Science in Tsukuba, Japan. For µRaman analysis, clasts were cut, bound in clear epoxy and polished into 35 µm-thick thin sections at the Lapidary Facility at UH Mānoa.

Appendix A3: *Sample collection and densities*

Table A3 a) Depository of data and corresponding IGSNs (International Geo Sample Number) for Havre 2012 samples used in FTIR analysis. Density of each analyzed clast was obtained using the methods in Appendix **A1**. Location, unit and depth is given for each collected HVR_sample.

IGSN	HVR_ sample	Clast number	Stratigraphic Unit	Density (kg m^{-3})	*In situ* depth (m)	Latitude (°)	Longitude (°)
IEHVR0007	7	17	DB	1360	804	-31.12565	-179.01231
IEHVR000V	31	24	AL	730	889	-31.12635	-179.03852
IEHVR001I	54	66	AL	390	1341	-31.11782	-179.04194
IEHVR001Y	70	158	LGL	850	952	-31.12107	-179.04856
IEHVR001Y	70	178	LGL	1030	"	"	"
IEHVR001Y	70	118	LGL	1420	"	"	"
IEHVR002C	84	6	AL	390	960	-31.12090	-179.04582
IEHVR002X	105	16	AL	730	963	-31.12713	-179.03217
IEHVR003C	120	84	ALB	310	756	-31.13263	-179.01270
IEHVR003C	120	85	ALB	780	"	"	"
IEHVR003O	132	5	AL	500	1513	-31.10265	-179.02862
IEHVR0059	189.198	54	ALB(DB)	350	773	-31.13123	-179.01575
IEHVR0059	189.3	16	ALB(DB)	510	"	"	"
IEHVR0059	189.3	60	DB	1010	"	"	"
IEHVR0059	189.3	74	DB	1280	"	"	"
IEHVR0059	189.3	46	DB	1770	"	"	"
IEHVR006F	231	43	GPX	410	826	-31.08778	-179.06050
IEHVR006U	246	59	ALB	510	1327	-31.11396	-179.02110
IEHVR007I	270	17	GPX	790	801	-31.08457	-179.04110
IEHVR0082	290	166	GPI	470	950	-31.12975	-179.03108
IEHVR0082	290	85	GPX	660	"	"	"
IEHVR0082	290	I162	Ba_I	-	"	"	"
IEHVR0082	290	Ext	Ba_I	-	"	"	"
IEHVR0082	290	Ext	Ba_G	-	"	"	"
IEHVR0082	290	I162	Ba_G	-	"	"	"
-	AUS	13	RP	560	0	-	-
-	AUS	15	RP	550	0	-	-
-	NSW	J13	RP	-	0	-	-

Table A3 b) Depository of data and corresponding IGSNs for Havre 2012 samples used in µRaman analysis. Density of each analyzed clast was obtained using the methods in Appendix **A1**. Location, unit and depth is given for each collected HVR_sample.

IGSN	HVR_ sample	Clast number	Stratigraphic Unit	Density (kg m^{-3})	*In situ* depth (m)	Latitude (°)	Longitude (°)
IEHVR0007	7	6	DB	1370	804	-31.12565	-179.01231
IEHVR001Y	70	24	LGL	830	952	-31.12107	-179.04856
IEHVR001Y	70	11	LGL	1000	"	"	"
IEHVR001Y	70	23	LGL	1290	"	"	"
IEHVR002Z	107	2	AL	340	963	-31.12715	-179.03181
IEHVR003C	120	1	ALB	420	756	-31.13263	-179.01270
IEHVR004V	175	1	AL	540	1307	-31.11197	-179.04947
IEHVR0054	184	8	ALB	340	841	-31.13205	-179.01749
IEHVR0054	184	1	ALB	930	"	"	"
IEHVR0059	189.4	26	ALB(DB)	400	773	-31.13123	-179.01575
IEHVR0059	189.4	2	ALB(DB)	590	"	"	"
IEHVR0059	189.4	15	DB	940	"	"	"
IEHVR0059	189.4	1	DB	1320	"	"	"
IEHVR0059	189.4	21	DB	1720	"	"	"
IEHVR006d	229	4	AL	850	778	-31.08989	-179.06378
IEHVR006F	231	31	GPX	350	826	-31.08778	-179.06050
IEHVR006F	231	12	GPX	450	"	"	"
IEHVR006F	231	17	GPX	400	"	"	"
IEHVR007I	270	13	GPX	770	801	-31.08457	-179.04110
IEHVR0082	290	90	GPX	850	950	-31.12975	-179.03108
IEHVR0082	290	26	GPX	620	"	"	"
IEHVR0082	290	42	GPX	760	"	"	"
IEHVR0082	290	I15	GPI	490	"	"	"
IEHVR0082	290	I18	Ba_W	-	"	"	"
IEHVR0082	290	I18	Ba_G	-	"	"	"

Appendix A4: *FTIR methodology*

Measuring volatile concentrations

For vesicular clasts, it was necessary to prepare thin sample wafers to avoid vesicles in the beampath. Shards were selected for FTIR analysis based on the following criteria: 1) no trapped vesicles, 2) relatively parallel flat faces, and 3) low microlite content (Von Aulock et al., 2014). The combination of thin glass wafers and relatively low water contents meant that the weak near-IR 5250 cm^{-1} H_2O_m and 4500 cm^{-1} OH absorption peaks were not observed. Instead, the stronger mid-IR 3500 cm^{-1} H_2O_t and 1630 cm^{-1} H_2O_m absorption peaks were used to find H_2O_t, H_2O_m and OH concentrations (Stolper, 1982). Molecular CO_2 was examined using the 2350 cm^{-1} absorption peak.

Transmission spectra were processed to find concentration in the standard way using the Beer-Lambert Law (Eq. **A11**):

$$wt\ \% = 100\left(\frac{M\,A}{\rho\,d\,\varepsilon}\right) \qquad \text{(Eq. A11)}$$

where M = molar mass (g mol^{-1}), A = absorbance (no units), d = glass thickness (cm), ρ = glass density (kg m^{-3}) and ε = molar absorptivity coefficient (L mol^{-1} cm^{-1}) (Stolper, 1982). M is 18.02 g mol^{-1} for water and 44.01 g mol^{-1} for carbon dioxide. Glass thickness was calculated from interference fringes in reflectance spectra using the relationship:

$$d = \frac{m}{2n(\nu 1 - \nu 2)} \qquad \text{(Eq. A12)}$$

where m = number of interference fringes in the wavenumber range 2700 – 2000 cm^{-1}, n = refractive index of glass (1.5 for rhyolite – Hodder, 1978), and ν_1 and ν_2 are the highest and lowest wavenumbers of the selected range (Wysoczanski and Tani, 2006; Nichols and Wysoczanski, 2007). Error on thickness using this method is given as ±3 µm, making it the dominant source of analytical error for thin samples. Glass density was calculated from XRF data as ρ = 2400 kg m^{-3} and is consistent with other Kermadec rhyolites (Barker et al., 2012a; Rotella et al., 2015). The choice of ε depends on the absorption peak of interest. For the 1630 cm^{-1} H_2O_m peak in rhyolite, ε1630 = 55 L mol^{-1} cm^{-1} (Newman et al., 1986). For the 2350 cm^{-1}, CO_{2m} peak in rhyolite, ε2350 = 1214 L mol^{-1} cm^{-1} (Behrens et al., 2004).

It is common for mid-IR studies to also use the Beer-Lambert law (Eq. **A11**) to find H_2O_t concentration from the 3500 cm^{-1} H_2O_t peak, with OH concentration then found by difference as $OH = H_2O_t - H_2O_m$. However, the ε value for the 3500 cm^{-1} H_2O_t peak varies with the proportions of H_2O species within the glass. This leads to errors on output H_2O_t (and OH-by-difference) concentrations if the correct ε3500 value is not known (Newman et al., 1986; McIntosh et al., 2017). For an endmember scenario in which a rhyolite contains 100% OH, the correct value would be $\varepsilon 3500_{OH} = 100$; for a rhyolite containing 100% H_2O_m the correct value would be $\varepsilon 3500_{H_2O_m} = 56$ (Newman et al., 1986). We therefore use the method of McIntosh et al (2017), which accounts for the species-dependence of ε3500 by using these endmember ε3500 values in a modified version of the Beer-Lambert law. In this method, OH concentration (in wt. %) is calculated directly by inputting the absorbance of the 3500 cm^{-1} H_2O_t peak and the H_2O_m concentration, according to:

$$C_{OH} = \frac{1}{\varepsilon 3500_{OH}}\left(\frac{100 M \bar{A}_{3500}}{\rho} - \varepsilon 3500_{H_2O_m} C_{H_2O_m}\right) \qquad \text{(Eq. A13)}$$

where $\bar{A}_{3500}$ is the measured 3500 cm^{-1} absorbance normalized for sample thickness (i.e., $\bar{A} = A/d$) in units of cm^{-1}, and $C_{H_2O_m}$ is H_2O_m wt. % found from the 1630 cm^{-1} peak via Eq. **A11**. H_2O_t concentration is then simply $H_2O_t = OH + H_2O_m$.

The species-dependent method is especially important when analyzing samples with disequilibrium H_2O_m/OH ratios. When Eq. **A11** is used with a fixed ε3500 value from the literature (which are generally derived from samples with equilibrium H_2O_m/OH ratios), disequilibrium samples commonly appear to have negative OH concentrations (McIntosh et al., 2017).

Advantages of FTIR imaging

With vesicular pumiceous samples it becomes difficult to find an area of glass with uniform thickness that is necessary for transmission FTIR analysis. The FPA camera attachment on the JAMSTEC FTIR consists of 64 x 64 channels that create a 350 x 350 µm image of the sample, with collection time on the order of ~15 minutes per image. As thickness is not uniform across our vesicular wafers or glass shards, these images cannot be used as maps of volatile concentration variation. However, selection of an individual channel within that image yields an individual spectrum with a spatial resolution of ~5.5 x 5.5 µm. By taking both transmission and reflectance FTIR images without moving the sample, and finding channels with both a high quality

transmission spectrum and good interference fringes in the corresponding reflectance spectrum, it is possible to derive the glass thickness at that point and thus output quantitative volatile concentrations (**Figure 2.2**). FTIR imaging thus produces data with the necessary spatial resolution in a fraction of the time that would be required for sequential spot analyses.

Baseline selection

Species absorbance is found as the height of the absorption peak above a baseline. FTIR spectra near glass edges (e.g., vesicle margins) tend to have complex baselines, with a characteristic 'trough' at low wavenumbers (McIntosh, 2013). This optical effect distorts spectra in vesicular samples and requires fitting of a curved baseline specific to each individual spectrum. This was done using OPUS 7.5 software to fit a polynomial baseline based on manually defined nodes. For the 3500 cm^{-1} H_2O_t peak, nodes were placed automatically at the peak margins at 3800 and 2700 cm^{-1} to reduce selective error in defining a baseline. Due to the increased baseline complexity at low wavenumbers, it was sometimes necessary to fit the 1630 cm^{-1} H_2O_m peak with more nodes, with no specific wavenumbers for node placement. However, as few nodes as possible were defined so as not to 'over-fit' the baseline to the spectrum and reduce the true absorbance.

Appendix A5: *MicroRaman methodology*

Spectra acquisition

µRaman analyses were acquired with an acquisition time of 3x 20 seconds to reduce noise relative to the background, with each spectrum analyzed at least four times to obtain < 5 % relative standard deviation. µRaman spots, in both bulk and profile analyses, were taken at a constant depth from the sample surface in a linear profile perpendicular to the vesicle edge. Spots were taken in the center of bubble nodes or within thick bubble walls in 2D thin sections (see **Appendix A7**); 16 spots were collected within each thin section. In profiles, 20 to 30 spots were acquired with spacing of < 1.5 µm and no spot overlap. Some profile collection was complicated by nearby epoxy within

vesicles. Profiles containing spots with > 10 % epoxy contamination were discarded (see below for epoxy correction).

Baseline selection

The baseline correction for finding peak areas in µRaman spectra uses the Matlab-based program SpeCTRa (Spectral Correction Tools for Raman) and an external calibration of known FTIR H_2O_t values from a suite of rhyolite standards (Shea et al., 2014; Shea et al., 2017). SpeCTRa inputs the raw µRaman spectrum; fits a polynomial baseline outside of defined regions (aluminosilicate peaks at 200 – 1300 cm^{-1}, epoxy – if present – at 2700 – 3150 cm^{-1}, and total water at 3180 – 3800 cm^{-1}); applies a 'long' correction to account for temperature and excitation line effects on intensity (I_R) at higher energy wavenumbers (Eq. **A14**) (Le Losq et al., 2012); and then determines the areas under the H_2O_t and aluminosilicate peak (see Appendix **A7**).

$$I = I_R \left(\nu_l^3 \left(1 - \exp\left[\frac{-hc\nu}{kT} \right] \right) \nu / (\nu_l - \nu)^4 \right) \qquad \text{(Eq. A14)}$$

where I = corrected intensity at a particular wavenumber (ν), ν_l = wavenumber of incident light from the laser used (green laser wavelength of 532 nm), h = Planck's constant, c = speed of light, k = Boltzmann constant and T = the absolute temperature. The polynomial baseline fitting was a manual selection of polynomial order based on the baseline that fits best without too much convolution under the peaks. Any epoxy signals present in a spectra were removed by separately analyzing a raw epoxy spectrum and subtracting a percentage of the epoxy peaks from the desired spectrum. The final H_2O_t value was calculated as the ratio of the aluminosilicate and water peak areas multiplied by an external calibration constant of 0.788. This value was determined from a suite of rhyolite glass standards with known FTIR H_2O_t contents of 0.1 to 5.1 wt. % relative to this peak ratio measured using the same µRaman microscope. µRaman analyses accumulate an error of ~0.1-0.2 wt. % after all corrections are applied.

Appendix A6: *FTIR analysis*

Table A6a. Summary of FTIR data including glass thickness, peak position, normalized absorbance, species-dependent ε_{3500} value and final wt. % calculations.

Stratigraphic Unit	Density mode	Density (kg m^{-3})	# spot analyses	IGSN (IEVHR_)	H_2O_t wt. %	± 1 SD error	OH wt. %	± 1 SD error	H_2O_m wt. %	± 1 SD error	Norm. Abs. 1630 cm-1	± 1 SD error	Norm. Abs. 3500 cm-1	± 1 SD error	Absorbance Ratio	± 1 SD error	Thickness (μm)	± 1 SD error	ε3500 (L mol-1 cm-1)	± 1 SD error	1630 peak (cm-1)	± 1 SD error	3500 peak (cm-1)	± 1 SD error
AL	L	390	5	001I	0.43	*0.05*	0.18	*0.03*	0.25	*0.03*	17.9	2.19	41.4	5.11	0.43	0.05	21.2	2.0	74.2	2.42	1631	3.2	3563	16.0
	L	390	11	002C	0.26	*0.12*	0.18	*0.09*	0.08	*0.05*	5.80	3.25	29.1	13.73	0.20	0.09	15.6	4.9	86.3	5.56	1630	4.2	3575	12.0
	M	500	15	003O	0.29	*0.08*	0.16	*0.04*	0.13	*0.06*	9.24	4.07	30.6	8.05	0.29	0.07	19.1	6.4	81.0	3.68	1630	5.6	3551	30.9
	H	730	20	002X	0.62	*0.17*	0.3	*0.11*	0.32	*0.12*	22.8	8.72	62.6	17.23	0.37	0.12	22.7	15.5	77.6	5.46	1632	2.3	3547	21.4
	H	730	3	000V	0.76	*0.2*	0.45	*0.11*	0.31	*0.11*	21.9	7.67	80.9	20.40	0.26	0.04	15.8	3.1	82.5	2.44	1634	3.0	3566	16.4
ALB	L	310	12	003C	0.18	*0.04*	0.1	*0.03*	0.08	*0.03*	5.78	2.17	19.0	4.29	0.30	0.11	23.4	4.0	80.6	5.71	1630	7.5	3549	18.5
	M	510	22	006U	0.37	*0.12*	0.19	*0.08*	0.18	*0.06*	12.9	4.45	38.4	12.81	0.35	0.11	15.2	4.5	78.4	5.77	1629	4.3	3564	13.2
	H	780	20	003C	0.45	*0.18*	0.28	*0.12*	0.18	*0.07*	12.6	5.33	48.7	20.17	0.26	0.06	20.7	8.6	82.7	3.57	1631	4.2	3565	13.6
GPI	M	470	21	0082	0.27	*0.09*	0.15	*0.06*	0.12	*0.04*	8.71	3.12	28.6	9.57	0.31	0.08	22.4	4.5	80.2	4.13	1630	4.9	3558	44.3
GPX	M	660	21	0082	0.36	*0.13*	0.16	*0.08*	0.2	*0.08*	14.5	6.00	35.4	13.25	0.41	0.12	19.8	4.5	75.4	5.43	1630	4.0	3535	47.5
	M	790	26	007I	0.27	*0.12*	0.13	*0.07*	0.14	*0.06*	9.78	4.15	26.8	11.36	0.37	0.09	20.2	4.9	76.7	5.38	1630	3.4	3540	44.0
	M	410	25	006F	0.38	*0.16*	0.22	*0.1*	0.15	*0.08*	10.7	5.45	40.2	16.86	0.27	0.10	21.1	6.3	82.1	5.47	1632	4.0	3526	72.8
*RP	-	560	15	-	0.68	*0.31*	0.38	*0.19*	0.3	*0.13*	15.1	3.10	55.9	13.49	0.27	0.05	27.0	6.0	82.0	3.07	1632	2.5	3579	8.9
	-	-	4	-	0.68	*0.01*	0.42	*0.12*	0.26	*0.12*	21.4	9.22	71.2	33.66	0.32	0.07	25.0	8.0	79.7	3.70	1631	3.8	3568	16.8
	-	550	16	-	0.52	*0.16*	0.3	*0.08*	0.22	*0.11*	18.7	0.92	73.7	15.54	0.26	0.05	22.8	9.5	82.6	2.95	1632	1.7	3561	12.9
Banded	White	-	14	0082	0.29	*0.13*	0.17	*0.01*	0.12	*0.05*	16.1	7.83	55.2	15.16	0.28	0.08	18.0	4.3	81.7	4.23	1631	4.5	3561	35.4
	White	-	14	"	0.53	*0.29*	0.26	*0.15*	0.27	*0.19*	8.84	3.38	30.8	15.24	0.31	0.11	20.4	6.3	80.5	5.66	1629	4.3	3556	33.2
	Grey	-	18	"	0.43	*0.14*	0.19	*0.1*	0.25	*0.09*	19.4	13.5	53.7	28.30	0.38	0.15	18.6	5.9	77.1	7.03	1631	4.2	3401	63.4
	Grey	-	8	"	0.18	*0.05*	0.11	*0.06*	0.07	*0.03*	17.6	6.47	42.4	15.12	0.45	0.17	16.8	5.9	74.3	7.43	1631	3.5	3473	70.0
LGL	L	850	22	001Y	0.65	*0.13*	0.41	*0.07*	0.25	*0.07*	5.15	2.37	19.8	6.85	0.30	0.18	17.4	2.9	81.3	9.29	1628	5.2	3558	66.9
	M	1030	10	"	0.78	*0.16*	0.58	*0.11*	0.2	*0.06*	17.8	4.82	70.9	13.03	0.24	0.03	22.6	6.2	83.4	1.82	1632	2.4	3561	13.4
	M	1030	5	"	0.78	*0.11*	0.55	*0.08*	0.23	*0.05*	14.3	4.22	89.8	17.99	0.15	0.02	31.3	5.1	88.8	1.71	1635	2.0	3561	10.5
	H	1420	26	"	0.9	*0.22*	0.53	*0.16*	0.37	*0.08*	16.8	3.32	88.1	12.51	0.19	0.02	32.7	2.7	86.8	1.37	1633	0.0	3570	7.2
DB	-	1360	30	0007	0.52	*0.12*	0.31	*0.08*	0.21	*0.05*	26.8	5.96	96.0	25.16	0.28	0.04	22.3	9.7	81.4	2.54	1632	2.2	3565	12.9
	VL	350	21	0059	0.23	*0.11*	0.09	*0.03*	0.14	*0.09*	10.2	6.43	22.3	9.18	0.42	0.14	18.3	10.1	75.2	6.75	1623	12.0	3496	54.5
	L	510	14	"	0.28	*0.09*	0.14	*0.05*	0.15	*0.07*	10.6	4.85	28.4	8.33	0.37	0.10	16.3	4.0	77.1	5.27	1632	4.6	3448	37.9
	M	1010	19	"	0.64	*0.15*	0.45	*0.12*	0.19	*0.05*	13.6	3.85	72.2	17.44	0.19	0.04	18.0	4.4	86.8	2.72	1633	2.6	3565	9.2
	H	1280	11	"	0.77	*0.08*	0.59	*0.07*	0.18	*0.07*	12.8	5.51	89.5	9.10	0.14	0.05	17.6	4.1	89.8	3.36	1633	2.9	3563	8.6
	VH	1770	9	"	1.18	*0.28*	0.42	*0.1*	0.76	*0.2*	54.4	14.5	110	25.47	0.49	0.05	41.3	8.9	71.7	2.07	1631	2.0	3597	53.2
	VH	1770	10	"	1.44	*0.26*	0.45	*0.1*	1	*0.18*	71.4	12.6	131	24.20	0.54	0.04	20.8	4.2	69.6	1.50	1629	2.1	3577	2.3

Table A6b. The table below gives all individual FTIR analyses for each sample:

Unit	Spot	Row	Col	# of fringes counted	v1 [cm^{-1}]	v2 [cm^{-1}]	Wafer/ Shard Thickness (µm)	Abs. 1630	Abs. 3500	Norm. Abs. 1630 [cm^{-1}]	Norm. Abs. 3500 [cm^{-1}]	Abs. 1630/3500	H_2O_m [wt. %]	OH [wt. %]	H_2O_t [wt. %]	H_2O_m /OH	ε_{3500} [$Lmol^{-1}$ cm^{-1}]	1630 peak [cm^{-1}]	3500 peak [cm^{-1}]
DB	1	12	16	5	2172.9	1561.2	27.2	0.0238	0.1429	8.74	52.45	0.167	0.122	0.334	0.456	0.365	88.2	1637	3577
Mode	2	22	37	2	1504.7	1345.2	41.8	0.0561	0.1361	13.42	32.56	0.412	0.187	0.145	0.332	1.291	75.2	1629	3573
-	3	31	54	5	2360.7	1592.3	21.7	0.0340	0.1514	15.68	69.80	0.225	0.219	0.413	0.631	0.529	84.8	1637	3588
Sample_Clast	4	35	61	2	1565.4	1342.2	29.9	0.0544	0.1582	18.21	52.97	0.344	0.254	0.264	0.518	0.962	78.4	1629	3577
7_17	5	15	34	3	2154.0	1746.6	24.5	0.0442	0.1497	18.01	60.99	0.295	0.251	0.327	0.578	0.768	80.9	1633	3588
Density(kgm^{-3})	6	9	9	3	1656.8	1373.6	35.3	0.0425	0.1085	12.04	30.73	0.392	0.168	0.142	0.309	1.185	76.1	1633	3566
1360	7	23	29	2	2137.0	1869.7	24.9	0.0357	0.1276	14.31	51.16	0.280	0.200	0.281	0.480	0.711	81.7	1637	3581
	8	6	57	3	2267.0	1864.7	24.9	0.0476	0.1599	19.15	64.33	0.298	0.267	0.344	0.611	0.777	80.8	1633	3577
	9	53	53	3	2691.9	2290.2	24.9	0.0340	0.1446	13.66	58.09	0.235	0.190	0.339	0.529	0.562	84.2	1633	3581
	10	37	22	3	1992.3	1534.5	21.8	0.0323	0.1207	14.79	55.26	0.268	0.206	0.308	0.514	0.669	82.4	1633	3573
	11	35	6	4	2552.8	2020.1	25.0	0.0255	0.1088	10.19	43.47	0.234	0.142	0.254	0.396	0.560	84.2	1629	3566
	12	19	48	3	1748.2	1533.0	46.5	0.0340	0.1020	7.32	21.95	0.333	0.102	0.111	0.213	0.917	78.9	1633	3581
	13	6	31	2	1716.4	1496.8	30.4	0.0221	0.1071	7.28	35.28	0.206	0.101	0.214	0.315	0.475	85.8	1629	3588
	14	28	18	3	3145.8	2592.2	18.1	0.0272	0.1156	15.06	64.00	0.235	0.210	0.373	0.583	0.563	84.2	1633	3581
	15	22	44	6	2732.3	1913.4	24.4	0.0323	0.1446	13.23	59.21	0.223	0.184	0.351	0.535	0.526	84.8	1629	3588
	16	47	27	5	2788.7	2131.3	25.4	0.0391	0.1480	15.42	58.38	0.264	0.215	0.327	0.542	0.657	82.6	1629	3566
	17	50	38	6	2871.5	2060.7	24.7	0.0374	0.1514	15.16	61.38	0.247	0.211	0.352	0.564	0.600	83.5	1633	3573
	18	13	48	2	1732.6	1446.0	23.3	0.0357	0.0850	15.35	36.54	0.420	0.214	0.160	0.374	1.334	74.9	1629	3592
	19	30	16	5	2944.5	2262.4	24.4	0.0425	0.1599	17.39	65.44	0.266	0.243	0.366	0.609	0.663	82.5	1637	3573
	20	18	20	4	1827.0	1490.8	39.7	0.0340	0.1548	8.57	39.03	0.220	0.120	0.232	0.352	0.514	85.1	1633	3573
	21	8	7	3	1969.0	1604.1	27.4	0.0442	0.1871	16.13	68.27	0.236	0.225	0.398	0.622	0.566	84.1	1633	3573
	22	49	32	4	2445.5	1921.2	25.4	0.0442	0.1514	17.38	59.53	0.292	0.242	0.321	0.563	0.755	81.1	1633	3577
	23	30	46	7	3014.3	2054.5	24.3	0.0442	0.1582	18.18	65.07	0.279	0.253	0.357	0.611	0.710	81.7	1633	3597
	24	22	35	6	2854.7	2024.2	24.1	0.0510	0.1633	21.18	67.81	0.312	0.295	0.355	0.650	0.833	80.0	1629	3588
	25	15	17	3	2186.6	1783.5	24.8	0.0425	0.1548	17.13	62.40	0.275	0.239	0.345	0.584	0.693	82.0	1633	3562
	26	4	46	7	2938.0	1976.3	24.3	0.0527	0.1718	21.72	70.81	0.307	0.303	0.373	0.676	0.811	80.3	1633	3581
	27	34	60	3	2183.3	1800.1	26.1	0.0357	0.1650	13.68	63.23	0.216	0.191	0.378	0.569	0.505	85.2	1633	3588
	28	54	57	6	2700.0	1882.0	24.4	0.0493	0.1837	20.16	75.13	0.268	0.281	0.419	0.700	0.671	82.3	1633	3566
	29	44	14	3	1775.0	1407.5	27.2	0.0408	0.1718	14.99	63.14	0.237	0.209	0.367	0.576	0.569	84.0	1633	3592
	30	11	46	7	2967.4	2010.8	24.4	0.0527	0.1718	21.61	70.43	0.307	0.301	0.371	0.673	0.811	80.3	1629	3573
		Mean		4.0	2319.9	1797.7	27.0	0.040	0.145	15.171	55.961	0.276	0.212	0.311	0.522	0.718	82.0	1632	3579
		1 S.D error		1.61	493.02	310.38	6.01	0.009	0.025	3.908	13.486	0.059	0.054	0.082	0.123	0.227	3.07	2.5	8.9
GPX	1	26	42	3	2984.1	2476.3	19.7	0.0102	0.0357	5.18	18.13	0.286	0.072	0.099	0.171	0.733	81.4	1633	3570
Mode	2	40	23	2	1946.6	1559.5	17.2	0.0102	0.0459	5.92	26.65	0.222	0.083	0.158	0.241	0.522	84.9	1633	3581
M	3	24	34	3	2863.9	2085.2	12.8	0.0150	0.0430	11.68	33.48	0.349	0.163	0.166	0.328	0.984	78.2	-	-
Sample_Clast	4	25	32	5	2939.4	1623.8	12.7	0.0187	0.0408	14.76	32.21	0.458	0.206	0.132	0.338	1.563	73.2	1624	3570
231_43	5	22	30	4	2908.0	1772.0	11.7	0.0204	0.0391	17.38	33.31	0.522	0.242	0.120	0.362	2.024	70.6	1633	3426
Density	6	22	35	4	2813.7	1587.6	10.9	0.0204	0.0612	18.76	56.28	0.333	0.262	0.285	0.547	0.917	78.9	1633	3566
410	7	27	34	4	2982.8	2035.2	14.1	0.0204	0.0697	14.50	49.54	0.293	0.202	0.267	0.469	0.758	81.0	1633	3566
	8	43	27	2	2963.2	2480.1	13.8	0.0068	0.0323	4.93	23.41	0.211	0.069	0.141	0.210	0.487	85.6	1629	3562
	9	45	25	4	2144.9	1490.7	20.4	0.0204	0.0680	10.01	33.36	0.300	0.140	0.178	0.317	0.785	80.6	1637	3615

	10	28	31	4	2911.8	2471.1	30.3	0.0340	0.1412	11.24	46.67	0.241	0.157	0.270	0.427	0.580	83.8	1633	3547
	11	34	30	4	3009.6	2471.1	24.8	0.0221	0.0595	8.93	24.03	0.371	0.124	0.115	0.239	1.086	77.1	1624	3438
	12	36	37	3	3114.0	2483.2	15.9	0.0204	0.0595	12.87	37.53	0.343	0.179	0.187	0.367	0.958	78.5	1637	3407
	13	38	32	3	2173.2	1771.9	24.9	0.0187	0.0935	7.50	37.52	0.200	0.105	0.229	0.334	0.457	86.2	1637	3431
	14	39	32	4	2300.7	1785.3	25.9	0.0170	0.0816	6.57	31.54	0.208	0.092	0.191	0.282	0.481	85.7	1637	3435
	15	26	26	4	2970.4	2450.2	25.6	0.0204	0.0425	7.96	16.58	0.480	0.111	0.065	0.176	1.707	72.3	1633	3570
	16	24	31	3	2285.2	1767.7	19.3	0.0527	0.1888	27.27	97.70	0.279	0.380	0.536	0.917	0.709	81.7	1624	3407
	18	23	30	5	2297.0	1760.8	31.1	0.0612	0.1922	19.69	61.83	0.318	0.275	0.320	0.595	0.857	79.7	1629	3387
	19	10	31	3	2063.5	1670.0	25.4	0.0136	0.1037	5.35	40.81	0.131	0.075	0.271	0.346	0.275	90.5	1633	3592
	20	20	34	5	2550.4	1749.8	20.8	0.0221	0.0714	10.62	34.30	0.310	0.148	0.180	0.328	0.822	80.2	1633	3573
	21	13	35	3	2197.9	1794.5	24.8	0.0153	0.1446	6.17	58.33	0.106	0.086	0.399	0.485	0.216	92.2	1637	3573
	22	19	36	3	2190.7	1725.4	21.5	0.0136	0.0697	6.33	32.43	0.195	0.088	0.199	0.288	0.443	86.5	1629	3588
	23	17	37	2	2250.3	1946.2	21.9	0.0187	0.1139	8.53	51.96	0.164	0.119	0.332	0.451	0.358	88.4	1633	3562
	24	12	38	4	3105.2	2677.7	31.2	0.0289	0.1395	9.27	44.73	0.207	0.129	0.271	0.400	0.477	85.8	1629	3573
	25	15	41	3	2022.6	1684.9	29.6	0.0221	0.1276	7.46	43.09	0.173	0.104	0.272	0.376	0.382	87.8	1633	3562
		Mean		3.5	2582.9	1971.7	21.1	0.022	0.086	10.786	40.226	0.279	0.150	0.224	0.375	0.774	82.1	1632	3526
		1 S.D error		0.87	399.89	365.35	6.27	0.012	0.047	5.448	16.855	0.105	0.076	0.104	0.155	0.443	5.47	4.0	72.8
GPX	1	20	59	2	2190.2	1779.4	16.2	0.0204	0.0561	12.57	34.57	0.364	0.175	0.167	0.342	1.050	77.5	1629	3551
Mode	2	25	63	3	2312.7	1743.2	17.6	0.0221	0.0663	12.59	37.76	0.333	0.175	0.191	0.367	0.917	78.9	1633	3478
M	3	23	61	2	2322.5	1955.3	18.2	0.0204	0.1003	11.24	55.25	0.203	0.157	0.336	0.493	0.466	86.0	1624	3527
Sample_Clast	4	11	43	2	2240.9	1762.3	13.9	0.0102	0.0205	7.32	14.72	0.498	0.102	0.059	0.161	1.833	71.5	1624	3581
270_17	5	28	20	2	3115.5	2652.3	14.4	0.0136	0.0340	9.45	23.62	0.400	0.132	0.107	0.239	1.227	75.8	1624	3588
Density	6	37	45	6	2877.9	2248.0	31.8	0.0153	0.0544	4.82	17.13	0.281	0.067	0.094	0.161	0.717	81.6	1629	3553
790	7	20	16	3	2629.7	1901.4	13.7	0.0183	0.0663	13.33	48.29	0.276	0.186	0.266	0.452	0.698	81.9	1629	3562
	8	18	14	3	2798.0	1988.3	12.4	0.0272	0.0731	22.02	59.19	0.372	0.307	0.282	0.589	1.089	77.1	1624	3570
	9	21	13	4	2143.7	1311.7	16.0	0.0255	0.0510	15.91	31.82	0.500	0.222	0.120	0.342	1.852	71.4	1633	3551
	10	10	24	9	3140.8	2167.1	30.8	0.0187	0.0595	6.07	19.31	0.314	0.085	0.101	0.185	0.840	79.9	1629	3558
	11	41	33	3	1936.3	1467.5	21.3	0.0110	0.0400	5.16	18.75	0.275	0.072	0.104	0.175	0.694	82.0	-	-
	12	47	34	5	2366.8	1728.0	26.1	0.0238	0.0510	9.12	19.55	0.467	0.127	0.079	0.206	1.617	72.8	1633	3562
	13	35	31	2	2265.6	1915.7	19.1	0.0255	0.0646	13.38	33.91	0.395	0.187	0.155	0.342	1.200	76.0	1637	3570
	14	29	25	4	2286.9	1568.3	18.6	0.0170	0.0408	9.16	21.99	0.417	0.128	0.097	0.225	1.316	75.0	1629	3512
	15	33	21	3	2240.6	1684.8	18.0	0.0289	0.0646	16.06	35.90	0.447	0.224	0.150	0.374	1.494	73.6	1629	3562
	16	36	19	4	2077.7	1474.2	22.1	0.0204	0.0680	9.23	30.78	0.300	0.129	0.164	0.293	0.785	80.6	1633	3437
	17	55	22	6	2552.7	1838.8	28.0	0.0170	0.0476	6.07	16.99	0.357	0.085	0.083	0.168	1.020	77.8	1633	3577
	18	57	26	3	2220.1	1716.8	19.9	0.0255	0.0493	12.83	24.81	0.517	0.179	0.090	0.269	1.987	70.7	1629	3573
	19	27	31	3	3277.7	2830.1	22.3	0.0136	0.0459	6.09	20.54	0.296	0.085	0.110	0.195	0.771	80.8	1633	3441
	20	24	31	4	2238.3	1570.6	20.0	0.0153	0.0289	7.66	14.47	0.529	0.107	0.051	0.158	2.088	70.2	1633	3570
	21	21	32	5	2250.7	1474.5	21.5	0.0170	0.0340	7.92	15.83	0.500	0.110	0.060	0.170	1.852	71.4	1633	3588
	22	20	29	5	2224.6	1447.7	21.5	0.0153	0.0493	7.13	22.98	0.310	0.099	0.121	0.220	0.825	80.1	1629	3504
	23	15	31	10	3338.0	1519.1	18.3	0.0102	0.0340	5.57	18.55	0.300	0.078	0.099	0.176	0.785	80.6	1633	3562
	24	29	31	4	1921.9	1380.8	24.6	0.0170	0.0391	6.90	15.87	0.435	0.096	0.068	0.164	1.418	74.2	1629	3562
	25	31	29	8	3297.2	1716.4	16.9	0.0204	0.0493	12.09	29.23	0.414	0.169	0.130	0.298	1.300	75.1	1629	3480
	26	35	28	3	1954.9	1511.1	22.5	0.0102	0.0391	4.53	17.35	0.261	0.063	0.098	0.161	0.646	82.7	1633	3480
		Mean		4.2	2470.1	1782.8	20.2	0.018	0.051	9.778	26.891	0.375	0.136	0.130	0.266	1.173	77.1	1630	3540
		1 S.D error		2.11	434.75	359.87	4.90	0.005	0.016	4.151	12.136	0.090	0.058	0.069	0.115	0.460	4.26	3.4	44.0

GPX	1	28	39	2	1930.0	1623.4	21.7	0.0408	0.0935	18.76	43.00	0.436	0.262	0.183	0.445	1.428	74.1	1633	3538
Mode	2	31	37	2	2933.0	2165.4	8.7	0.0289	0.0714	33.28	82.21	0.405	0.464	0.371	0.835	1.252	75.5	1629	3523
M	3	26	44	3	1895.7	1496.4	25.0	0.0578	0.0969	23.08	38.69	0.596	0.322	0.117	0.438	2.762	67.7	1624	3426
Sample_Clast	4	23	39	4	2172.4	1640.1	25.0	0.0272	0.0884	10.86	35.29	0.308	0.151	0.186	0.337	0.815	80.2	1633	3577
290_85	5	37	25	4	2534.6	1671.4	15.4	0.0187	0.0425	12.11	27.51	0.440	0.169	0.116	0.285	1.449	74.0	1633	3553
Density	6	36	20	2	2070.3	1615.6	14.7	0.0306	0.0391	20.87	26.67	0.783	0.291	0.042	0.333	7.004	61.5	1624	3547
660	7	40	26	4	2500.9	1677.5	16.2	0.0221	0.0510	13.65	31.50	0.433	0.190	0.135	0.325	1.410	74.3	1633	3547
	8	29	39	2	2163.0	1791.6	18.0	0.0119	0.0374	6.63	20.84	0.318	0.092	0.108	0.200	0.856	79.7	1622	3476
	9	17	27	2	2186.8	1762.0	15.7	0.0255	0.0510	16.25	32.50	0.500	0.227	0.122	0.349	1.852	71.4	1633	3504
	10	32	39	2	1977.1	1653.3	20.6	0.0255	0.0561	12.39	27.25	0.455	0.173	0.112	0.285	1.538	73.3	1633	3562
	11	35	39	3	2075.9	1614.5	21.7	0.0204	0.1122	9.41	51.77	0.182	0.131	0.323	0.455	0.406	87.3	1629	3407
	12	32	45	2	2988.3	2501.5	13.7	0.0255	0.0731	18.62	53.38	0.349	0.260	0.264	0.524	0.984	78.2	1629	3538
	13	33	42	6	2765.6	1679.7	18.4	0.0204	0.0595	11.08	32.31	0.343	0.154	0.161	0.316	0.958	78.5	1629	3570
	14	27	41	3	2148.0	1636.5	19.6	0.0170	0.0544	8.70	27.83	0.313	0.121	0.145	0.267	0.833	80.0	1629	3500
	15	40	24	4	2204.4	1607.3	22.3	0.0306	0.0663	13.70	29.69	0.462	0.191	0.121	0.312	1.583	73.0	1624	3558
	16	39	25	4	2215.8	1608.4	22.0	0.0323	0.0714	14.71	32.53	0.452	0.205	0.135	0.340	1.525	73.4	1629	3573
	17	42	21	4	2200.7	1588.4	21.8	0.0221	0.0680	10.15	31.23	0.325	0.141	0.160	0.302	0.883	79.4	1629	3566
	18	43	25	4	2179.8	1649.5	25.1	0.0374	0.0680	14.87	27.05	0.550	0.207	0.091	0.299	2.273	69.4	1633	3551
	19	44	26	3	2235.9	1805.3	23.2	0.0374	0.0765	16.10	32.94	0.489	0.225	0.127	0.351	1.770	71.9	1637	3581
	20	46	22	2	2274.5	1930.1	19.4	0.0255	0.0748	13.17	38.64	0.341	0.184	0.193	0.377	0.949	78.6	1629	3553
	21	47	21	6	2668.9	1935.5	27.3	0.0170	0.0595	6.23	21.82	0.286	0.087	0.119	0.206	0.733	81.4	1637	3592
		Mean		3.2	2301.0	1745.4	19.8	0.027	0.067	14.506	35.458	0.417	0.202	0.159	0.361	1.584	75.4	1630	3535
		1 S.D error		1.23	304.46	223.90	4.45	0.010	0.019	5.995	13.251	0.126	0.084	0.075	0.131	1.327	5.43	4.0	47.5

GPI	1	39	22	4	2186.8	1581.4	22.0	0.0136	0.0850	6.18	38.59	0.160	0.086	0.248	0.334	0.348	88.7	1637	3562
Mode	2	38	16	3	2088.5	1661.6	23.4	0.0170	0.0816	7.26	34.84	0.208	0.101	0.210	0.312	0.481	85.7	1637	3588
M	3	40	20	4	2106.1	1532.7	23.3	0.0255	0.0765	10.97	32.90	0.333	0.153	0.167	0.320	0.917	78.9	1624	3585
Sample_Clast	4	41	17	5	2177.9	1695.8	34.6	0.0255	0.1105	7.38	31.96	0.231	0.103	0.188	0.290	0.548	84.4	1629	3585
290_166	5	24	41	4	2070.4	1583.5	27.4	0.0136	0.0527	4.97	19.24	0.258	0.069	0.109	0.178	0.636	82.9	1624	3431
Density	6	39	33	3	2111.1	1575.9	18.7	0.0153	0.0459	8.19	24.57	0.333	0.114	0.124	0.239	0.917	78.9	1624	3562
470	7	36	34	4	3093.2	2478.3	21.7	0.0187	0.0442	8.62	20.38	0.423	0.120	0.089	0.209	1.351	74.7	1629	3547
	8	32	26	3	2153.8	1772.7	26.2	0.0221	0.0510	8.42	19.44	0.433	0.117	0.083	0.201	1.410	74.3	1637	3585
	9	30	25	3	2256.0	1814.9	22.7	0.0068	0.0306	3.00	13.50	0.222	0.042	0.080	0.122	0.522	84.9	1629	3570
	10	41	27	2	2059.2	1823.6	28.3	0.0204	0.0595	7.21	21.03	0.343	0.101	0.105	0.205	0.958	78.5	1633	3588
	11	43	27	3	2390.8	1953.8	22.9	0.0170	0.0731	7.43	31.94	0.233	0.104	0.187	0.291	0.554	84.3	1624	3577
	12	44	27	2	2187.2	1882.1	21.9	0.0153	0.0731	7.00	33.45	0.209	0.098	0.202	0.299	0.484	85.7	1629	3566
	13	38	37	2	2820.0	2275.0	12.2	0.0187	0.0578	15.29	47.25	0.324	0.213	0.243	0.456	0.877	79.4	1624	3588
	14	34	35	4	2201.5	1615.5	22.8	0.0102	0.0323	4.48	14.20	0.316	0.063	0.074	0.136	0.846	79.8	1633	3504
	15	41	39	2	2106.6	1762.8	19.4	0.0204	0.0527	10.52	27.18	0.387	0.147	0.126	0.273	1.162	76.4	1624	3592
	16	39	31	2	2170.2	1757.8	16.2	0.0221	0.0629	13.67	38.91	0.351	0.191	0.192	0.382	0.995	78.1	1633	3596
	17	34	28	2	1935.7	1637.1	22.3	0.0221	0.0663	9.90	29.70	0.333	0.138	0.150	0.288	0.917	78.9	1629	3570
	18	37	25	2	2278.3	1966.4	21.4	0.0272	0.0731	12.73	34.20	0.372	0.177	0.163	0.340	1.089	77.1	1637	3547
	19	26	20	3	2177.8	1754.6	23.6	0.0306	0.1037	12.95	43.89	0.295	0.181	0.235	0.416	0.767	80.9	1637	3480
	20	25	22	2	2069.7	1692.7	17.7	0.0187	0.0561	10.57	31.72	0.333	0.147	0.161	0.308	0.917	78.9	1633	3484
	21	23	22	2	2240.5	1939.0	22.1	0.0136	0.0289	6.15	13.07	0.471	0.086	0.052	0.138	1.643	72.6	1633	3605
		Mean		2.9	2232.4	1798.0	22.4	0.019	0.063	8.708	28.665	0.313	0.121	0.152	0.273	0.873	80.2	1630	3558
		1 S.D error		0.92	255.71	227.64	4.45	0.006	0.021	3.115	9.574	0.080	0.043	0.058	0.088	0.327	4.13	4.9	44.3

ALB	1	35	24	2	2134.5	1812.6	20.7	0.0102	0.0289	4.93	13.95	0.353	0.069	0.069	0.137	1.002	78.0	1637	3547
Mode	2	23	12	3	2958.4	2528.4	23.3	0.0153	0.0493	6.58	21.20	0.310	0.092	0.111	0.203	0.825	80.1	1629	3542
L	3	22	13	3	2025.5	1645.6	26.3	0.0068	0.0340	2.58	12.92	0.200	0.036	0.079	0.115	0.457	86.2	1629	3527
Sample_Clast	4	16	35	4	2389.2	1603.9	17.0	0.0136	0.0408	8.01	24.03	0.333	0.112	0.122	0.233	0.917	78.9	1633	3543
120_84	5	13	34	3	2074.2	1695.4	26.4	0.0068	0.0561	2.58	21.25	0.121	0.036	0.143	0.179	0.251	91.2	1629	3553
Density	6	12	33	4	2129.3	1626.3	26.5	0.0102	0.0510	3.85	19.24	0.200	0.054	0.117	0.171	0.457	86.2	1629	3566
310	7	9	30	3	2260.5	1766.2	20.2	0.0170	0.0391	8.40	19.33	0.435	0.117	0.083	0.200	1.418	74.2	1622	3566
	8	6	30	2	1989.8	1668.1	20.7	0.0085	0.0272	4.10	13.13	0.313	0.057	0.069	0.126	0.833	80.0	1624	3562
	9	37	52	4	1959.8	1484.3	28.0	0.0272	0.0493	9.70	17.58	0.552	0.135	0.059	0.194	2.289	69.4	1633	3534
	10	42	49	5	2491.9	1938.2	30.1	0.0187	0.0595	6.21	19.77	0.314	0.087	0.103	0.190	0.840	79.9	1618	3566
	11	44	50	4	2276.3	1708.3	23.5	0.0136	0.0663	5.79	28.24	0.205	0.081	0.171	0.252	0.471	85.9	1648	3573
	12	45	35	2	2088.3	1714.5	17.8	0.0119	0.0323	6.67	18.11	0.368	0.093	0.087	0.180	1.072	77.2	1624	3508
		Mean		3.3	2231.5	1766.0	23.4	0.013	0.044	5.784	19.062	0.309	0.081	0.101	0.182	0.903	80.6	1630	3549
		1 S.D error		0.92	268.28	253.85	3.98	0.006	0.012	2.172	4.293	0.112	0.030	0.032	0.039	0.520	5.71	7.5	18.5

ALB	1	47	20	6	3269.0	1619.9	12.1	0.0153	0.0340	12.62	28.03	0.450	0.176	0.116	0.292	1.510	73.5	1624	3566
Mode	2	45	26	4	2532.9	1453.5	12.4	0.0170	0.0323	13.76	26.15	0.526	0.192	0.093	0.285	2.062	70.4	1624	3562
M	3	44	21	6	2903.0	1321.8	12.6	0.0187	0.0374	14.78	29.57	0.500	0.206	0.111	0.317	1.852	71.4	1629	3553
Sample_Clast	4	42	27	4	3398.2	1573.0	7.3	0.0136	0.0374	18.62	51.20	0.364	0.260	0.247	0.507	1.050	77.5	1629	3570
246_59	5	43	52	5	3293.9	1705.0	10.5	0.0187	0.0374	17.83	35.65	0.500	0.249	0.134	0.383	1.852	71.4	1624	3570
Density	6	45	49	5	3313.8	1628.4	9.9	0.0187	0.0442	18.91	44.70	0.423	0.264	0.195	0.459	1.351	74.7	1633	3573
510	7	17	33	6	2478.8	1539.8	21.3	0.0187	0.0697	8.78	32.72	0.268	0.122	0.182	0.305	0.671	82.3	1629	3553
	8	17	29	7	3314.2	1745.9	14.9	0.0153	0.0578	10.28	38.85	0.265	0.143	0.218	0.361	0.659	82.5	1622	3570
	9	19	33	6	2693.6	1410.6	15.6	0.0221	0.0680	14.18	43.62	0.325	0.198	0.224	0.421	0.883	79.4	1637	3570
	10	23	34	4	3561.6	1768.0	7.4	0.0153	0.0561	20.58	75.47	0.273	0.287	0.418	0.705	0.686	82.1	1633	3570
	11	15	31	6	2795.3	1628.8	17.1	0.0187	0.0697	10.91	40.65	0.268	0.152	0.227	0.379	0.671	82.3	1633	3566
	12	13	32	4	2138.0	1512.9	21.3	0.0221	0.0697	10.36	32.68	0.317	0.144	0.170	0.314	0.851	79.8	1622	3573
	13	11	31	4	2212.5	1558.3	20.4	0.0119	0.0833	5.84	40.87	0.143	0.081	0.268	0.349	0.304	89.7	1633	3573
	14	10	33	8	2922.7	1525.7	19.1	0.0085	0.0595	4.45	31.17	0.143	0.062	0.204	0.266	0.304	89.7	1629	3588
	15	54	16	3	2052.3	1466.9	17.1	0.0153	0.0425	8.96	24.88	0.360	0.125	0.121	0.246	1.033	77.6	1629	3566
	16	53	19	4	2465.3	1747.8	18.6	0.0170	0.0306	9.15	16.47	0.556	0.128	0.055	0.182	2.326	69.2	1633	3588
	17	52	16	5	2437.5	1528.5	18.3	0.0221	0.0595	12.05	32.45	0.371	0.168	0.155	0.323	1.086	77.1	1633	3547
	18	50	14	3	2527.0	1652.4	11.4	0.0187	0.0561	16.36	49.07	0.333	0.228	0.249	0.477	0.917	78.9	1633	3547
	19	48	13	3	2531.3	1681.5	11.8	0.0221	0.0663	18.78	56.34	0.333	0.262	0.285	0.547	0.917	78.9	1629	3558
	20	45	11	2	2224.9	1738.6	13.7	0.0238	0.0646	17.36	47.12	0.368	0.242	0.226	0.468	1.072	77.2	1624	3562
	21	41	11	2	2195.0	1892.0	22.0	0.0238	0.0493	10.82	22.41	0.483	0.151	0.087	0.238	1.726	72.1	1633	3566
	22	38	5	2	2225.0	1897.6	20.4	0.0170	0.0952	8.35	46.75	0.179	0.116	0.293	0.410	0.397	87.5	1633	3527
		Mean		4.5	2703.9	1618.0	15.2	0.018	0.055	12.896	38.492	0.352	0.180	0.194	0.374	1.099	78.4	1629	3564
		1 S.D error		1.62	462.14	144.04	4.49	0.004	0.017	4.449	12.814	0.116	0.062	0.082	0.117	0.558	5.77	4.3	13.2

ALB	1	17	28	4	3121.7	2427.2	19.2	0.0153	0.0697	7.97	36.30	0.220	0.111	0.216	0.327	0.514	85.1	1633	3558
Mode	2	20	26	5	2460.0	1655.8	20.7	0.0272	0.0935	13.12	45.12	0.291	0.183	0.243	0.426	0.752	81.1	1637	3566
H	3	22	27	3	2399.7	1960.7	22.8	0.0238	0.1105	10.45	48.51	0.215	0.146	0.290	0.436	0.502	85.3	1629	3558

Sample_Clast	4	25	22	3	2850.4	2098.0	13.3	0.0187	0.0646	14.07	48.61	0.289	0.196	0.263	0.459	0.746	81.2	1629	3578
120_85	5	14	15	3	2438.2	1516.5	10.8	0.0238	0.0697	21.94	64.24	0.341	0.306	0.321	0.627	0.952	78.5	1637	3558
Density	6	16	14	4	2936.6	1537.4	9.5	0.0238	0.0748	24.98	78.50	0.318	0.348	0.407	0.755	0.856	79.7	1629	3570
780	7	36	45	2	3481.8	2744.5	9.0	0.0187	0.0867	20.68	95.89	0.216	0.288	0.574	0.862	0.503	85.3	1633	3577
	8	34	50	3	2913.5	2403.3	19.6	0.0119	0.0578	6.07	29.49	0.206	0.085	0.179	0.263	0.474	85.9	1629	3585
	9	32	48	2	3060.1	2623.1	15.3	0.0136	0.0850	8.91	55.72	0.160	0.124	0.358	0.482	0.348	88.7	1633	3577
	10	16	34	3	3000.1	1938.3	9.4	0.0204	0.0935	21.66	99.28	0.218	0.302	0.592	0.894	0.510	85.1	1633	3573
	11	46	39	5	2139.3	1491.2	25.7	0.0238	0.1207	9.25	46.94	0.197	0.129	0.288	0.417	0.449	86.4	1629	3566
	12	44	43	2	2167.6	1928.0	27.8	0.0374	0.1173	13.44	42.16	0.319	0.187	0.218	0.406	0.858	79.7	1633	3577
	13	51	40	2	2294.1	2019.2	24.3	0.0187	0.0969	7.71	39.96	0.193	0.108	0.246	0.354	0.437	86.6	1633	3570
	14	33	46	2	2221.9	1913.0	21.6	0.0255	0.0799	11.82	37.02	0.319	0.165	0.192	0.356	0.860	79.7	1629	3534
	15	32	40	3	1799.6	1477.7	31.1	0.0289	0.1395	9.30	44.91	0.207	0.130	0.272	0.401	0.477	85.8	1633	3558
	16	30	49	2	1812.2	1509.3	22.0	0.0170	0.0748	7.72	33.99	0.227	0.108	0.200	0.308	0.538	84.6	1618	3570
	17	29	46	2	2201.1	1744.4	14.6	0.0187	0.0493	12.81	33.77	0.379	0.179	0.159	0.338	1.124	76.7	1629	3581
	18	32	14	3	2047.3	1532.3	19.4	0.0238	0.0595	12.26	30.64	0.400	0.171	0.139	0.310	1.227	75.8	1624	3545
	19	23	11	2	1982.2	1814.0	39.6	0.0374	0.1173	9.44	29.59	0.319	0.132	0.153	0.285	0.858	79.7	1633	3566
	20	21	12	3	2244.8	1983.8	38.3	0.0340	0.1276	8.87	33.30	0.266	0.124	0.186	0.310	0.665	82.4	1633	3538
		Mean		2.9	2478.6	1915.9	20.7	0.023	0.089	12.624	48.696	0.265	0.176	0.275	0.451	0.682	82.7	1631	3565
		1 S.D																	
		error		0.94	466.71	376.29	8.61	0.007	0.025	5.327	20.174	0.066	0.074	0.123	0.182	0.240	3.57	4.2	13.6

AL	1	31	34	2	2846.1	2530.2	21.1	0.0408	0.0969	19.33	45.92	0.421	0.270	0.201	0.471	1.340	74.8	1633	3566
Mode	2	32	33	2	2746.5	2451.8	22.6	0.0357	0.0850	15.78	37.57	0.420	0.220	0.165	0.385	1.334	74.9	1629	3581
L	3	32	32	1	2201.1	2035.5	20.1	0.0323	0.0918	16.05	45.61	0.352	0.224	0.224	0.448	0.997	78.0	1629	3534
Sample_Clast	4	32	35	1	2763.5	2624.4	24.0	0.0408	0.0799	17.03	33.34	0.511	0.237	0.123	0.360	1.934	71.0	1637	3562
54_66	5	31	36	1	2170.4	1986.7	18.1	0.0391	0.0816	21.55	44.97	0.479	0.300	0.177	0.477	1.701	72.3	1629	3573
Density																			
390																			
		Mean		1.4	2545.5	2325.7	21.2	0.038	0.087	17.947	41.482	0.437	0.250	0.178	0.428	1.461	74.2	1631	3563
		1 S.D																	
		error		0.49	295.84	263.09	2.01	0.003	0.006	2.193	5.106	0.055	0.031	0.034	0.047	0.325	2.42	3.2	16.0

AL	1	32	29	2	2219.9	1898.8	20.8	0.0102	0.0476	4.91	22.93	0.214	0.068	0.137	0.206	0.498	85.4	1633	3592
Mode	2	36	30	3	2146.3	1770.3	26.6	0.0085	0.0714	3.20	26.85	0.119	0.045	0.181	0.225	0.246	91.3	1624	3566
L2	3	37	31	5	2736.9	1871.2	19.3	0.0034	0.0459	1.77	23.84	0.074	0.025	0.169	0.194	0.146	94.4	1629	3570
Sample_Clast	4	17	22	3	2746.8	2149.3	16.7	0.0017	0.0408	1.02	24.38	0.042	0.014	0.179	0.193	0.079	96.8	1633	3566
84_6	5	15	17	2	2167.0	1629.4	12.4	0.0068	0.0238	5.48	19.19	0.286	0.076	0.104	0.181	0.733	81.4	1633	3570
Density	6	14	14	3	3383.0	2543.9	11.9	0.0068	0.0306	5.71	25.68	0.222	0.080	0.152	0.232	0.522	84.9	1633	3566
390	7	46	33	3	2595.5	1781.9	12.3	0.0136	0.0544	11.06	44.26	0.250	0.154	0.253	0.407	0.610	83.3	1637	3588
	8	7	13	3	2279.2	1616.4	15.1	0.0068	0.0272	4.51	18.03	0.250	0.063	0.103	0.166	0.610	83.3	1622	3588
	9	10	15	2	2682.2	1828.2	7.8	0.0085	0.0510	10.89	65.33	0.167	0.152	0.416	0.568	0.365	88.2	1629	3553
	10	41	16	3	3067.4	2400.2	15.0	0.0085	0.0238	5.67	15.88	0.357	0.079	0.077	0.157	1.020	77.8	1633	3588
	11	44	16	2	2189.5	1720.6	14.2	0.0136	0.0493	9.57	34.68	0.276	0.133	0.191	0.325	0.697	81.9	1629	3577
		Mean		2.8	2564.9	1928.2	15.6	0.008	0.042	5.798	29.185	0.205	0.081	0.179	0.259	0.502	86.3	1630	3575
		1 S.D																	
		error		0.83	390.14	292.45	4.86	0.003	0.014	3.252	13.731	0.091	0.045	0.088	0.121	0.265	5.56	4.2	12.0

AL	1	61	61	3	2565.3	2183.6	26.2	0.0306	0.0884	11.68	33.74	0.346	0.163	0.168	0.330	0.972	78.3	1633	3547
Mode	2	61	58	3	2196.4	1838.3	27.9	0.0238	0.0765	8.52	27.39	0.311	0.119	0.144	0.262	0.828	80.1	1629	3573
M	3	13	44	2	2995.7	2533.0	14.4	0.0136	0.0442	9.44	30.68	0.308	0.132	0.162	0.293	0.815	80.2	1624	3445
Sample_Clast	4	10	42	2	1781.5	1457.0	20.5	0.0136	0.0425	6.62	20.69	0.320	0.092	0.107	0.199	0.863	79.6	1624	3553
132_5	5	56	45	3	2249.4	1890.3	27.8	0.0221	0.0731	7.94	26.25	0.302	0.111	0.139	0.250	0.794	80.5	1633	3566
Density	6	32	19	3	2267.6	1883.1	26.0	0.0238	0.1173	9.15	45.10	0.203	0.128	0.274	0.402	0.465	86.0	1629	3562
500	7	33	15	4	2178.2	1694.8	27.6	0.0153	0.0816	5.55	29.58	0.188	0.077	0.184	0.261	0.421	87.0	1629	3577
	8	36	20	3	3051.2	2332.9	13.9	0.0119	0.0476	8.55	34.19	0.250	0.119	0.195	0.315	0.610	83.3	1624	3547
	9	33	52	3	2651.6	2121.5	18.9	0.0102	0.0323	5.41	17.12	0.316	0.075	0.089	0.164	0.846	79.8	1624	3577
	10	30	23	3	2476.9	1676.7	12.5	0.0051	0.0221	4.08	17.68	0.231	0.057	0.104	0.161	0.548	84.4	1629	3538
	11	31	17	2	2265.6	1918.7	19.2	0.0136	0.0595	7.08	30.96	0.229	0.099	0.182	0.281	0.542	84.5	1633	3566
	12	33	25	3	2279.0	1611.7	15.0	0.0153	0.0527	10.21	35.17	0.290	0.142	0.190	0.332	0.749	81.2	1629	3547
	13	35	24	2	2788.3	2366.8	15.8	0.0204	0.0612	12.90	38.69	0.333	0.180	0.196	0.376	0.917	78.9	1633	3573
	14	43	23	3	2833.2	1762.7	9.3	0.0204	0.0408	21.84	43.68	0.500	0.304	0.164	0.469	1.852	71.4	1629	3551
	15	44	19	3	2634.0	1695.9	10.7	0.0102	0.0306	9.57	28.71	0.333	0.133	0.145	0.279	0.917	78.9	1647	3547
		Mean		2.8	2480.9	1931.1	19.1	0.017	0.058	9.235	30.643	0.297	0.129	0.163	0.292	0.809	81.0	1630	3551
		1 S.D error		0.54	338.28	300.81	6.39	0.006	0.025	4.069	8.046	0.073	0.057	0.044	0.082	0.326	3.68	5.6	30.9

AL	1	28	30	3	3023.6	2250.5	12.9	0.0272	0.0697	21.03	53.89	0.390	0.293	0.249	0.542	1.177	76.2	1629	3515
Mode	2	32	29	3	3097.1	1883.8	8.2	0.0340	0.0850	41.25	103.13	0.400	0.575	0.469	1.044	1.227	75.8	1633	3515
H	3	38	32	3	3224.6	2045.8	8.5	0.0204	0.0476	24.05	56.11	0.429	0.335	0.243	0.578	1.382	74.5	1633	3512
Sample_Clast	4	33	36	6	2962.9	1703.3	15.9	0.0238	0.0731	14.99	46.04	0.326	0.209	0.236	0.445	0.886	79.3	1633	3558
105_16	5	30	32	4	2714.8	1868.8	15.8	0.0391	0.0935	24.81	59.33	0.418	0.346	0.261	0.607	1.324	74.9	1633	3566
Density	6	28	34	5	3008.3	1894.0	15.0	0.0544	0.0816	36.37	54.56	0.667	0.507	0.134	0.641	3.774	65.2	1629	3531
730	7	33	35	3	2285.7	1694.6	16.9	0.0289	0.0782	17.08	46.22	0.370	0.238	0.221	0.459	1.077	77.2	1629	3566
	8	35	34	6	3159.6	1921.5	16.2	0.0306	0.0782	18.94	48.41	0.391	0.264	0.223	0.487	1.183	76.2	1629	3534
	9	36	31	3	3176.8	2497.9	14.7	0.0306	0.1173	20.77	79.63	0.261	0.290	0.448	0.738	0.646	82.7	1633	3515
	10	38	32	5	2407.6	1641.5	21.8	0.0391	0.1412	17.97	64.90	0.277	0.251	0.357	0.608	0.701	81.9	1633	3553
	11	23	31	3	2596.7	1888.1	14.1	0.0442	0.0765	31.32	54.21	0.578	0.437	0.171	0.608	2.552	68.4	1633	3562
	12	29	32	5	2624.7	1684.4	17.7	0.0391	0.1259	22.06	71.03	0.311	0.308	0.372	0.680	0.826	80.1	1629	3577
	13	20	23	3	3541.0	2497.4	9.6	0.0374	0.0612	39.03	63.87	0.611	0.544	0.185	0.729	2.941	67.2	1633	3527
	14	20	29	4	2058.8	1809.3	53.4	0.0833	0.2585	15.59	48.37	0.322	0.217	0.249	0.467	0.872	79.5	1633	3551
	15	21	32	5	2067.0	1756.3	53.6	0.0765	0.3895	14.26	72.61	0.196	0.199	0.445	0.644	0.446	86.4	1633	3577
	16	24	34	6	2818.9	2415.6	49.6	0.1224	0.4456	24.68	89.86	0.275	0.344	0.496	0.840	0.693	82.0	1633	3566
	17	26	35	7	2961.1	2502.3	50.9	0.0748	0.3231	14.71	63.53	0.232	0.205	0.372	0.577	0.551	84.4	1637	3573
	18	36	30	4	3487.8	1985.9	8.9	0.0289	0.0816	32.55	91.92	0.354	0.454	0.451	0.905	1.007	77.9	1629	3547
	19	38	28	2	2925.9	2578.4	19.2	0.0340	0.1020	17.72	53.17	0.333	0.247	0.269	0.516	0.917	78.9	1629	3542
	20	40	16	3	2217.3	1901.1	31.6	0.0272	0.1020	8.60	32.25	0.267	0.120	0.180	0.300	0.666	82.4	1629	3551
		Mean		4.2	2818.0	2021.0	22.7	0.045	0.142	22.890	62.652	0.370	0.319	0.302	0.621	1.242	77.6	1632	3547
		1 S.D error		1.35	426.71	307.14	15.45	0.025	0.113	8.724	17.225	0.122	0.122	0.111	0.167	0.839	5.46	2.3	21.4

AL	2			2	3168.5	2690.8	14.0	0.0221	0.0918	15.84	65.78	0.241	0.221	0.381	0.602	0.580	83.9	1637	3558
Mode	5			2	3150.5	2636.0	13.0	0.0374	0.1071	28.86	82.65	0.349	0.402	0.408	0.811	0.985	78.2	1629	3542
Hspot	6			1	3009.0	2824.6	18.1	0.0289	0.1327	15.99	73.41	0.218	0.223	0.438	0.661	0.509	85.2	1633	3566

Sample_Clast 31_24 Density 730	9			2	3118.0	2614.4	13.2	0.0442	0.1582	33.39	119.50	0.279	0.466	0.656	1.121	0.710	81.7	1637	3592
	10			2	2012.1	1693.2	20.9	0.0323	0.1327	15.45	63.48	0.243	0.215	0.366	0.582	0.588	83.7	1633	3572
		Mean		1.8	2891.6	2491.8	15.8	0.033	0.125	21.905	80.965	0.266	0.305	0.450	0.755	0.674	82.5	1634	3566
		1 S.D error		0.40	443.23	405.94	3.14	0.007	0.023	7.666	20.404	0.046	0.107	0.106	0.200	0.168	2.44	3.0	16.4
LGL Mode L Sample_Clast 70_158 Density 850	1	28	45	2	2241.2	1672.3	11.7	0.0369	0.1166	31.49	99.50	0.316	0.439	0.517	0.956	0.849	79.8	1628	3546
	2	22	10	4	2227.4	1793.0	30.7	0.0425	0.1803	13.85	58.74	0.236	0.193	0.342	0.535	0.564	84.1	1632	3553
	3	14	26	4	2269.6	1774.5	26.9	0.0306	0.1480	11.36	54.96	0.207	0.158	0.333	0.491	0.476	85.8	1629	3561
	4	27	28	6	2616.9	1751.3	23.1	0.0306	0.1344	13.24	58.17	0.228	0.185	0.343	0.527	0.539	84.6	1633	3553
	5	21	41	5	2763.4	1951.0	20.5	0.0323	0.1378	15.74	67.17	0.234	0.220	0.392	0.612	0.560	84.2	1637	3566
	6	36	34	6	3128.4	1899.5	16.3	0.0306	0.1480	18.80	90.94	0.207	0.262	0.551	0.813	0.476	85.8	1633	3566
	7	30	25	6	3004.9	1984.8	19.6	0.0255	0.1071	13.01	54.63	0.238	0.181	0.317	0.499	0.571	84.0	1633	3527
	8	24	41	5	2608.4	1875.0	22.7	0.0374	0.1667	16.46	73.35	0.224	0.229	0.434	0.663	0.529	84.8	1633	3566
	9	30	38	3	2405.2	1929.3	21.0	0.0425	0.1684	20.23	80.14	0.252	0.282	0.457	0.739	0.618	83.2	1633	3573
	10	48	24	2	2097.8	1814.1	23.5	0.0493	0.1480	20.98	62.98	0.333	0.292	0.319	0.612	0.916	79.0	1633	3566
	11	47	41	4	2991.9	2221.5	17.3	0.0323	0.1207	18.66	69.74	0.268	0.260	0.389	0.649	0.669	82.4	1633	3581
	12	48	43	5	3178.2	2133.0	15.9	0.0238	0.1054	14.93	66.10	0.226	0.208	0.390	0.598	0.533	84.7	1633	3577
	13	44	44	5	3499.0	2263.9	13.5	0.0204	0.0850	15.12	62.99	0.240	0.211	0.365	0.576	0.577	83.9	1624	3585
	14	17	13	3	2205.2	1779.7	23.5	0.0425	0.1854	18.08	78.89	0.229	0.252	0.464	0.716	0.544	84.5	1633	3547
	15	10	20	4	2247.2	1852.7	33.8	0.0408	0.1514	12.07	44.80	0.269	0.168	0.249	0.418	0.675	82.3	1633	3547
	16	13	16	3	2692.1	2269.8	23.7	0.0527	0.1990	22.26	84.04	0.265	0.310	0.471	0.781	0.659	82.5	1633	3562
	17	16	21	6	2266.8	1661.2	33.0	0.0510	0.2330	15.44	70.55	0.219	0.215	0.420	0.636	0.512	85.1	1633	3578
	18	18	26	3	2957.8	2202.8	13.2	0.0374	0.1224	28.24	92.41	0.306	0.394	0.488	0.882	0.806	80.4	1633	3547
	19	18	19	3	2761.6	2431.0	30.2	0.0459	0.2041	15.17	67.48	0.225	0.212	0.399	0.610	0.530	84.8	1633	3553
	20	26	24	4	2096.0	1650.9	30.0	0.0510	0.2211	17.03	73.81	0.231	0.237	0.433	0.670	0.548	84.4	1633	3558
	21	27	20	3	2271.6	1840.8	23.2	0.0459	0.1735	19.77	74.74	0.265	0.276	0.419	0.694	0.658	82.5	1633	3558
	22	30	24	3	2127.3	1716.6	24.3	0.0493	0.1820	20.25	74.75	0.271	0.282	0.415	0.697	0.680	82.2	1633	3562
		Mean		4.0	2575.4	1930.4	22.6	0.039	0.156	17.826	70.949	0.249	0.249	0.405	0.653	0.613	83.4	1632	3561
		1 S.D error		1.26	402.22	220.83	6.23	0.009	0.038	4.824	13.028	0.033	0.067	0.070	0.126	0.115	1.82	2.4	13.4
LGL Mode M Sample_Clast 70_178 Density 1030	1	6	34	2	2174.1	1999.6	38.2	0.0544	0.3095	14.24	81.01	0.176	0.199	0.510	0.709	0.389	87.7	1633	3558
	2	26	61	2	2833.1	2570.4	25.4	0.0374	0.2398	14.74	94.49	0.156	0.205	0.610	0.815	0.337	88.9	1633	3570
	3	14	57	1	2310.5	2235.1	44.2	0.0340	0.2721	7.69	61.55	0.125	0.107	0.412	0.519	0.260	90.9	1633	3578
	4	37	22	2	2250.7	2047.5	32.8	0.0272	0.1973	8.29	60.14	0.138	0.116	0.396	0.512	0.292	90.1	1637	3542
	5	20	24	2	2692.8	2467.0	29.5	0.0578	0.2891	19.58	97.92	0.200	0.273	0.598	0.871	0.456	86.2	1637	3553
	6	44	22	3	2715.9	2368.2	28.8	0.0391	0.2874	13.60	99.93	0.136	0.190	0.660	0.850	0.287	90.2	1637	3570
	7	55	40	2	2607.5	2368.3	27.9	0.0340	0.2517	12.20	90.31	0.135	0.170	0.597	0.767	0.285	90.2	1637	3577
	8	12	19	3	2699.2	2387.6	32.1	0.0544	0.2585	16.95	80.55	0.210	0.236	0.485	0.722	0.487	85.6	1633	3562
	9	36	34	2	2752.0	2515.3	28.2	0.0391	0.2925	13.88	103.85	0.134	0.194	0.688	0.882	0.281	90.3	1637	3553
	10	28	9	2	2731.9	2524.6	32.2	0.0425	0.2585	13.22	80.38	0.164	0.184	0.513	0.697	0.359	88.4	1633	3558
	12	51	39	2	2616.9	2382.6	28.5	0.0680	0.3639	23.90	127.89	0.187	0.333	0.794	1.127	0.420	87.0	1633	3551
	13	31	23	2	2742.3	2499.1	27.4	0.0391	0.2755	14.26	100.50	0.142	0.199	0.659	0.858	0.302	89.8	1637	3558
		Mean		2.1	2593.9	2363.8	31.3	0.044	0.275	14.378	89.877	0.159	0.200	0.577	0.777	0.346	88.8	1635	3561

		1 S.D error		0.49	210.97	175.75	5.06	0.011	0.039	4.215	17.989	0.027	0.059	0.112	0.160	0.073	1.71	2.0	10.5
LGL	2			3	2085.5	1810.5	36.4	0.0629	0.2857	17.30	78.57	0.220	0.241	0.467	0.709	0.516	85.0	1633	3570
Mode	3			2	2207.0	2009.0	33.7	0.0578	0.2942	17.17	87.38	0.196	0.239	0.536	0.775	0.447	86.4	1633	3566
Mspot	4			5	2640.7	2095.1	30.5	0.0493	0.2670	16.14	87.41	0.185	0.225	0.544	0.769	0.413	87.1	1633	3577
Sample_Clast	5			2	2685.6	2489.7	34.0	0.0391	0.2585	11.49	75.96	0.151	0.160	0.493	0.653	0.325	89.2	1633	3577
70_178	6			2	2858.5	2626.2	28.7	0.0629	0.3197	21.92	111.40	0.197	0.306	0.683	0.989	0.447	86.4	1633	3558
Density 1030																			
		Mean		2.8	2495.5	2206.1	32.7	0.054	0.285	16.802	88.142	0.190	0.234	0.545	0.779	0.430	86.8	1633	3570
		1 S.D error		1.17	296.76	304.82	2.71	0.009	0.022	3.323	12.507	0.022	0.046	0.075	0.114	0.062	1.37	0.0	7.2
LGL	1	45	34	4	2748.5	2274.5	28.1	0.0510	0.1429	18.13	50.80	0.357	0.253	0.248	0.501	1.019	77.8	1637	3588
Mode	2	17	33	3	2765.7	2205.0	17.8	0.0514	0.1635	28.79	91.68	0.314	0.401	0.478	0.880	0.839	79.9	1637	3565
H	3	42	36	4	2239.0	1780.2	29.1	0.0688	0.2968	23.67	102.13	0.232	0.330	0.598	0.928	0.552	84.4	1637	3571
Sample_Clast	4	28	25	6	2648.5	2026.5	32.2	0.0816	0.3810	25.38	118.49	0.214	0.354	0.710	1.064	0.498	85.4	1632	3566
70_118	5	20	32	7	3068.9	2376.3	33.7	0.1168	0.4002	34.67	118.79	0.292	0.483	0.640	1.124	0.755	81.1	1632	3553
Density	6	17	31	5	2939.3	2437.3	33.2	0.0748	0.3129	22.53	94.25	0.239	0.314	0.547	0.861	0.574	83.9	1633	3566
1420	7	27	34	7	2183.4	1712.9	49.6	0.1270	0.5238	25.61	105.62	0.242	0.357	0.610	0.967	0.585	83.8	1632	3570
	8	42	32	6	2824.5	1778.0	19.1	0.0635	0.1565	33.23	81.89	0.406	0.463	0.369	0.832	1.257	75.5	1632	3585
	9	29	20	8	3232.0	1894.1	19.9	0.0612	0.2154	30.70	108.07	0.284	0.428	0.589	1.017	0.727	81.5	1636	3570
	10	23	26	9	3106.1	2186.1	32.6	0.0839	0.3571	25.73	109.51	0.235	0.359	0.639	0.998	0.562	84.2	1632	3574
	11	34	33	7	3091.1	2008.0	21.5	0.0578	0.1780	26.83	82.63	0.325	0.374	0.424	0.798	0.882	79.4	1632	3574
	12	45	28	7	2582.5	1764.7	28.5	0.0601	0.2347	21.06	82.26	0.256	0.294	0.466	0.760	0.630	83.0	1632	3566
	13	24	22	5	2936.4	2223.2	23.4	0.0737	0.2868	31.54	122.73	0.257	0.440	0.695	1.135	0.633	82.9	1632	3574
	14	12	26	5	2702.0	2001.1	23.8	0.0635	0.2494	26.70	104.88	0.255	0.372	0.596	0.968	0.625	83.1	1632	3553
	15	27	31	4	2451.5	2000.0	29.5	0.0737	0.2404	24.96	81.41	0.307	0.348	0.429	0.777	0.810	80.3	1632	3570
	16	12	46	5	2782.3	1754.9	16.2	0.0363	0.0952	22.38	58.69	0.381	0.312	0.275	0.587	1.133	76.6	1632	3538
	17	16	40	4	3234.5	2500.0	18.2	0.0408	0.1338	22.48	73.71	0.305	0.313	0.390	0.703	0.804	80.4	1632	3566
	18	15	38	4	2613.2	1768.4	15.8	0.0306	0.0930	19.39	58.92	0.329	0.270	0.300	0.571	0.900	79.2	1632	3553
	19	13	40	5	2614.0	1698.6	18.2	0.0431	0.1304	23.67	71.62	0.331	0.330	0.364	0.694	0.906	79.1	1632	3542
	20	38	25	3	3384.8	2863.5	19.2	0.0488	0.2041	25.44	106.40	0.239	0.355	0.617	0.972	0.575	83.9	1632	3566
	21	38	19	3	1978.5	1591.6	25.8	0.0522	0.2109	20.20	81.60	0.248	0.282	0.468	0.750	0.602	83.5	1628	3574
	22	49	30	2	3174.1	2221.0	7.0	0.0283	0.0850	40.46	121.52	0.333	0.564	0.616	1.180	0.916	79.0	1628	3570
	23	49	33	4	2964.0	1850.3	12.0	0.0306	0.0998	25.56	83.36	0.307	0.356	0.440	0.796	0.811	80.3	1632	3557
	24	35	38	4	3347.9	1943.8	9.5	0.0220	0.0840	23.17	88.46	0.262	0.323	0.497	0.820	0.649	82.7	-	-
	25	47	37	3	3708.1	2433.1	7.8	0.0261	0.1032	33.28	131.58	0.253	0.464	0.749	1.213	0.619	83.2	1632	3570
	26	45	28	3	3345.6	2213.1	8.8	0.0374	0.1474	42.36	166.93	0.254	0.591	0.949	1.540	0.622	83.1	1632	3534
		Mean		4.9	2871.8	2057.9	22.3	0.058	0.213	26.842	96.073	0.287	0.374	0.527	0.901	0.749	81.4	1632	3565
		1 S.D error		1.74	397.44	301.86	9.68	0.025	0.111	5.957	25.161	0.049	0.083	0.158	0.223	0.188	2.54	2.2	12.9
ALB_DB	1	54	26	4	2152.0	1463.9	19.4	0.0085	0.0255	4.39	13.16	0.333	0.061	0.067	0.128	0.917	78.9	1629	3596
Mode	2	55	27	4	2593.5	1972.4	21.5	0.0153	0.0374	7.13	17.42	0.409	0.099	0.078	0.177	1.275	75.3	1629	3538

VL	3	52	24	2	2155.2	1815.1	19.6	0.0085	0.0323	4.34	16.48	0.263	0.060	0.092	0.153	0.654	82.6	1617	3377
Sample_Clast	4	40	15	5	3061.1	2613.1	37.2	0.0102	0.0612	2.74	16.45	0.167	0.038	0.105	0.143	0.365	88.2	1590	3558
189.198_54	5	34	16	3	2311.1	1987.8	30.9	0.0051	0.0391	1.65	12.64	0.130	0.023	0.084	0.107	0.273	90.6	1622	3519
Density	6	46	8	6	2693.1	2113.0	34.5	0.0136	0.0340	3.94	9.86	0.400	0.055	0.045	0.100	1.227	75.8	1594	3542
350	7	48	16	4	1988.7	1680.1	43.2	0.0119	0.0391	2.75	9.05	0.304	0.038	0.048	0.086	0.802	80.4	1629	3538
	8	61	45	2	2913.7	2496.2	16.0	0.0119	0.0340	7.45	21.29	0.350	0.104	0.105	0.209	0.989	78.1	1637	3480
	9	63	49	4	2967.4	1965.9	13.3	0.0119	0.0323	8.94	24.26	0.368	0.125	0.116	0.241	1.072	77.2	1624	3422
	10	27	28	2	3576.4	2761.6	8.2	0.0102	0.0204	12.47	24.93	0.500	0.174	0.094	0.268	1.852	71.4	1622	3523
	11	18	27	3	2040.3	1519.1	19.2	0.0153	0.0391	7.97	20.38	0.391	0.111	0.094	0.205	1.183	76.2	1629	3519
	12	12	28	2	3061.6	2576.1	13.7	0.0374	0.0578	27.24	42.09	0.647	0.380	0.110	0.490	3.448	65.9	1637	3411
	13	31	42	4	3259.3	1835.8	9.4	0.0136	0.0323	14.52	34.48	0.421	0.202	0.151	0.353	1.340	74.8	1624	3449
	14	38	36	3	3288.6	1667.1	6.2	0.0119	0.0272	19.30	44.10	0.438	0.269	0.188	0.457	1.434	74.1	1629	3452
	15	43	30	4	3143.8	1674.3	9.1	0.0153	0.0255	16.86	28.10	0.600	0.235	0.084	0.319	2.804	67.6	1618	3465
	16	22	29	5	3661.3	1940.9	9.7	0.0150	0.0250	15.48	25.81	0.600	0.216	0.077	0.293	2.804	67.6	-	-
	17	31	36	7	3338.0	1679.6	14.1	0.0170	0.0323	12.08	22.96	0.526	0.168	0.082	0.250	2.062	70.4	1633	3527
	18	30	38	3	3630.1	2931.6	14.3	0.0153	0.0306	10.69	21.37	0.500	0.149	0.080	0.229	1.852	71.4	1624	3495
	19	37	34	7	3455.5	1757.2	13.7	0.0221	0.0306	16.09	22.27	0.722	0.224	0.045	0.269	4.962	63.4	1629	3538
	20	42	31	3	3268.4	2459.1	12.4	0.0102	0.0238	8.25	19.26	0.429	0.115	0.083	0.198	1.382	74.5	1629	3484
		Mean		3.9	2928.0	2045.5	18.3	0.014	0.034	10.214	22.319	0.425	0.142	0.091	0.234	1.635	75.2	1623	3496
		1 S.D error		1.49	536.39	427.22	10.11	0.006	0.010	6.428	9.183	0.147	0.090	0.033	0.107	1.105	6.75	12.0	54.5

ALB_DB	1	28	31	6	3015.7	1947.3	18.7	0.0204	0.0612	10.90	32.69	0.333	0.152	0.166	0.318	0.917	78.9	1629	3437
Mode	2	29	33	5	2716.6	1840.9	19.0	0.0204	0.0442	10.72	23.22	0.462	0.149	0.094	0.244	1.583	73.0	1629	3422
L	3	27	34	3	2468.8	2016.1	22.1	0.0221	0.0561	10.00	25.40	0.394	0.139	0.117	0.256	1.196	76.0	1624	3416
Sample_Clast	4	32	32	3	2115.9	1530.7	17.1	0.0102	0.0629	5.97	36.81	0.162	0.083	0.236	0.319	0.353	88.5	1629	3437
189.3_16	5	29	27	3	2142.1	1683.7	21.8	0.0255	0.0527	11.69	24.16	0.484	0.163	0.094	0.257	1.734	72.1	1629	3488
Density	6	32	31	5	2820.4	1752.7	15.6	0.0187	0.0425	11.98	27.23	0.440	0.167	0.115	0.282	1.449	74.0	1637	3407
510	7	31	31	5	2581.3	1542.3	16.0	0.0170	0.0476	10.60	29.67	0.357	0.148	0.145	0.293	1.020	77.8	1633	3508
	8	30	35	5	2644.3	1494.6	14.5	0.0102	0.0187	7.04	12.90	0.545	0.098	0.044	0.142	2.230	69.6	1633	3515
	9	25	28	4	2763.3	2133.2	21.2	0.0153	0.0510	7.23	24.10	0.300	0.101	0.128	0.229	0.785	80.6	1637	3450
	10	25	26	3	2602.5	1948.3	15.3	0.0102	0.0306	6.67	20.02	0.333	0.093	0.101	0.194	0.917	78.9	1637	3476
	11	51	43	4	3078.0	1726.8	9.9	0.0170	0.0425	17.23	43.07	0.400	0.240	0.196	0.436	1.227	75.8	1637	3426
	12	50	42	3	2818.5	1614.9	8.3	0.0204	0.0374	24.55	45.01	0.545	0.342	0.153	0.496	2.230	69.6	1637	3450
	13	44	38	2	2214.4	1746.5	14.2	0.0085	0.0391	5.97	27.44	0.217	0.083	0.164	0.247	0.508	85.2	1624	3377
	14	52	36	4	2662.6	1724.5	14.2	0.0119	0.0374	8.37	26.31	0.318	0.117	0.136	0.253	0.856	79.7	1629	3469
		Mean		3.9	2617.5	1764.5	16.3	0.016	0.045	10.637	28.431	0.378	0.148	0.135	0.283	1.215	77.1	1632	3448
		1 S.D error		1.10	286.58	185.46	3.97	0.005	0.012	4.851	8.330	0.109	0.068	0.046	0.087	0.554	5.27	4.6	37.9

DB	1	33	32	5	2308.7	1522.7	21.2	0.0187	0.1122	8.82	52.91	0.167	0.123	0.337	0.460	0.365	88.2	1633	3566
Mode	2	26	33	5	2228.2	1598.2	26.5	0.0238	0.1327	9.00	50.16	0.179	0.125	0.314	0.440	0.399	87.5	1633	3573
M	3	48	34	4	2526.9	1756.6	17.3	0.0255	0.0952	14.73	55.00	0.268	0.205	0.307	0.512	0.670	82.4	1633	3588
Sample_Clast	4	33	23	5	2212.1	1504.4	23.6	0.0391	0.1820	16.60	77.28	0.215	0.231	0.463	0.694	0.500	85.3	1629	3570
189.3_60	5	22	16	6	3010.5	2034.6	20.5	0.0221	0.1633	10.78	79.68	0.135	0.150	0.527	0.677	0.285	90.2	1637	3551
Density	6	27	38	6	2470.7	1557.4	21.9	0.0272	0.2058	12.42	93.98	0.132	0.173	0.624	0.797	0.278	90.4	1633	3562
1010	7	20	42	8	3503.9	2198.0	20.4	0.0255	0.1395	12.49	68.31	0.183	0.174	0.426	0.600	0.408	87.2	1633	3573
	8	12	33	3	2077.7	1606.9	21.2	0.0289	0.1276	13.61	60.07	0.226	0.190	0.354	0.544	0.535	84.7	1633	3551

	9	27	16	3	2235.5	1831.3	24.7	0.0306	0.1684	12.37	68.07	0.182	0.172	0.425	0.598	0.405	87.3	1633	3551
	10	45	50	4	2635.6	1830.0	16.6	0.0221	0.0935	13.35	56.49	0.236	0.186	0.329	0.515	0.566	84.1	1637	3553
	11	28	36	5	2984.8	2070.0	18.2	0.0289	0.1054	15.86	57.85	0.274	0.221	0.320	0.541	0.692	82.0	1629	3562
	12	39	36	4	3828.4	2768.4	12.6	0.0238	0.1378	18.92	109.55	0.173	0.264	0.692	0.956	0.381	87.9	1633	3562
	13	31	42	4	3584.6	2509.2	12.4	0.0170	0.1020	13.71	82.27	0.167	0.191	0.524	0.715	0.365	88.2	1633	3566
	14	32	19	7	3735.4	1959.9	13.1	0.0255	0.1327	19.40	100.98	0.192	0.271	0.623	0.893	0.434	86.7	1633	3566
	15	37	36	5	2566.8	1620.7	17.6	0.0204	0.1259	11.58	71.47	0.162	0.161	0.458	0.619	0.353	88.5	1633	3562
	16	31	31	5	2847.9	1665.4	14.1	0.0085	0.0833	6.03	59.10	0.102	0.084	0.406	0.490	0.207	92.5	1629	3562
	17	23	23	4	2795.1	1774.8	13.1	0.0238	0.0918	18.21	70.25	0.259	0.254	0.396	0.650	0.640	82.8	1629	3562
	18	38	34	3	3094.5	2267.7	12.1	0.0255	0.1207	21.08	99.79	0.211	0.294	0.601	0.895	0.489	85.5	1637	3573
	19	48	34	4	2752.0	1827.4	14.4	0.0153	0.0850	10.61	58.94	0.180	0.148	0.369	0.517	0.401	87.4	1629	3573
		Mean		4.7	2810.5	1889.7	18.0	0.024	0.127	13.662	72.219	0.192	0.190	0.447	0.638	0.441	86.8	1633	3565
		1 S.D error		1.29	524.66	338.36	4.41	0.006	0.033	3.847	17.440	0.045	0.054	0.116	0.150	0.130	2.72	2.6	9.2
DB	2			4	3288.7	2479.4	16.5	0.0170	0.1633	10.32	99.12	0.104	0.144	0.679	0.823	0.212	92.3	1633	3573
Mode	3			2	3035.4	2670.6	18.3	0.0272	0.1684	14.88	92.15	0.162	0.208	0.590	0.798	0.351	88.6	1637	3558
Hspot	4			4	3028.9	2357.3	19.9	0.0153	0.1871	7.71	94.24	0.082	0.107	0.662	0.770	0.162	93.9	1637	3547
Sample_Clast	6			4	3207.3	2304.1	14.8	0.0204	0.1463	13.82	99.10	0.139	0.193	0.652	0.845	0.295	90.0	1633	3573
189.3_74	7			5	3250.4	2146.8	15.1	0.0204	0.1395	13.51	92.37	0.146	0.188	0.603	0.791	0.312	89.5	1633	3566
Density	8			5	3252.4	2166.5	15.3	0.0391	0.1361	25.48	88.67	0.287	0.355	0.481	0.836	0.738	81.3	1629	3573
1280	9			4	2790.0	1927.5	15.5	0.0187	0.1395	12.10	90.24	0.134	0.169	0.598	0.766	0.282	90.3	1637	3558
	10			3	2227.0	1872.9	28.2	0.0238	0.1922	8.43	68.05	0.124	0.117	0.456	0.574	0.258	91.0	1633	3558
	11			4	3152.9	2237.9	14.6	0.0136	0.1190	9.33	81.66	0.114	0.130	0.553	0.683	0.235	91.6	1629	3558
		Mean		3.9	3025.9	2240.3	17.6	0.022	0.155	12.841	89.512	0.144	0.179	0.586	0.765	0.316	89.8	1633	3563
		1 S.D error		0.87	318.65	237.37	4.13	0.007	0.023	5.058	9.100	0.055	0.071	0.073	0.082	0.158	3.36	2.9	8.6
DB	1			1	2807.2	2682.8	26.8	0.1735	0.3707	64.75	138.35	0.468	0.903	0.555	1.458	1.626	72.8	1629	3573
Mode	2			3	2881.8	2658.4	44.8	0.2228	0.4864	49.78	108.68	0.458	0.694	0.445	1.139	1.561	73.2	1633	3585
VHspot	3			2	2329.8	2122.3	32.1	0.2619	0.4881	81.52	151.92	0.537	1.136	0.529	1.665	2.150	70.0	1633	3578
Sample_Clast	4			3	2705.6	2500.6	48.8	0.1905	0.4133	39.05	84.73	0.461	0.544	0.345	0.889	1.579	73.1	1633	3585
189.3_46	5			5	2169.6	1773.3	42.1	0.2381	0.5000	56.62	118.89	0.476	0.789	0.470	1.259	1.681	72.4	1633	3587
Density	6			1	2128.2	2016.7	29.9	0.2058	0.4082	68.84	136.54	0.504	0.960	0.510	1.469	1.884	71.3	1633	3551
1770	7			2	2155.2	2008.9	45.6	0.2296	0.3793	50.39	83.24	0.605	0.702	0.245	0.947	2.869	67.4	1629	3588
	8			3	1921.5	1707.5	46.7	0.1718	0.3861	36.77	82.63	0.445	0.513	0.347	0.859	1.479	73.7	1633	3453
	9			2	2176.0	2059.3	57.1	0.1973	0.4456	34.53	78.00	0.443	0.481	0.328	0.810	1.466	73.8	1629	3592
	10			2	2071.6	1902.3	39.4	0.2500	0.4481	63.49	113.79	0.558	0.885	0.377	1.262	2.348	69.1	1629	3577
		Mean		2.4	2334.7	2143.2	41.3	0.214	0.433	54.573	109.676	0.495	0.761	0.415	1.176	1.864	71.7	1631	3567
		1 S.D error		1.11	320.54	333.25	8.92	0.030	0.046	14.549	25.472	0.052	0.203	0.096	0.281	0.435	2.07	2.0	39.5
DB	1	42	29	2	2813.5	2464.2	19.1	0.1446	0.2500	75.76	130.99	0.578	1.056	0.413	1.469	2.558	68.4	1629	3573
Mode	2	30	33	3	2754.9	2306.9	22.3	0.1224	0.2398	54.83	107.42	0.510	0.764	0.396	1.160	1.932	71.0	1629	3581
VH	3	18	41	2	2727.0	2435.9	22.9	0.1344	0.2517	58.69	109.90	0.534	0.818	0.385	1.203	2.128	70.1	1629	3577

Sample_Clast	4	52	38	2	2836.4	2579.9	26.0	0.1497	0.2874	57.60	110.58	0.521	0.803	0.398	1.201	2.016	70.6	1629	3577
189.3_46	5	49	39	2	2754.9	2306.9	14.9	0.1429	0.2823	96.02	189.69	0.506	1.339	0.705	2.044	1.899	71.2	1629	3577
Density	7	11	31	2	2926.3	2448.1	13.9	0.1139	0.1786	81.70	128.11	0.638	1.139	0.344	1.484	3.307	66.2	1624	3577
1770	8	7	54	2	2761.7	2512.5	26.8	0.2126	0.3844	79.47	143.69	0.553	1.108	0.481	1.589	2.302	69.3	1629	3577
	9	41	30	3	2858.0	2408.5	22.2	0.1480	0.2653	66.53	119.25	0.558	0.928	0.395	1.323	2.348	69.1	1633	3573
	10	42	26	2	2832.5	2485.0	19.2	0.1395	0.2704	72.71	140.95	0.516	1.014	0.513	1.527	1.976	70.8	1629	3577
		Mean		2.2	2807.2	2438.7	20.8	0.145	0.268	71.479	131.175	0.546	0.997	0.448	1.444	2.274	69.6	1629	3577
		1 S.D																	
		error		0.42	59.88	84.27	4.20	0.026	0.051	12.687	24.195	0.040	0.177	0.103	0.259	0.420	1.50	2.1	2.3

Band_W	1	27	14	2	1998.4	1664.5	20.0	0.0119	0.0442	5.96	22.14	0.269	0.083	0.123	0.206	0.674	82.3	1629	3573
Mode	2	23	37	3	2363.3	1773.1	16.9	0.0272	0.1088	16.05	64.21	0.250	0.224	0.367	0.591	0.610	83.3	1624	3562
Interior	3	22	38	2	1786.4	1434.9	19.0	0.0238	0.1293	12.55	68.17	0.184	0.175	0.425	0.600	0.412	87.2	1629	3523
Sample_Clast	4	29	32	3	2221.1	1825.9	25.3	0.0136	0.0714	5.37	28.22	0.190	0.075	0.174	0.249	0.430	86.8	1633	3553
290_I162	5	49	16	3	2273.1	1474.5	12.5	0.0119	0.0272	9.50	21.72	0.438	0.132	0.092	0.225	1.434	74.1	1624	3553
Density	6	47	25	5	2746.9	1591.5	14.4	0.0170	0.0425	11.79	29.46	0.400	0.164	0.134	0.298	1.227	75.8	1624	3553
n/a	7	52	19	1	1813.0	1627.9	18.0	0.0119	0.0544	6.61	30.21	0.219	0.092	0.180	0.272	0.512	85.1	1637	3469
	8	48	24	2	1992.1	1590.5	16.6	0.0170	0.0408	10.24	24.58	0.417	0.143	0.109	0.251	1.316	75.0	1637	3566
	9	39	25	3	1942.9	1645.1	33.6	0.0119	0.0510	3.54	15.19	0.233	0.049	0.089	0.138	0.556	84.3	1629	3596
	10	41	37	3	2479.2	2073.0	24.6	0.0170	0.0561	6.91	22.79	0.303	0.096	0.121	0.217	0.797	80.5	1633	3551
	11	11	15	2	1969.0	1501.2	14.3	0.0119	0.0459	8.35	32.21	0.259	0.116	0.182	0.298	0.640	82.8	1629	3519
	12	19	62	2	2139.6	1676.5	14.4	0.0170	0.0442	11.81	30.70	0.385	0.165	0.143	0.308	1.149	76.5	1624	3588
	13	44	32	2	1980.8	1714.5	25.0	0.0255	0.0425	10.19	16.98	0.600	0.142	0.051	0.193	2.804	67.6	1629	3592
	14	40	32	3	2245.7	1922.8	31.0	0.0153	0.0782	4.94	25.25	0.196	0.069	0.155	0.224	0.444	86.5	1629	3588
		Mean		2.6	2139.4	1679.7	20.4	0.017	0.060	8.843	30.845	0.310	0.123	0.167	0.291	0.929	80.5	1629	3556
		1 S.D																	
		error		0.90	258.57	168.79	6.29	0.005	0.027	3.381	15.236	0.117	0.047	0.101	0.132	0.620	5.66	4.3	33.2

Band_G	1	25	18	2	2472.3	2037.1	15.3	0.0017	0.0408	1.11	26.63	0.042	0.015	0.196	0.211	0.079	96.8	1629	3573
Mode	2	32	50	2	3097.4	2670.8	15.6	0.0119	0.0187	7.61	11.97	0.636	0.106	0.032	0.138	3.286	66.3	1624	3596
Interior	3	26	47	2	2147.8	1702.9	15.0	0.0051	0.0136	3.40	9.08	0.375	0.047	0.043	0.090	1.103	76.9	1618	3626
Sample_Clast	4	34	51	2	2876.8	2481.1	16.8	0.0119	0.0306	7.06	18.16	0.389	0.098	0.084	0.183	1.171	76.3	1633	3534
290_I162	5	33	50	4	2872.4	2177.8	19.2	0.0170	0.0374	8.86	19.48	0.455	0.123	0.080	0.204	1.538	73.3	1629	3588
Density	6	21	11	2	3062.8	2649.7	16.1	0.0068	0.0340	4.21	21.07	0.200	0.059	0.129	0.187	0.457	86.2	1633	3585
n/a	7	23	11	2	2208.6	1804.1	16.5	0.0068	0.0527	4.13	31.98	0.129	0.058	0.213	0.271	0.270	90.6	1633	3407
	8	43	10	2	2216.0	1944.4	24.5	0.0119	0.0493	4.85	20.08	0.241	0.068	0.116	0.184	0.582	83.8	1629	3431
		Mean		2.3	2619.3	2183.5	17.4	0.009	0.035	5.154	19.806	0.308	0.072	0.112	0.183	1.061	81.3	1629	3543
		1 S.D																	
		error		0.66	375.97	353.01	2.97	0.005	0.013	2.368	6.854	0.180	0.033	0.062	0.049	0.960	9.29	4.9	75.4

Band_W	1	32	38	3	2742.6	1565.1	8.5	0.0170	0.0425	20.02	50.04	0.400	0.279	0.227	0.507	1.227	75.8	1624	3442
Mode	2	27	31	2	2225.9	1853.4	17.9	0.0442	0.1446	24.70	80.80	0.306	0.344	0.427	0.771	0.807	80.4	1633	3383
Exterior	3	25	28	1	1906.7	1699.6	16.1	0.0272	0.0374	16.90	23.24	0.727	0.236	0.046	0.282	5.096	63.2	1633	3435
Sample_Clast	4	47	40	2	2286.9	1891.5	16.9	0.0289	0.1156	17.14	68.56	0.250	0.239	0.392	0.631	0.610	83.3	1629	3411
290_X	5	17	17	2	1998.7	1550.2	14.9	0.0306	0.1190	20.59	80.06	0.257	0.287	0.453	0.740	0.633	82.9	1629	3387

Density	6	15	15	3	2558.9	1974.8	17.1	0.0306	0.1003	17.87	58.59	0.305	0.249	0.310	0.559	0.805	80.4	1629	3364
n/a	7	13	17	2	2808.1	2460.3	19.2	0.0238	0.1378	12.42	71.89	0.173	0.173	0.454	0.627	0.381	87.9	1629	3381
	8	11	22	3	2505.0	2079.0	23.5	0.1310	0.2636	55.81	112.29	0.497	0.778	0.425	1.203	1.829	71.6	1633	3364
	9	10	16	2	2240.8	1824.6	16.0	0.0170	0.0442	10.61	27.59	0.385	0.148	0.129	0.277	1.149	76.5	1637	3384
	10	39	28	2	2127.9	1753.7	17.8	0.0765	0.1310	42.94	73.53	0.584	0.599	0.229	0.827	2.619	68.2	1637	3377
	11	31	34	3	2200.0	1641.7	17.9	0.0170	0.0884	9.49	49.35	0.192	0.132	0.304	0.437	0.435	86.7	1633	3306
	12	30	31	2	2000.5	1703.8	22.5	0.0170	0.0561	7.57	24.97	0.303	0.105	0.132	0.238	0.797	80.5	1624	3566
	13	27	32	3	2575.0	1939.7	15.7	0.0119	0.0221	7.56	14.04	0.538	0.105	0.049	0.154	2.167	69.9	1624	3488
	14	44	47	2	2774.1	2587.8	35.8	0.0289	0.0612	8.08	17.10	0.472	0.113	0.068	0.181	1.654	72.6	1633	3330
		Mean		2.3	2353.7	1894.7	18.6	0.036	0.097	19.406	53.718	0.385	0.271	0.260	0.531	1.443	77.1	1631	3401
		1 S.D																	
		error		0.59	293.64	297.01	5.85	0.031	0.061	13.511	28.298	0.155	0.188	0.150	0.286	1.204	7.03	4.2	63.4
Band_G	1	32	28	5	3069.2	1799.0	13.1	0.0340	0.0493	25.91	37.57	0.690	0.361	0.086	0.447	4.211	64.4	1624	3470
Mode	2	31	30	3	2870.4	1822.9	9.5	0.0221	0.0595	23.15	62.33	0.371	0.323	0.297	0.620	1.086	77.1	1629	3407
Exterior	3	33	28	5	3272.5	1937.4	12.5	0.0323	0.0714	25.87	57.20	0.452	0.361	0.237	0.597	1.525	73.4	1629	3465
Sample_Clast	4	35	29	4	3148.0	1830.0	10.1	0.0187	0.0442	18.48	43.69	0.423	0.258	0.191	0.448	1.351	74.7	1633	3431
290_X	5	35	31	5	3442.2	1858.7	10.5	0.0221	0.0289	21.00	27.46	0.765	0.293	0.047	0.339	6.280	62.0	1624	3566
Density	6	37	33	4	2659.2	1982.7	19.7	0.0289	0.0374	14.66	18.98	0.773	0.204	0.031	0.235	6.589	61.8	1633	3469
n/a	7	33	31	5	3020.3	1932.7	15.3	0.0187	0.0323	12.20	21.08	0.579	0.170	0.066	0.236	2.564	68.3	1633	3562
	8	29	30	6	2268.9	1539.0	27.4	0.0306	0.0867	11.17	31.64	0.353	0.156	0.155	0.311	1.002	78.0	1629	3562
	9	28	28	5	2614.3	1977.8	26.2	0.0442	0.1173	16.88	44.80	0.377	0.235	0.212	0.447	1.112	76.8	1629	3504
	10	29	27	5	2294.5	1694.4	27.8	0.0408	0.1156	14.69	41.62	0.353	0.205	0.204	0.409	1.002	78.0	1637	3442
	11	23	24	3	2196.1	1740.4	21.9	0.0323	0.1037	14.72	47.26	0.311	0.205	0.247	0.453	0.829	80.1	1633	3403
	12	30	38	3	2275.7	1700.4	17.4	0.0204	0.0527	11.74	30.32	0.387	0.164	0.141	0.304	1.162	76.4	1629	3446
	13	29	37	5	2858.8	1903.5	17.4	0.0255	0.0408	14.62	23.39	0.625	0.204	0.065	0.269	3.125	66.7	1637	3562
	14	29	35	3	2946.9	2045.6	11.1	0.0374	0.0629	33.71	56.69	0.595	0.470	0.172	0.642	2.740	67.8	1633	3454
	15	27	34	4	3051.7	2093.4	13.9	0.0306	0.0850	21.99	61.09	0.360	0.307	0.297	0.603	1.033	77.6	1633	3392
	16	32	59	2	2271.7	1921.9	19.1	0.0102	0.0680	5.35	35.68	0.150	0.075	0.232	0.306	0.322	89.3	1629	3323
	17	25	44	3	2249.9	1704.8	18.3	0.0289	0.0918	15.75	50.04	0.315	0.220	0.261	0.480	0.842	79.9	1629	3469
	18	24	42	2	2691.2	2040.7	10.2	0.0170	0.0748	16.59	72.99	0.227	0.231	0.430	0.661	0.538	84.6	1633	3585
		Mean		4.0	2733.4	1862.5	16.8	0.027	0.068	17.694	42.434	0.450	0.247	0.187	0.434	2.073	74.3	1631	3473
		1 S.D																	
		error		1.15	388.47	142.93	5.86	0.009	0.027	6.470	15.117	0.175	0.090	0.101	0.140	1.824	7.43	3.5	70.0
RP	1	40	35	4	3026.3	1973.4	12.7	0.0493	0.1514	38.93	119.56	0.326	0.543	0.613	1.156	0.886	79.3	1633	3573
Mode	2	30	32	3	2007.8	1778.4	43.6	0.1054	0.3537	24.18	81.14	0.298	0.337	0.433	0.771	0.778	80.7	1633	3570
-	3	29	31	6	2273.0	1772.5	40.0	0.1054	0.4014	26.38	100.45	0.263	0.368	0.564	0.932	0.652	82.6	1629	3562
Sample_Clast	4	40	29	3	2639.8	2291.3	28.7	0.0697	0.1905	24.29	66.39	0.366	0.339	0.319	0.658	1.060	77.4	1633	3566
AUS_13	5	23	43	2	1976.3	1648.3	20.3	0.0238	0.1429	11.71	70.31	0.167	0.163	0.448	0.611	0.365	88.2	1633	3566
Density	6	48	49	3	2398.8	2008.4	25.6	0.0493	0.1190	19.25	46.46	0.414	0.268	0.206	0.474	1.303	75.1	1637	3592
560	7	50	51	3	2128.7	1778.9	28.6	0.0561	0.1871	19.62	65.45	0.300	0.274	0.349	0.622	0.785	80.7	1629	3566
	8	47	50	3	2411.3	1978.1	23.1	0.0459	0.1429	19.88	61.90	0.321	0.277	0.319	0.597	0.868	79.6	1633	3573
	9	17	13	3	2130.2	1619.9	19.6	0.0153	0.0306	7.81	15.62	0.500	0.109	0.059	0.168	1.852	71.4	1622	3532
	10	19	21	4	1999.0	1532.2	28.6	0.0510	0.1820	17.86	63.72	0.280	0.249	0.349	0.598	0.713	81.7	1633	3588
	11	24	48	2	2880.6	2503.6	17.7	0.0680	0.2517	38.45	142.34	0.270	0.536	0.791	1.327	0.678	82.2	1633	3588
	12	22	51	2	1826.7	1433.3	16.9	0.0561	0.1888	33.10	111.41	0.297	0.462	0.596	1.057	0.775	80.8	1633	3570
	13	18	51	3	2030.5	1581.5	22.3	0.0272	0.0765	12.21	34.35	0.356	0.170	0.168	0.338	1.013	77.9	1629	3577

	14	11	15	2	1928.5	1632.5	22.5	0.0374	0.1310	16.61	58.16	0.285	0.232	0.316	0.548	0.732	81.4	1629	3531
	15	27	11	3	2044.9	1635.6	24.4	0.0289	0.0765	11.83	31.31	0.378	0.165	0.148	0.313	1.116	76.8	1624	3566
		Mean		3.1	2246.8	1811.2	25.0	0.053	0.175	21.474	71.237	0.321	0.299	0.379	0.678	0.905	79.7	1631	3568
		1 S.D error		1.00	346.33	283.54	7.95	0.026	0.096	9.224	33.655	0.074	0.129	0.193	0.312	0.333	3.70	3.8	16.8
RP	1	26	23	6	2904.2	1729.9	17.0	0.0136	0.0612	7.99	35.93	0.222	0.111	0.213	0.325	0.522	84.9	1629	3562
Mode	2	24	22	5	3013.6	2061.2	17.5	0.0153	0.0680	8.74	38.86	0.225	0.122	0.230	0.352	0.531	84.7	1629	3558
-	3	24	31	5	2198.1	1352.6	19.7	0.0102	0.0714	5.17	36.22	0.143	0.072	0.237	0.309	0.304	89.7	1622	3562
Sample_Clast	4	31	31	4	2218.4	1549.0	19.9	0.0340	0.1088	17.07	54.62	0.313	0.238	0.286	0.524	0.833	80.0	1633	3551
AUS_15	5	26	29	4	2135.9	1528.6	22.0	0.0323	0.0833	14.71	37.94	0.388	0.205	0.176	0.381	1.165	76.3	1629	3431
Density	6	16	35	5	2735.1	1798.9	17.8	0.0340	0.1259	19.10	70.72	0.270	0.266	0.393	0.659	0.677	82.2	1637	3562
550	7	14	36	5	2764.4	1866.8	18.6	0.0357	0.1241	19.23	66.84	0.288	0.268	0.362	0.630	0.740	81.3	1633	3570
	8	13	28	4	2565.8	1829.3	18.1	0.0221	0.0595	12.21	32.87	0.371	0.170	0.157	0.327	1.086	77.1	1633	3570
	9	13	39	6	2700.8	1683.7	19.7	0.0272	0.1259	13.83	64.03	0.216	0.193	0.383	0.576	0.504	85.3	1633	3562
	10	12	38	5	2729.8	1836.8	18.7	0.0323	0.1310	17.31	70.19	0.247	0.241	0.403	0.644	0.599	83.5	1633	3588
	11	42	45	3	2531.5	2081.0	22.2	0.0238	0.1037	10.72	46.72	0.230	0.149	0.275	0.424	0.545	84.5	1637	3585
	12	45	44	4	2916.0	2222.4	19.2	0.0289	0.1088	15.03	56.60	0.266	0.210	0.317	0.526	0.662	82.5	1624	3562
	13	47	45	9	2907.7	1557.2	22.2	0.0340	0.1207	15.31	54.34	0.282	0.213	0.297	0.511	0.718	81.6	1629	3588
	14	48	43	4	2731.3	2056.8	19.8	0.0272	0.1224	13.76	61.92	0.222	0.192	0.367	0.559	0.522	84.9	1633	3577
	15	50	48	3	3201.1	1591.3	6.2	0.0238	0.0493	38.31	79.36	0.483	0.534	0.309	0.844	1.726	72.1	1622	3581
	16	52	45	3	3282.3	2142.4	8.8	0.0255	0.0680	29.07	77.51	0.375	0.405	0.367	0.773	1.103	76.9	1633	3573
		Mean		4.7	2721.0	1805.5	18.0	0.026	0.096	16.097	55.291	0.284	0.224	0.298	0.523	0.765	81.7	1631	3561
		1 S.D error		1.45	322.94	246.57	4.27	0.008	0.028	7.828	15.157	0.082	0.109	0.076	0.158	0.341	4.23	4.5	35.4
RP																			
Mode	2	56	40	2	3102.3	2194.3	7.3	0.0136	0.0629	18.52	85.67	0.216	0.258	0.512	0.771	0.504	85.3	1633	3553
-	4	19	50	5	2768.8	2037.9	22.8	0.0442	0.2109	19.38	92.49	0.210	0.270	0.558	0.828	0.484	85.6	1633	3547
Sample_Clast	5	19	56	3	1972.2	1642.0	30.3	0.0527	0.1752	17.40	57.85	0.301	0.243	0.308	0.550	0.788	80.6	1629	3581
J13	6	40	56	2	1847.5	1631.6	30.9	0.0612	0.1820	19.82	58.94	0.336	0.276	0.297	0.574	0.930	78.8	1633	3562
Density n/a																			
		Mean		3.0	2422.7	1876.5	22.8	0.043	0.158	18.782	73.737	0.266	0.262	0.419	0.681	0.677	82.6	1632	3561
		1 S.D error		1.22	528.07	245.97	9.49	0.018	0.056	0.923	15.535	0.054	0.013	0.117	0.121	0.189	2.95	1.7	12.9

Water speciation and clast vesicularity

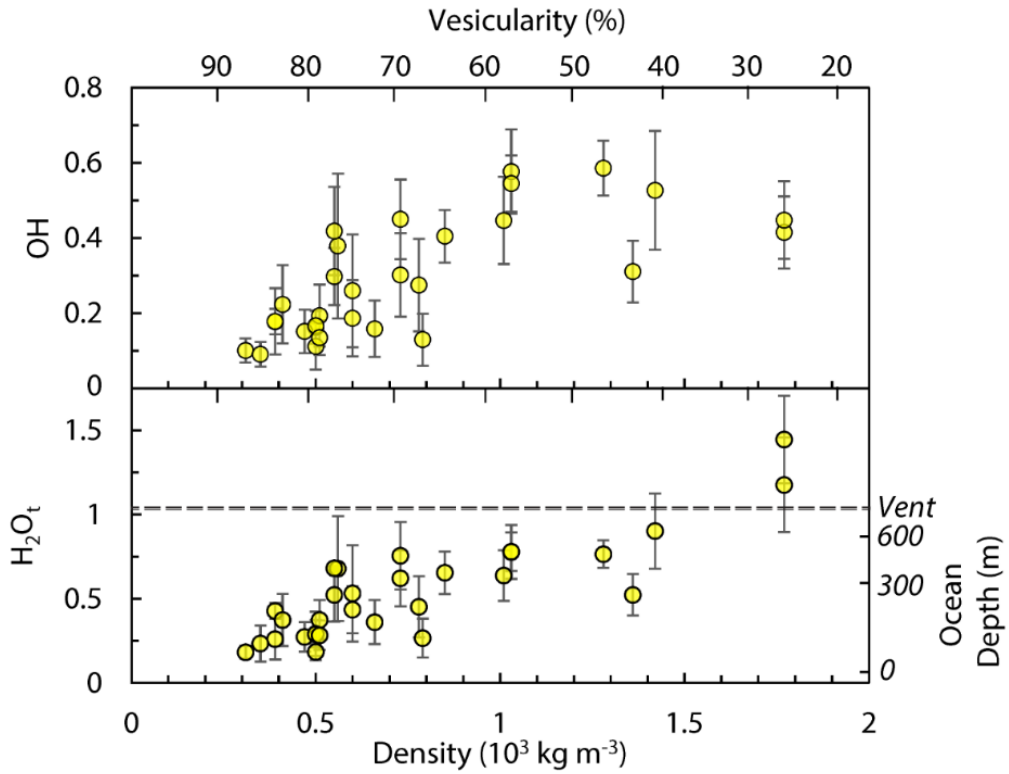

Figure A6. Density (and corresponding vesicularity) vs. OH and H_2O_t concentration for each analyzed clast (error in density is smaller than the symbol size). The ocean depth axis is calculated based on the assumption of hydrostatic pressure and the equilibrium H_2O_t solubility vs. pressure for rhyolite at an eruption temperature of 800°C (Newman and Lowenstern, 2002). Clast density is converted into an equivalent vesicularity using a dense rock equivalent of 2400 kg m^{-3} (Rotella et al., 2015; Carey et al., 2018).

The H_2O_t data (**Figure A6**) suggest that, even before the effects of rehydration are considered, the majority of samples quenched within the water column above the vent. High vesicularity clasts have both low OH and H_2O_t contents. OH contents increases as vesicularity decreases until 60% vesicularity where maximum OH is 0.7 wt. % (**Figure A6**). This is the OH content equivalent to equilibrium solubility when quenching at a vent depth of 900 m at T_g < 500°C. Even before considering the water added by rehydration, H_2O_t contents are still too low for the majority of clasts to be quenched near the vent depth. The trend in H_2O_t vs. density is the opposite to observations common in subaerial rhyolitic deposits where denser, effusively erupted material

tends to be more degassed with little remaining H_2O_t, whereas pumice water contents may be higher due to higher quench pressures resulting from deeper fragmentation within the conduit (Giachetti and Gonnermann, 2013; Bindeman and Lowenstern, 2016). There is also considerable overlap in the H_2O_t range between very texturally diverse units: those with vesicularity >70% and thin bubbles walls <3 µm, and dense dome fragments with over 30 µm between vesicles (Appendices **A7** and **A10**).

Appendix A7: *FTIR vs. microRaman techniques*

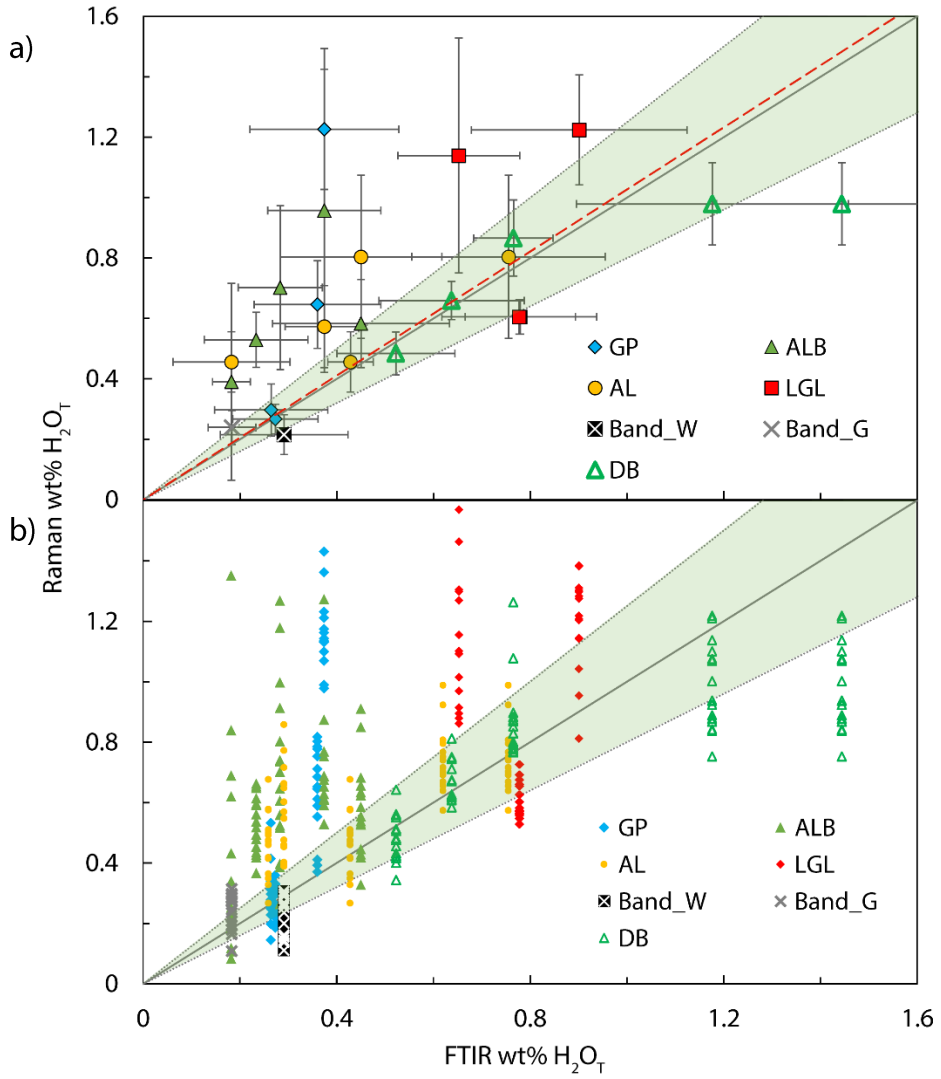

Figure A7i (previous). Comparison of FTIR and µRaman analysis of H_2O_t data for a) clast averages ± 1 standard deviation of error, and b) individual measurements per spot. Green area = 1:1 correlation with an 80% confidence interval. Due to different sample preparation and analytical resolution for FTIR and µRaman, individual clasts may not reflect the (**Figure A7i. cont.**) exact same water content given evidence of a range of rehydration observed within the Havre pumice, despite both samples having the same whole-clast density. No individual clast was analyzed by both FTIR and Raman; instead, each comparison point is between clasts of equivalent density taken from the same unit. Rehydration is also spatially variable, so there is expected to be greater variation in H_2O_t content found with the higher resolution technique (see below). A linear best fit is given for the average data (a) which lies within the confidence interval. The majority of data lies within an 80% confidence interval down to the detection limits (0.05–0.2 wt. %).

FTIR vs. microRaman analytical volume

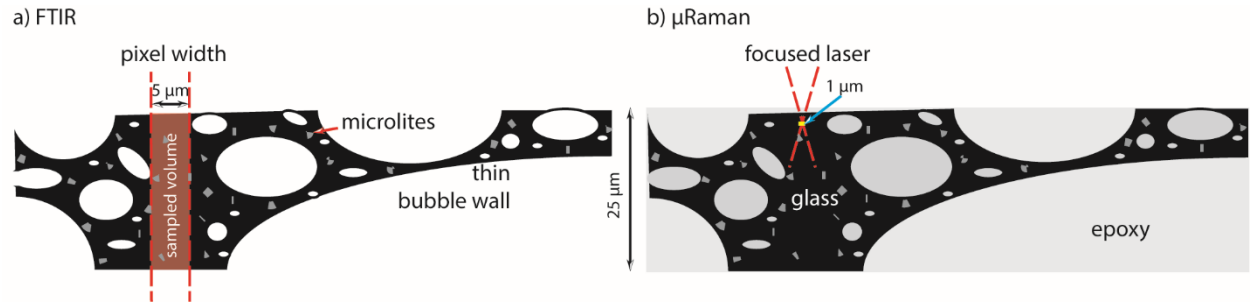

Figure A7ii. A comparison of the FTIR imaging and µRaman technique shows the difference in analytical volume and difficulty in avoiding interstitial vesicles and, particularly in transmission FTIR analysis of the full glass thickness. The µRaman laser is focused slightly below the surface to maximize the output spectra whilst still being sure that there is no microlite or vesicle interference. µRaman is more likely to identify small-scale variation in water content, hence its use for obtaining diffusion profiles. The schematic sample shown would actually correspond to a relatively dense wafer of <40% vesicularity, highlighting the extreme challenges in analyzing highly vesicular pumiceous clasts and the importance of spot choice and analytical method.

MicroRaman spectra and spot analysis

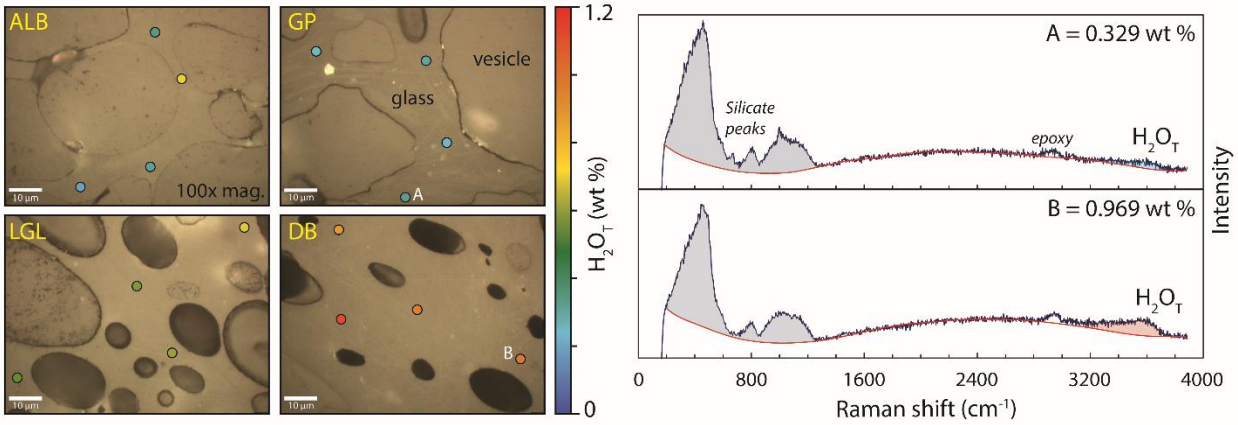

Figure A7iii. Example spots from µRaman analysis of vesicular glass from the Ash-Lapilli-Block unit (ALB), a giant pumice interior (GP_{in}), Lava-G-lapilli (LGL) and a dome fragment (DB) are given in the plot below. Each microscope image highlights four 1 µm µRaman spots taken at 100x magnification, with spot color corresponding to H_2O_t concentration (see color bar). The ALB image illustrates that elevated H_2O_t contents are often measured within a thin bubble walls (here < 2 µm thick). These pervasive, diffusion-induced enrichments would also explain the variability observed in the µRaman spot analysis for GP, ALB and AL (Appendix **A7**). Two raw spectra from spot A (GP_{in}) and B (DB_VH) correspond to H_2O_t wt. % of 0.33 and 0.97. Each spectra contains the low wavenumber alumina-silicate peaks typical of rhyolite, some epoxy peak(s), and the H_2O_t peak between 3180 and 3800 cm^{-1}. A 4^{th} order polynomial baseline is fit to each spectra using SPeCTRa (Appendix **A5**).

Appendix A8: *MicroRaman analysis*

Table A8. Summary of μRaman H_2O_t (wt. %) data for each thin section analyzed. Each thin section has four spots per area (A, B, C and D). Each measurement is made up of at least four SpeCTRa iterations.

Unit		GPX			DB	GPI	ALB			AL			LGL			ALB(DB)		DB			Band_W	Band_G
Density Mode		M	M	M	M	M	L	M	H	L	M	H	L	M	H	VL	L	M	H	VH	-	-
Sample		231_12	290_26	270_13	007_6	290_15	184_8	120_1	184_1	107_2	175_1	229_4	070_24	070_11	070_23	189(4)_26	189(4)_2	189(4)_15	189(4)_1	189(4)_21	290I_18	290I_18
A	1	1.21	0.82	0.28	0.48	0.25	0.62	0.69	0.43	0.68	0.40	1.77	1.27	0.53	1.30	0.66	0.52	0.67	0.78	0.89	0.29	0.24
	2	1.13	0.75	0.20	0.51	0.33	0.31	0.75	0.66	0.51	0.55	0.64	0.88	0.56	1.38	0.61	1.18	0.67	0.77	1.22	0.16	0.28
	3	1.13	0.59	0.30	0.56	0.26	0.25	0.77	0.55	0.58	0.48	0.67	1.02	0.55	1.28	0.59	0.56	0.61	0.78	0.84	0.20	0.27
	4	1.36	0.80	0.34	0.55	0.26	0.19	0.61	0.62	0.48	0.39	0.72	0.91	0.56	1.63	0.45	0.70	0.74	0.80	0.84	0.14	0.30
B	1	0.99	0.61	0.15	0.56	0.23	1.35	0.61	0.85	0.35	0.45	0.77	1.76	0.57	1.31	0.65	0.26	0.71	0.85	0.75	0.31	0.19
	2	0.98	0.71	0.23	0.40	0.23	0.43	0.69	0.54	0.36	0.55	0.67	0.97	0.63	0.95	0.52	0.40	0.75	0.77	0.94	0.11	0.20
	3	1.07	0.37	0.31	0.48	0.25	0.34	0.53	0.53	0.33	0.46	0.69	0.10	0.66	1.14	0.49	0.39	0.63	0.83	0.94	0.30	0.31
	4	1.14	0.78	0.25	0.42	0.25	0.69	0.65	0.42	0.27	0.66	0.57	1.46	0.57	1.22	0.56	0.52	0.62	0.90	0.87	0.26	0.16
C	1	1.43	0.78	0.26	0.51	0.19	0.11	2.31	0.45	0.47	0.77	0.75	1.30	0.58	1.28	0.44	0.91	0.81	0.88	0.92	0.24	0.29
	2	1.14	0.79	0.30	0.48	0.20	0.84	2.03	0.53	0.58	0.65	0.80	1.30	0.57	0.81	0.43	0.65	0.58	0.79	0.88	0.16	0.11
	3	1.16	0.65	0.31	0.46	0.22	0.12	1.64	0.68	0.42	0.40	0.74	0.90	0.60	1.21	0.48	0.61	0.61	0.87	1.08	0.14	0.18
	4	1.23	0.55	0.25	0.42	0.30	0.23	1.27	0.33	0.50	0.72	0.66	1.16	0.56	1.14	0.37	0.74	0.62	0.80	1.00	0.15	0.21
D	1	1.17	0.39	0.53	0.34	0.31	0.28	0.87	0.63	0.41	0.66	0.92	1.57	0.73	1.20	0.60	1.27	0.61	0.87	1.07	0.16	0.27
	2	1.68	0.69	0.41	0.64	0.33	0.19	0.59	0.62	0.46	0.57	0.70	1.68	0.65	1.38	0.54	0.80	0.62	1.08	1.21	0.25	0.28
	3	1.64	0.41	0.35	0.43	0.32	0.08	0.63	0.59	0.49	0.60	0.81	0.86	0.68	1.30	0.65	1.00	0.67	1.26	1.10	0.27	0.29
	4	1.10	0.65	0.28	0.51	0.36	0.22	0.68	0.91	0.42	0.86	0.99	1.09	0.69	1.04	0.42	0.74	0.61	0.83	1.14	0.31	0.25

Averages and error of one standard deviation are given for each area (4) and for each thin section (16). Data plotted in Appendix **A7**.

Unit	GPX			DB	GPI	ALB			AL			LGL			ALB (DB)		DB			Band_W	Band_G
Density Mode	M	M	M	M	M	L	M	H	L	M	H	L	M	H	VL	L	M	H	VH	-	-
Sample	231_12	290_26	270_13	007_6	290_15	184_8	120_1	184_1	107_2	175_1	229_4	070_24	070_11	070_23	189(4)_26	189(4)_2	189(4)_15	189(4)_1	189(4)_21	290I_18	290I_18
A Average (4)	1.21	0.74	0.28	0.52	0.28	0.34	0.71	0.57	0.56	0.45	0.95	1.02	0.55	1.40	0.58	0.74	0.67	0.78	0.95	0.20	0.27
± 1 SD error	*0.09*	*0.05*	*0.03*	*0.03*	*0.17*	*0.06*	*0.09*	*0.08*	*0.06*	*0.48*	*0.00*	0.15	0.01	0.14	*0.26*	*0.05*	*0.01*	*0.16*	*0.06*	*0.02*	*0.02*
B Average (4)	1.04	0.62	0.23	0.47	0.24	0.70	0.62	0.58	0.33	0.53	0.68	1.07	0.61	1.16	0.56	0.39	0.68	0.84	0.87	0.24	0.22
± 1 SD error	*0.16*	*0.06*	*0.06*	*0.01*	*0.40*	*0.06*	*0.16*	*0.04*	*0.08*	*0.07*	*0.00*	0.63	0.04	0.13	*0.09*	*0.05*	*0.05*	*0.08*	*0.08*	*0.06*	*0.058*
C Average (4)	1.24	0.69	0.28	0.46	0.22	0.32	1.81	0.50	0.49	0.63	0.74	1.16	0.58	1.11	0.43	0.73	0.66	0.84	0.97	0.17	0.20
± 1 SD error	*0.10*	*0.02*	*0.03*	*0.04*	*0.30*	*0.39*	*0.13*	*0.06*	*0.14*	*0.05*	*0.00*	0.17	0.02	0.18	*0.12*	*0.09*	*0.04*	*0.08*	*0.04*	*0.07*	*0.067*
D Average (4)	1.40	0.54	0.39	0.48	0.33	0.19	0.69	0.69	0.45	0.67	0.86	1.30	0.69	1.23	0.55	0.95	0.63	1.01	1.13	0.25	0.27
± 1 SD error	*0.13*	*0.09*	*0.11*	*0.02*	*0.07*	*0.11*	*0.13*	*0.03*	*0.11*	*0.11*	*0.00*	0.34	0.03	0.13	*0.21*	*0.03*	*0.17*	*0.05*	*0.05*	*0.02*	*0.016*
Average (16)	**1.22**	**0.65**	**0.30**	**0.48**	**0.27**	**0.39**	**0.96**	**0.58**	**0.46**	**0.57**	**0.80**	**1.14**	**0.61**	**1.22**	**0.53**	**0.70**	**0.66**	**0.87**	**0.98**	**0.22**	**0.24**
± 1 SD error	*0.20*	*0.14*	*0.09*	*0.07*	*0.05*	*0.33*	*0.54*	*0.15*	*0.10*	*0.14*	*0.27*	0.39	0.06	0.18	*0.09*	*0.27*	*0.06*	*0.13*	*0.14*	*0.07*	*0.06*

Appendix A9: *Examining potential CO_2 effect on H_2O solubility*

Although Havre melt inclusions contain <150 ppm CO_2 and matrix glasses contain no CO_2 above FTIR detection limits, we consider here the potential for undetected CO_2 to affect H_2O solubility, hence calculated quench pressures. FTIR detection limits are inversely proportional to glass thickness and, for CO_2, are calculated using the Beer-Lambert law (Eq. **A11**) based on a minimum detectable absorbance of $A = 0.01$ and using a molar absorptivity coefficient of 1214 L mol^{-1} cm^{-1} (Behrens et al., 2004). For the thickness of analyzed Havre glasses (Appendix **A6**), CO_2 detection limits are ~30–100 ppm (**Figure A9ia**).

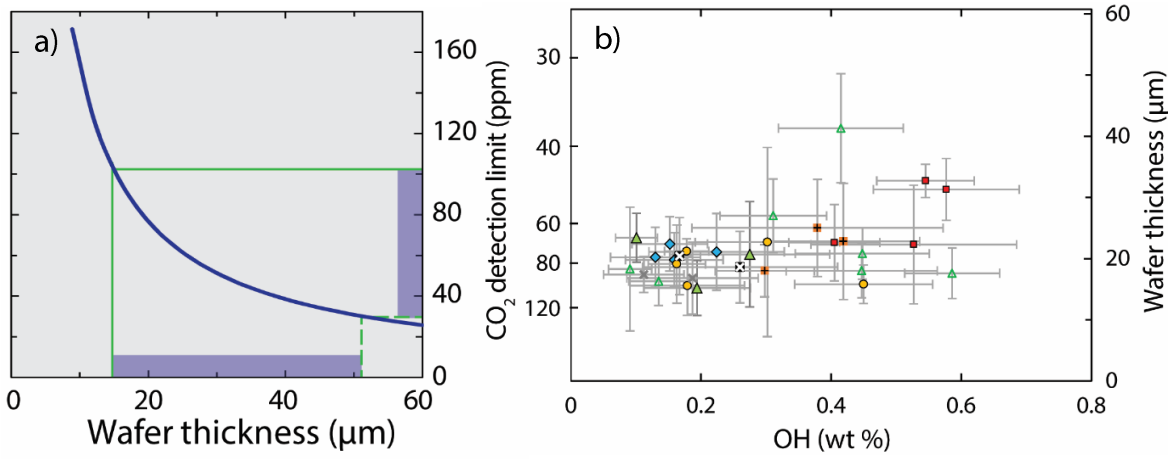

Figure A9i. Measured wafer thickness vs. OH content (wt. %) and the CO_2 detection limits that correspond to the range of Havre glass wafer thicknesses.

Wafer thickness increases somewhat in denser samples where interstitial vesicles within shards are less of an analytical issue. (b) There is a slight increase observed in wafer thickness with increasing OH content, reflecting that thinner shards from more vesicular samples experienced more degassing of volatiles. Although the CO_2 detection limit is higher, there is actually likely to be less CO_2 in low OH samples than high OH samples (**Figure A9i**). Samples from Lava-G-Lapilli and dome fragments generally had the highest OH contents and lowest vesicularities, suggesting least degassing. These samples, could also be made into thicker wafers, corresponding to lower CO_2 detections limits. However even in these samples there was still no detectable CO_2.

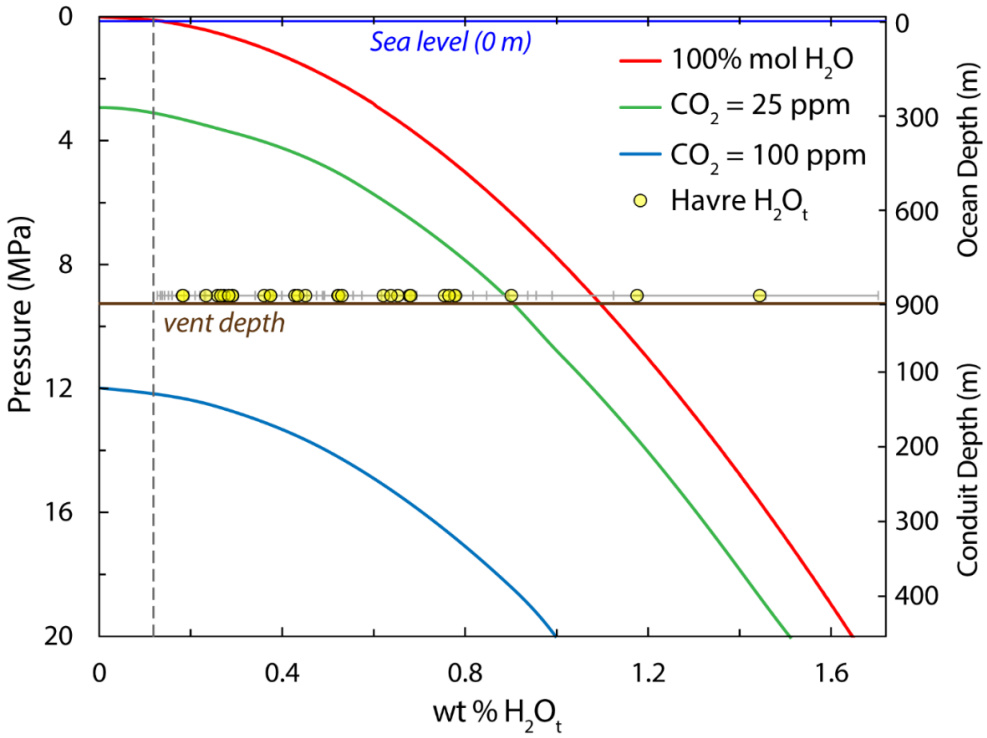

Figure A9ii. H_2O_t solubility vs. pressure was calculated for an eruptive temperature of 800°C using VolatileCalc (Newman and Lowenstern, 2002). Corresponding ocean and conduit depths were calculated using hydrostatic and lithostatic pressure assumptions of density = 1027 and 2400 kg m^{-3}, respectively. Assuming hydrostatic equivalence, sea level and the 900 mbsl vent are plotted at 0.1 and 9.2 MPa, respectively; the dashed line represents minimum H_2O_t Havre values. FTIR H_2O_t concentrations for each clast (±1 standard deviation) are plotted at near-vent-equivalent pressure (9 MPa) to highlight the H_2O_t undersaturation of most clasts at 900 m water depth.The red curve assumes a pure H_2O phase whereas the green and blue curves include a constant proportion of CO_2 within the melt (25 and 100 ppm) with decreasing pressure (based on FTIR detection limits).

Equilibrium H_2O_t content for a given pressure would be lower for a mixed H_2O-CO_2 fluid rather than pure H_2O fluid (Newman and Lowenstern, 2002). However, several tens of ppm of undetected CO_2 would be required to make measured H_2O_t contents consistent with quench at vent depth (**Figure A9ii**). Given that H_2O_t data have been affected by rehydration, we further examine the potential effects of the undetected CO_2 hypothesis by outputting isobars of H_2O–CO_2 solubility for an eruption temperature of 800°C (Newman and Lowenstern, 2002). From these we calculate

equivalent OH–CO_2 isobars (**Figure A9iii**) by applying endmember T_g values of 400 and 800°C (Nowak and Behrens, 2001).

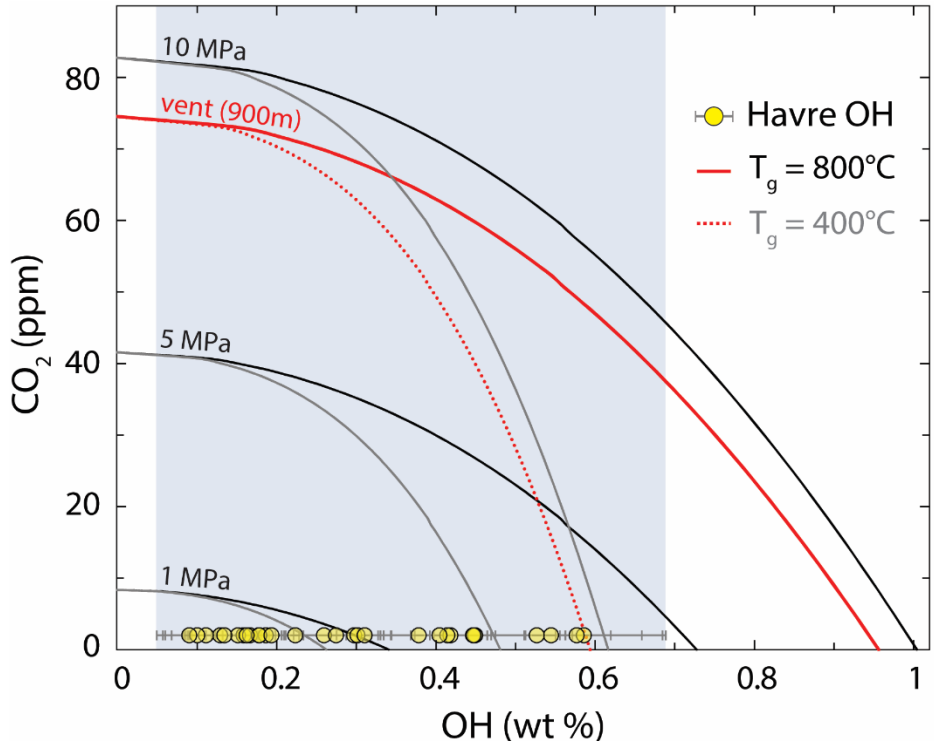

Figure A9iii. OH-CO_2 isobars from VolatileCalc using the methods as described above. OH values are given for the average of Havere 2012 clasts.

Assuming instant quench (T_g = 800°C), 45 to 73 ppm CO_2 would be required to produce the observed average OH range of 0.58 and 0.08 wt. %, respectively, at a pressure consistent with quenching at vent depth. For the lowest possible T_g of 400 °C, <5 ppm CO_2 would be required to quench the highest OH dome fragments and Lava-G-Lapilli at vent depth; the low OH clasts would still require tens of ppm of CO_2. FTIR analyses found no CO_2 with detection limits of 30–100 ppm imposed by our wafer thicknesses of 52–15 µm, where thinner shards usually corresponded to highly vesicular clasts with lower OH (**Figure A9iii**). Significant alteration of their calculated quench pressures by undetected CO_2 therefore seems unlikely, and we can infer the quenching of Giant Pumice, Raft Pumice, Ash-Lapilli-Block and Ash-Lapilli clasts at depths well above the 900

m deep vent. FTIR detection limits for the dome fragment wafers were ~30 ppm CO_2, and the dome deposit is likely to have had the slowest cooling history and lowest T_g. It is therefore possible that dome fragments quenched closer to vent depth, rather than higher in the ocean. This is consistent with the hypothesis of lateral transport of dome breccia to the sampled location at 773 mbsl (Appendix **A3**). However, it is not necessary to invoke undetected CO_2 to explain observed DB volatile concentrations. Alteration of hydrostatic pressure conditions above the vent may be a more likely cause, especially given the lack of evidence for a CO_2-rich magma at depth (section 4.1.3).

Appendix A10: *Vesicularity and speciation within stratigraphy*

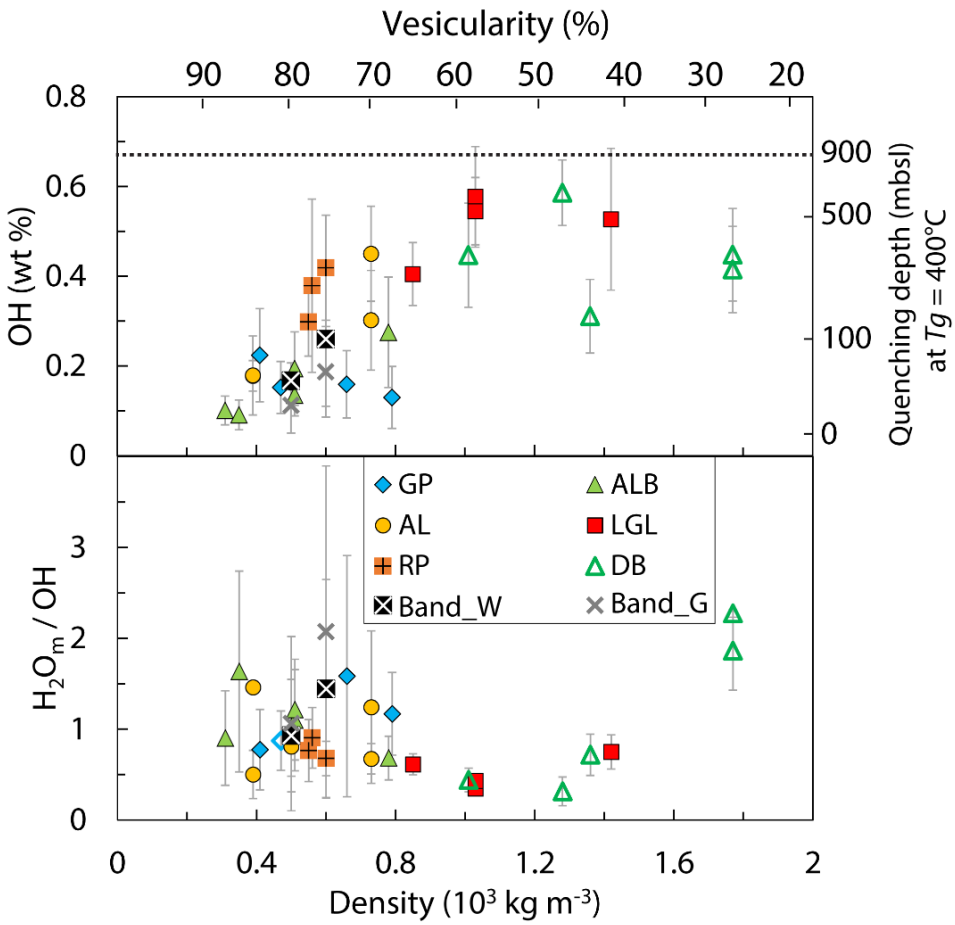

Figure A10 (previous). Variations on plots from **Figure 2.3** and Appendix **A6** plotting OH and the speciation ratio (H_2O_m/OH) vs. density (and corresponding vesicularity) with stratigraphic unit symbology. This highlights again the lowest OH and significant degassing inferred from high vesicularity associated with Giant Pumice (GP) and Ash-Lapilli-Block (ALB) in particular.

Equivalent quench depths are derived from measured OH assuming hydrostatic pressure conditions and using T_g = 400°C (which gives the greatest possible quench depth for a given OH content (Nowak and Behrens, 2001; Newman and Lowenstern, 2002)). Even at T_g = 400°C, no clasts will quench at or below vent depth (**Figure A10**). Clasts with very high vesicularity (>70 %) will undoubtedly quench within the top few hundred meters of the water column.

Appendix A11: *1D H_2O_t diffusion modeling*

The diffusion model was developed on the basis of Fick's 2nd law (Eq. **A15**):

$$\frac{\partial C}{\partial t} = \left(\frac{\partial D}{\partial x}\right)\left(\frac{\partial C}{\partial x}\right) + D\left(\frac{\partial^2 C}{\partial x^2}\right) \quad \text{(Eq. A15)}$$

where D is the diffusion coefficient [m^2 s^{-1}] and C is concentration [wt. %]. This equation is expressed as finite differences (Eq. **A16**), and taken through a series of time steps of duration $\Delta\tau$ and distance increments with spacing Δx. Subscripts i and j define the distance position along the profile and time step position, respectively, where Δx is the distance between each profile measurement (~ 1 µm) (Eq. **A16**):

$$C_{i,j+1} = C_{i,j} + \Delta\tau\left[\left(\frac{(D_{i+1,j}-D_{i-1,j})(C_{i+1,j}-C_{i-1,j})}{\Delta x}\right) + \left(D\left(\frac{C_{i+1,j}-2C_{i,j}+C_{i-1,j}}{(\Delta x)^2}\right)\right)\right] \quad \text{(Eq. A16)}$$

This expression requires a stability criterion to be obeyed (Eq. **A17**), where:

$$\Delta\tau < \frac{0.5(\Delta x)^2}{D} \quad \text{(Eq. A17)}$$

Initial model input parameters are: C_o is the initial concentration at the vesicle edge based on the maximum value of the µRaman profile (for simplicity this was assumed constant with time); C_i is the initial concentration in the matrix glass defined by the plateau of the µRaman profile; τ is

the duration for diffusion; and T is the temperature at which the diffusion occurs. For ambient (low) temperature modeling ($T < 35$°C), D is independent of temperature and is an input parameter (Giachetti and Gonnermann, 2013). For higher temperatures (400 – 800°C), D was calculated according to its dependency on H_2O_t concentration and temperature, with faster diffusion at higher H_2O_t and higher temperature (Ni and Zhang, 2008). The dependency on C in these higher temperature scenarios means that D varies along the profile and is recalculated with each time step. Rehydration is assumed to occur via addition of H_2O_m under disequilibrium conditions, i.e., without ongoing conversion of newly added H_2O_m to OH. For D we therefore use the faster diffusivity of H_2O_m, rather than of H_2O_t, calculated using the model of Ni and Zhang, (2008).

The best model fit for each dome breccia fragment μRaman profile (**Figure 2.5**) was determined from the lowest sum of the residual root-mean-square value (Σ_{RMS}) for a series of diffusion durations (τ) at a constant temperature. τ was varied over many orders of magnitude to first identify the order with lower Σ_{RMS}; the lowest Σ_{RMS} value was subsequently found through manual iteration. Each lowest Σ_{RMS} value applies to a small timescale range that would fit the diffusion profile equally well; the median value of this range is given in **Table 2.2**. We also use the low temperature model to calculate inversely the characteristic diffusivity (D_{ch}) values required to form the observed DB profiles in the time between eruption and sampling (300 – 1000 days; **Figure 2.8**).

Appendix A12: *FTIR peak shape and positions*

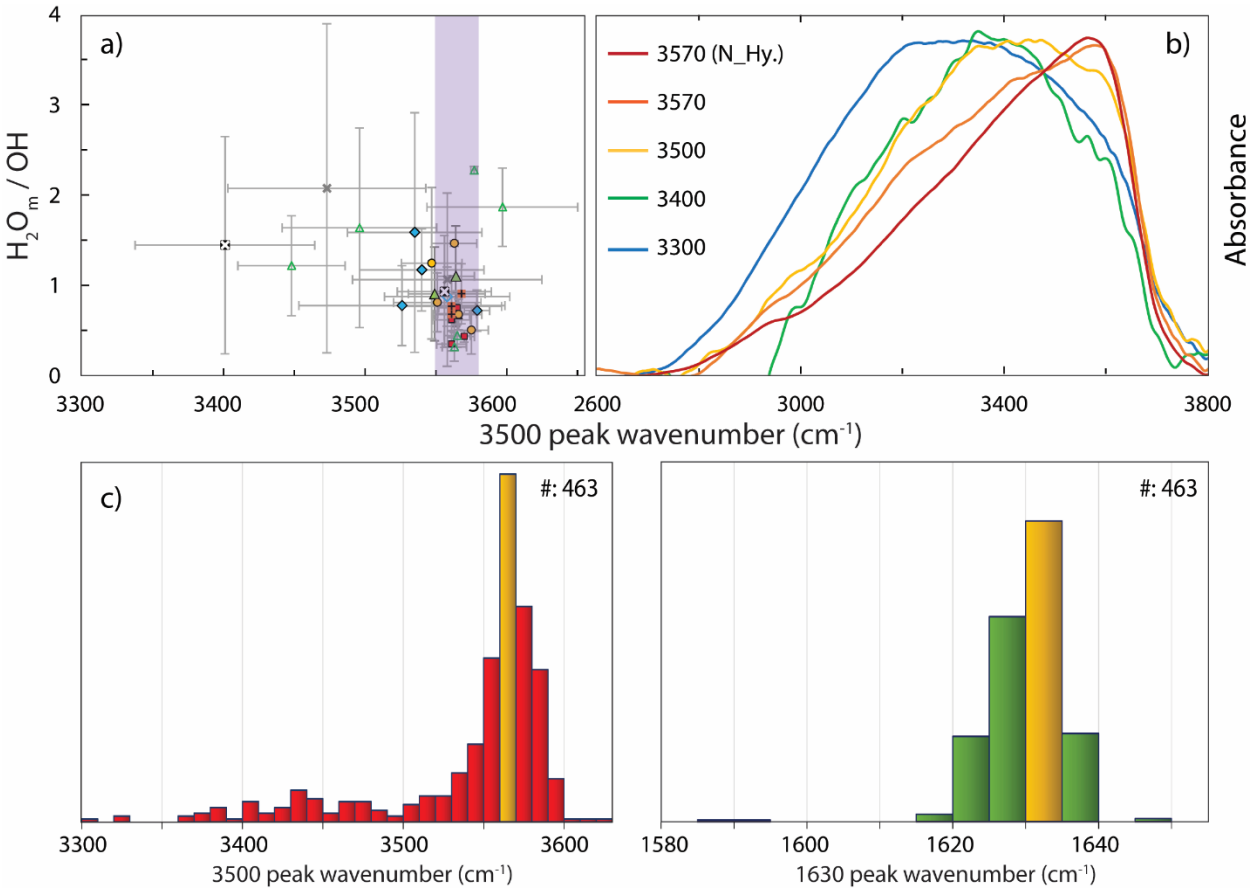

Figure A12. Analysis of the individual FTIR spectra showed that excess H_2O_m also affects the shape of the raw absorbance peaks. Symbols match with that of Appendix **A10**. The wavenumber peak height and shape of the 3500 cm^{-1} H_2O_t peak varies with H_2O_m/OH, reflecting that the peak combines both OH and H_2O_m. The maximum peak position may shift down to 3300 cm^{-1} in low wt. % OH clasts with high H_2O_m/OH, whereas those samples within equilibrium speciation (Lava-G-Lapilli) have peaks at 3500 – 3570 cm^{-1} (a), e.g., red symbol (not rehydrated). Similarly, clasts with high H_2O_m/OH trend to show a more symmetrical 3500 peak in comparison to those with expected equilibrium speciation (b), e.g., blue line. Comparatively, the location of the 1630 cm^{-1} peak attributed to H_2O_m shows much less variation (c). Deviations from 1630 cm^{-1} are attributed to the complex nature of the spectra at lower wavenumbers in thin vesicular shards (d). Raw spectra analysis can be used as a first order indicator of relative excess H_2O_m.

APPENDIX B – SUPPLEMENTARY MATERIAL FOR CHAPTER 3

Appendix B1: *Sample collection*

In March-April 2015, an expedition aboard the R/V Roger Revelle spent three weeks mapping, exploring and sampling the 2012 Havre eruption using the ROV *Jason* and AUV *Sentry*. A total of 290 samples were collected across the stratigraphic sequences, using the ROV manipulator, push cores, a vacuum pipe and scoops to effectively sample all lava and clastic deposit types. The 29 giant pumice exterior samples were collected using the ROV manipulator (**Figure B1**). Collected seafloor samples were immediately washed thoroughly and dried at 80°C for over 24 hours.

Giant pumice fragment densities were analyzed following the method of Houghton and Wilson (1989). Fragments 8 – 32 mm in diameter were cleaned again to remove any fine ash from exterior vesicles and then their exteriors finely coated in hydrophobic silicon spray with negligible mass addition. Fragments were numbered in descending size order for every sample, their dry weight measured, and then their submerged wet weight measured relative to a ballast. Analytical uncertainty in density measurements is given by the precision of the mass measurements where ± 2 standard deviations = 30 kg m^{-3}. Using Archimedes principle (Eq. **B1**), the density for each clast was acquired.

$$density = \frac{dry\ mass}{dry\ mass - wet\ mass} \qquad \text{(Eq. B1)}$$

For each of 13 samples analyzed, a single fragment was chosen from the modal density bin from each density distribution. Fragments of modal density / vesicularity were then cut, bound with clear epoxy and thin sectioned with a 0.5 µm diamond polish at the Lapidary Facility at UH Mānoa.

Corresponding vesicularities were calculated using a dense rock equivalent (DRE) density of 2380 kg m^{-3} as determined from averaging the bulk density of 28 finely crushed powders (one from each GP) (**Figure 3.2b**). This density value corresponds well with the DRE used in the Manga

et al., (2018) model and previous Kermadec pumice studies: 2400 kg m^{-3} (Barker et al., 2012a; Rotella et al., 2015).

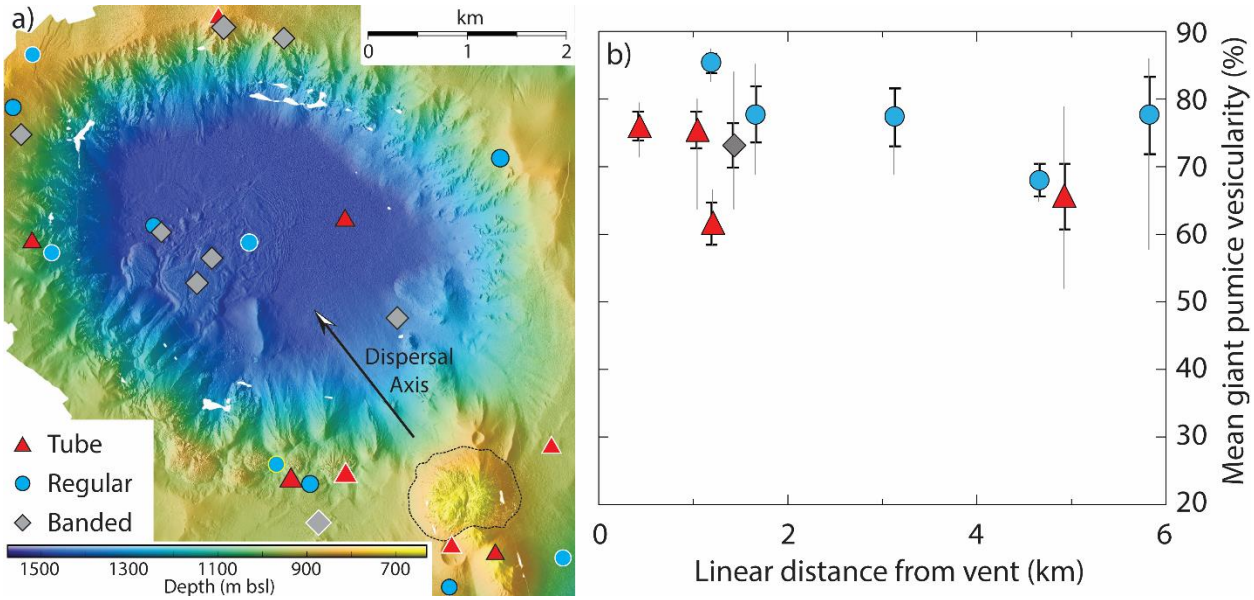

Figure B1. Original location of samples analyzed within this study (a) and the corresponding density distributions of samples studied 'in-detail' (b). A textural classification is given for all samples. Samples outlined in white (a) correspond to those chosen for more detailed 2D microtextural analysis in (b) and throughout the rest of this study. Giant pumice density distributions of exterior fragments (b) are presented as vesicularity (DRE = 2380 kg m^{-3}) with clast distance from the vent. The symbol marks the mean, the black error bars represent one standard deviation, and the grey line marks the maximum and minimum vesicularities measured.

Table B1. Repository of data and corresponding International Geo Sample Numbers (IGSNs) for Havre 2012 samples used in this study. Location, unit, macrotextural classification and depth are given for each collected HVR_sample.

IGSN	HVR_sample	Stratigraphic Unit	Classification	*In situ* depth (m)	Latitude (°)	Longitude (°)
IEHVR0003	003	GP	Tube	944	-31.12352	-179.00642
IEHVR000M	022	"	"	954	-31.12627	-179.02861
IEHVR002V	103	"	"	972	-31.12671	-179.03373
IEHVR0037	115	"	"	844	-31.13238	-179.01682
IEHVR003D	121	"	"	717	-31.13332	-179.01219
IEHVR003P	133	"	"	1513	-31.10265	-179.02862
IEHVR0067	223	"	"	1020	-31.10493	-179.06059
IEHVR007I	270	"	"	801	-31.08457	-179.04110
IEHVR0015	041	"	Regular	1507	-31.10463	-179.03825
IEHVR002O	096	"	"	989	-31.12497	-179.03510
IEHVR002Y	106	"	"	963	-31.12713	-179.03218
IEHVR003H	125	"	"	875	-31.13727	-179.01718
IEHVR004K	164	"	"	1518	-31.09933	-179.04855
IEHVR005C	192	"	"	1012	-31.13414	-179.00538
IEHVR0065	221	"	"	1057	-31.10542	-179.05910
IEHVR006B	227	"	"	852	-31.09300	-179.06230
IEHVR006F	231	"	"	826	-31.08778	-179.06050
IEHVR007T	281	"	"	966	-31.09748	-179.01182
IEHVR0018	044	"	Banded	1482	-31.10747	-179.04341
IEHVR003V	139	"	"	1489	-31.10640	-179.04226
IEHVR004L	165	"	"	1509	-31.10284	-179.04730
IEHVR006A	226	"	"	926	-31.09528	-179.06230
IEHVR006R	243	"	"	1437	-31.11175	-179.02250
IEHVR007F	267	"	"	803	-31.08515	-179.04076
IEHVR007Q	278	"	"	895	-31.08622	-179.03485
IEHVR0082	290 (GP290)	"	"	950	-31.12975	-179.03108

Appendix B2: *BSE images processing, nesting and 3D bubble stereo-conversion*

Binary Image Processing

Backscattered electron (BSE) images were acquired using an electron microprobe and processed using the imaging software FijiApp (containing ImageJ). Whole-fragment scans were acquired at 46.5 pixel/mm resolution. All raw BSE images were processed into black and white binary images using Adobe Photoshop, where black represents vesicles and white represents melt and crystals. For large crystals and phenocrysts, crystals were separated out in separate images. Images were "repaired" by fixing broken thin bubble walls, removing vesicle pits (the very bottom of a vesicle intersection not representative of any true vesicle diameter), erasing fragments of broken material inside vesicles, and strengthening very thin bubble walls to a 3 pixel width (individual objects in FijiApp can only be differentiated with a 3 pixel difference between them). All vesicles were then "decoalesced", where coalesced vesicles with clear bubble throats were manually separated with a three-pixel wall. Each stage of processing was done within a different layer in Photoshop to track changes and to remove layers if needed, e.g., to assess real, un-strengthened bubble wall thicknesses.

In ImageJ, each image was first converted to an 8-bit binary format, and then smoothed to remove any one pixel binary impurities. Any incomplete vesicles at the image edge were placed within a "mask" and removed from the binary image to produce an accurate vesicularity area and to remove incomplete vesicles from vesicle size distribution (VSDs). Complete vesicles touching the edges of the image were included within images. Within each image at each magnification, ImageJ measured image area without the mask, image vesicularity, number of vesicles inside the mask, the areal fraction of phenocrysts, and the size and shape of all vesicles in each image.

The image nests were the same for all analyses (**Figure B2i**): one full thin section scan at 5x magnification, eight 50x images stitched into two large 50x area, eight 250x images and then, if needed, four 500x images. The diagram below shows the nesting structure with an example of a giant pumice fragment nest where in each image, the masks have been removed. Only the vesicles analyzed are displayed:

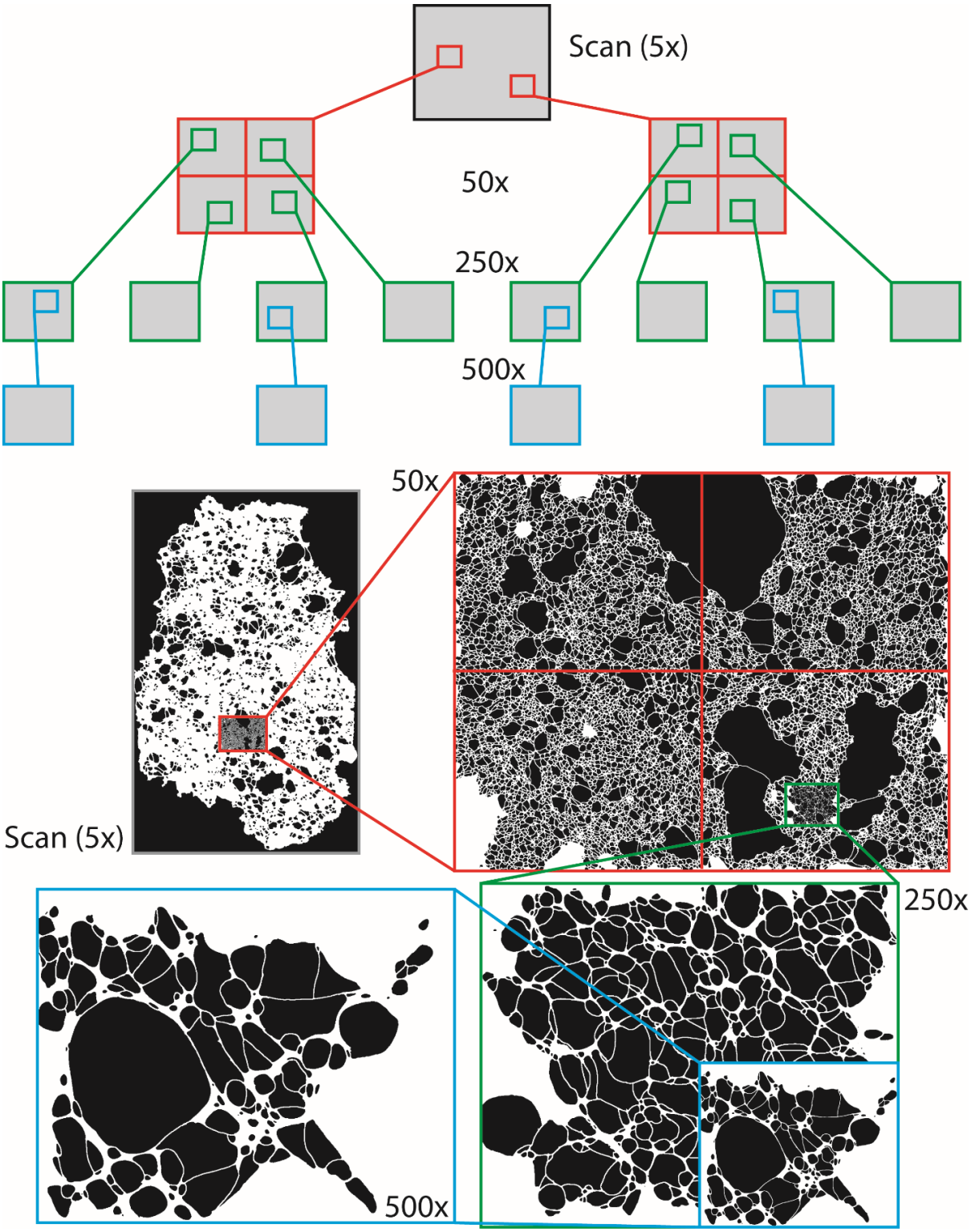

Figure B2i. Image nesting structurefor 2D binary image microtextural analysis.

The 500x images were rarely of additional value to the nest as most vesicles could be accurately analyzed up to 250x, i.e., an extremely microvesicular population was lacking. Our cut off for accurate vesicle width was 10 pixels (Shea et al., 2010). Using this image nest structure, I analyzed vesicles with equant diameters from 2.4 μm up to 3.78 mm; thin sections with vesicles >4 mm in diameter were not viable for analysis. For each vesicle, the area (A) was converted to an equivalent best-fit ellipse where the circular-equivalent diameter: $EqD = \sqrt{4/\pi A}$. All vesicle sizes within the size distribution are reported as EqD for the later spherical stereoconversion calculations. VSDs were binned geometrically using a $10^{0.1}$ bin factor. This produced 32 geometrically-equivalent bins within the 2.4 μm to 3.78 mm size range. Magnification cutoffs were chosen based on overlaps in the VSDs from each magnification where the higher magnification had at least 20 vesicles per total area for one set of magnifications. Using ImageJ, we were able to produce VSDs for each thin section over 32 size bins, where vesicle number densities were given as N_A (number of vesicles of a given size range for a total magnification area).

2D to 3D bubble stereoconversion

VSDs and N_A values were then used to determine VVDs and N_V values using a 2D to 3D stereoconversion assuming a spherical vesicle geometry based on the EqD obtained (Sahagian and Proussevitch, 1998). Each geometric bin of vesicle sizes (N_A value) was converted into an N_V value for the same bin size. Sahagian and Proussevitch (1998) determined the intersection probabilities (P) for spheres of 12 classes with a $10^{0.1}$ geometric bin factor using 10^6 Monte Carlo simulations of planes of variable angles intersecting spheres of various sizes. P values were then converted into conversion coefficients (α) for ease of incorporating P into N_V calculations where j denotes the chosen class number and i denotes the number of classes analyzed:

$$\alpha_i = \frac{1}{P_1}\left(\alpha_1 P_i - \sum_{j=1}^{i-2} \alpha_{j+1} P_{i-j}\right) \qquad \text{(Eq. } \mathbf{B2}\text{)}$$

For the spherical assumption, a logarithmic extrapolation was applied to classes 5 to 12 to extrapolate α values for 32 classes. The extrapolation fit of classes 5 to 12 had $R^2 = 0.9999$ whereas using all 12 classes gave $R^2 = 0.9966$; a small variation but critical when assessing α values over 10 orders of magnitude. Each bin size limit was converted into a volume and then an average to determine a projected mean vesicle height (H)

With H, N_A and α values determined for each of the 32 classes, the 3D stereo-conversion could be applied to obtain vesicle number densities per unit volumes for each geometric bin (N_{Vi}). This calculation is applied to every bin size:

$$N_{Vi} = \frac{1}{H_i}\left(\alpha_1 N_{Ai} - \sum_{j=1}^{i-1} \alpha_{j+1} A_{A(i-j)}\right) \quad \text{(Eq. } \mathbf{B3}\text{)}$$

The sum of N_{Vi} across all 32 bins gives the total vesicle number density for the entire thin section for vesicle equant diameters of 2.4 μm to 3.78 mm (N_V). All N_V values quoted within this paper are in units of cm^{-3}. N_V values are also corrected for bulk clast vesicularity (ϕ) where:

$$\mathrm{N_{Vm}} = \frac{100 N_V}{100-\phi} \quad \text{(Eq. } \mathbf{B4}\text{)}$$

Vesicle volume distributions (VVDs) were determined after the stereo-conversion. Each H value was converted into a volume of the EqD sphere (V_H). The absolute volume fraction of each class (V_i) was simply calculated as $V_i = V_{Hi} N_{Vi}$. These were adjusted by a factor of $\sum Vi$ and subsequently converted into cumulative % volume.

For tube pumice with extremely elongate vesicles, we used previously determined P and α values from Sahagian and Proussevitch (1998) for pre-defined vesicle geometries. The details of this non-spherical stereo-conversion are given within Appendix A.

Bubble decoalescence

To test the subjectivity of manual bubble decoalescence and the effects on resulting vesicle number density values, we determined total N_{Vm} values using both fully decoalesced and coalesced bubble 250x magnification images where the masks and areas analyzed are kept the same. We only used the 250x images for this test, as the 5× and 50× images contribute a negligible addition to N_{Vm} values (**Figure B2ii**).

We observe a strong relationship between the two ratios where it can be seen that decoalescence allows decoalesced N_{Vm} value to remain consistent with the change in number of vesicles (**Figure B2ii**). The ratio of coalesced to decoalesced bubbles scales linearly with calculated changes in N_{Vm} and manual decoalescence never changes N_{Vm} more than three-fold.

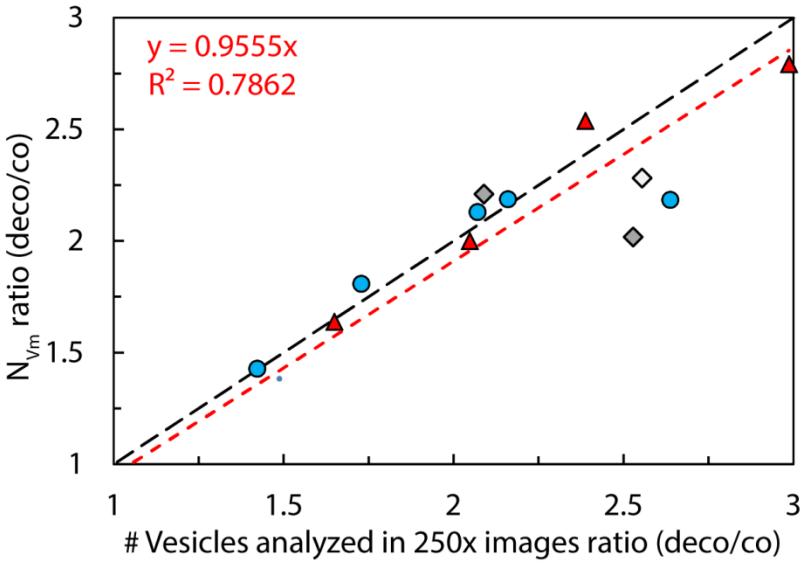

Figure B2ii. For each sample analyzed, we compare the ratio of N_{Vm} after decoalescence to N_{Vm} before decoalescence, i.e., coalesced, to the ratio of the number of decoalesced vesicles analyzed in all eight 250x images per samples to the number of coalesced vesicles prior to decoalescence.

Vesicle shape analysis

Coalesced vesicles were manually decoalesced across all magnifications for accurate representation of the area, perimeter and shape parameters of individual vesicles during subsequent size and shape analysis. We assess the 2D cross sections of vesicles in BSE images using four main shape parameters commonly used in ash morphology analysis (Liu et al., 2015b): circularity, roundness, regularity and solidity. *A* is the vesicle area, *P* is the vesicle perimeter, *a* is the primary (major) axis of the best-fit ellipse, D_f is Feret's diameter – the longest distance between any two points on the vesicle edge, and A_C is the convex area of the vesicle (Schindelin et al., 2012).

$$Circularity = \frac{4\pi A}{P^2} \quad \text{(Eq. B5)}$$

$$Roundness = \frac{4A}{\pi a^2} \quad \text{(Eq. B6)}$$

$$Regularity = \frac{a}{D_f} \quad \text{(Eq. B7)}$$

$$Solidity = \frac{A}{A_C} \quad \text{(Eq. B8)}$$

For vesicles over 19 µm in diameter, we assess the four shape parameters for vesicles in all 250x BSE images; smaller vesicle sizes are too pixelated.

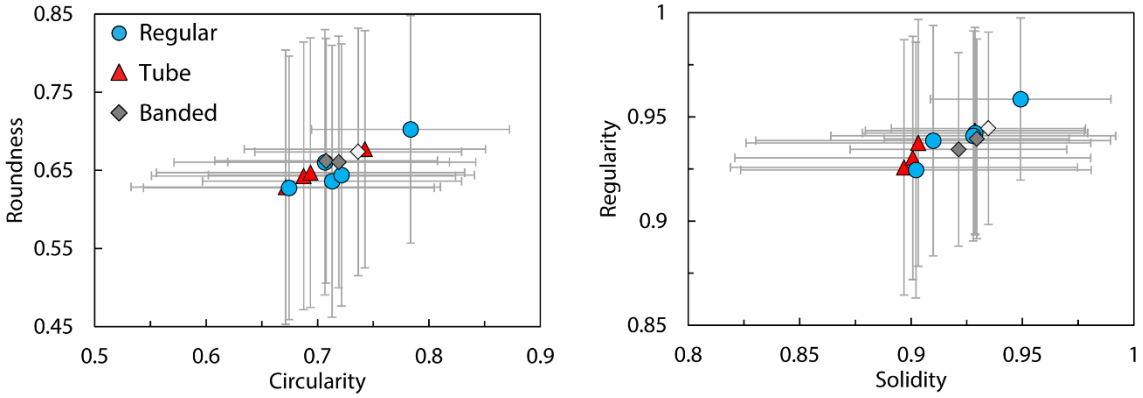

Figure B2iii. Vesicle shape analysis for all vesicles >50 pixels (19 µm) in diameter from all 250x magnification images. Four shape factors are compared to display the most significant difference between macrotextural groups: solidity, regularity, roundness and circularity (formula in text). Error bars given are ±1 standard deviation.

There is no clear distinction between giant pumice macrotextural groups, although one regular giant pumice stands out with very equant and circular vesicles (HVR_221) (**Figure B2iii**). HVR_221 has lower vesicularity with less coalescence, therefore vesicle shapes remain very circular and unaffected by the merging of vesicle edges. Discounting the tube vesicles, a decrease in circularity and regularity may reflect a maturation of bubble textures to the beginning of permeable pathway collapse. We do note that a 2D cross section results in some vesicles not sectioned directly through their diameter and that 3D vesicle orientation will affect the shape results of sheared vesicles (Sahagian and Proussevitch, 1998). We also note that in highly vesicular samples with significant bubble coalescence, manual decoalescence will not preserve original vesicle shape. For this reason, we do not over-interpret the difference between regular, tube and banded giant pumice samples. See the next table for full breakdown of vesicle shape analysis.

Vesicle shape analyses

Table B2i. All parameters are given as the mean value ±1 standard deviation error. Mean is given for all the vesicles analyzed per sample. Each section of the table average vesicles with different pixel limits.

Analysis	Sample (HVR_)	Texture	Area	Perim.	Major	Minor	Angle	Circ.	Feret	FeretX	FeretY	FeretAngle	MinFeret	AR	Round	Solidity	Eq Diameter	Regularity	#Vesicles analyzed
All vesicle sizes analyzed																			
Mean	3	Tub	0.000	0.055	0.019	0.011	93.368	0.717	0.021	0.227	0.191	96.827	0.012	2.024	0.576	0.892	0.014	0.934	3670
	22	Tub	0.000	0.042	0.015	0.009	84.405	0.807	0.016	0.234	0.194	88.017	0.010	1.708	0.648	0.918	0.012	0.944	5082
	115	Tub	0.000	0.056	0.019	0.011	89.975	0.733	0.021	0.235	0.190	92.745	0.012	1.993	0.588	0.896	0.015	0.937	3312
	270	Tub	0.000	0.045	0.016	0.009	85.449	0.761	0.017	0.230	0.191	88.368	0.010	1.904	0.607	0.896	0.012	0.940	4426
	41	Sph	0.000	0.067	0.024	0.014	100.735	0.724	0.025	0.227	0.191	102.662	0.015	2.006	0.583	0.910	0.018	0.943	2354
	96	Sph	0.000	0.068	0.024	0.014	81.367	0.731	0.025	0.233	0.189	81.281	0.015	1.933	0.591	0.918	0.018	0.943	2341
	192	Sph	0.001	0.090	0.030	0.018	87.826	0.684	0.033	0.231	0.188	87.696	0.019	2.081	0.569	0.895	0.023	0.932	1404
	221	Sph	0.000	0.054	0.019	0.013	89.243	0.844	0.020	0.236	0.189	93.529	0.013	1.526	0.705	0.931	0.015	0.950	2251
	231	Sph	0.000	0.068	0.023	0.014	82.925	0.729	0.025	0.222	0.188	84.690	0.015	1.904	0.605	0.903	0.018	0.940	2140
	290	Band	0.001	0.086	0.029	0.018	87.002	0.713	0.031	0.230	0.190	86.779	0.020	1.804	0.619	0.912	0.023	0.937	1434
	Band_W	Band	0.001	0.084	0.029	0.018	81.092	0.741	0.030	0.226	0.195	83.068	0.019	1.752	0.630	0.927	0.023	0.945	1612
	Band_G	Band	0.001	0.100	0.034	0.021	91.751	0.713	0.036	0.230	0.188	92.431	0.022	1.777	0.625	0.924	0.026	0.941	1278
	Dome_O	Dome	0.000	0.078	0.025	0.013	83.261	0.603	0.028	0.231	0.196	81.039	0.015	1.981	0.572	0.852	0.018	0.915	1212
	DB_007	Brec	0.000	0.061	0.019	0.012	81.800	0.714	0.020	0.236	0.195	83.548	0.013	1.657	0.651	0.879	0.015	0.929	1496
	DB_118	Brec	0.000	0.047	0.016	0.009	78.967	0.750	0.017	0.233	0.183	85.354	0.010	1.647	0.655	0.886	0.012	0.928	2101
±1 SD	3	Tub	0.001	0.047	0.015	0.010	51.360	0.171	0.016	0.128	0.106	49.522	0.011	0.983	0.194	0.077	0.012	0.055	-
	22	Tub	0.000	0.037	0.012	0.008	55.829	0.138	0.013	0.136	0.107	54.232	0.008	0.688	0.175	0.051	0.010	0.044	-
	115	Tub	0.001	0.052	0.017	0.011	54.155	0.173	0.018	0.136	0.107	52.636	0.012	1.054	0.194	0.079	0.013	0.054	-
	270	Tub	0.001	0.043	0.014	0.009	54.240	0.174	0.015	0.133	0.109	52.422	0.010	0.919	0.195	0.075	0.011	0.051	-
	41	Sph	0.001	0.053	0.018	0.012	44.923	0.156	0.019	0.136	0.108	43.056	0.012	1.052	0.193	0.063	0.014	0.047	-
	96	Sph	0.001	0.054	0.018	0.012	47.746	0.145	0.019	0.132	0.105	46.646	0.012	0.881	0.185	0.063	0.014	0.048	-
	192	Sph	0.001	0.075	0.024	0.016	57.223	0.162	0.026	0.136	0.104	56.059	0.017	1.150	0.193	0.077	0.019	0.057	-
	221	Sph	0.001	0.053	0.018	0.012	53.189	0.118	0.019	0.135	0.106	51.370	0.012	0.508	0.162	0.048	0.014	0.038	-
	231	Sph	0.001	0.055	0.018	0.012	49.216	0.164	0.019	0.129	0.100	48.380	0.013	0.920	0.193	0.079	0.014	0.054	-
	290	Band	0.001	0.058	0.018	0.013	54.376	0.125	0.020	0.131	0.103	53.503	0.014	0.744	0.176	0.056	0.015	0.046	-
	Band_W	Band	0.001	0.056	0.018	0.013	57.821	0.115	0.019	0.133	0.104	56.881	0.014	0.670	0.173	0.045	0.015	0.044	-
	Band_G	Band	0.001	0.066	0.023	0.013	42.830	0.110	0.024	0.131	0.106	42.056	0.014	0.729	0.173	0.045	0.017	0.048	-
	Dome_O	Dome	0.001	0.071	0.023	0.009	42.577	0.151	0.025	0.134	0.107	40.345	0.011	0.824	0.179	0.066	0.014	0.055	-
	DB_007	Brec	0.001	0.072	0.021	0.012	45.345	0.176	0.022	0.127	0.108	43.968	0.013	0.535	0.159	0.060	0.015	0.046	-
	DB_118	Brec	0.001	0.054	0.017	0.009	56.873	0.168	0.019	0.134	0.106	55.467	0.010	0.513	0.165	0.057	0.012	0.048	-
All vesicles >20 pixels analyzed																			
Mean	3	Tub	0.000	0.076	0.026	0.015	95.483	0.678	0.028	0.223	0.190	96.227	0.016	1.974	0.586	0.895	0.019	0.930	2405
	22	Tub	0.000	0.058	0.020	0.013	84.750	0.770	0.021	0.233	0.194	84.340	0.014	1.686	0.651	0.927	0.016	0.949	3307
	115	Tub	0.000	0.078	0.027	0.016	90.381	0.698	0.029	0.234	0.188	90.723	0.017	1.911	0.603	0.900	0.020	0.935	2149
	270	Tub	0.000	0.068	0.023	0.014	86.197	0.709	0.025	0.229	0.192	86.550	0.015	1.868	0.614	0.899	0.018	0.940	2492

	41	Sph	0.001	0.085	0.030	0.017	103.379	0.705	0.032	0.229	0.190	104.680	0.019	1.936	0.596	0.919	0.022	0.944	1739
	96	Sph	0.001	0.083	0.029	0.017	81.638	0.718	0.031	0.232	0.189	80.007	0.018	1.860	0.607	0.924	0.022	0.942	1825
	192	Sph	0.001	0.106	0.036	0.021	90.386	0.666	0.039	0.231	0.186	89.727	0.023	2.000	0.582	0.901	0.027	0.930	1110
	221	Sph	0.001	0.077	0.027	0.018	89.500	0.810	0.028	0.238	0.189	90.555	0.019	1.516	0.701	0.945	0.022	0.960	1437
	231	Sph	0.001	0.086	0.029	0.018	83.699	0.705	0.031	0.219	0.187	84.019	0.019	1.836	0.621	0.907	0.022	0.939	1588
	290	Band	0.001	0.097	0.033	0.021	88.386	0.703	0.035	0.227	0.192	87.657	0.022	1.761	0.629	0.915	0.026	0.936	1234
	Band_W	Band	0.001	0.093	0.032	0.020	80.116	0.731	0.034	0.224	0.197	81.677	0.022	1.731	0.636	0.931	0.025	0.946	1408
	Band_G	Band	0.001	0.100	0.034	0.021	91.751	0.713	0.036	0.230	0.188	92.431	0.022	1.777	0.625	0.924	0.026	0.941	1109
	Dome_O	Dome	0.000	0.089	0.029	0.015	82.680	0.577	0.031	0.231	0.198	79.917	0.017	1.984	0.571	0.847	0.020	0.912	1020
	DB_007	Brec	0.001	0.097	0.029	0.018	80.839	0.634	0.032	0.232	0.195	81.748	0.020	1.613	0.663	0.877	0.023	0.926	834
	DB_118	Brec	0.000	0.073	0.024	0.014	77.874	0.664	0.026	0.230	0.184	80.451	0.015	1.729	0.625	0.885	0.018	0.933	1137
±1 SD	3	Tub	0.001	0.046	0.015	0.010	50.573	0.154	0.016	0.127	0.105	49.812	0.011	0.948	0.191	0.084	0.011	0.059	-
	22	Tub	0.000	0.037	0.012	0.008	54.779	0.122	0.013	0.135	0.106	54.114	0.008	0.650	0.169	0.050	0.009	0.044	-
	115	Tub	0.001	0.052	0.017	0.011	53.209	0.155	0.018	0.133	0.105	52.938	0.012	0.970	0.188	0.085	0.013	0.057	-
	270	Tub	0.001	0.045	0.015	0.009	53.072	0.157	0.016	0.132	0.106	52.373	0.010	0.875	0.192	0.082	0.011	0.056	-
	41	Sph	0.001	0.050	0.017	0.012	43.015	0.137	0.018	0.135	0.107	41.866	0.012	0.964	0.188	0.059	0.013	0.048	-
	96	Sph	0.001	0.053	0.017	0.012	47.640	0.133	0.019	0.131	0.105	46.809	0.012	0.830	0.179	0.064	0.014	0.050	-
	192	Sph	0.001	0.073	0.023	0.016	57.838	0.145	0.025	0.133	0.103	57.124	0.017	1.051	0.189	0.079	0.018	0.060	-
	221	Sph	0.001	0.054	0.018	0.012	54.085	0.099	0.019	0.131	0.105	53.521	0.013	0.449	0.152	0.040	0.015	0.035	-
	231	Sph	0.001	0.053	0.017	0.012	48.341	0.151	0.018	0.129	0.098	47.782	0.012	0.867	0.190	0.082	0.014	0.056	-
	290	Band	0.001	0.055	0.017	0.013	54.911	0.115	0.018	0.129	0.102	54.263	0.014	0.707	0.170	0.056	0.015	0.047	-
	Band_W	Band	0.001	0.053	0.017	0.013	58.239	0.107	0.018	0.132	0.104	57.492	0.013	0.661	0.172	0.044	0.014	0.045	-
	Band_G	Band	0.001	0.066	0.023	0.013	42.830	0.110	0.024	0.131	0.106	42.056	0.014	0.729	0.173	0.045	0.017	0.048	-
	Dome_O	Dome	0.001	0.072	0.023	0.009	41.281	0.138	0.025	0.134	0.106	38.998	0.011	0.829	0.178	0.065	0.014	0.055	-
	DB_007	Brec	0.001	0.080	0.023	0.012	41.376	0.155	0.025	0.126	0.106	40.868	0.014	0.487	0.154	0.062	0.016	0.048	-
	DB_118	Brec	0.001	0.060	0.019	0.009	56.984	0.132	0.021	0.134	0.105	56.727	0.011	0.536	0.159	0.054	0.013	0.047	-
All vesicles >50 pixels analyzed																			
Mean	3	Tub	0.001	0.116	0.039	0.024	98.007	0.671	0.042	0.224	0.190	99.105	0.026	1.756	0.628	0.897	0.030	0.926	968
	22	Tub	0.001	0.104	0.035	0.023	84.929	0.743	0.037	0.228	0.196	82.854	0.024	1.575	0.677	0.929	0.028	0.943	847
	115	Tub	0.001	0.120	0.040	0.025	90.411	0.687	0.043	0.228	0.188	90.004	0.027	1.713	0.643	0.901	0.031	0.930	902
	270	Tub	0.001	0.115	0.038	0.024	85.196	0.694	0.041	0.228	0.197	86.130	0.026	1.694	0.647	0.903	0.030	0.938	818
	41	Sph	0.001	0.118	0.041	0.025	104.595	0.713	0.043	0.230	0.190	105.907	0.026	1.733	0.636	0.929	0.031	0.942	902
	96	Sph	0.001	0.118	0.040	0.025	80.388	0.721	0.043	0.229	0.195	78.358	0.027	1.704	0.644	0.928	0.031	0.941	912
	192	Sph	0.001	0.143	0.047	0.029	91.818	0.674	0.051	0.229	0.185	89.382	0.032	1.746	0.628	0.902	0.037	0.925	696
	221	Sph	0.001	0.121	0.041	0.028	89.670	0.784	0.043	0.235	0.194	89.977	0.029	1.503	0.702	0.949	0.034	0.959	632
	231	Sph	0.001	0.120	0.040	0.026	82.670	0.707	0.042	0.214	0.187	83.817	0.027	1.649	0.660	0.910	0.032	0.939	824
	290	Band	0.001	0.123	0.041	0.027	88.936	0.708	0.043	0.224	0.191	87.039	0.028	1.626	0.662	0.921	0.033	0.934	800
	Band_W	Band	0.001	0.120	0.040	0.027	77.925	0.737	0.043	0.221	0.201	79.130	0.028	1.588	0.674	0.935	0.033	0.944	876
	Band_G	Band	0.001	0.127	0.043	0.027	91.739	0.719	0.046	0.239	0.185	92.013	0.029	1.644	0.661	0.929	0.034	0.939	709
	Dome_O	Dome	0.001	0.151	0.048	0.024	80.983	0.521	0.053	0.220	0.208	79.394	0.027	2.100	0.545	0.845	0.033	0.915	386
	DB_007	Brec	0.001	0.153	0.045	0.027	78.236	0.559	0.049	0.227	0.197	79.278	0.030	1.668	0.642	0.871	0.035	0.927	394
	DB_118	Brec	0.001	0.134	0.043	0.024	75.345	0.586	0.046	0.227	0.193	75.357	0.027	1.830	0.600	0.877	0.032	0.927	366
±1 SD	3	Tub	0.001	0.046	0.015	0.010	49.054	0.139	0.016	0.127	0.101	48.663	0.011	0.640	0.176	0.078	0.011	0.061	-
	22	Tub	0.001	0.045	0.015	0.009	55.531	0.108	0.016	0.131	0.104	55.287	0.010	0.472	0.152	0.049	0.011	0.050	-

	115	Tub	0.001	0.056	0.018	0.011	52.848	0.137	0.020	0.127	0.105	52.657	0.012	0.673	0.171	0.080	0.013	0.058	-
	270	Tub	0.001	0.051	0.016	0.011	52.865	0.138	0.018	0.130	0.102	52.241	0.011	0.604	0.172	0.077	0.012	0.059	-
	41	Sph	0.001	0.049	0.017	0.011	40.723	0.116	0.018	0.132	0.105	39.417	0.012	0.647	0.174	0.051	0.013	0.049	-
	96	Sph	0.001	0.055	0.018	0.012	46.038	0.119	0.019	0.129	0.104	45.748	0.012	0.654	0.168	0.064	0.014	0.050	-
	192	Sph	0.002	0.072	0.023	0.015	57.834	0.131	0.025	0.131	0.101	57.543	0.017	0.630	0.169	0.079	0.018	0.061	-
	221	Sph	0.001	0.054	0.019	0.012	53.816	0.089	0.020	0.126	0.103	53.543	0.012	0.415	0.146	0.040	0.014	0.039	-
	231	Sph	0.001	0.052	0.017	0.012	46.804	0.135	0.018	0.127	0.097	46.748	0.012	0.562	0.170	0.080	0.013	0.055	-
	290	Band	0.001	0.052	0.016	0.012	56.574	0.100	0.017	0.127	0.102	55.728	0.013	0.546	0.157	0.049	0.014	0.046	-
	Band_W	Band	0.001	0.050	0.016	0.012	59.739	0.093	0.017	0.129	0.103	58.916	0.013	0.464	0.158	0.044	0.013	0.046	-
	Band_G	Band	0.002	0.067	0.025	0.013	41.950	0.100	0.025	0.128	0.105	40.913	0.013	0.592	0.161	0.041	0.016	0.048	-
	Dome_O	Dome	0.001	0.084	0.028	0.010	37.349	0.125	0.030	0.133	0.103	36.277	0.011	0.887	0.180	0.064	0.015	0.054	-
	DB_007	Brec	0.001	0.085	0.025	0.013	33.934	0.129	0.027	0.129	0.109	34.238	0.014	0.494	0.154	0.056	0.017	0.045	-
	DB_118	Brec	0.001	0.076	0.025	0.011	56.793	0.114	0.027	0.130	0.102	56.605	0.013	0.629	0.168	0.052	0.016	0.049	-
All vesicles 20 – 50 pixels analyzed																			
Mean	3	Tub	0.000	0.048	0.017	0.009	93.783	0.683	0.019	0.223	0.190	94.288	0.010	2.120	0.557	0.894	0.012	0.933	1436
	22	Tub	0.000	0.042	0.015	0.009	84.689	0.780	0.016	0.235	0.194	84.851	0.010	1.723	0.642	0.927	0.012	0.952	2459
	115	Tub	0.000	0.048	0.017	0.009	90.359	0.705	0.019	0.238	0.188	91.244	0.010	2.055	0.575	0.900	0.012	0.939	1246
	270	Tub	0.000	0.046	0.016	0.009	86.687	0.717	0.017	0.230	0.190	86.756	0.010	1.953	0.597	0.898	0.012	0.941	1673
	41	Sph	0.000	0.049	0.018	0.009	102.069	0.696	0.019	0.227	0.191	103.358	0.010	2.155	0.552	0.909	0.013	0.946	836
	96	Sph	0.000	0.048	0.018	0.010	82.886	0.715	0.019	0.235	0.182	81.654	0.010	2.017	0.570	0.920	0.013	0.944	912
	192	Sph	0.000	0.052	0.019	0.009	87.555	0.651	0.021	0.231	0.189	89.907	0.010	2.418	0.508	0.898	0.013	0.938	413
	221	Sph	0.000	0.043	0.015	0.010	89.366	0.831	0.016	0.240	0.185	91.010	0.011	1.526	0.700	0.942	0.012	0.961	804
	231	Sph	0.000	0.048	0.017	0.009	84.808	0.703	0.019	0.224	0.187	84.237	0.010	2.039	0.578	0.903	0.013	0.939	763
	290	Band	0.000	0.051	0.018	0.010	87.373	0.695	0.019	0.230	0.193	88.796	0.011	2.011	0.567	0.904	0.013	0.940	433
	Band_W	Band	0.000	0.049	0.018	0.010	83.724	0.721	0.019	0.230	0.190	85.872	0.011	1.967	0.575	0.924	0.013	0.948	531
	Band_G	Band	0.000	0.050	0.018	0.010	91.784	0.702	0.019	0.215	0.194	93.178	0.011	2.015	0.562	0.915	0.013	0.944	399
	Dome_O	Dome	0.000	0.050	0.016	0.009	83.714	0.611	0.018	0.237	0.193	80.235	0.010	1.913	0.587	0.848	0.012	0.910	633
	DB_007	Brec	0.000	0.046	0.015	0.010	83.170	0.701	0.016	0.237	0.193	83.960	0.011	1.564	0.682	0.882	0.012	0.926	439
	DB_118	Brec	0.000	0.047	0.016	0.010	79.206	0.694	0.017	0.230	0.182	82.870	0.011	1.684	0.635	0.888	0.012	0.936	770
±1 SD	3	Tub	0.000	0.020	0.007	0.004	52.061	0.179	0.008	0.128	0.108	49.800	0.004	1.063	0.197	0.077	0.005	0.052	-
	22	Tub	0.000	0.013	0.005	0.003	54.517	0.126	0.005	0.136	0.107	53.694	0.003	0.697	0.173	0.050	0.003	0.042	-
	115	Tub	0.000	0.015	0.006	0.003	53.469	0.166	0.006	0.137	0.105	53.135	0.003	1.117	0.193	0.089	0.003	0.056	-
	270	Tub	0.000	0.014	0.005	0.003	53.165	0.165	0.006	0.133	0.108	52.436	0.003	0.968	0.199	0.085	0.003	0.054	-
	41	Sph	0.000	0.014	0.006	0.003	45.319	0.156	0.006	0.138	0.108	44.317	0.003	1.178	0.194	0.065	0.003	0.047	-
	96	Sph	0.000	0.013	0.005	0.003	49.157	0.146	0.005	0.132	0.105	47.789	0.003	0.949	0.183	0.064	0.003	0.049	-
	192	Sph	0.000	0.015	0.006	0.003	57.746	0.166	0.007	0.137	0.105	56.412	0.003	1.418	0.196	0.080	0.003	0.058	-
	221	Sph	0.000	0.012	0.004	0.003	54.295	0.102	0.004	0.135	0.106	53.499	0.003	0.474	0.157	0.039	0.003	0.032	-
	231	Sph	0.000	0.015	0.006	0.003	49.922	0.167	0.006	0.131	0.099	48.871	0.003	1.069	0.200	0.085	0.003	0.058	-
	290	Band	0.000	0.014	0.005	0.003	51.689	0.138	0.006	0.133	0.102	51.432	0.003	0.880	0.177	0.066	0.003	0.049	-
	Band_W	Band	0.000	0.014	0.006	0.003	55.492	0.125	0.006	0.137	0.105	54.810	0.003	0.843	0.177	0.043	0.003	0.043	-
	Band_G	Band	0.000	0.013	0.005	0.003	44.297	0.126	0.006	0.135	0.106	43.949	0.003	0.876	0.175	0.051	0.003	0.048	-
	Dome_O	Dome	0.000	0.015	0.005	0.003	43.468	0.134	0.006	0.134	0.107	40.561	0.003	0.782	0.175	0.066	0.003	0.056	-
	DB_007	Brec	0.000	0.014	0.004	0.003	46.929	0.145	0.005	0.123	0.104	45.889	0.003	0.476	0.151	0.067	0.003	0.051	-
	DB_118	Brec	0.000	0.014	0.005	0.003	56.992	0.126	0.005	0.135	0.106	56.602	0.003	0.479	0.153	0.054	0.003	0.046	-

(previous) Vesicle area in mm^2. Major and minor axes of the best fitting ellipses to vesicle area in mm. Angle is the angle between the major and minor axis direction. Feret diameter is the maximum vesicle diameter (without ellipse application). FeretX, Y and Feret Angle are the same as the prior columns but for the true vesicle shape (not ellipse). Circularity, roundness, solidity and regularity given in the equations above. Eq diameter is the circular-equivalent diameter of the vesicle area. We also include here the vesicle shape analyses for the three dome samples (the Dome O carapace, and two dome talus samples (Brec, otherwise known as DB).

N_A analyses prior to stereo-conversion

Table B2ii. Vesicle number density per unit area for each sample of vesicle size distributions prior to stereo-conversion. Ranges correspond to image magnification.

Geometric Bins (EqD, mm)	Number density per unit area before stereo-conversion (N_A [mm^{-2}])													
	Type HVR_	Tub 3	Tub 22	Tub 115	Tub 270	Reg 41	Reg 96	Reg 192	Reg 221	Reg 231	Band 290X_blk	Band 290I_G	Band 290I_W	Band 290I_blk
0.0015	**500x**	27.490	0.000	34.393	47.402	0.000	0.000	6.899	28.627	0.000	0.000	0.000	0.000	0.000
0.0019		38.001	56.083	52.371	67.943	0.000	0.000	13.797	31.808	0.000	0.000	0.000	0.000	0.000
0.0024		57.405	105.436	64.878	121.666	26.051	25.017	16.385	54.074	36.194	3.226	7.285	9.723	7.379
0.0030		84.086	155.537	91.454	184.079	47.505	30.666	32.769	51.688	40.215	16.130	10.523	17.015	12.299
0.0038		144.726	182.457	111.778	203.830	52.103	30.666	37.081	97.810	61.932	16.130	12.951	14.585	19.678
0.0048		180.301	233.305	132.882	249.653	72.790	75.050	43.980	108.147	71.583	25.807	28.331	21.877	28.697
0.0060		197.280	289.388	171.965	270.194	83.517	86.348	38.805	122.461	75.605	44.356	29.950	37.272	33.617
0.0075	**250x**	234.472	345.471	195.415	316.016	122.594	121.049	56.915	125.642	119.037	46.776	42.092	53.477	45.096
0.0095		264.387	364.165	230.590	355.518	117.231	126.698	64.676	143.931	131.102	64.518	55.853	80.215	55.755
0.0119		299.962	465.115	241.912	368.948	171.632	196.099	77.611	155.064	147.188	58.873	69.134	97.191	86.912
0.0150		322.601	421.744	230.952	304.165	175.463	204.976	106.068	186.077	176.948	108.068	82.961	110.370	92.652
0.0189		281.366	389.590	277.142	293.895	182.359	218.695	113.829	162.221	168.100	125.004	119.562	152.376	122.169
0.0238		287.026	280.415	238.781	227.531	204.579	242.905	126.765	134.389	205.903	163.715	153.722	199.324	140.208
0.0300		206.173	177.970	189.459	189.609	190.787	194.485	137.975	109.738	161.666	183.877	154.536	185.322	148.407
0.0377		135.023	84.498	121.348	113.766	138.685	132.347	118.141	98.605	139.145	132.262	111.428	148.258	153.327
0.0475		88.129	39.535	75.940	64.783	91.946	75.857	94.858	75.544	78.822	87.100	74.828	107.075	84.453
0.0598		30.724	23.642	43.857	30.827	31.472	45.192	62.951	30.899	37.802	41.049	43.740	43.028	35.787
0.0753		17.486	10.181	14.157	19.310	17.298	13.680	28.457	16.283	14.706	22.164	15.859	16.248	20.109
0.0948		9.829	6.957	8.170	10.314	8.370	6.896	14.553	9.225	7.609	11.591	6.900	7.708	10.566
0.1193	**50x**	4.686	3.450	3.861	5.271	4.297	4.504	6.546	4.168	4.599	5.937	2.894	4.048	5.340
0.1502		2.343	1.301	2.910	3.209	2.065	1.668	3.740	1.612	1.817	3.845	2.059	1.608	2.783
0.1891		1.200	0.582	1.175	1.375	0.893	1.223	1.578	1.278	1.192	1.809	0.835	0.776	1.193
0.2381		0.461	0.520	0.951	0.802	0.419	0.520	0.994	0.872	0.728	0.961	0.402	0.507	0.738
0.2997		0.314	0.385	0.434	0.344	0.342	0.362	0.643	0.528	0.545	0.240	0.257	0.263	0.625
0.3774		0.316	0.207	0.264	0.290	0.220	0.204	0.339	0.258	0.344	0.139	0.134	0.178	0.189
0.4751		0.189	0.122	0.131	0.202	0.147	0.168	0.106	0.123	0.190	0.068	0.169	0.070	0.092
0.5981		0.139	0.078	0.122	0.113	0.080	0.082	0.084	0.066	0.072	0.023	0.093	0.080	0.051
0.7529	**scan**	0.071	0.025	0.052	0.067	0.049	0.061	0.053	0.037	0.048	0.037	0.105	0.038	0.039
0.9479		0.027	0.009	0.026	0.046	0.014	0.025	0.035	0.025	0.035	0.012	0.058	0.014	0.028
1.1933		0.017	0.000	0.015	0.025	0.014	0.029	0.031	0.010	0.011	0.008	0.023	0.028	0.014
1.5023		0.015	0.003	0.009	0.000	0.010	0.011	0.004	0.000	0.000	0.008	0.012	0.000	0.002
1.8913		0.004	0.003	0.004	0.000	0.010	0.000	0.013	0.000	0.000	0.008	0.012	0.000	0.007
2.3810		0.004	0.000	0.000	0.000	0.003	0.000	0.000	0.002	0.000	0.002	0.006	0.005	0.002
2.9975		0.000	0.000	0.002	0.000	0.000	0.000	0.000	0.000	0.000	0.000	0.000	0.000	0.000
3.7736		0.000	0.000	0.000	0.000	0.000	0.000	0.000	0.000	0.000	0.000	0.000	0.000	0.000

Continued N_V and VVD analysis

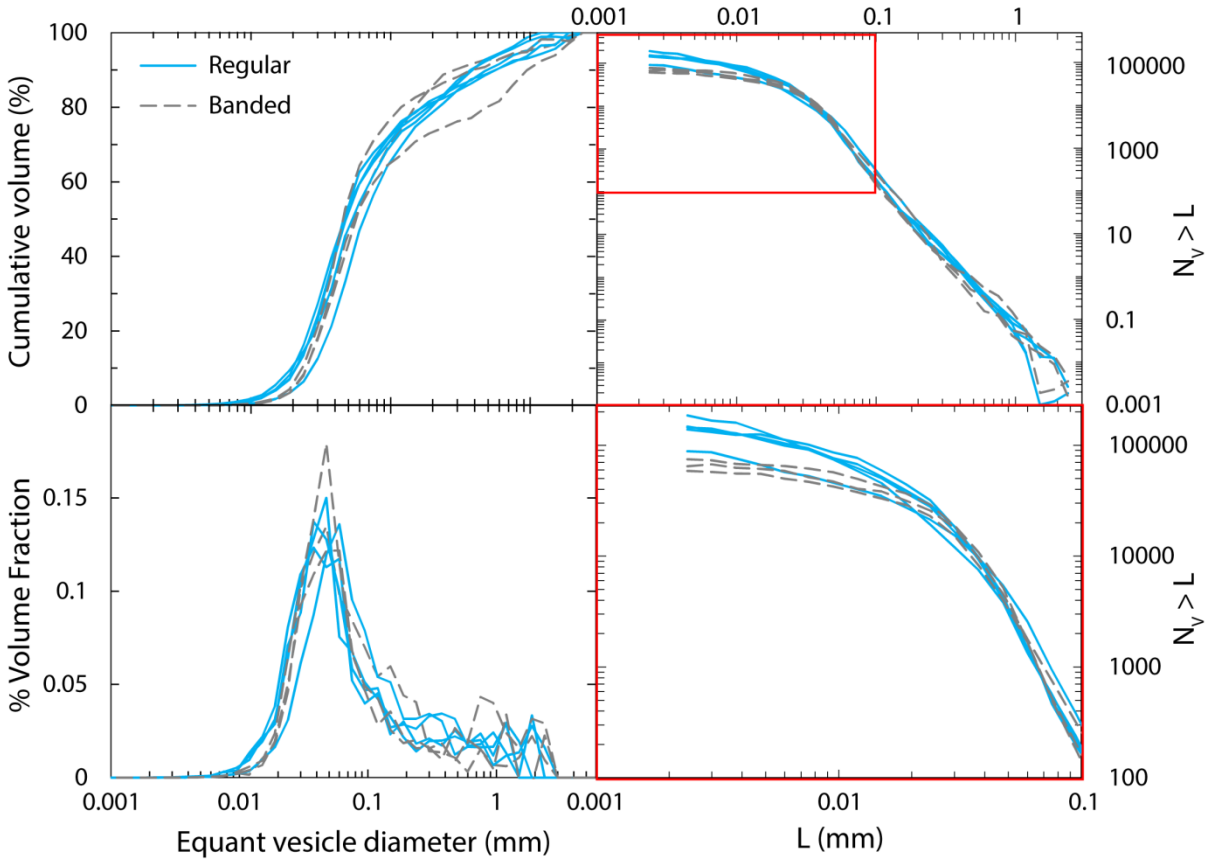

Figure B2iv. Distribution of volume fraction and number density across vesicles size from 2.4 µm to 3.78 mm for all textural classifications except for tube pumice (as in **Figure 3.7**). Cumulative and adjusted % volume distributions are given in a) and b). The number density of vesicles (N_V) greater than the mid value of each size bin (L) is given in c) with the highest N_V>L values expanded in d) to display the major differences in N_V of vesicles <100 µm between classifications.

All giant pumice samples have consistent N_V > L trends from ~40 – 500 µm, after which deviations between samples arise, as vesicle numbers become very small at large diameters (> 1 mm). The apparent higher N_{Vm} values in regular pumice than banded pumice come from contribution of vesicles < 20 µm except for HVR_192 (the highest vesicularity) where N_V > L are similar to banded pumice (**Figure B2iv**). These differences in small vesicle number densities could result from differing decompression rates in the shallow conduit between regular and banded pumice.

Appendix B3: *Prolate geometry 3D stereo-conversion*

For the prolate 3D stereo-conversion of sheared and tube vesicles, we used the same calculations steps from Sahagian and Proussevitch (1998) as in Appendix **B2**, but by applying intersection probabilities (*P*) and conversion coefficients (α) to the smallest 12 classes of vesicle sizes. This accounted for all vesicles from 2.4 – 38 μm. Larger vesicles were not included or counted towards in the revised N_{Vm} values as they present a negligible addition to total N_{Vm} in either case. For N_{Vi} calculations, N_{Ai} remains the same but V_{Hi} (the projected mean height of a vesicle with the equivalent equant volume) changes depending on the vesicle geometry assumed.

Three vesicle geometries were suitable and available from Sahagian and Proussevitch (1998); prolate vesicles with dimensions of 1:1:2, 1:2:5 and 1:3:10. We applied the appropriate conversions to tube and regular giant pumice vesicles <38 μm in diameter based on macrotextural and microtextural observations, and from the results of vesicle aspect ratios of the 3D XRT analysis (see Appendix **B4**).

Table B3. *P* and α values for the three prolate and spherical geometries are as given:

Class #	**Intersection probability (*P*)**				**Conversion coefficient (α)**			
Geometry	**Sphere**	**1:1:2**	**1:2:5**	**1:3:10**	**Sphere**	**1:1:2**	**1:2:5**	**1:3:10**
1 (largest)	60.749	31.700	1.760	0.349	1.646	3.151	3.151	3.151
2	16.833	43.370	14.181	2.602	0.456	4.305	7.052	38.43
3	8.952	17.467	41.317	12.264	0.116	4.149	20.54	181.1
4	5.200	5.374	37.077	25.122	0.041	3.833	41.42	482.5
5	3.134	1.239	4.570	49.266	0.017	3.560	69.24	1253
6	1.925	0.459	0.774	9.262	0.0078	3.335	99.6	4540
7	1.195	0.195	0.211	0.756	0.0037	3.128	121.7	17000
8	0.747	0.084	0.072	0.193	0.0018	2.934	114.3	62000
9	0.468	0.039	0.026	0.064	0.0009	2.750	43.62	200000
10	0.294	0.018	0.010	0.021	0.0004	2.579	137.0	670000
11	0.185	0.008	0.003	0.009	0.0002	2.418	481.8	2300000
12	0.117	0.004	0.001	0.003	0.0001	2.267	1036	8100000

For each vesicle geometry, the new V_{Hi} values are calculated by converting the observed bin values into equivalent diameters (*EqD*) for a sphere assuming the observed diameter (D_{Ai}) is the cross section of the smallest axis of a prolate vesicle:

$$EqD_{i(1:1:2)} = \left(2{D_{Ai}}^3\right)^{\frac{1}{3}} \quad \text{(Eq. } \mathbf{B9}\text{)}$$

$$EqD_{i(1:2:5)} = \left(10{D_{Ai}}^3\right)^{\frac{1}{3}} \quad \text{(Eq. } \mathbf{B10}\text{)}$$

$$EqD_{i(1:3:10)} = \left(30{D_{Ai}}^3\right)^{\frac{1}{3}} \quad \text{(Eq. } \mathbf{B11}\text{)}$$

V_{Hi} values are calculated as per Appendix **B2** using the conventional methods of the stereo-conversion to determine final N_{Vm} values. Individual N_{Vi} values were discounted if negative.

Suitability of the chosen vesicle geometry, e.g., 1:3:10, for a single sample could be confirmed by comparing the modal vesicle diameter from the 2D BSE images with the modal N_{Vi} diameter after the 3D stereo-conversion (D_{3V}). For tube vesicles, D_{Ai} will be significantly smaller than D_{3V} unless the prolate stereo-conversion is applied. By testing all three geometries, the best geometry to use was where $D_{Ai} \approx D_{3V}$. For tube vesicles, the appropriate geometry was 1:3:10, and regular = 1:1:2.

There are caveats with this modification of the Sahagian and Proussevitch (1998) stereo-conversion. Accurate VVDs cannot be determined after stereo-conversion of tube vesicles, as calculated-equant tube vesicle sizes do not correspond to the original vesicle bin sizes of the large vesicles, and so there is not a smooth transition from smaller to larger vesicles outside of the 12 classes. Aspect ratio of vesicles varies with size, as seen in Appendix **B4**. Smaller vesicles are likely to undergo less deformation if nucleated at a later stage in the conduit. It is very complicated to apply a varying vesicle geometry across the bin classifications as conversion coefficients are looped calculations based on adjacent geometric bins. By exploring several vesicle geometries, we can see the effect that different aspect ratios may have on number density. We aim to show that, by applying prolate geometries, the obtained N_{Vm} values obtained for tube pumice are reduced by an order of magnitude and roughly match those observed in banded and regular giant pumice (**Figure 3.6**).

The new V_{Hi} values appear to be the greatest control on final number density as the volume calculated for each bin is dependent on the interpreted volume from the 2D vesicle size analyzed. Changing the intersection probabilities and alpha values actually has little effect on the final number density (**Figure B3**). The main reduction in vesicle number density comes from changing the mean projected height of a vesicle observed in 2D that is assumed to be intersected through the narrowest diameter. For example, a vesicle with an assumed geometry of 1:3:10 and observed 2D (smallest) diameter of 10 μm has a total volume of ~1.26×10^5 μm^3 and a spherical-equivalent

diameter (EqD) of 31 µm. This increase in true vesicle diameter from inferred diameter results in an overall decrease in total vesicle number density (N_{Vm}) (as shown in **Figures 3.6** and **B3**).

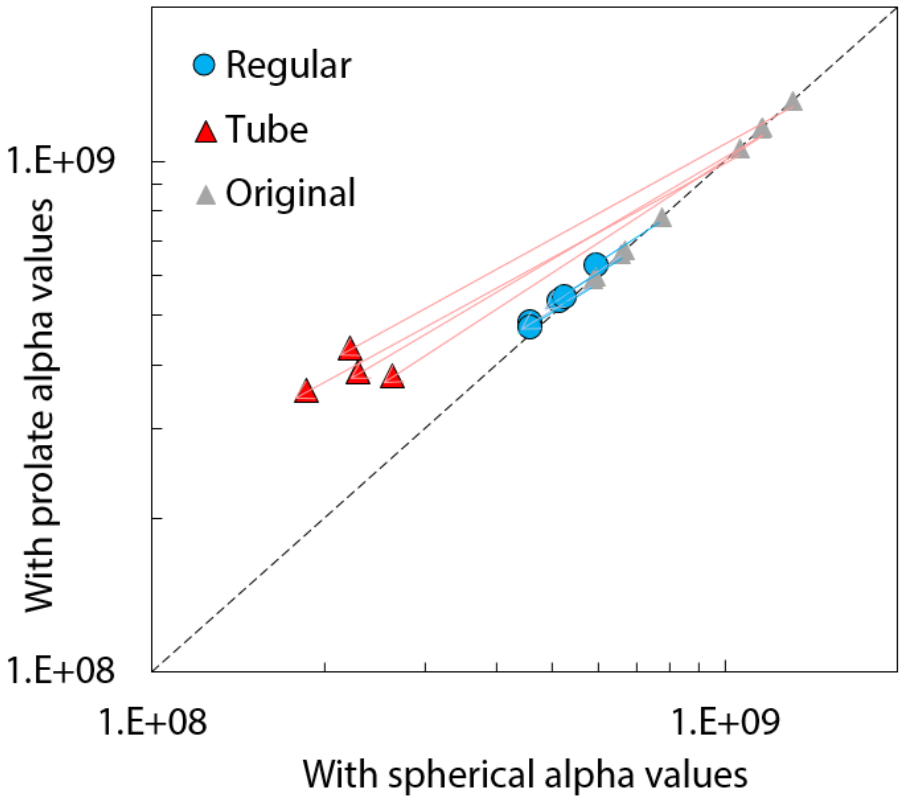

Figure B3. A comparison of the stereo-conversion with the spherical vs. prolate intersection probabilities, but with both using prolate V_{Hi} values for a geometry of 1:3:10 for tube vesicles and 1:1:2 for regular vesicles.

It can be seen from **Figure B3** that the original values are still reduced even just by changing *H* (projected mean vesicle height). There is little difference between applying prolate intersection probabilities from random particle intersections vs. spherical intersection probabilities. With this in mind, I can still state with some confidence that the prolate conversion will reduce the number density significantly for elongated vesicles with narrower diameters. The tube-vesicle pumices do in fact have original vesicle number densities similar to that of the regular and banded giant pumice (**Figure 3.6**).

Appendix B4: *X-ray computed microtomography*

The scans were done with monochromatic X-rays at ~25kev and were reconstructed using the TomoPy gridrec algorithm (Gürsoy et al., 2014). The image stacks were then binarized based on greyscale thresholds. Because 3-dimensional porosity is entirely connected in most Havre pumice, a bubble decoalescence technique was used to quantify bubble size distributions and aspect ratios. We used an Avizo step-by-step watershed technique to separate bubbles in 3D and make AR and bubble size measurements. Watershed separation of highly elongated pumice (e.g., tube pumice) resulted in bubble over separation. We therefore only report vesicle orientation and elongation results for "regular" Havre pumice and talus .

The step-by-step watershed technique we used to decoalesce bubbles is described in detail in the Supplement to Fauria et al. (2017). Briefly, we applied a Gaussian filter before separation was attempted on some data sets and used a neighborhood value of 26 during the watershed separations. We found that the bubble decoalescence was satisfying for most regular pumice. Once the bubble separation was complete, we measured bubble sizes and aspect ratios using the "Label Analysis" module in Avizo. We report 3D aspect ratios (ratio of major to minor axis) of four samples below.

The four samples come from the pumice raft (1b_try2 and s1_small_try) and seafloor pumice in a talus deposit near Dome OP (white_A and dark_A). The AR of every vesicle in the uXRT scan is plotted against each vesicle's volume-equivalent spherical diameter (EqD) in the four panels (**Figure B4i**). We also show the average AR for each geometric size bin in the second panel above and assess the frequency of vesicles with a particular AR.

White_A vesicles have distinct elongation that varies with EqD but is captured in part by the watershedding analysis (**Figure B4ii**). The low vesicularity of white_A and dark_A (51 and 28% respectively) makes bubble decoalescence more straightforward and robust compared to decoalescence of higher vesicularity tube pumice. White_A and dark_A elongate vesicles also display strong orientation to a particular axis. The two raft samples (1b_try2 and s1_small_try) had less of a preferred vesicle orientation and more consistent aspect ratios where over 80% of the vesicle analyzed have AR <5 (these non-tube samples have 69 and 72% vesicularity). In White_A 80% of vesicles have AR > 5 (**Figure B4ii**).

In general, these results demonstrate that many samples contained highly oriented and elongated vesicles and that the degree of elongation can be quantified in 3D by the aspect ratio.

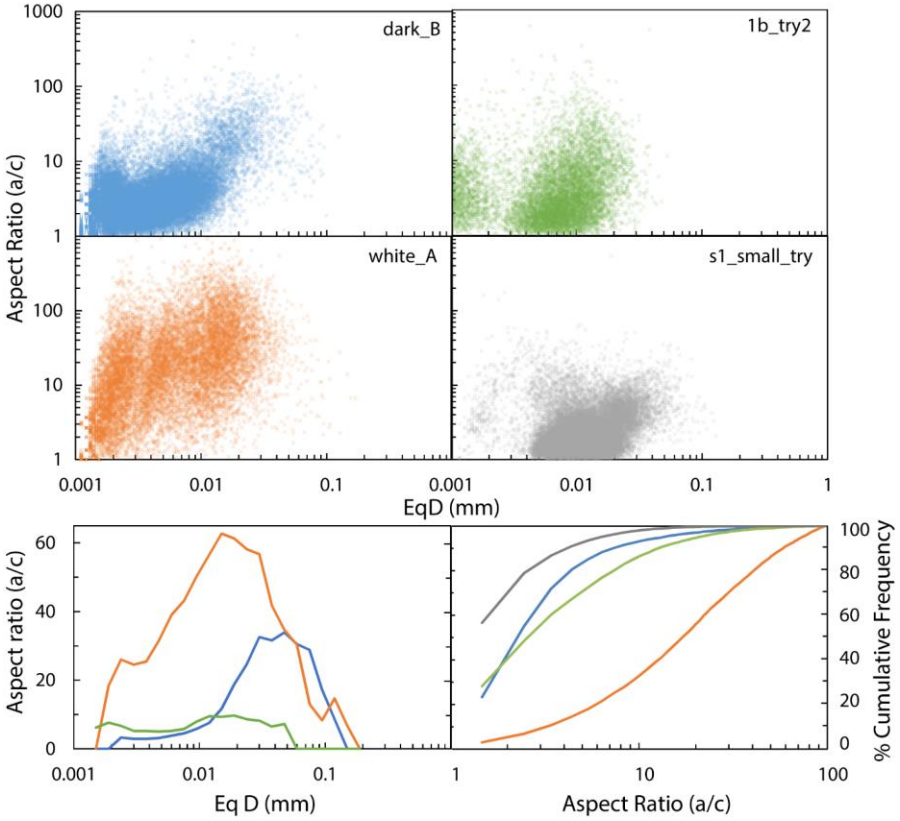

Figure B4i. Vesicle aspect ratios vs. vesicle spherical-equivalent-diameter (EqD) from 3D XRT analysis.

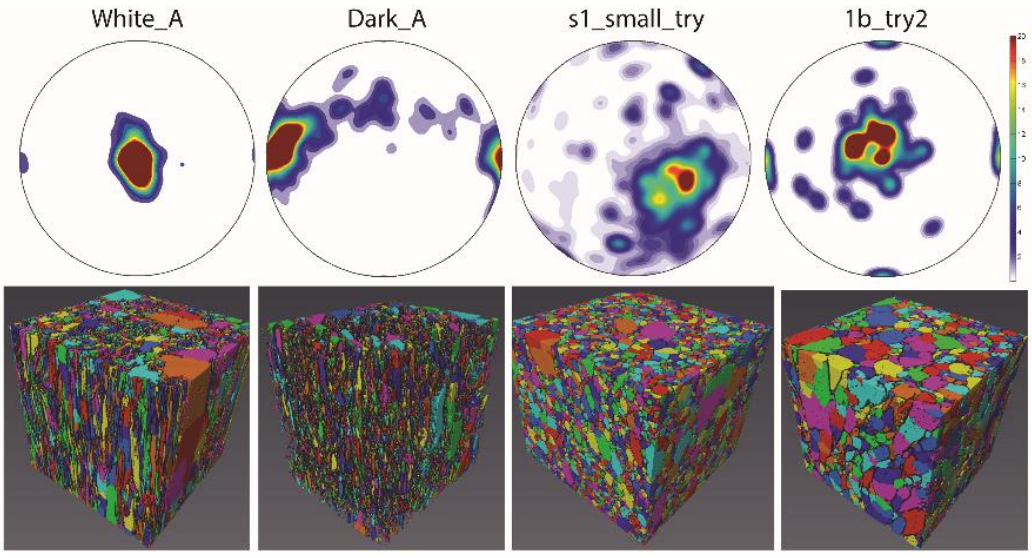

Figure B4ii. Pole figures of aspect ratios with respect to vesicle orientation, where the scale bar corresponds to aspect ratio. THis demonstrate that the bubbles are aligned in similar directions, particularly in tube pumice.

Appendix B5: *XRF analyses and standards*

Pumice samples were prepared for whole-rock geochemical analysis by cutting away altered surfaces and crushing material to obtain fresh ~1x1 cm pieces, which were washed in running hot water (~50°C) for 7–14 days to leach seawater. Once leached, pieces were broken in an iron mortar into 2–5 mm chips that were then washed in an ultrasonic bath using deionised water and acetone. The cleaned chips were dried in an oven at 110°C for >12 hours and then powdered. Before the major element analysis, 0.4 g of powder was weighed on a Metler Toledo dual balance system and ignited at 1025°C for 4 hours in an electric muffle furnace to determine loss-on-ignition (LOI). After the LOI determination, glass beads containing lithium tetraborate flux (10 to 1 dilution of sample) were prepared. The glass beads were analyzed by X-ray fluorescence (Rigaku RIX1000) at the National Museum of Nature and Science, Tokyo, Japan for major elements. Values for analytical precision and accuracy (± 2 standard deviations), as estimated from repeated analysis of well-established reference standard JB-1, are provided in the table below:

Table B5i. Concentrations are given as oxide concentration wt. % for all elements except Cl, S and the trace elements.

Element (wt. %)	SiO_2	TiO_2	Al_2O_3	Fe_2O_3	MnO	MgO	CaO	Na_2O	K_2O	P_2O_5
JB-1 average	52.7	1.3	14.4	8.9	0.2	7.9	9.3	2.8	1.5	0.3
2 SD	0.05	0.01	0.02	0.01	0.00	0.001	0.01	0.02	0.00	0.00
JB-1 GeoRem	52.4	1.3	14.5	9.0	0.2	7.7	9.3	2.8	1.4	0.3
% offset	0.55	0.53	-0.7	-0.75	-1.96	2.48	0.68	-0.47	1.4	1.96

XRF analysis of all samples

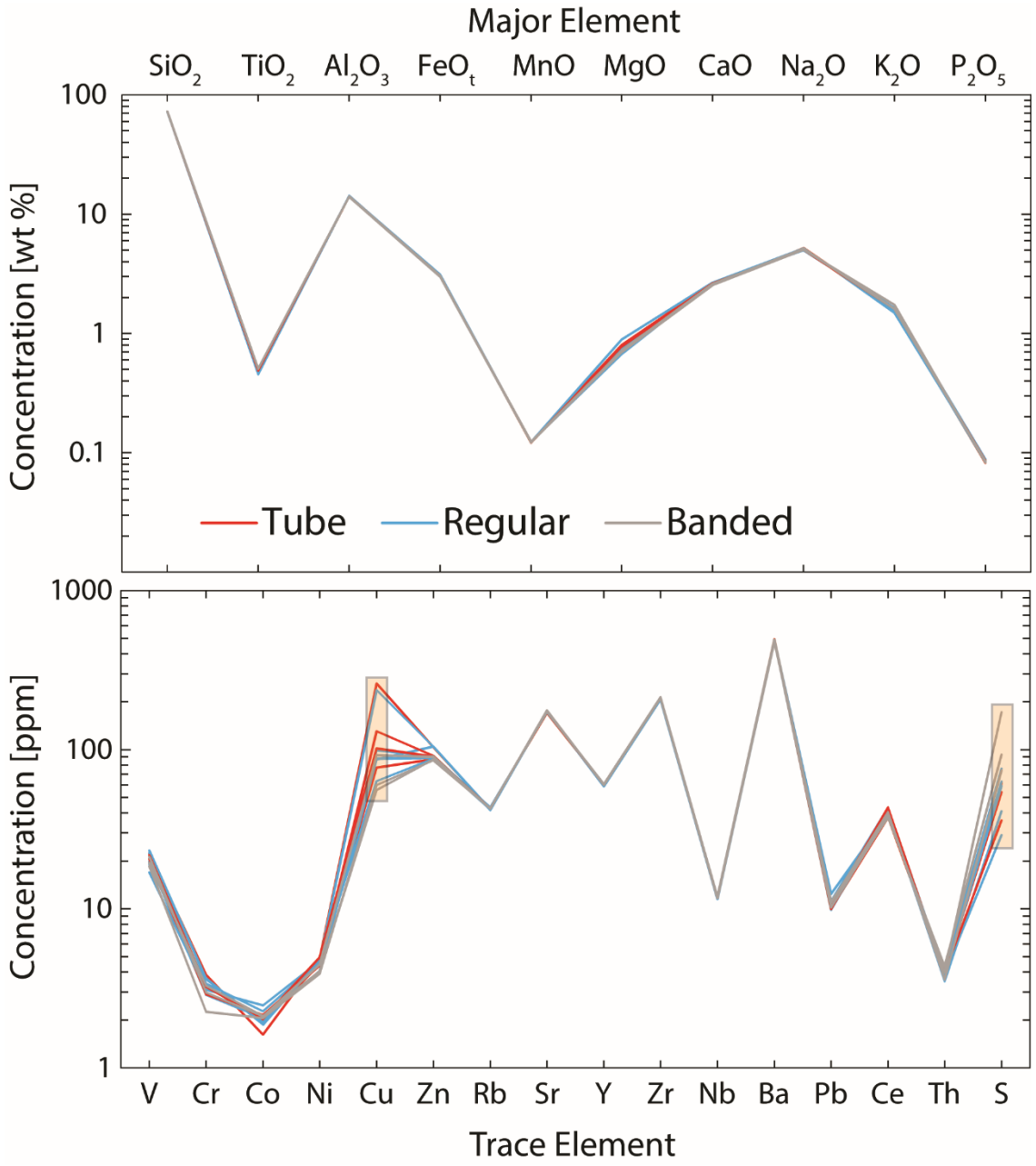

Figure B5ii. A compilation of all XRF analyses with major elements normalized to 100 total wt. %. Colored lines correspond to macrotextural classifications. In the trace element plot, orange boxes denote elements with deviation outside of 80% confidence with a 1:1 relationship: Cu and S.

S variations are an artifact of low volatilization temperatures during XRF analyses and Cu variations could be the result of hydrothermal alteration on clast exteriors or Cu-rich water diffusing into the glass at higher temperature during rapid rehydration (Mitchell et al., 2018a).

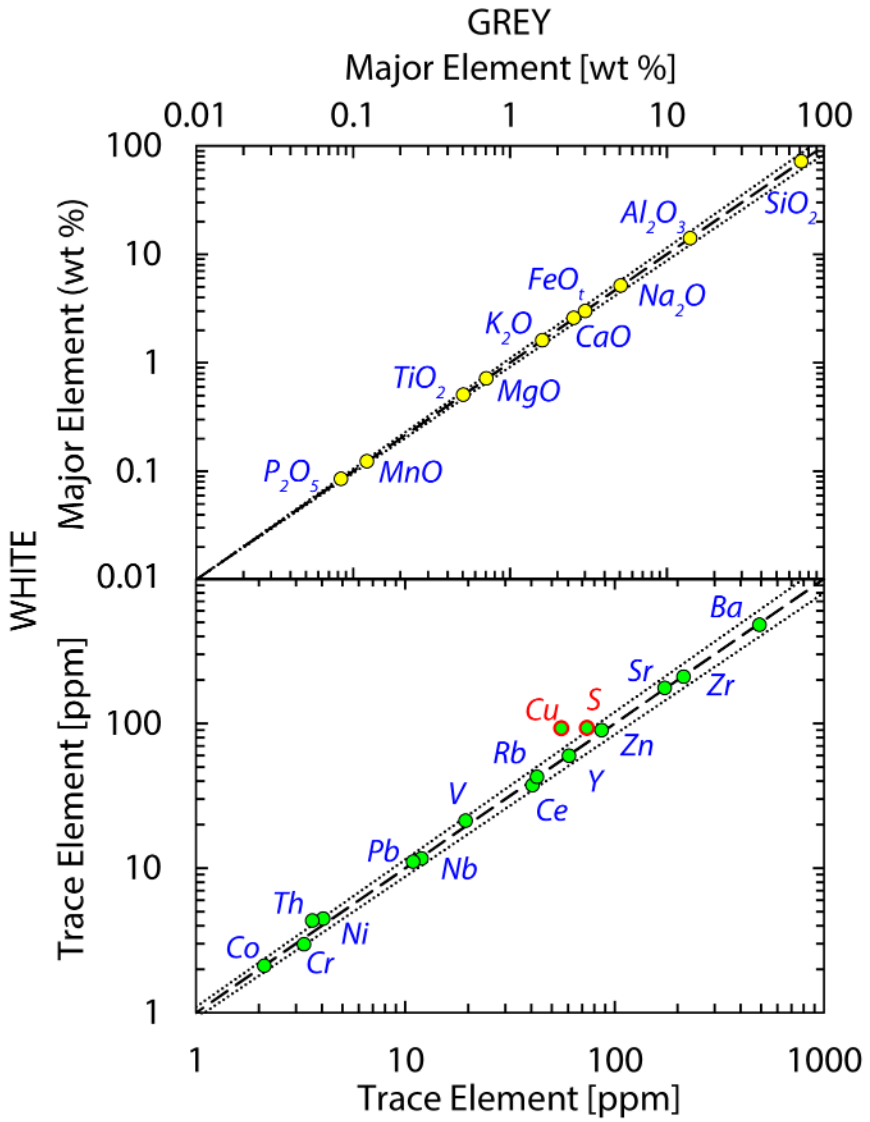

Figure B5ii. A comparison of major, minor and trace element content within adjacent white and grey bands from whole rock XRF analysis of GP290. The dashed line gives a 1:1 relationship with an 80% confidence interval bounded by the dotted lines. Cu and S lie outside of this confidence (highlighted in red).

Major Element Geochemistry (XRF and glass)

Table B5ii. XRF whole rock and EPMA glass (*italics*) major element geochemistry for GP samples after normalization to 100 wt. %. All values given in wt. %. Samples are defined by their HVR_ sample number and macrotextural classification. Iron is corrected to FeO_t from Fe_2O_3 (XRF analysis only). *S and Cl values given in ppm, and Cl is only available for glass analyses.

Group	**Regular**					**Tube**				**Banded**		
HVR_	041	096	192	221	231	003	022	115	270	290	290_Grey	290_White
SiO_2	72.07	72.02	71.85	72.15	72.21	71.95	72.18	72.09	72.11	72.34	72.17	72.11
	74.12	*73.92*	*73.76*	*73.89*	*74.05*	*74.15*	*74.35*	*73.90*	*74.19*	*75.38*		
TiO_2	0.48	0.47	0.50	0.46	0.45	0.47	0.46	0.46	0.49	0.51	0.51	0.51
	0.38	*0.37*	*0.41*	*0.36*	*0.39*	*0.38*	*0.40*	*0.40*	*0.38*	*0.46*		
Al_2O_3	14.16	14.24	14.16	14.14	14.09	14.22	14.05	14.18	14.10	13.98	14.09	14.08
	13.88	*13.87*	*13.89*	*13.94*	*14.01*	*13.90*	*13.87*	*13.88*	*13.92*	*13.09*		
FeO_t	3.05	3.05	3.11	3.04	3.01	3.06	3.02	3.04	3.05	2.99	3.06	3.03
	2.44	*2.51*	*2.57*	*2.43*	*2.41*	*2.53*	*2.36*	*2.45*	*2.40*	*2.42*		
MnO	0.12	0.12	0.12	0.12	0.12	0.12	0.12	0.12	0.12	0.12	0.12	0.12
	0.11	*0.11*	*0.11*	*0.10*	*0.11*	*0.11*	*0.11*	*0.10*	*0.11*	*0.11*		
MgO	0.71	0.67	0.89	0.69	0.74	0.80	0.73	0.77	0.78	0.70	0.71	0.72
	0.37	*0.44*	*0.46*	*0.37*	*0.36*	*0.44*	*0.35*	*0.42*	*0.38*	*0.34*		
CaO	2.64	2.67	2.67	2.60	2.59	2.66	2.58	2.63	2.63	2.54	2.56	2.60
	2.09	*2.13*	*2.20*	*2.07*	*2.09*	*2.13*	*1.95*	*2.13*	*2.04*	*1.64*		
Na_2O	5.07	5.17	4.97	5.16	5.17	5.05	5.20	5.08	5.03	5.01	5.09	5.14
	4.68	*4.75*	*4.75*	*4.94*	*4.77*	*4.55*	*4.80*	*4.91*	*4.74*	*4.56*		
K_2O	1.61	1.49	1.63	1.55	1.52	1.58	1.58	1.55	1.61	1.73	1.61	1.61
	1.61	*1.63*	*1.58*	*1.63*	*1.57*	*1.54*	*1.57*	*1.56*	*1.58*	*1.75*		
P_2O_5	0.09	0.09	0.09	0.08	0.09	0.09	0.08	0.08	0.09	0.08	0.08	0.08
	0.03	*0.05*	*0.06*	*0.06*	*0.04*	*0.06*	*0.05*	*0.05*	*0.05*	*0.06*		
***S**	41	29	63	76	59	62	61	54	36	172	74	93
	67	*120*	*57*	*136*	*37*	*78*	*23*	*129*	*51*	*112*		
Cl	-	-	-	-	-	-	-	-	-	-	-	-
	0.19	*0.22*	*0.22*	*0.20*	*0.19*	*0.19*	*0.19*	*0.19*	*0.20*	*0.21*		

Trace Element Geochemistry

Table B5iii. Raw XRF whole rock minor and trace element geochemistry GP samples. Samples are defined by their HVR_ sample number and macrotextural classification. Iron is corrected to FeO_t from Fe_2O_3. All concentration values are given in ppm.

Group	**Regular**					**Tube**				**Banded**		
HVR_	041	096	192	221	231	003	022	115	270	290	290_Grey	290_White
V	22.46	19.89	23.29	16.95	19.06	22.25	19.57	20.58	21.68	18.51	19.44	19.44
Cr	3.61	2.87	3.66	3.09	3.39	3.86	3.29	2.90	3.23	2.25	3.28	3.28
Co	1.93	2.06	1.87	2.47	2.27	1.62	1.96	2.15	2.04	2.06	2.12	2.12
Ni	4.79	4.06	4.77	4.68	4.65	4.89	4.45	4.41	4.96	3.92	4.05	4.05
Cu	63.53	86.67	236.25	87.85	99.20	260.28	77.18	130.69	101.97	59.85	55.8	55.8
Zn	87.64	104.46	104.78	88.74	90.80	103.74	87.13	91.61	90.41	85.68	86.65	86.65
Rb	42.17	42.21	41.74	42.96	43.37	42.15	43.10	42.73	42.61	42.75	42.72	42.72
Sr	175.72	176.31	174.58	172.93	172.52	174.27	170.50	173.53	174.04	174.93	173.74	173.74
Y	59.38	59.1	58.76	59.96	60.13	59.42	59.96	59.65	59.90	59.94	60.61	60.61
Zr	209.29	206.95	206.72	212.99	213.53	207.85	211.88	210.61	211.94	211.99	213.84	213.84
Nb	11.66	11.62	11.52	11.75	11.82	11.61	11.79	11.68	11.74	11.74	11.94	11.94
Ba	484.89	485.27	479.35	489.45	491.20	485.61	494.03	488.18	483.47	486.29	491.66	491.66
Pb	9.85	12.37	10.96	11.14	10.25	10.08	10.02	9.98	10.40	10.19	10.92	10.92
Ce	40.44	39.44	41.56	43.22	40.61	43.02	37.50	40.73	43.27	38.23	40.46	40.46
Th	3.51	3.91	3.79	4.05	3.85	3.83	3.94	3.95	3.98	3.98	3.59	3.59

Phenocryst compositions in GP290

Table B5iv. Major element compositions the two major phenocryst phases found throughout GP samples: Plagioclase and Pyroxene.

Phenocryst	SiO_2 wt. %	TiO_2 wt. %	Al_2O_3 wt. %	Cr_2O_3 wt. %	FeO wt. %	MgO wt. %	CaO wt. %	Na_2O wt. %	K_2O wt. %	Mg#	Ca/Al	Na+K
Pyroxene	51.23	0.23	0.68	0.03	23.33	20.57	1.45	0.02	0.00	46.85	2.12	0.02
	51.24	0.25	0.59	0.00	22.83	20.80	1.37	0.02	0.00	47.67	2.33	0.02
	51.14	0.21	0.75	0.03	23.10	20.43	1.39	0.04	0.00	46.92	1.86	0.04
	51.02	0.22	0.90	0.00	23.17	20.43	1.45	0.03	0.00	46.85	1.61	0.03
	50.93	0.18	0.47	0.02	25.82	18.42	1.35	0.01	0.00	41.64	2.86	0.01
	50.47	0.22	0.85	0.00	25.09	18.96	1.38	0.03	0.00	43.04	1.63	0.03
Average	*51.00*	*0.22*	*0.71*	*0.01*	*23.89*	*19.93*	*1.40*	*0.02*	*0.00*	*45.48*	*1.98*	*0.02*
Plagioclase	57.30	0.04	25.36	0.01	0.35	0.02	7.94	6.83	0.13	5.46	0.31	6.96
	57.23	0.02	25.49	0.01	0.35	0.02	7.85	6.77	0.13	4.94	0.31	6.90
	55.92	0.01	26.24	0.00	0.34	0.02	8.85	6.29	0.11	6.52	0.34	6.40
	55.84	0.04	26.26	0.00	0.40	0.02	8.85	6.39	0.12	5.76	0.34	6.50
	57.07	0.03	25.52	0.00	0.42	0.03	8.02	6.77	0.13	7.28	0.31	6.89
	56.24	0.04	26.15	0.03	0.46	0.03	8.68	6.46	0.12	7.09	0.33	6.58
	55.46	0.02	26.43	0.01	0.47	0.05	9.21	6.11	0.11	8.71	0.35	6.22
	55.32	0.01	26.43	0.00	0.45	0.04	9.13	6.08	0.09	7.36	0.35	6.17
	56.21	0.00	26.01	0.01	0.40	0.04	8.57	6.57	0.11	8.09	0.33	6.68
	56.21	0.02	26.00	0.00	0.33	0.03	8.62	6.34	0.13	8.19	0.33	6.46
	55.39	0.03	26.48	0.02	0.46	0.03	8.93	6.20	0.12	5.63	0.34	6.32
	55.61	0.00	26.63	0.00	0.40	0.04	9.09	6.35	0.12	8.62	0.34	6.47
	55.39	0.01	26.64	0.00	0.45	0.04	9.36	6.05	0.11	8.15	0.35	6.16
	55.74	0.02	26.04	0.01	0.44	0.03	8.85	6.15	0.13	7.08	0.34	6.28
	56.03	0.07	25.81	0.00	0.57	0.05	9.01	5.68	0.19	8.34	0.35	5.87
	54.98	0.03	26.67	0.00	0.52	0.03	9.48	5.86	0.12	5.78	0.36	5.98
Average	*56.00*	*0.02*	*26.13*	*0.01*	*0.43*	*0.03*	*8.78*	*6.31*	*0.12*	*7.12*	*0.34*	*6.43*

Appendix B6: *Alkali metals bivariate plot*

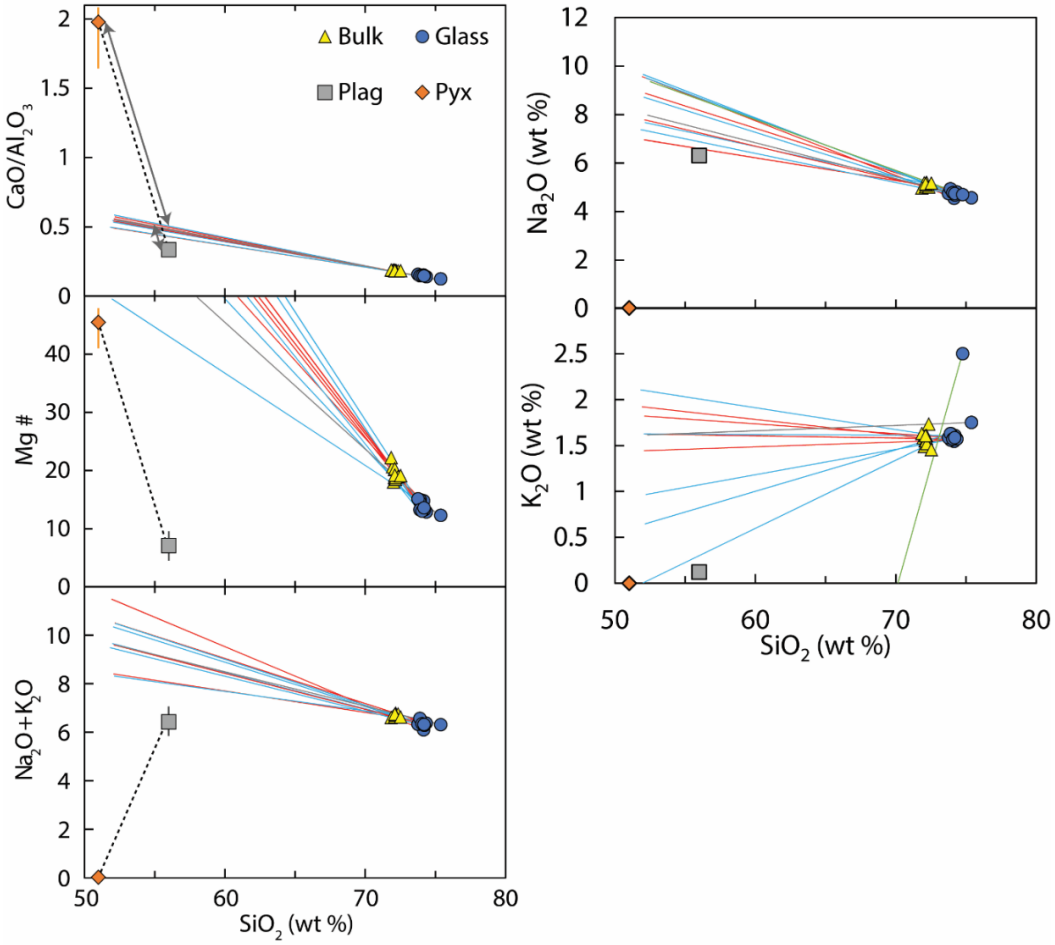

Figure B6. Bivariate major elemnet plots of giant pumice whole rock (bulk), matrix glass and phenocryst compositions with equilibrium crystalliation lines corresponding to the macroscale textural classifications.

Based on major element variations with SiO_2, variations in Ca, Al and Na within glass are attributed to the equilibrium crystallization of plagioclase and orthopyroxene, both in the phenocryst and microlite assemblages (**Figures 3.2** and **B6**). Mg and Fe variations cannot be explained by the equilibrium crystallization of phenocrysts, but could be explained by the crystallization of orthopyroxene and Fe-Ti oxide microlites (**Figure B6**). The grey banding crystallization trends in GP290 match those of other giant pumice. Banding in GP290 appears to be textural rather than due to whole rock composition. The nucleation and growth of more sodic "albite" feldspar microlites at lower temperature conditions can account for the need of more Na-rich crystal source to produce the determined glass compositions.

Appendix B7: *Porosity and permeability*

Table B7. Results from Helium pycnometry and permeability analysis. k_1 (Darcian perm.) and k_2 (inertial perm.) were acquired through capillary flow porometry of cylindrical cores. *Data acquired from Manga et al. (2018).

HVR_Sample	Total porosity (%)	Connected porosity (%)	Isolated porosity (%)	Connectivity	k_1 (m^2)	k_2 (m^2)
003a	88.52	1.57	86.95	0.98	-	-
003b	89.94	0.91	89.03	0.99	-	-
003c	90.02	1.27	88.75	0.99	-	-
022Yi	78.25	40.97	37.28	0.48	-	-
022Yii	71.15	-12.88	84.03	1.18	-	-
103X	84.11	3.04	81.07	0.96	4.57E-13	2.38E-09
103Yi	84.84	2.20	82.64	0.97	2.44E-11	5.11E-07
103Yii	84.40	1.54	82.86	0.98	2.67E-11	7.40E-07
103Yiii	85.56	1.54	84.02	0.98	1.30E-09	1.43E-05
115X	84.52	1.13	83.39	0.99	-	-
115Yi	83.17	2.83	80.34	0.97	5.54E-12	2.03E-07
115Yii	85.15	1.90	83.25	0.98	3.53E-11	5.11E-07
115Yiii	84.36	2.27	82.09	0.97	3.72E-11	5.61E-07
121Yi	87.04	1.82	85.21	0.98	2.07E-09	1.89E-05
121Yii	87.41	1.78	85.62	0.98	2.27E-09	2.49E-05
121Yiii	85.23	2.17	83.06	0.97	6.75E-11	8.91E-07
121Yiv	84.35	1.80	82.55	0.98	1.18E-10	8.91E-07
133X	86.52	0.99	85.53	0.99	2.03E-11	1.85E-07
133Y	84.70	1.88	82.82	0.98	1.27E-11	1.68E-07
223Yi	77.59	4.87	72.72	0.94	6.08E-12	1.40E-07
223Yii	75.93	3.15	72.79	0.96	2.20E-12	3.49E-08
281Xi	84.99	2.47	82.52	0.97	7.23E-13	4.55E-09
281Xii	85.31	1.83	83.48	0.98	1.38E-12	1.66E-08
281Xiii	85.04	2.32	82.72	0.97	3.83E-12	4.61E-08
281Yi	85.54	1.67	83.88	0.98	-	-
281Yii	87.12	1.50	85.62	0.98	-	-
041Yi	83.49	2.83	80.66	0.97	6.75E-11	5.61E-07
041Yii	85.49	1.95	83.54	0.98	6.15E-11	4.66E-07
096Yi	88.85	0.95	87.89	0.99	3.49E-12	3.83E-08
096Yii	89.87	0.57	89.30	0.99	2.90E-12	3.49E-08
106	87.38	0.79	86.59	0.99	2.44E-11	2.22E-07
125X	89.43	-0.32	89.76	1.00	3.83E-12	7.32E-08
125Y	88.40	0.46	87.94	0.99	3.83E-12	2.90E-08
164Yi	68.37	3.78	64.59	0.94	7.32E-12	8.03E-08
192a	90.18	0.48	89.70	0.99	1.27E-11	3.87E-07
192b	90.14	0.52	89.62	0.99	5.11E-11	6.75E-07
192c	89.83	0.34	89.49	1.00	2.71E-10	5.67E-06
221	84.42	2.86	81.57	0.97	1.53E-11	1.53E-07
227Xi	78.51	4.02	74.49	0.95	-	-
227Xii	82.76	3.26	79.50	0.96	8.03E-12	1.27E-07
227Y	82.53	2.28	80.25	0.97	1.16E-11	1.40E-07
*227_a	85.74	1.62	84.12	0.98	2.27E-10	1.37E-06
*227_b	85.09	1.80	83.30	0.98	5.39E-12	4.70E-08
231a	79.76	3.28	76.47	0.96	2.41E-12	3.18E-08
231b	80.71	2.32	78.38	0.97	2.64E-12	3.18E-08
*262_a	87.25	1.17	86.08	0.99	8.17E-12	1.24E-07
*262_b	87.40	-2.19	89.59	1.03	3.10E-12	3.25E-08

044a	81.56	3.63	77.94	0.96	8.03E-12	1.40E-07
044b	79.94	4.57	75.37	0.94	1.85E-11	2.22E-07
044c	81.34	3.94	77.41	0.95	1.83E-11	2.22E-07
139a	82.92	2.47	80.45	0.97	2.00E-12	2.20E-08
139b	84.41	2.10	82.32	0.98	2.20E-12	3.18E-08
139c	83.02	2.84	80.18	0.97	2.41E-12	2.64E-08
139d	79.81	4.28	75.53	0.95	3.83E-12	2.00E-08
165X	87.75	-0.39	88.14	1.00	8.12E-11	4.66E-07
165Yi	85.92	1.48	84.45	0.98	1.42E-10	2.05E-06
165Yii	82.94	2.78	80.16	0.97	5.17E-10	1.3E-05
226a	79.45	2.73	76.72	0.97	6.22E-10	2.27E-05
226b	81.67	2.44	79.23	0.97	2.47E-10	1.87E-06
243a	81.30	3.20	78.10	0.96	2.97E-10	3.92E-06
243b	80.11	3.64	76.47	0.95	6.83E-10	3.00E-05
267Yi	81.85	2.98	78.87	0.96	6.67E-12	1.16E-07
267Yii	81.50	2.99	78.51	0.96	6.22E-10	2.49E-05
278a	81.61	1.85	79.76	0.98	3.49E-12	2.90E-08
278b	79.06	2.61	76.45	0.97	2.00E-12	1.52E-08
*290	78.21	-0.70	78.91	1.01	1.18E-12	5.36E-09
*"	80.31	-0.93	81.25	1.01	1.43E-10	3.75E-07
"	78.62	0.28	78.34	1.00	1.23E-12	5.62E-09
"	74.80	1.66	73.14	0.98	1.13E-11	7.8E-08
"	79.49	0.34	79.15	1.00	2.14E-12	9.33E-09
"	74.73	1.19	73.54	0.98	1.42E-11	1.36E-07
"	80.55	-0.10	80.65	1.00	3.1E-12	1.55E-08
"	79.59	-0.04	79.63	1.00	3.4E-12	2.83E-08
"	60.90	24.91	35.99	0.59	-	-
"	79.93	0.02	79.91	1.00	9.33E-13	8.91E-09
"	78.50	-0.09	78.59	1.00	1.49E-11	1.62E-08
"	77.69	1.30	76.40	0.98	2.96E-12	7.76E-09
"	79.24	0.44	78.80	0.99	2.96E-12	2.35E-08
"	78.73	0.91	77.82	0.99	1.86E-12	1.18E-08
"	76.63	1.68	74.95	0.98	2.35E-12	1.29E-08
"	80.23	0.55	79.67	0.99	1.42E-11	1.56E-07
"	80.28	0.41	79.87	0.99	5.65E-12	7.80E-08
"	79.94	0.41	79.53	0.99	3.25E-12	4.09E-08
"	78.06	0.76	77.29	0.99	1.62E-12	6.75E-09
"	83.02	-1.16	84.18	1.01	1.08E-11	7.45E-08
"	78.71	-2.04	80.75	1.03	1.48E-12	3.71E-09
"	77.04	-0.38	77.41	1.00	3.25E-12	4.48E-08
"	77.15	-0.65	77.79	1.01	1.18E-12	3.71E-09
"	77.39	-0.60	77.99	1.01	1.30E-11	1.30E-07
"	80.16	-1.33	81.49	1.02	2.05E-12	1.23E-08
"	77.90	-0.29	78.19	1.00	1.95E-12	1.23E-08
"	76.74	-0.39	77.13	1.01	3.56E-12	1.07E-08

Appendix B8: *Microlite number densities*

Table B8. Breakdown of microlite number densities for all giant pumice samples including different microlite phases identified: Plagioclase feldspar, Fe-Ti oxides, pyroxenes and quartz.

Sample (HVR_)		3	22	41	96	115	192	221	231	270	290	290I
Images analyzed		2	6	4	6	5	3	4	6	7	5	5
Total melt area (mm^2)		0.02	0.05	0.03	0.05	0.03	0.01	0.13	0.07	0.06	0.01	0.05
Total area (mm^2)		0.09	0.14	0.19	0.42	0.23	0.14	0.46	0.28	0.22	0.04	0.13
Vesic. (%)		78.84	65.72	81.39	87.27	85.73	89.45	70.97	74.96	73.41	62.48	67.25
Phase (mN)	Plag	2	23	101	4	7	1	22	31	19	505	527
	Oxide	44	623	816	141	444	31	811	1084	604	1367	1684
	Pyx.	0	14	38	7	32	4	59	25	1	45	63
	Quartz	0	1	0	0	0	2	0	0	0	0	0
Total mN		46	661	955	152	483	38	892	1140	624	1917	2274
Phase (mN_A) (mm^{-2})	Plag	101	468	2907	86	210	68	174	442	320	34684	11168
	Oxide	2229	12675	23489	3026	13337	2100	6404	15461	10160	93887	35686
	Pyx.	0	285	1094	150	961	271	466	357	17	3091	1335
	Quartz	0	20	0	0	0	135	0	0	0	0	0
mN_A (mm^{-2})		2330	13449	27490	3263	14509	2574	7044	16260	10496	131662	48188
Corrected Phase (mN_A cr) (mm^{-2})	Plag	21	165	541	10	30	7	48	111	86	12594	4108
	Oxide	472	4479	4373	338	1903	221	1759	3871	2733	34090	13125
	Pyx.	0	101	204	17	137	29	128	89	5	1122	491
	Quartz	0	7	0	0	0	14	0	0	0	0	0
mN_A (cr) (mm^{-2})		493	4752	5118	364	2070	271	1935	4071	2824	47805	17724

Appendix B9: *Secondary vesicle growth*

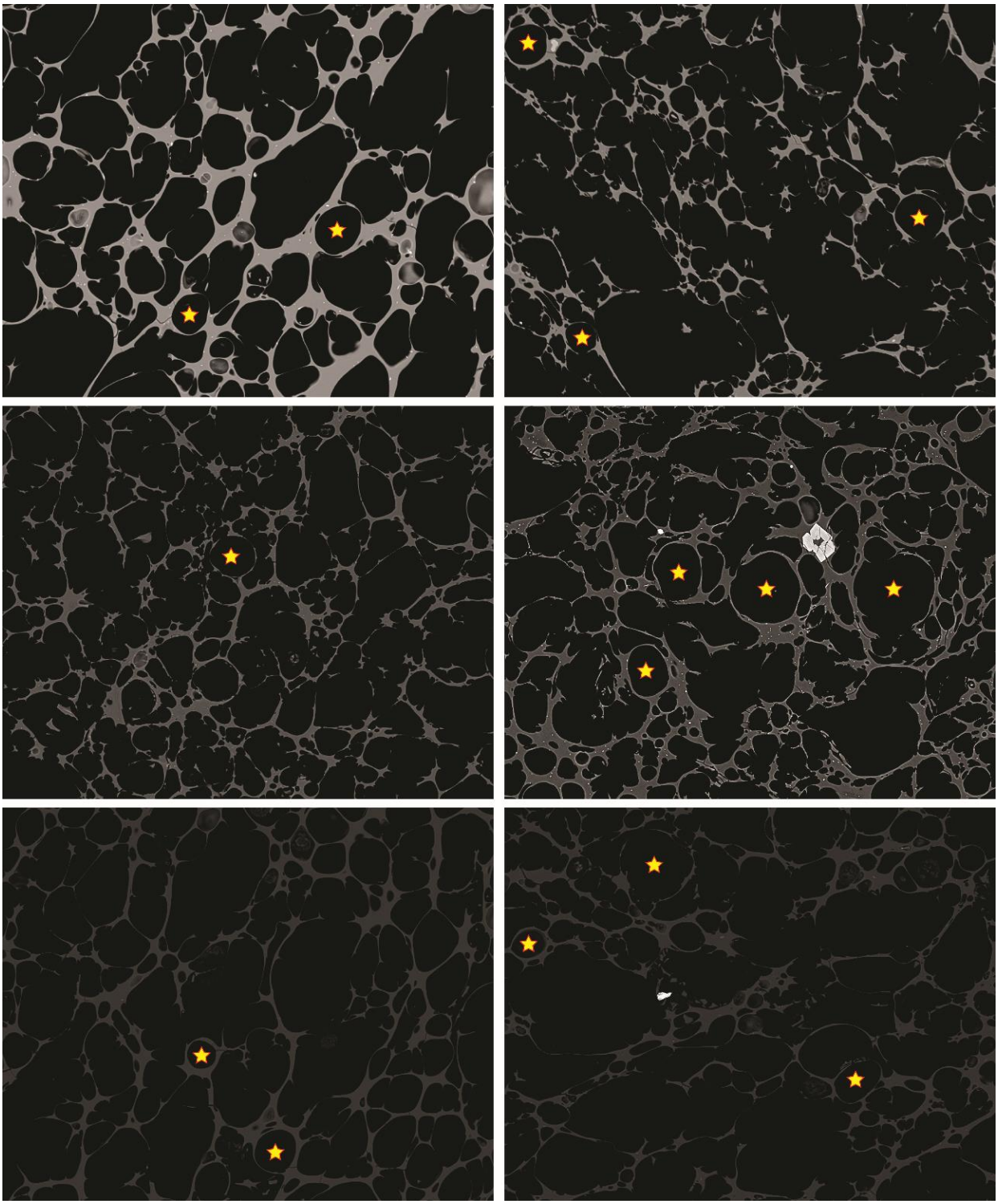

Figure B9. BSE images at 250x magnification of vesicles with implied secondary growth. Each image is 480 µm wide. Stars denote vesicles with inferred secondary growth. Images have different contrasts.

Very circular vesicles (starred) are surrounded by vesicles with deformed shapes. We propose that these textures represent two stage of bubble growth: 1) growth of bubbles following the primary conduit nucleation driven by decompression during magma ascent, and 2) the growth of vesicles after eruption of magma into the water column driven by decompression during buoyant clast ascent while melt / glass was ductile and bubble were able to grow. These post-disruption vesicles tend not to have coalesced with the surrounding older vesicles (**Figure B9**).

Appendix B10: 2D conduit strain model

The deformation model developed to assess vesicle shearing and expected aspect ratios was based the results of the conduit ascent model for Havre in Manga et al. (2018) (see **Figure B10i**). This 1D two-phase steady flow model was modified from Degruyter et al. (2012) and Kozono and Koyaguchi, (2009). The model calculates the magma pressure, viscosity (μ), velocity (u), strain rate ($\dot{\gamma}$) and gas fraction (ϕ) for a set of pre-determined parameters (Manga et al., 2018). Vesicle size (x_b) is calculated based on an input vesicle number density of 2.5×10^8 cm^{-3} (**Table 3.1**) as an average for the giant pumice N_{Vm} data from the results:

$$x_b = \left(\frac{3\phi}{4\pi(1-\phi)N_{Vm}}\right)^{1/3} \quad \text{(Eq. B12)}$$

Viscosity, gas fraction, pressure and vesicle size remain constant over the conduit width (R_C). We assume two values for conduit radii (25 and 50 m) with a constant mass discharge rate of 10^7 kg s^{-1} (Carey et al., 2018; Manga et al., 2018). We chose 50 m to assess the possibility of a flaring shallow conduit on the strain approaching the vent; the doubling of the conduit radius required a reduction of the mean velocity by a factor of four for conservation of mass. In the laminar regime the velocity (u) profile (Eq. **B13**) is parabolic follows a simple parabolic (Llewellin and Manga, 2005):

$$u(r,z) = u_l(z)\left(1 - \frac{r^2}{{R_C}^2}\right) \quad \text{(Eq. B13)}$$

where R_C is the conduit radius and r is the distance from the conduit center. Subscripts g and l denote gas and liquid phases; the calculated melt and gas velocities were very similar for the Havre

conditions, i.e., the bubbles remain coupled to the melt (Manga et al., 2018). Shear strain rate ($\dot{\gamma}$) across the conduit was calculated from (e.g., Llewellin and Manga, 2005):

$$\dot{\gamma}(r,z) = \frac{4u(r,z)r}{{R_C}^2} \qquad \text{(Eq. } \mathbf{B14}\text{)}$$

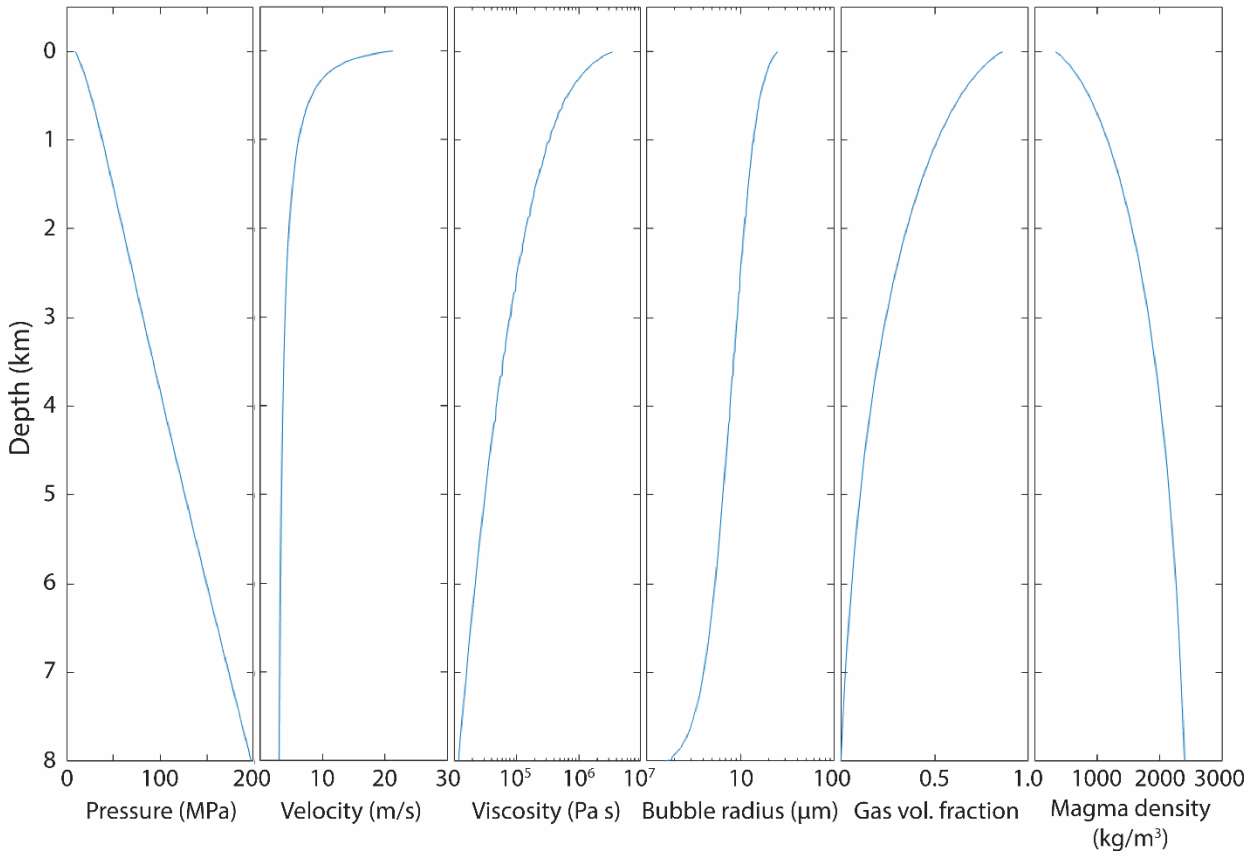

Figure B10i. Results of the 1D conduit ascent model (Manga et al., 2018) when reapplied into the strain model for magma pressure, mean bubble radius, magma viscosity, gas fraction and bulk magma density vs. conduit depth. Initial conditions are set as crystal fraction of 0.05, initial H_2O content of 5.8 wt. %, bubble number density of $2x10^8$ cm^{-3}, conduit depth of 8 km in depth steps (*z*) of 5 m, initial storage pressure of 200 MPa, melt density of 2400 kg m^{-3}, mass eruption rate of 10^7 kg s^{-1} (Carey et al., 2018), and a vent pressure of 9 MPa.

The Reynolds number (Re) calculated throughout the conduit (Re < 100 at all depths) supports our use of a laminar velocity profile:

$$\mathrm{Re}(z) = 2u_l(z)R_c\frac{(\phi(z)\rho_g(z)+(1-\phi(z))\rho_l(z))}{(\phi(z)\mu_g(z)+(1-\phi(z))\mu_l(z))} \quad \text{(Eq. } \mathbf{B15}\text{)}$$

The maximum upward velocity (u_{max}) and radial velocity across the conduit (u_r) was calculated at all depths using the mean liquid velocity (u_l) from Manga et al. (2018). Strain at each point in the conduit was calculated from:

$$\gamma(r,z) = \int^z \frac{\gamma(\dot{r},z)}{u_l(r,z)} \cdot dz \quad \text{(Eq. } \mathbf{B16}\text{)}$$

The capillary number (Ca), i.e., the ratio of bubble shearing to relaxation timescales, was calculated across the 2D conduit for a single evolving bubble size (x_b) through the conduit. We assume homogeneous bubble nucleation due to the very low crystallinity, using a bubble surface tension (σ) for rhyolite of 0.075 N m^{-1} (Shea, 2017). We then used Ca, together with the deformation models of Canedo et al. (1993) and Rust and Manga (2002) and basic geometric relations to determine the *maximum* expected bubble aspect ratios (AR) where AR is the ratio of the longest to shortest bubble axis.

$$\mathrm{Ca}(r,z) = \frac{x_b(z)\dot{\gamma}(r,z)\mu_l(r,z)}{\sigma} \quad \text{(Eq. } \mathbf{B17}\text{)}$$

$$AR(r,z) = 5.46\left(\frac{x_b(z)\dot{\gamma}(r,z)\mu_l(r,z)}{\sigma}\right)^{0.645} = 5.46\mathrm{Ca}(r,z)^{0.645} \quad \text{(Eq. } \mathbf{B18}\text{)}$$

A heterogeneous bubble nucleation assumption (lower surface tension ~0.02 N m^{-1}; Shea, 2017) would only increase AR by a factor of ~2.4. Decompression rate (dP/dt) as a function of lateral position across the conduit was calculated using the obtained pressure gradient (Manga et al., 2018):

$$\frac{dP}{dt}(r,z) = u_z\frac{\partial P}{\partial z} \quad \text{(Eq. } \mathbf{B19}\text{)}$$

We also note that the vesicle size chosen affects the capillary number and expected aspect ratio (**Figure B10ii**).

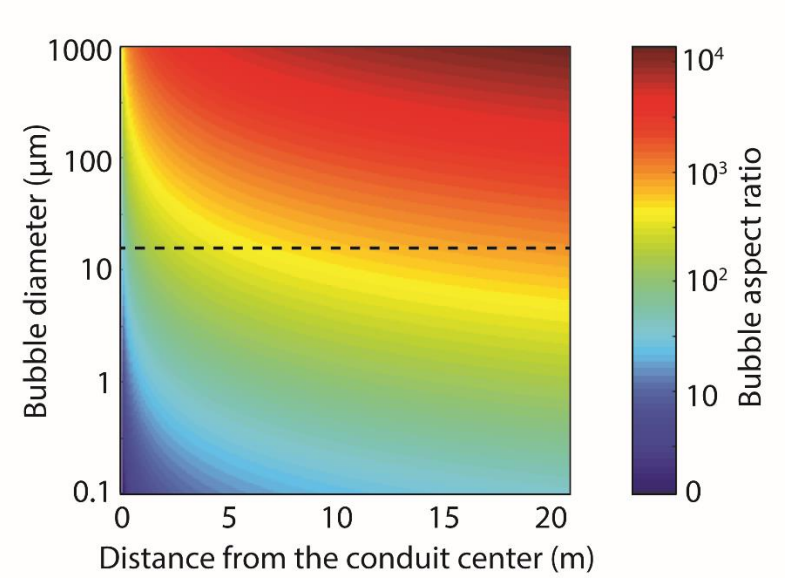

Figure B10ii. An example of how aspect ratios may be expected to change laterally across the top of conduit with vesicle size changing from 0.1 μm to 1 mm. The actual predicted vesicle diameter at this location in the conduit (4 m below the top of the 900 m deep conduit) from the Manga et al. (2018) model is 17 μm (given by dashed line).

APPENDIX C – SUPPLEMENTARY MATERIAL FOR CHAPTER 4

Appendix C1: *SIMS standards, calibration and sample preparation*

For SIMS analysis, melt inclusions were prepared by polishing a single quartz or plagioclase crystal face until a melt inclusion was exposed. Multiple crystals were then pressed into indium mounts at temperatures >50°C and polished down to a 1 µm finish; thickness of the crystal did not matter for SIMS analysis. The mounts were then coated with a few nm of gold particulate. Melt inclusions were only deemed suitable for analysis under several criteria: 1) no vapor bubbles present, 2) no contact with the crystal edge (melt embayment), 3) no cracks or fractures running through the melt inclusion. This reduced the possibility of recording melt inclusion degassing, rehydration or contamination signatures.

For matrix glasses, we mounted small chips of pumice (<5 mm^3) into an epoxy mount that was then also polished down to a 1 µm finish; these mounts were also coated with gold. Matrix glass analyses were challenging in the epoxy mount as there was little glass space within bubble walls and triple joints to avoid contact with the vesicle edge in high vesicularity samples; incomplete saturation of the pumice by epoxy could produce uneven surfaces at vesicle edges causing the sputtering of ions, particularly ^{12}C ions. The presence of epoxy also required a background correction that would remove unwanted $^{1}H^{16}O$ signatures from the matrix glass. By monitoring this background over time, it could be removed. Matrix glasses were analyzed using a spot size of 5 µm and melt inclusions were analyzed using a 10 µm spot size and a smaller field aperture.

Calibration curves were determined using a suite of basalt and rhyolite standards. Ion ratios from SIMS analysis were then converted into volatile concentrations (**Figure C1**).

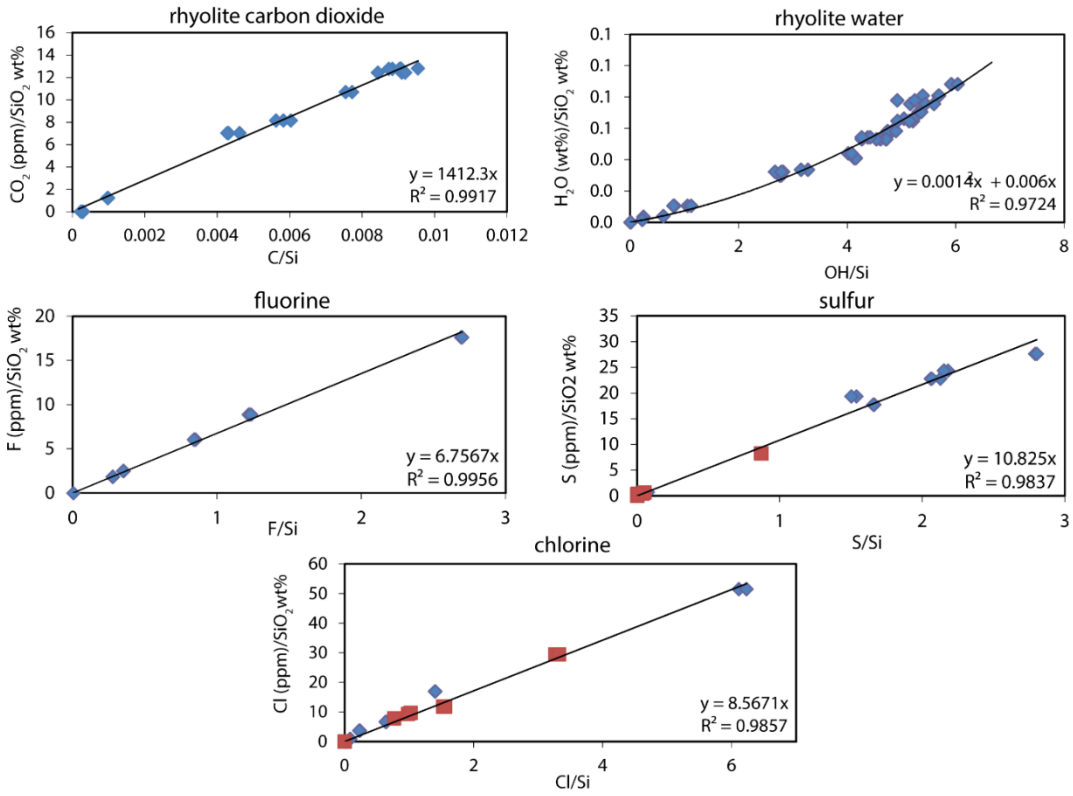

Figure C1. All standards had known SiO_2 concentrations from EPMA analysis and the relevant volatile concentrations pre-determined by either FTIR (H_2O, CO_2) or EPMA (S, Cl, F). Standards were provided by the Woods Hole Oceanographic Institution and analyzed by the in-house technician.

Appendix C2: *Density data of all units*

Table C2. Seafloor location and depth of all samples used in density analysis. For density and vesicularity, we give the mean, ±1 standard deviation of error, maximum and minimum values.

Unit	Sample (HVR_)	Latitude	Longitude	Depth (m)	Vesicularity (%)				Density (10^3 g cm^{-3})				Distance from vent (km) (±0.05)
					Mean	1σ	Min.	Max.	Mean	1σ	Max.	Min.	
GP	3	-31.1235154	-179.006419	943.65	76.1	2.6	64.3	80.3	0.57	0.06	0.85	0.47	1.03
	22	-31.1262671	-179.028607	954.01	62.2	3.0	58.8	66.8	0.90	0.07	0.98	0.79	1.20
	41	-31.104633	-179.038248	1506.54	77.7	4.4	69.3	81.9	0.53	0.10	0.73	0.43	3.12
	95	-31.1249872	-179.035137	989.44	87.8	1.1	87.4	88.7	0.29	0.03	0.30	0.27	1.81
	96	-31.1267127	-179.03372	972.03	78.2	4.2	69.3	85.3	0.52	0.10	0.73	0.35	1.65
	115	-31.1323813	-179.016820	844.39	76.5	2.0	71.8	79.8	0.56	0.05	0.67	0.48	0.42
	192	-31.1341369	-179.005382	1012.28	85.7	1.5	82.8	87.4	0.34	0.03	0.41	0.30	1.19
	221	-31.1054191	-179.059096	1056.46	68.5	2.4	65.5	71.0	0.75	0.06	0.82	0.69	4.65
	231	-31.0877823	-179.060500	826.41	78.2	5.7	58.4	86.6	0.52	0.13	0.99	0.32	5.81
	270	-31.0845673	-179.041096	800.89	66.4	4.9	52.5	79.4	0.80	0.11	1.13	0.49	4.92
	290	-31.1297531	-179.031076	950.39	73.5	3.2	64.3	84.5	0.63	0.08	0.85	0.37	1.43
ALB	120	-31.13262652	-179.012698	756.25	79.8	9.4	24.8	88.2	0.48	0.22	1.79	0.28	0.54
	124	-31.13722351	-179.017192	874.38	79.8	3.0	73.5	84.5	0.48	0.07	0.63	0.37	0.90
	127	-31.1384347	-179.013123	960.79	77.3	6.8	63.9	85.7	0.54	0.16	0.86	0.34	1.05
	131	-31.1342714	-179.011934	695.75	75.2	4.8	65.5	82.4	0.59	0.11	0.82	0.42	0.71
	184	-31.1320453	-179.017485	841.01	76.5	12.8	15.1	87.0	0.56	0.30	2.02	0.31	0.40
(DB)	189.3	-31.1312349	-179.015753	773.4	59.2	20.5	14.3	83.2	0.97	0.48	2.04	0.40	0.30
(DB)	189.4	-31.1312349	-179.015753	773.4	58.4	19.3	23.1	83.2	0.99	0.45	1.83	0.40	0.30
(DB)	189.198	-31.1312349	-179.015753	773.4	58.8	19.1	11.3	89.1	0.98	0.45	2.11	0.26	0.61
(DB)	198	-31.1298142	-179.009840	876.7	56.7	19.7	18.1	84.9	1.03	0.46	1.95	0.36	0.61
	246	-31.11396036	-179.021095	1326.73	76.9	9.7	47.5	89.5	0.55	0.23	1.25	0.25	1.50
	247	-31.11415966	-179.021122	1316.09	77.3	7.4	50.4	85.7	0.54	0.17	1.18	0.34	1.48
TC	257	-31.12234163	-179.014289	845.19	63.0	10.2	37.8	79.0	0.88	0.24	1.48	0.50	0.61
	258	-31.1223514	-179.014300	845.27	67.2	11.2	39.1	82.8	0.78	0.26	1.45	0.41	0.61
	259	-31.12320148	-179.014474	838.7	67.2	12.6	33.6	81.9	0.78	0.29	1.58	0.43	0.53
	260	-31.1232224	-179.014468	838.44	68.1	10.9	33.2	84.5	0.76	0.26	1.59	0.37	0.53
AL	2	-31.12351646	-179.006412	943.75	47.1	15.9	28.2	58.0	1.26	0.37	1.71	1.00	1.03
	5	-31.12292781	-179.005817	945.97	72.7	13.2	35.7	79.0	0.65	0.31	1.53	0.50	1.11
	19	-31.1260315	-179.027282	992.69	79.0	3.0	74.8	82.4	0.50	0.07	0.60	0.42	1.08
	31	-31.12635316	-179.038524	889.32	76.5	7.2	43.3	85.3	0.56	0.17	1.35	0.35	2.10
	40	-31.1041279	-179.037901	1508.06	76.9	13.6	65.5	84.5	0.55	0.32	0.82	0.37	3.14
	54	-31.1178165	-179.041936	1341.08	81.5	5.3	64.3	87.8	0.44	0.12	0.85	0.29	2.65
	84	-31.12090091	-179.045816	960	74.4	6.2	60.9	86.1	0.61	0.15	0.93	0.33	2.89
	91	-31.1252021	-179.040908	975.24	54.2	17.1	35.3	80.7	1.09	0.40	1.54	0.46	2.36
	100	-31.12531064	-179.034764	988.24	44.5	11.6	29.8	58.0	1.32	0.27	1.67	1.00	1.77
	105	-31.12713113	-179.032170	962.64	77.7	7.3	56.3	87.4	0.53	0.17	1.04	0.30	1.53
	107	-31.1271539	-179.031808	962.74	80.7	8.1	67.6	85.7	0.46	0.19	0.77	0.34	1.49
	108	-31.12715151	-179.031809	963.14	82.4	5.8	78.2	86.1	0.42	0.14	0.52	0.33	1.49
	122	-31.13334664	-179.012183	716.98	75.6	0.7	74.8	76.1	0.58	0.02	0.60	0.57	0.63
	123	-31.1372168	-179.017163	873.09	85.3	0.4	85.3	85.7	0.35	0.01	0.35	0.34	0.90
	132	-31.1026467	-179.028623	1512.51	76.5	4.7	64.7	84.5	0.56	0.11	0.84	0.37	2.79
	134	-31.1046489	-179.036444	1508.61	69.7	15.4	45.4	80.3	0.72	0.36	1.30	0.47	3.03
	158	-31.1197975	-179.054900	953.04	68.5	19.5	38.2	79.0	0.75	0.46	1.47	0.50	3.76
	159	-31.1197974	-179.054900	953.04	65.5	16.5	45.8	85.3	0.82	0.39	1.29	0.35	3.76
	160	-31.1197974	-179.054900	953.04	73.9	0.8	73.1	74.4	0.62	0.02	0.64	0.61	3.76
	161	-31.1197974	-179.054900	953.04	73.1	19.9	29.8	81.9	0.64	0.47	1.67	0.43	3.76
	162	-31.0993213	-179.048566	1517.88	76.5	7.8	62.6	83.6	0.56	0.18	0.89	0.39	4.18
	175	-31.111973	-179.049469	1307.08	76.1	2.6	71.4	79.0	0.57	0.06	0.68	0.50	3.54
	180	-31.113082	-179.052123	1175.49	26.9	0.0	26.9	26.9	1.74	0.00	1.74	1.74	3.73
	181	-31.1132288	-179.052036	1164.25	76.1	8.9	65.5	83.6	0.57	0.21	0.82	0.39	3.71
	182	-31.1133125	-179.052051	1134.32	68.5	34.2	11.3	82.8	0.75	0.80	2.11	0.41	3.70
	191	-31.1341666	-179.005250	1014.73	74.8	4.0	71.8	77.7	0.60	0.09	0.67	0.53	1.19

	196	-31.1302687	-179.009341	891.44	43.3	13.7	22.7	63.4	1.35	0.32	1.84	0.87	0.67
	229	-31.0898893	-179.063776	788.02	77.3	7.4	64.3	84.0	0.54	0.17	0.85	0.38	5.89
	232	-31.0877823	-179.060500	826.41	75.2	3.1	71.4	79.0	0.59	0.07	0.68	0.50	5.80
	236	-31.0891555	-179.055567	918.7	71.8	2.2	69.3	73.9	0.67	0.05	0.73	0.62	5.37
	241	-31.11174188	-179.022475	1437.13	77.3	4.6	61.3	84.5	0.54	0.11	0.92	0.37	1.73
	242	-31.11174387	-179.022473	1437.01	73.9	6.6	49.2	85.3	0.62	0.16	1.21	0.35	1.73
	255	-31.124133	-179.012109	870.26	38.7	0.0	38.7	38.7	1.46	0.00	1.46	1.46	0.55
	256	-31.12046865	-179.010635	966.6	48.7	7.8	33.6	55.0	1.22	0.18	1.58	1.07	0.93
	272	-31.0842763	-179.039838	806.13	74.4	9.7	52.9	83.2	0.61	0.23	1.12	0.40	4.89
	283	-31.0974662	-179.011661	964.25	81.9	1.3	81.1	82.8	0.43	0.03	0.45	0.41	3.08
LGL	62	-31.1210966	-179.048557	950.71	54.2	15.5	6.3	88.7	1.09	0.37	2.23	0.27	3.10
	70	-31.1211415	-179.047883	954.44	55.5	8.9	29.4	87.8	1.06	0.21	1.68	0.29	3.03
Nrim	222	-31.105507	-179.059196	1050.36	71.4	24.1	-4.6	86.1	0.68	0.57	2.49	0.33	4.65
	263	-31.0857721	-179.040025	858.69	73.9	29.0	5.9	89.9	0.62	0.68	2.24	0.24	4.78
	265	-31.0851193	-179.040318	807.42	78.2	6.2	49.2	91.6	0.52	0.15	1.21	0.20	4.84
	266	-31.0851461	-179.040492	803.74	79.8	3.5	62.2	85.7	0.48	0.08	0.90	0.34	4.84
	268	-31.0850596	-179.041605	807.53	73.5	8.2	43.7	79.0	0.63	0.19	1.34	0.50	4.91
	275	-31.0843817	-179.036839	863.54	80.7	4.5	64.3	86.1	0.46	0.11	0.85	0.33	4.76
	279	-31.0862869	-179.034280	899.19	78.2	5.8	60.9	87.8	0.52	0.14	0.93	0.29	4.49
	285	-31.0973702	-179.011911	970.35	82.4	6.8	59.7	89.9	0.42	0.16	0.96	0.24	3.08
RP	AUS	n/a	n/a	0	73.4	5.4	63.9	83.2	0.63	0.13	0.86	0.40	n/a
	FJ	n/a	n/a	0	78.3	5.4	65.5	90.4	0.52	0.13	0.82	0.23	n/a
Dome	7	-31.1256502	-179.012308	804.43	41.6	1.6	38.7	45.0	1.39	0.04	1.46	1.31	0.43
	118	-31.130570	-179.013731	744.2	53.4	0.0	53.4	53.4	1.11	0.00	1.11	1.11	0.33
	187	-31.131401	-179.016137	789.19	37.0	9.5	21.8	45.8	1.50	0.23	1.86	1.29	0.51
(O)	10	-31.127249	-179.015026	698.7	24.9	4.7	20.2	29.8	1.79	0.11	1.90	1.67	0.05
(P)	13	-31.128586	-179.016302	671.84	14.3	6.5	5.0	20.2	2.04	0.16	2.26	1.90	0.05

Appendix C3: *Componentry breakdown and all Havre clasts*

Table C3. The breakdown of each unit's componentry histogram from **Figure 4.5** for vesicularity bin sizes of 5% width.

Unit	Vesicularity (%)		<5	10	15	20	25	30	35	40	45	50	55	60	65	70	75	80	85	90	95	100
ALL	**Regular**	*1*	0	0	2	0	0	1	0	8	5	8	20	41	65	113	206	486	515	142	2	0
	Banded	*2*	0	0	0	0	1	1	1	0	2	7	7	7	16	42	94	87	73	14	0	0
	Tube	*3*	0	0	0	0	1	2	7	20	36	68	106	152	94	85	121	207	121	23	0	0
	Dome	*4*	0	0	3	6	9	18	29	29	39	6	6	2	1	0	1	0	1	0	0	0
	Lithic	*5*	5	12	11	11	5	3	2	6	5	4	2	2	0	0	0	1	2	0	0	0
ALB (all)	**Regular**	*1*	0	0	0	0	0	0	0	5	1	10	14	37	37	39	74	142	151	27	0	0
	Banded	*2*	0	0	0	0	0	0	0	3	4	8	12	3	5	10	7	8	17	1	0	0
	Tube	*3*	0	0	0	0	1	1	2	5	4	11	19	33	40	29	37	38	13	2	0	0
	Dome	*4*	0	0	3	4	7	11	25	20	16	3	6	2	1	0	1	0	1	0	0	0
	Lithic	*5*	0	0	0	2	1	1	0	0	0	0	0	0	0	0	0	0	0	0	0	0
GP	**Regular**	*1*	0	0	0	0	0	0	0	0	0	0	0	1	4	10	20	56	50	16	0	0
	Banded	*2*	0	0	0	0	0	0	0	0	0	0	0	0	1	12	54	32	1	0	0	0
	Tube	*3*	0	0	0	0	0	0	0	0	0	0	1	5	10	17	10	35	1	0	0	0
	Dome	*4*	0	0	0	0	0	0	0	4	16	0	0	0	0	0	0	0	0	0	0	0
	Lithic	*5*	0	0	0	0	0	0	0	0	0	0	0	0	0	0	0	0	0	0	0	0
RP	**Regular**	*1*	0	0	0	0	0	0	0	0	0	0	0	0	0	11	33	41	39	10	1	0
	Banded	*2*	0	0	0	0	0	0	0	0	0	0	0	0	0	8	15	7	12	4	0	0
	Tube	*3*	0	0	0	0	0	0	0	0	0	0	0	0	0	0	6	8	4	1	0	0
	Dome	*4*	0	0	0	0	0	0	0	0	0	0	0	0	0	0	0	0	0	0	0	0
	Lithic	*5*	0	0	0	0	0	0	0	0	0	0	0	0	0	0	0	0	0	0	0	0
ALB	**Regular**	*1*	0	0	0	0	0	0	0	0	0	0	1	3	15	15	40	76	119	25	0	0
	Banded	*2*	0	0	0	0	0	0	0	0	0	0	4	2	2	6	2	6	17	1	0	0
	Tube	*3*	0	0	0	0	0	0	0	0	0	2	4	4	5	11	20	20	7	2	0	0
	Dome	*4*	0	0	0	1	2	1	0	0	0	0	0	0	0	0	0	0	1	0	0	0
	Lithic	*5*	0	0	0	0	0	0	0	0	0	0	0	0	0	0	0	0	0	0	0	0
AL	**Regular**	*1*	0	0	0	0	0	0	0	2	3	0	6	4	12	35	52	132	93	25	0	0
	Banded	*2*	0	0	0	0	1	1	1	0	0	1	0	0	3	6	5	10	8	2	0	0
	Tube	*3*	0	0	0	0	0	0	0	1	1	4	6	4	2	21	36	30	14	3	0	0
	Dome	*4*	0	0	0	2	2	7	3	5	6	3	0	0	0	0	0	0	0	0	0	0
	Lithic	*5*	0	1	1	3	3	0	0	0	1	0	0	1	0	0	0	0	0	0	0	0
LGL	**Regular**	*1*	0	0	0	0	0	0	0	0	1	1	2	2	4	1	0	2	4	7	0	0
	Banded	*2*	0	0	0	0	0	0	0	0	0	0	0	0	0	0	0	0	0	0	0	0
	Tube	*3*	0	0	0	0	0	1	5	14	31	52	85	111	40	8	2	2	2	0	0	0
	Dome	*4*	0	0	0	0	0	0	1	0	0	0	0	0	0	0	0	0	0	0	0	0
	Lithic	*5*	0	3	1	1	0	1	0	6	1	3	2	0	0	0	0	0	0	0	0	0

DB	**Regular**	*1*	0	0	0	0	0	0	0	2	1	7	6	6	6	11	15	22	19	2	0	0
	Banded	*2*	0	0	0	0	0	0	0	3	2	2	5	0	1	1	0	1	0	0	0	0
	Tube	*3*	0	0	0	0	1	1	2	4	2	4	7	9	11	7	5	8	1	0	0	0
	Dome	*4*	0	0	3	3	5	10	23	19	13	3	5	1	1	0	0	0	0	0	0	0
	Lithic	*5*	0	0	0	2	1	1	0	0	0	0	0	0	0	0	0	0	0	0	0	0
TC	**Regular**	*1*	0	0	0	0	0	0	0	3	0	3	7	28	16	13	19	44	13	0	0	0
	Banded	*2*	0	0	0	0	0	0	0	0	2	6	3	1	2	3	5	1	0	0	0	0
	Tube	*3*	0	0	0	0	0	0	0	1	2	5	8	20	24	11	12	10	5	0	0	0
	Dome	*4*	0	0	0	0	0	0	2	1	3	0	1	1	0	0	1	0	0	0	0	0
	Lithic	*5*	0	0	0	0	0	0	0	0	0	0	0	0	0	0	0	0	0	0	0	0
Nrim	**Regular**	*1*	0	0	2	0	0	1	0	1	0	0	0	0	8	17	29	113	172	53	1	0
	Banded	*2*	0	0	0	0	0	0	0	0	0	0	0	4	7	6	12	29	27	5	0	0
	Tube	*3*	0	0	0	0	0	0	0	0	1	1	0	2	5	11	33	92	76	14	0	0
	Dome	*4*	0	0	0	0	0	0	0	0	1	0	0	0	0	0	0	0	0	0	0	0
	Lithic	*5*	5	8	9	5	1	1	2	0	3	1	0	1	0	0	0	1	2	0	0	0

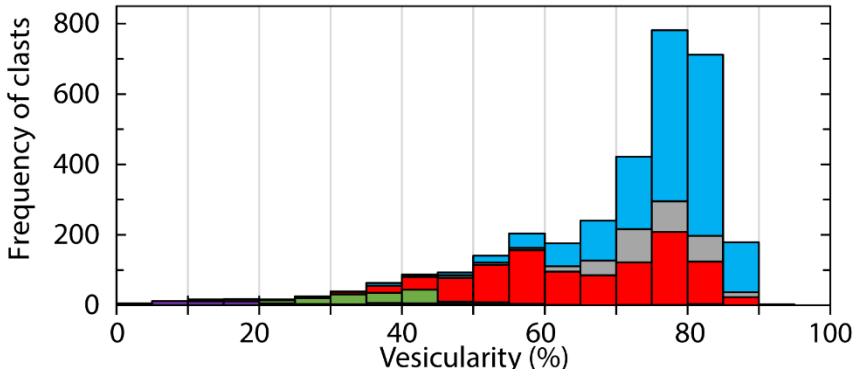

Figure C3. Compilation of all Havre componentry (3230 lapilli-sized clasts and fragments). Blue = regular pumice, grey = banded pumice, red = tube pumice, green = dome material, and purple = non-juvenile 2012 or pre-2012 material. We note the strong mode of vesicularity between 75 and 85% and the bimodal distribution of tube pumice with modes at 55-60 and 75-80% vesicularity.

Appendix C4: *Pycnometry data and permeability plots*

Table C4. Helium pycnometry and permeability (perm.) data for RP, ALB and Dome samples; GP data and method details are given in **Appendix B7**. Permeability is given in m^2 for k_1 and m for k_2. *Pycnometry data from Manga et al. (2018).

Unit	Sample (HVR_)	Total porosity (%)	Isolated porosity (%)	Connected porosity (%)	Connectivity	Darcian Perm. (k1)	Inertial Perm. (k2)
ALB	120_a	87.06	-0.43	87.49	1.00	-	-
	120_b	86.84	-0.92	87.77	1.01	-	-
	120_c	85.85	-0.10	85.95	1.00	-	-
	120_d	88.90	-3.38	92.28	1.04	-	-
	120_e	90.60	-2.59	93.19	1.03	-	-
	120_f	89.01	-2.94	91.95	1.03	-	-
	189_a	85.37	0.32	85.05	1.00	-	-
	189_b	89.86	-0.63	90.49	1.01	-	-
	189_c	87.30	-2.38	89.68	1.03	-	-
	189_d	71.25	13.04	58.21	0.82	-	-
	189_e	80.26	12.88	67.38	0.84	-	-
	189_f	87.25	-0.48	87.73	1.01	-	-
	246_a	62.63	28.19	34.44	0.55	-	-
	246_b	79.07	8.31	70.76	0.89	-	-
	246_c	83.18	4.26	78.92	0.95	-	-
	246_d	90.90	-3.61	94.51	1.04	-	-
	246_e	87.05	-2.30	89.35	1.03	-	-
	246_f	89.02	-1.74	90.76	1.02	-	-
	247_a	86.64	-2.30	88.94	1.03	-	-
	247_b	85.70	-1.34	87.04	1.02	-	-
	247_c	87.41	0.14	87.26	1.00	-	-
	247_d	86.34	1.90	84.44	0.98	-	-
	247_e	78.35	7.19	71.16	0.91	-	-
	247_f	80.79	0.81	79.98	0.99	-	-
RP	001_a*	75.80	38.23	37.58	0.50	1.18E-12	4.46E-09
	001_b*	82.49	46.88	35.60	0.43	2.05E-12	4.46E-09
	002_a*	81.96	53.63	28.33	0.35	-	-
	002_b*	76.13	50.19	25.94	0.34	9.77E-13	2.23E-09
	003_a*	91.37	6.52	84.85	0.93	1.62E-12	1.02E-08
	003_b*	91.51	7.65	83.86	0.92	1.41E-12	3.71E-09
	003_c*	91.32	6.50	84.82	0.93	2.83E-12	1.86E-08
	004_a*	87.70	13.34	74.36	0.85	1.08E-11	4.09E-08
	004_b*	87.26	16.25	71.00	0.81	4.09E-12	4.67E-09
	005_a*	85.62	6.26	79.36	0.93	3.73E-12	2.46E-08
	005_b*	85.83	9.22	76.61	0.89	1.18E-12	2.81E-09
	006_a*	89.04	7.48	81.56	0.92	2.46E-12	8.51E-09
	006_b*	88.88	7.86	81.02	0.91	1.86E-12	7.07E-09
	006_c*	88.90	4.76	84.14	0.95	8.17E-12	5.91E-08
	007_b*	76.94	44.69	32.25	0.42	7.41E-13	9.33E-09
	C31_01*	88.86	7.33	81.53	0.92	2.27E-10	7.11E-08
	01_01*	88.38	6.50	81.88	0.93	2.70E-12	3.38E-09
	01_02*	89.13	4.88	84.25	0.95	-	-
	01_03*	89.29	5.35	83.94	0.94	9.33E-13	3.23E-09
	01_04*	89.62	4.88	84.74	0.95	2.96E-12	3.73E-08
	03_01*	87.71	7.39	80.32	0.92	1.41E-12	4.67E-09
	03_02*	88.43	4.62	83.81	0.95	2.24E-12	4.67E-09
	FJ_a	84.47	19.76	64.71	0.77	-	-
	FJ_b	88.32	8.30	80.01	0.91	-	-
	FJ_c	84.12	27.21	56.91	0.68	-	-
	FJ_d	90.55	4.11	86.44	0.95	-	-
	FJ_e	88.75	6.34	82.41	0.93	-	-
	FJ_f	89.81	3.03	86.78	0.97	-	-
	FJ_g	75.98	39.78	36.20	0.48	-	-
	FJ_h	85.83	25.27	60.55	0.71	-	-

	FJ_i	89.60	5.71	83.89	0.94	-	-
	FJ_j	73.77	36.69	37.08	0.50	-	-
	FJ_k	90.50	4.61	85.89	0.95	-	-
	FJ_l	81.11	37.53	43.58	0.54	-	-
	FJ_m	81.90	35.66	46.23	0.56	-	-
	FJ_n	89.53	1.54	87.99	0.98	-	-
	FJ_o	86.54	8.19	78.35	0.91	-	-
Dome	007a	50.28	-0.42	50.70	1.01	-	-
	007b	49.38	0.04	49.34	1.00	-	-
	007c	50.12	0.17	49.95	1.00	-	-
	010a	20.48	-5.78	26.25	1.28	2.20E-12	1.26E-08
	010b	31.83	1.52	30.31	0.95	6.59E-13	4.55E-09
	118A	31.30	-6.70	38.00	1.21	1.38E-12	2.38E-09
	118B	28.52	2.49	26.03	0.91	1.66E-12	1.83E-08

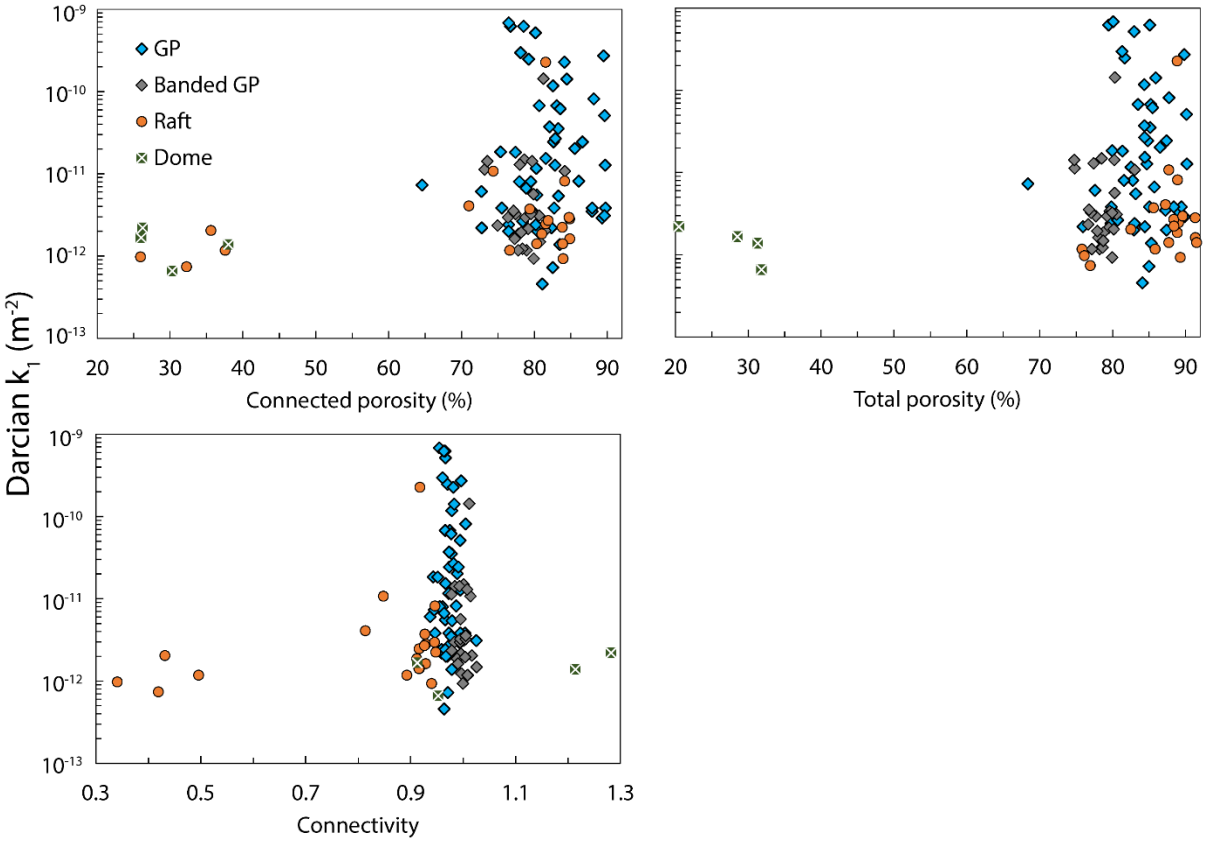

Figure C4. Darcian permeability of GP, RP and Dome samples vs. connected porosity, total porosity, and vesicle connectivity; there were no permeability data acquired for ALB samples due to the wide spread identified from the first GP permeability analysis.

Appendix C5: *Raw N_A data*

Table C5. 2D VSD data prior to stereo-conversion given as number of vesicles per unit area (in mm^{-2}) for vesicle size bins that increase geometrically ($\times 10^{0.1}$ per step). We identify the magnification used to acquire those specific N_A values. EqD is the equivalent diameter of a circular vesicle with the same area as the vesicle analyzed. *Highest magnification used in RP were 750x and 1000x in LGL.

Geometric Bins (EqD, mm)	Number density per area before stereo-conversion (N_A [mm^{-2}])																	
	Unit	Dome	Dome	Dome	Dome	ALB	ALB	ALB	ALB	ALB	RP	RP	RP	RP	RP	LGL	LGL	LGL
	HVR_	007	010	118	189	184L	189L	189VL	120M	184H	FJL	FJ49M	FJ84M	FJH	Fjband	70L	70M	70H
0.0015	500x	3.186	0.000	0.000	77.46	0.000	0.000	0.000	3.658	0.000	15.37*	13.13	15.33*	22.58	34.90*	9.201	32.46*	498.1*
0.0019		11.15	0.000	0.000	98.59	0.000	0.000	0.000	6.401	23.91	13.83*	20.09	21.46	32.05	38.61*	19.93	54.10*	498.1*
0.0024		25.49	0.000	42.69	117.6	10.03	32.75	9.747	5.487	52.31	30.74	44.05	46.00	54.63	60.14	31.43	53.38*	787.8*
0.0030		57.35	1.442	60.78	151.4	15.88	50.68	8.122	14.63	64.27	46.88	54.10	70.54	80.13	89.85	34.50	84.40*	880.5*
0.0038		72.67	2.883	76.70	192.2	16.72	62.38	16.24	11.88	92.67	75.32	80.38	102.7	93.24	116.5	46.77	116.1*	1343.9*
0.0048		115.8	14.41	103.4	252.1	36.79	102.9	25.17	16.46	107.6	108.3	103.5	124.2	145.6	147.7	67.47	189.7*	1425.0*
0.0060		119.7	42.52	117.2	256.3	54.35	137.2	33.30	29.26	118.0	160.6	145.3	165.6	228.7	193.8	67.47	205.6*	1842.1*
0.0075		121.3	77.84	141.1	282.3	68.57	151.2	54.41	50.29	210.7	206.7	202.4	214.6	278.9	248.7	108.8	315.9*	1448.1*
0.0095		91.84	119.6	160.6	290.1	91.14	187.1	64.97	50.29	246.6	264.3	231.0	259.9	306.6	308.9	109.6	385.2*	878.8
0.0119	250x	94.23	115.3	146.1	247.8	117.0	246.4	83.65	67.66	297.4	313.5	292.1	312.8	329.9	376.4	161.7	448.7*	574.8
0.0150		91.84	114.6	147.6	186.6	163.9	249.5	107.2	95.10	272.0	359.7	265.1	299.0	383.8	329.7	216.2	477.5*	333.7
0.0189		75.07	111.7	136.0	116.1	183.1	283.8	129.9	121.6	300.4	329.7	240.3	279.0	348.2	343.8	252.2	415.5*	164.0
0.0238		89.44	82.89	92.62	78.87	200.6	238.6	164.0	128.9	269.0	244.4	216.4	194.7	252.7	261.3	268.3	252.5*	108.1
0.0300		41.57	62.71	64.40	38.02	174.7	201.1	157.5	132.5	180.8	172.9	169.2	157.9	150.0	158.1	202.4	133.4*	46.66
0.0377		35.79	51.26	32.06	29.95	141.3	136.4	141.3	111.5	110.6	106.0	116.7	105.0	74.30	86.13	96.61	56.98	29.44
0.0475		27.09	31.56	21.59	15.74	79.44	84.99	105.5	79.55	71.74	64.56	49.46	59.80	35.06	41.58	57.50	30.81	16.98
0.0598		17.78	21.04	14.07	7.360	51.01	35.86	54.41	50.29	27.04	33.04	31.42	34.50	20.02	34.90	28.37	14.48	8.822
0.0753		10.60	12.38	9.997	5.078	25.92	26.76	34.11	37.49	13.74	14.73	20.31	23.00	11.30	7.734	10.73	7.494	4.292
0.0948		7.966	7.207	5.442	3.651	9.978	12.39	7.214	13.12	7.231	8.852	10.59	6.553	4.649	4.208	6.166	4.362	4.411
0.1193	50x	3.590	3.778	3.667	2.510	5.797	6.197	4.283	7.751	3.698	4.343	5.468	2.817	3.329	2.331	2.130	1.901	1.788
0.1502		2.468	1.918	2.248	1.255	2.787	2.303	1.747	3.564	1.932	2.089	2.418	1.724	1.894	1.365	1.289	1.342	1.431
0.1891		1.290	0.314	1.538	0.571	1.672	1.700	1.014	2.207	0.938	1.979	1.439	1.150	1.090	1.422	0.729	0.559	0.894
0.2381		0.617	0.095	0.543	0.571	0.725	0.603	0.556	0.962	0.453	0.880	0.560	0.920	0.467	0.497	0.409	0.298	0.500
0.2997		0.228	0.053	0.393	0.372	0.420	0.405	0.542	0.495	0.327	0.533	0.457	0.555	0.388	0.463	0.409	0.328	0.421
0.3774		0.191	0.019	0.183	0.213	0.303	0.215	0.287	0.257	0.186	0.313	0.274	0.316	0.243	0.284	0.251	0.194	0.303
0.4751		0.085	0.005	0.077	0.130	0.123	0.118	0.152	0.154	0.094	0.209	0.129	0.194	0.161	0.194	0.102	0.118	0.250
0.5981		0.072	0.000	0.061	0.054	0.065	0.038	0.108	0.075	0.044	0.097	0.066	0.124	0.082	0.101	0.111	0.077	0.132
0.7529	scan	0.055	0.002	0.028	0.018	0.047	0.027	0.067	0.034	0.022	0.072	0.032	0.055	0.049	0.055	0.065	0.057	0.118
0.9479		0.017	0.000	0.009	0.007	0.029	0.003	0.054	0.021	0.009	0.030	0.009	0.026	0.030	0.038	0.042	0.034	0.132
1.1933		0.003	0.000	0.009	0.000	0.018	0.005	0.031	0.006	0.006	0.013	0.003	0.012	0.005	0.015	0.028	0.030	0.039
1.5023		0.000	0.000	0.007	0.000	0.014	0.000	0.004	0.002	0.003	0.011	0.002	0.010	0.009	0.013	0.009	0.007	0.000
1.8913		0.000	0.000	0.002	0.000	0.008	0.000	0.000	0.003	0.000	0.004	0.002	0.004	0.000	0.006	0.014	0.009	0.000
2.3810		0.000	0.000	0.002	0.000	0.006	0.000	0.004	0.000	0.000	0.006	0.000	0.000	0.008	0.006	0.009	0.009	0.000
2.9975		0.000	0.000	0.007	0.000	0.000	0.000	0.004	0.000	0.000	0.002	0.000	0.000	0.002	0.000	0.005	0.002	0.000
3.7736		0.000	0.000	0.000	0.000	0.000	0.000	0.000	0.000	0.000	0.000	0.000	0.000	0.000	0.000	0.005	0.000	0.013

Appendix C6: *Computed minimum wall thicknesses*

Minimum wall thicknesses were calculated using an algorithm to determine the distances between vesicles in a 2D binary image (Biass, unpublished). The basis of the algorithm is such that for every vesicle in every image, the algorithm determines the nearest vesicle (ellipse-equivalent center to center) and measure the amount of glass (white pixels) between the two vesicles (black pixels). The thickness of the glass is classified as the minimum wall thickness. This analysis was run for eight 250x magnification BSE images per sample, where all vesicle are decoalesced prior to analysis. By keeping vesicles coalesced, vesicle sizes would not represent the original vesicle number density. There is some bias in the analysis, as all vesicles are required to be separated by at least three pixels of melt for successful image analysis (corresponding to 1.12 µm in 250 x images). The acquired wall thicknesses were averaged to acquire a mean minimum wall thickness.

The statistical results of the analysis can be found in the plots and table below (**Figure C6**).

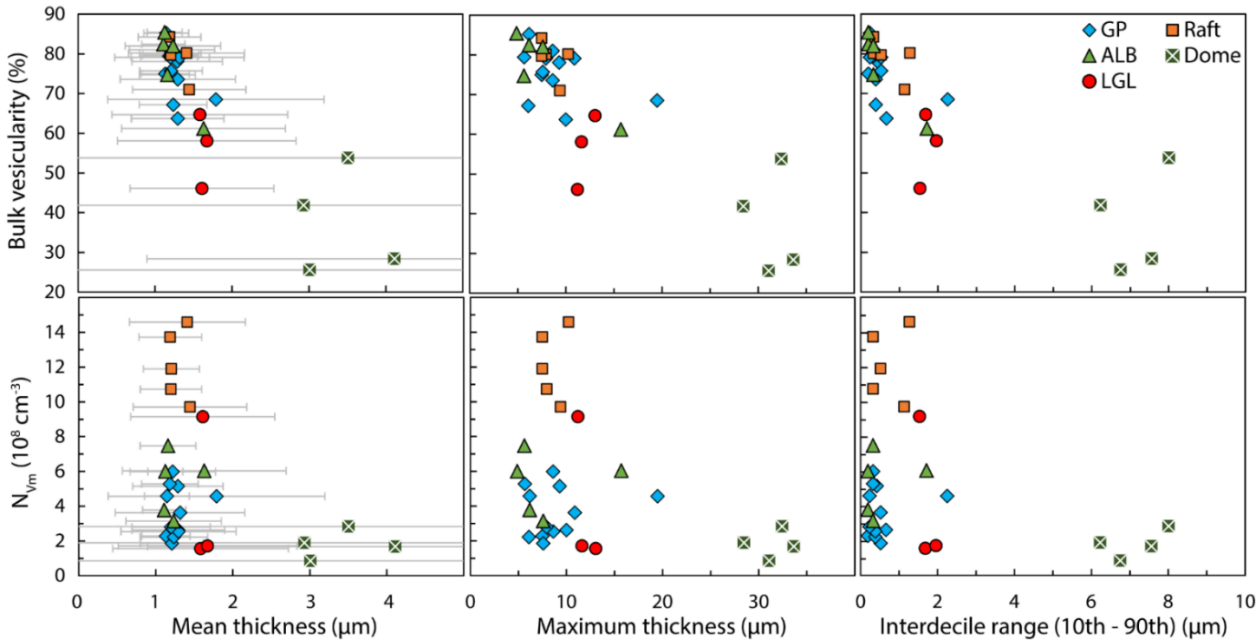

Table C6. Statistical analysis of each sample including percentile values and ranges,

Samples	Mean thickness (μm)	Median thickness (μm)	1 SD (μm)	Min (μm)	Max (μm)	Interquartile range (μm)	25th pct. (μm)	75th pct. (μm)	10th pct. (μm)	90th pct. (μm)	Interdecile range (μm)	#vesicles analyzed	Bulk vesic (%)	N_{Vm} (cm^{-3})	V_g/V_l
RPM_49	1.20	1.12	0.40	0.37	7.94	0	1.12	1.12	0.98	1.3	0.32	2788	80.1	1.07E+09	4.03
RPM_84	1.20	1.12	0.36	0.37	7.49	0.05	1.12	1.17	0.98	1.5	0.52	2984	79.7	1.19E+09	3.93
RPL_75	1.19	1.12	0.41	0.37	7.49	0	1.12	1.12	0.98	1.3	0.32	2959	84.2	1.37E+09	5.33
RPH_64	1.44	1.12	0.74	0.37	9.39	0.38	1.12	1.5	1.12	2.25	1.13	3385	71	9.71E+08	2.45
RPM_band	1.41	1.12	0.75	0.37	10.23	0.18	1.12	1.3	0.98	2.25	1.27	3456	80.2	1.46E+09	4.05
ALB189_VL	1.11	1.12	0.28	0.37	6.17	0.14	0.98	1.12	0.98	1.17	0.19	1358	82.4	3.78E+08	4.68
ALB189_L	1.16	1.12	0.36	0.37	5.63	0.14	0.98	1.12	0.98	1.3	0.32	2598	74.7	7.48E+08	2.95
ALB184_L	1.13	1.12	0.23	0.37	4.87	0	1.12	1.12	0.98	1.17	0.19	1669	85.4	5.99E+08	5.85
ALB120_M	1.23	1.12	0.62	0.46	7.59	0	1.12	1.12	0.98	1.3	0.32	1077	82	3.14E+08	4.56
ALB120_H	1.63	1.17	1.06	0.37	15.71	0.52	1.12	1.64	1.12	2.832	1.712	3904	61.2	6.04E+08	1.58
GPX_003	1.13	1.12	0.31	0.37	7.49	0	1.12	1.12	0.98	1.17	0.19	3670	75	2.29E+08	3.00
GPX_022	1.29	1.12	0.60	0.37	9.98	0.05	1.12	1.17	0.98	1.64	0.66	5082	63.7	2.62E+08	1.75
GPX_115	1.21	1.12	0.41	0.37	7.59	0	1.12	1.12	0.98	1.5	0.52	3312	75.7	1.86E+08	3.12
GPX_270	1.24	1.12	0.44	0.37	6.09	0.05	1.12	1.17	1.12	1.5	0.38	4426	67.2	2.22E+08	2.05
GPX_041	1.29	1.12	0.59	0.37	9.29	0.05	1.12	1.17	1.12	1.54	0.42	2354	78.1	5.14E+08	3.57
GPX_096	1.18	1.12	0.37	0.37	5.66	0	1.12	1.12	0.98	1.3	0.32	2341	79.4	5.28E+08	3.85
GPX_192	1.15	1.12	0.29	0.37	6.18	0	1.12	1.12	0.98	1.21	0.23	1404	85.2	4.58E+08	5.76
GPX_221	1.79	1.17	1.41	0.37	19.48	0.79	1.12	1.91	1.12	3.37	2.25	2251	68.5	4.58E+08	2.17
GPX_231	1.22	1.12	0.55	0.37	8.61	0	1.12	1.12	0.98	1.3	0.32	2140	81	5.98E+08	4.26
GPX290	1.30	1.12	0.75	0.37	8.63	0	1.12	1.12	1.12	1.5	0.38	1434	73.6	2.55E+08	2.79
Band_W	1.20	1.12	0.51	0.37	7.92	0	1.12	1.12	0.98	1.21	0.23	1612	79.1	2.80E+08	3.78
Band_G	1.32	1.12	0.84	0.37	10.87	0	1.12	1.12	0.98	1.5	0.52	1278	79.1	3.62E+08	3.78
ALBDB_VH	4.11	3.08	3.22	0.37	33.64	4.12	1.54	5.66	1.12	8.68	7.56	2892	28.4	1.69E+08	0.40
DB_007	2.93	1.50	3.20	0.37	28.46	2.25	1.12	3.37	1.12	7.35	6.23	1212	41.9	1.90E+08	0.72
DB_118	3.51	1.50	3.79	0.37	32.42	3.75	1.12	4.87	0.98	8.99	8.01	1496	53.8	2.84E+08	1.16
DB_DomeO	3.01	1.17	3.85	0.68	31.10	2.04	1.12	3.16	1.12	7.87	6.75	2101	25.6	8.55E+07	0.34
LGL_L	1.58	1.12	1.14	0.37	13.04	0.38	1.12	1.5	1.12	2.8	1.68	2071	64.7	1.56E+08	1.83
LGL_M	1.67	1.17	1.16	0.37	11.62	0.52	1.12	1.64	1.12	3.08	1.96	3791	58.1	1.72E+08	1.39
LGL_H	1.61	1.21	0.94	0.37	11.19	0.52	1.12	1.64	1.12	2.65	1.53	9736	46.1	9.15E+08	0.86

Appendix C7: *Cristobalite correction, Raman spectra and composition*

The specific identification of cristobalite as the silica polymorph present in vesicles was identified by comparing Raman shift spectra from the crystals with that of pre-determined cristobalite spectra from natural and experimental crystals from the RRUFF database (Lafuente et al., 2015) (**Figure C7i**):

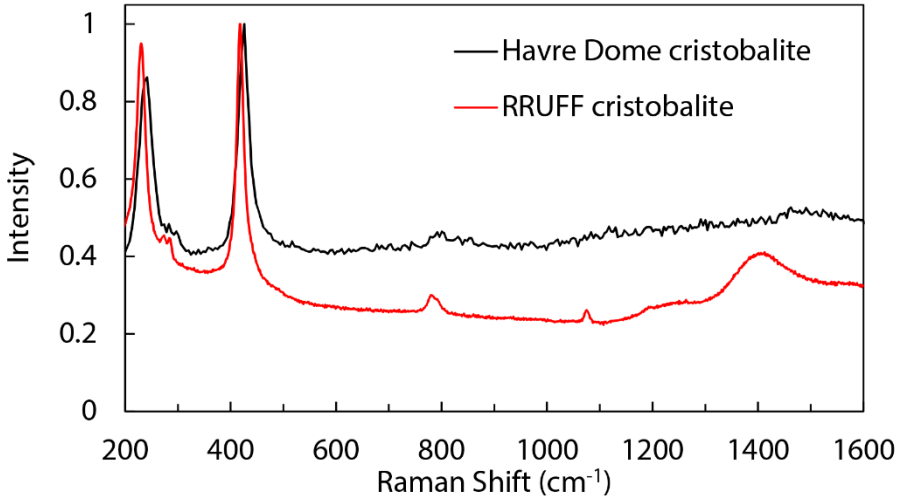

Figure C7i. Comparison of microRaman analysis on a HVR_010 cristobalite crystal (Dome carapace) and RRUFF cristobalite spectra where the wavenumber is the Raman shift.

Cristobalite proved a difficulty in microtextural analysis of the dome carapace (and some talus) samples, where cristobalite crystals could make up to 20% of the total image area and up to 45% of the total vesicularity (**Figure 4.12**). Assuming all cristobalite crystals were secondary vapor-phase crystals, we infer that vesicle areas and size without cristobalite were the same as when the cristobalite was present. Images were processed similarly to the methods of **Appednix B2**, with the additional step of removing cristobalite crystals to produce binary images of just melt and vesicles (**Figure C7ii**). Vesicles had to be hand drawn to include the area with cristobalite and, in the case where crystals may have taken up an entire vesicle; bubbles were interpreted as having previously filled the same area. An example of this processing is given below:

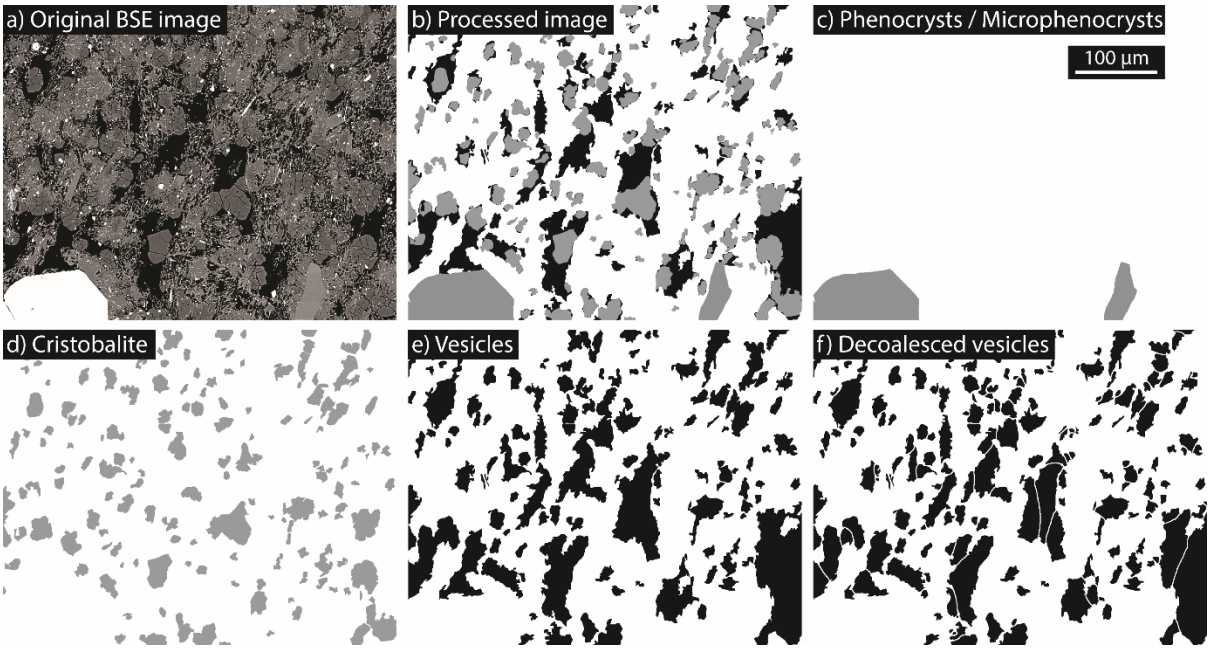

Figure C7ii. Image processing of original backscattered electron images of cristobalite to a cristobalite-free 2D ninary image of melt and vesicles.

We do note that a combination of some permeable pathway collapse, cristobalite growth glass dissolution, and manual definition of vesicle edges may have induced some bias or uncertainty to interpreting the original vesicle number density (N_{Vm}) for the dome carapace (**Figure 4.8**). However, the N_{Vm} value for the carapace is just over half that of all other adjusted giant pumice and dome talus number densities. This could suggest that bubble number density remained similar through the transition from giant pumice production to slow dome effusion. Many microtextural similarities between talus and dome carapace samples (as in **Figure 4.7**) suggest that talus samples simply erupted sooner, quenched and then broke off the dome edifice, which prevented continued thermal processes of crystal growth and glass dissolution, hence the observed lower levels of textural maturity in dome talus.

Compositional data for cristobalite in the Dome talus and carapace are presemted below (**Figure C7iii**). The carapace samples correspond to the highest mean crystal diameter and % area in vesicles. F was negligible in all crystals. Sodium appears to partition the greatest in the

precipitate phase during crystal growth; Na is known to diffuse quickly from warm glass and melt in comparison to K and other volatile species.

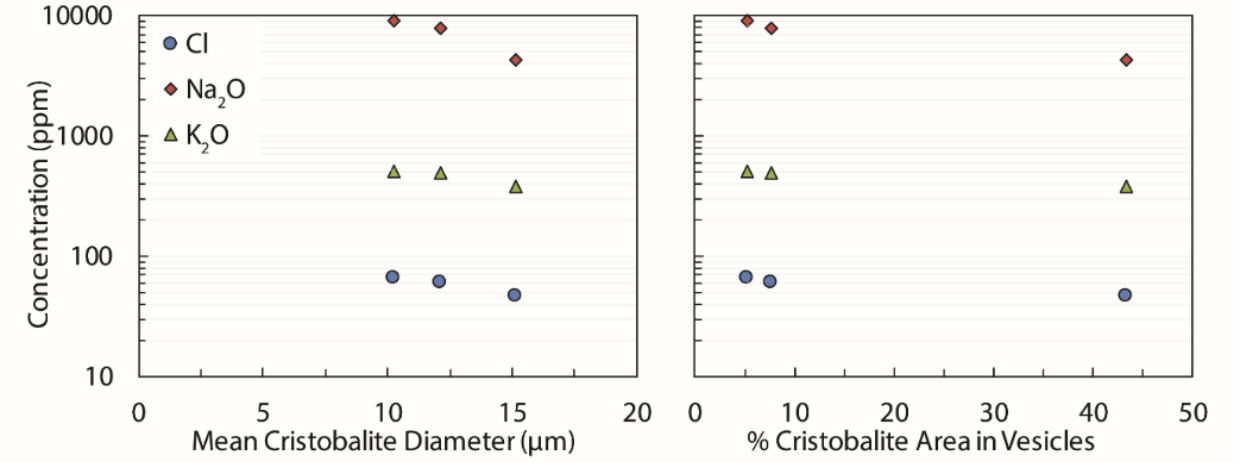

Figure C7iii. Cristobalite impurity analysis of alkali metals and halogens; F was negligible in all samples. Mean element concentrations given against mean cristobalite diameter and abundance per dome sample analyzed.

Appendix C8: *Raman melt inclusion analysis of H_2O_t*

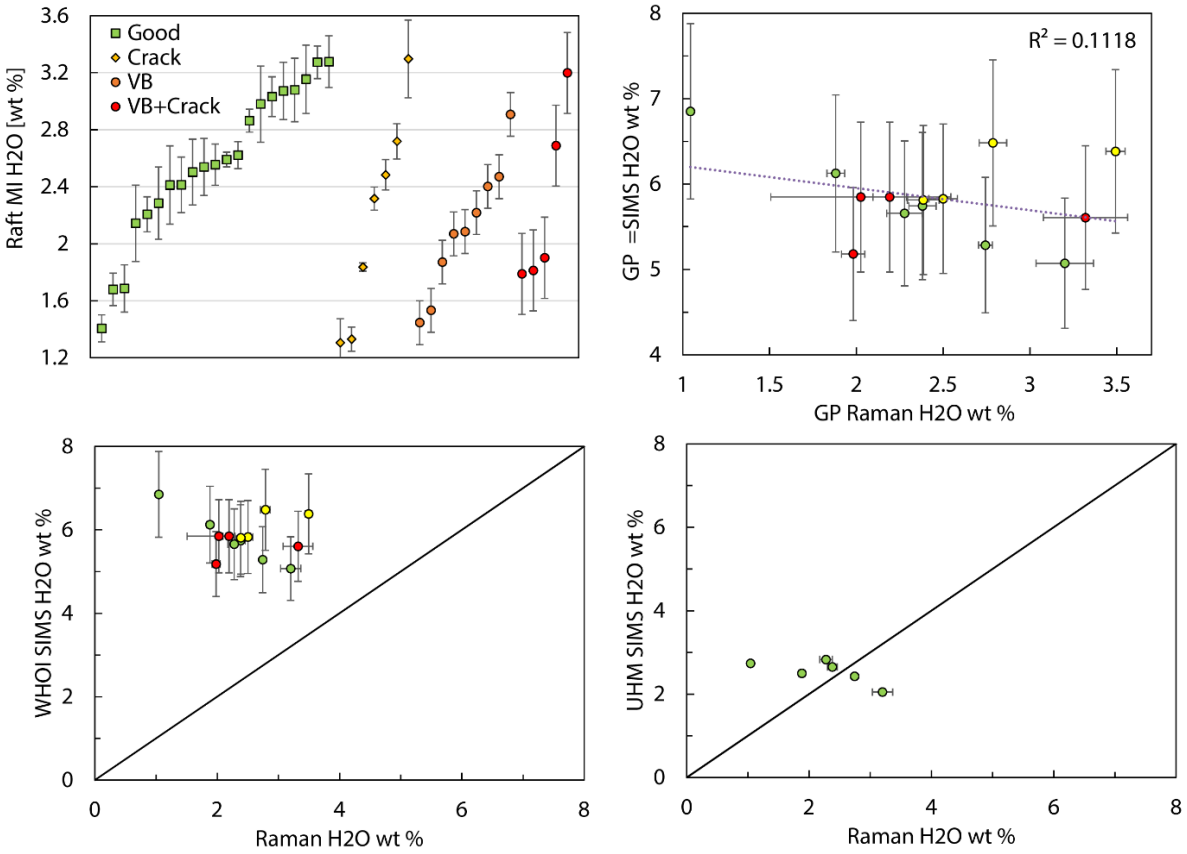

Figure C8. H_2O_t concentration of exposed melt inclusions within thin sections of raft pumice from Fiji using microRaman. Crystals within these thin sections (<0.5 mm diameter) are smaller than those used in SIMS analysis (1-2 mm). Analyses are classified by the apparent quality of the melt inclusions with section; good MIs have no observable cracks or large vapor bubbles (VB) present. The other three plots compare analyses of SIMS and µRaman of melt inclusions from GP290.

SIMS analyses performed at UH Mānoa are comparable with measurements using µRaman whereas SIMS analyses performed at Woods Hole Oceanographic Institution (WHOI) produce H_2O_t values almost twice those of the UH SIMS (**Figure C8**). As stated in section **4.6**, the surface H_2O_t content of these inclusions may have been affected by the first round of SIMS analyses, despite additional polishing between WHO and UH analyses. Lower H_2O_t in smaller crystals is expected due to crystal nucleation and growth during ascent and subsequent trapping of more degassed melt within melt inclusions. FTIR analysis of the GP290 melt inclusions could prove a useful verification of the true H_2O_t; this will be followed up in subsequent work.

Appendix C9: *Melt inclusion and matrix glass contents*

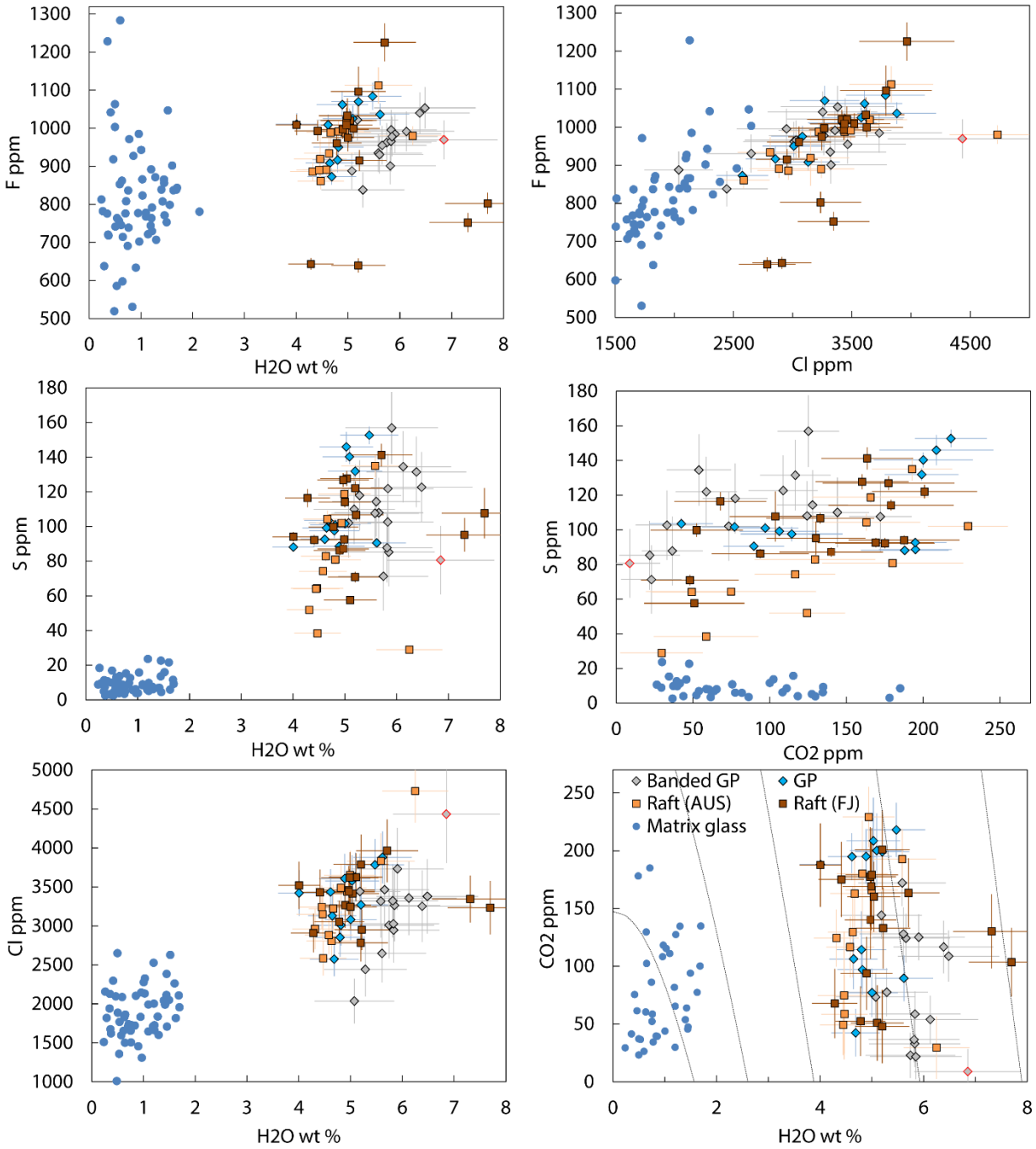

Figure C9. Matirx glass and melt inclusion volatile concentrations plotted on the same graphs as shown in Figure 4.14. This is primarily to indicate the extent of degassing of each volatile phase. CO_2 is variable, almost all H_2O and S has been degassed (remembering that many of the clasts are rehydrated as shown in Chapter 2), and Cl and F only show partial degassing, but a decrease nonetheless.

REFERENCES

Airey, M.W., Mather, T.A., Pyle, D.M., Glaze, L.S., Ghail, R.C. and Wilson, C.F., 2015. Explosive volcanic activity on Venus: the roles of volatile contribution, degassing, and external environment. *Planetary and Space Science*, 113, pp. 33-48, doi: 10.1016/j.pss.2015.01.009

Alfano, F., Bonadonna, C., Volentik, A.C., Connor, C.B., Watt, S.F., Pyle, D.M. and Connor, L.J., 2011. Tephra stratigraphy and eruptive volume of the May, 2008, Chaitén eruption, Chile. *Bulletin of Volcanology*, 73(5), pp. 613-630, doi: 10.1007/s00445-010-0428-x

Allen, S.R. and McPhie, J., 2000. Water-settling and resedimentation of submarine rhyolitic pumice at Yali, eastern Aegean, Greece. *Journal of Volcanology and Geothermal Research*, 95(1-4), pp. 285-307, doi: 10.1016/S0377-0273(99)00127-4

Allen, S.R., Fiske, R.S. and Cashman, K.V., 2008. Quenching of steam-charged pumice: Implications for submarine pyroclastic volcanism. *Earth and Planetary Science Letters*, 274(1-2), pp. 40-49, doi: 10.1016/j.epsl.2008.06.050

Allen, S.R. and McPhie, J., 2009. Products of neptunian eruptions. *Geology*, 37(7), pp. 639-642, doi: 10.1130/G30007A.1

Allen, S.R., Fiske, R.S. and Tamura, Y., 2010. Effects of water depth on pumice formation in submarine domes at Sumisu, Izu-Bonin arc, western Pacific. *Geology*, 38(5), pp. 391-394, doi: 10.1130/G30500.1

Anovitz, L.M., Riciputi, L.R., Cole, D.R., Fayek, M. and Elam, J.M., 2006. Obsidian hydration: a new paleothermometer. *Geology*, 34(7), pp. 517-520, doi: 10.1130/G22326.1

Aravena, A., Cioni, R., de' Michieli Vitturi, M., Pistolesi, M., Ripepe, M. and Neri, A., 2018. Evolution of Conduit Geometry and Eruptive Parameters during Effusive Events. *Geophysical Research Letters*, 45(15), pp. 7471-7480, doi: 10.1029/2018GL077806

Barberi, F., Cioni, R., Rosi, M., Santacroce, R., Sbrana, A. and Vecci, R., 1989. Magmatic and phreatomagmatic phases in explosive eruptions of Vesuvius as deduced by grain-size and

component analysis of the pyroclastic deposits. *Journal of Volcanology and Geothermal Research*, 38(3-4), pp. 287-307, doi: 10.1016/0377-0273(89)90044-9

Barker, S.J., Wilson, C.J.N., Baker, J.A., Millet, M.A., Rotella, M.D., Wright, I.C. and Wysoczanski, R.J., 2012(a). Geochemistry and petrogenesis of silicic magmas in the intra-oceanic Kermadec arc. *Journal of Petrology*, 54(2), pp. 351-391, doi: 10.1093/petrology/egs071

Barker, S.J., Rotella, M.D., Wilson, C.J., Wright, I.C. and Wysoczanski, R.J., 2012(b). Contrasting pyroclast density spectra from subaerial and submarine silicic eruptions in the Kermadec arc: implications for eruption processes and dredge sampling. *Bulletin of volcanology*, 74(6), pp. 1425-1443, doi: 10.1007/s00445-012-0604-2

Baxter, P.J., Bonadonna, C., Dupree, R., Hards, V.L., Kohn, S.C., Murphy, M.D., Nichols, A., Nicholson, R.A., Norton, G., Searl, A. and Sparks, R.S.J., 1999. Cristobalite in volcanic ash of the soufriere hills volcano, montserrat, british west indies. *Science*, 283(5405), pp. 1142-1145, doi: 10.1126/science.283.5405.1142

Befus, K.S., Watkins, J., Gardner, J.E., Richard, D., Befus, K.M., Miller, N.R. and Dingwell, D.B., 2015. Spherulites as in-situ recorders of thermal history in lava flows. *Geology*, 43(7), pp. 647-650, doi: 10.1130/G36639.1, doi: 10.1130/G36639.1

Behrens, H., Ohlhorst, S., Holtz, F. and Champenois, M., 2004. CO_2 solubility in dacitic melts equilibrated with H_2O-CO_2 fluids: Implications for modeling the solubility of CO_2 in silicic melts. *Geochimica et Cosmochimica Acta*, 68(22), pp. 4687-4703, doi: 10.1016/j.gca.2004.04.019

Bindeman, I.N. and Lowenstern, J.B., 2016. Low-δD hydration rinds in Yellowstone perlites record rapid syneruptive hydration during glacial and interglacial conditions. *Contributions to Mineralogy and Petrology*, 171(11), pp. 89(1-24), doi: 10.1007/s00410-016-1293-1

Bischoff, J.L. and Rosenbauer, R.J., 1984. The critical point and two-phase boundary of seawater, 200–500 C. *Earth and Planetary Science Letters*, 68(1), pp. 172-180, doi: 10.1016/0012-821X(84)90149-3

Bohnenstiehl, D.R., Dziak, R.P., Matsumoto, H. and Lau, T.K.A., 2013. Underwater acoustic records from the March 2009 eruption of Hunga Ha'apai-Hunga Tonga volcano in the Kingdom of Tonga. *Journal of Volcanology and Geothermal Research*, 249(1), pp. 12-24, doi: 10.1016/j.jvolgeores.2012.08.014

Bonadonna, C. and Houghton, B.F., 2005. Total grain-size distribution and volume of tephra-fall deposits. *Bulletin of Volcanology*, 67(5), pp. 441-456, doi: 10.1007/s00445-004-0386-2

Bonatti, E., 1965. Palagonite, hyaloclastites and alteration of volcanic glass in the ocean. *Bulletin Volcanologique*, 28(1), pp. 257-269, doi: 10.1007/BF02596930

Bottinga, Y. and Weill, D.F., 1972. The viscosity of magmatic silicate liquids; a model calculation. *American Journal of Science*, 272(5), pp. 438-475, doi: 10.2475/ajs.272.5.438

Brugger, C.R. and Hammer, J.E., 2010. Crystallization kinetics in continuous decompression experiments: implications for interpreting natural magma ascent processes. *Journal of Petrology*, 51(9), pp. 1941-1965, doi: 10.1093/petrology/egq044

Bryan, S.E., Cook, A., Evans, J.P., Colls, P.W., Wells, M.G., Lawrence, M.G., Jell, J.S., Greig, A. and Leslie, R., 2004. Pumice rafting and faunal dispersion during 2001–2002 in the Southwest Pacific: record of a dacitic submarine explosive eruption from Tonga. *Earth and Planetary Science Letters*, 227(1-2), pp. 135-154, doi: 10.1016/j.epsl.2004.08.009

Bryan, S.E., Cook, A.G., Evans, J.P., Hebden, K., Hurrey, L., Colls, P., Jell, J.S., Weatherley, D. and Firn, J., 2012. Rapid, long-distance dispersal by pumice rafting. *PLoS One*, 7(7), pp. e40583, doi: 10.1371/journal.pone.0040583

Burgisser, A., Poussineau, S., Arbaret, L., Druitt, T. H., Giachetti, T., and Bourdier, J. L., 2010. Pre-explosive conduit conditions of the 1997 Vulcanian explosions at Soufrière Hills Volcano, Montserrat: I. Pressure and vesicularity distributions. *Journal of Volcanology and Geothermal Research*, 194(1), pp. 27-41, doi: 10.1016/j.jvolgeores.2010.04.008

Burgisser, A., Chevalier, L., Gardner, J.E. and Castro, J.M., 2017. The percolation threshold and permeability evolution of ascending magmas. *Earth and Planetary Science Letters*, 470, pp. 37-47, doi: 10.1016/j.epsl.2017.04.023

Campbell, K.J., Kinnear, S. and Thame, A., 2015. AUV technology for seabed characterization and geohazards assessment. *The Leading Edge*, 34(2), pp. 170-178, doi: 10.1190/tle34020170.1

Canedo, E.L., Favelukis, M., Tadmor, Z. and Talmon, Y., 1993. An experimental study of bubble deformation in viscous liquids in simple shear flow. *AIChE journal*, 39(4), pp. 553-559, doi: 10.1002/aic.690390403

Carey, R.J., Manga, M., Degruyter, W., Gonnermann, H., Swanson, D., Houghton, B., Orr, T. and Patrick, M., 2013. Convection in a volcanic conduit recorded by bubbles. *Geology*, 41(4), pp. 395–398, doi: 10.1130/G33685.1

Carey, R.J., Wysoczanski, R., Wunderman, R. and Jutzeler, M., 2014. Discovery of the largest historic silicic submarine eruption. *Eos, Transactions American Geophysical Union*, 95(19), pp. 157-159, doi: 10.1002/2014EO190001

Carey, R.J., Soule, S.A., Manga, M., White, J.D.L., McPhie, J., Wysoczanski, R., Jutzeler, M., Tani, K., Fornari, D., Caratori-Tontini, F., Houghton, B.F., Mitchell, S.J., Ikegami, F., Conway, C., Murch, A., Fauria, K., Jones, M., Cahalan, R. and McKenzie, W., 2018. The largest deep-ocean silicic volcanic eruption of the past century. *Science advances*, 4(1), e1701121, doi: 10.1126/sciadv.1701121

Carracedo, J.C., Torrado, F.P., González, A.R., Soler, V., Turiel, J.L.F., Troll, V.R. and Wiesmaier, S., 2012. The 2011 submarine volcanic eruption in El Hierro (Canary Islands). *Geology Today*, 28(2), pp. 53-58, doi: 10.1111/j.1365-2451.2012.00827.x

Carroll, M.R. and Webster, J.D., 1994. Solubilities of sulfur, noble gases, nitrogen, chlorine, and fluorine in magmas. *Reviews in Mineralogy and Geochemistry*, 30(1), pp. 231-279.

Cas, R.A. and Giordano, G., 2014. Submarine volcanism: a review of the constraints, processes and products, and relevance to the Cabo de Gata volcanic succession. *Italian Journal of Geosciences*, 133(3), pp. 362-377, doi: 10.3301/IJG.2014.46

Casadevall, T.J., 1994. Volcanic ash and aviation safety: proceedings of the first international symposium on volcanic ash and aviation safety (Vol. 2047). *US Government Printing Office*.

Cashman, K.V. and Fiske, R.S., 1991. Fallout of pyroclastic debris from submarine volcanic eruptions. *Science*, 253(5017), pp. 275-280, doi: 10.1126/science.253.5017.275

Cashman, K.V. and Sparks, R.S.J., 2013. How volcanoes work: A 25 year perspective. *Bulletin*, 125(5-6), pp. 664-690, doi: 10.1130/B30720.1

Cashman, K.V. and Scheu, B., 2015. Magmatic fragmentation. *In The Encyclopedia of Volcanoes (Second Edition)*, pp. 459-471, doi: 10.1016/B978-0-12-385938-9.00025-0.

Cassidy, M., Manga, M., Cashman, K. and Bachmann, O., 2018. Controls on explosive-effusive volcanic eruption styles. *Nature communications*, 9(1):2839, doi: 10.1038/s41467-018-05293-3

Clague, D.A., Paduan, J.B. and Davis, A.S., 2009. Widespread strombolian eruptions of mid-ocean ridge basalt. *Journal of Volcanology and Geothermal Research*, 180(2), pp. 171-188, doi: 10.1016/j.jvolgeores.2008.08.007

Cluzel, N., Laporte, D., Provost, A. and Kannewischer, I., 2008. Kinetics of heterogeneous bubble nucleation in rhyolitic melts: implications for the number density of bubbles in volcanic conduits and for pumice textures. *Contributions to Mineralogy and Petrology*, 156(6), pp. 745-763, doi: 10.1007/s00410-008-0313-1

Coats, R.R., 1962. Magma type and crustal structure in the Aleutian arc. *In The Crust of the Pacific Basin*, 6, pp. 92-109, doi: 10.1029/GM006p0092

Collins, S.J., Pyle, D.M. and Maclennan, J., 2009. Melt inclusions track pre-eruption storage and dehydration of magmas at Etna. *Geology*, 37(6), pp. 571-574, doi: 10.1130/G30040A.1

Coombs, D.S. and Landis, C.A., 1966. Pumice from the south sandwich eruption of march 1962 reaches new zealand. *Nature*, 209(5020), pp. 289-290, doi: 10.1038/209289b0

Crisp, J.A., 1984. Rates of magma emplacement and volcanic output. *Journal of Volcanology and Geothermal Research*, 20(3-4), pp. 177-211, doi: 10.1016/0377-0273(84)90039-8

Dawson, A.G., 1999. Linking tsunami deposits, submarine slides and offshore earthquakes. *Quaternary International*, 60(1), pp. 119-126, doi: 10.1016/S1040-6182(99)00011-7

Degruyter, W., Bachmann, O., Burgisser, A. and Manga, M., 2012. The effects of outgassing on the transition between effusive and explosive silicic eruptions. *Earth and Planetary Science Letters*, 349, pp. 161-170, doi: 10.1016/j.epsl.2012.06.056

Del Gaudio, P., Behrens, H. and Deubener, J., 2007. Viscosity and glass transition temperature of hydrous float glass. *Journal of Non-crystalline solids*, 353(3), pp. 223-236, doi: 10.1016/j.jnoncrysol.2006.11.009

Denton, J.S., Tuffen, H., Gilbert, J.S. and Odling, N., 2009. The hydration and alteration of perlite and rhyolite. *Journal of the Geological Society*, 166(5), pp. 895-904, doi: 10.1144/0016-76492008-007

Deubener, J., Müller, R., Behrens, H. and Heide, G., 2003. Water and the glass transition temperature of silicate melts. *Journal of Non-Crystalline Solids*, 330(1), pp. 268-273, doi: 10.1016/S0022-3093(03)00472-1

Devine, J.D., Gardner, J.E., Brack, H.P., Laynet, G.D. and Rutherford, M.J., 1995. Comparison of microanalytical methods for estimating H_2O contents of silicic volcanic glasses. *American Mineralogist*, 80(3-4), pp. 319-328, doi: 10.2138/am-1995-3-414

Dingwell, D.B., Scarfe, C.M. and Cronin, D.J., 1985. The effect of fluorine on viscosities in the system Na_2O-Al_2O_3-SiO_2: implications for phonolites, trachytes and rhyolites. *American Mineralogist*, (1-2), pp. 80-87, doi: 10.5282/ubm/epub.5978

Dingwell, D.B. and Webb, S.L., 1990. Relaxation in silicate melts. *European Journal of Mineralogy*, 4, pp. 427-449.

Dingwell, D.B., Lavallée, Y., Hess, K.U., Flaws, A., Martí Molist, J., Nichols, A.R., Gilg, H.A. and Schillinger, B., 2016. Eruptive shearing of tube pumice: pure and simple. *Solid Earth*, 7(5), pp. 1383–1393, doi: 10.5194/se-7-1383-2016

Dixon, J.E., Stolper, E.M. and Holloway, J.R., 1995. An experimental study of water and carbon dioxide solubilities in mid-ocean ridge basaltic liquids. Part I: calibration and solubility models. *Journal of Petrology*, 36(6), pp. 1607-1631, doi: 10.1093/oxfordjournals.petrology.a037267

Dominey-Howes, D.T.M., Papadopoulos, G.A. and Dawson, A.G., 2000. Geological and historical investigation of the 1650 Mt. Columbo (Thera Island) eruption and tsunami, Aegean Sea, Greece. *Natural Hazards*, 21(1), pp. 83-96, doi: 10.1023/A:1008178100633

Driesner, T., 2007. The system H_2O–NaCl. Part II: Correlations for molar volume, enthalpy, and isobaric heat capacity from 0 to 1000 C, 1 to 5000 bar, and 0 to 1 XNaCl. *Geochimica et Cosmochimica Acta*, 71(20), pp. 4902-4919, doi: 10.1016/j.gca.2007.05.026

Driesner, T. and Heinrich, C.A., 2007. The system H_2O–NaCl. Part I: Correlation formulae for phase relations in temperature–pressure–composition space from 0 to 1000 C, 0 to 5000 bar, and 0 to 1 XNaCl. *Geochimica et Cosmochimica Acta*, 71(20), pp. 4880-4901, doi: 10.1016/j.gca.2006.01.033

Eichelberger, J.C. and Westrich, H.R., 1981. Magmatic volatiles in explosive rhyolitic eruptions. *Geophysical research letters*, 8(7), pp. 757-760, doi: 10.1029/GL008i007p00757

Embley, R.W. and Rubin, K.H., 2018. Extensive young silicic volcanism produces large deep submarine lava flows in the NE Lau Basin. *Bulletin of Volcanology*, 80(4):36, doi: 10.1007/s00445-018-1211-7

Ewart, A., Brothers, R.N. and Mateen, A., 1977. An outline of the geology and geochemistry, and the possible petrogenetic evolution of the volcanic rocks of the Tonga-Kermadec-New Zealand island arc. *Journal of volcanology and geothermal research*, 2(3), pp. 205-250, doi: 10.1016/0377-0273(77)90001-4

Fauria, K. E., 2017. Dynamics of pyroclastic density currents and submarine eruptions (*Doctoral Dissertation, University of California, Berkeley*).

Fauria, K.E., Manga, M. and Wei, Z., 2017. Trapped bubbles keep pumice afloat and gas diffusion makes pumice sink. *Earth and Planetary Science Letters*, 460, pp. 50-59, doi: 10.1016/j.epsl.2016.11.055

Fauria, K. F. & Manga, M. 2018, Pyroclast cooling and saturation in water, *Journal of Volcanology and Geothermal Research*, 352, pp.17-31, doi: 10.1016/j.jvolgeores.2018.07.002

Ferguson, D.J., Gonnermann, H.M., Ruprecht, P., Plank, T., Hauri, E.H., Houghton, B.F. and Swanson, D.A., 2016. Magma decompression rates during explosive eruptions of Kīlauea volcano, Hawaii, recorded by melt embayments. *Bulletin of Volcanology*, 78(10):71, doi: 10.1007/s00445-016-1064-x

Fiske, R.S., Naka, J., Iizasa, K., Yuasa, M. and Klaus, A., 2001. Submarine silicic caldera at the front of the Izu-Bonin arc, Japan: Voluminous seafloor eruptions of rhyolite pumice. *Geological Society of America Bulletin*, 113(7), pp. 813-824, doi: 10.1130/0016-7606(2001)113<0813:SSCATF>2.0.CO;2

Francis, P. and Self, S., 1983. The eruption of Krakatau. *Scientific American*, 249(5), pp.172-187.

Frogner, P., Gíslason, S.R. and Óskarsson, N., 2001. Fertilizing potential of volcanic ash in ocean surface water. *Geology*, 29(6), pp. 487-490, doi: 10.1130/0091-7613(2001)029<0487:FPOVAI>2.0.CO;2

Gardner, J.E., Rutherford, M., Carey, S. and Sigurdsson, H., 1995. Experimental constraints on pre-eruptive water contents and changing magma storage prior to explosive eruptions of Mount St Helens volcano. *Bulletin of Volcanology*, 57(1), pp. 1-17, doi: 10.1007/BF00298703

Gardner, J.E., Jackson, B. A., Gonnermann, H. and Soule, S.A., 2016. Rapid ascent and emplacement of basaltic lava during the 2005–06 eruption of the East Pacific Rise at ca. 9 51′ N as inferred from CO_2 contents. *Earth and Planetary Science Letters*, 453, pp. 152-160, doi: 10.1016/j.epsl.2016.08.007

Gardner, J.E. and Webster, J.D., 2016. The impact of dissolved CO_2 on bubble nucleation in water-poor rhyolite melts. *Chemical Geology*, 420, pp. 180-185, doi: 10.1016/j.chemgeo.2015.11.017

Gardner, J.E., Hajimirza, S., Webster, J.D. and Gonnermann, H.M., 2018. The impact of dissolved fluorine on bubble nucleation in hydrous rhyolite melts. *Geochimica et Cosmochimica Acta*, 226, pp. 174-181, doi: 10.1016/j.gca.2018.02.013

Gass, I.G., Harris, P.G. and Holdgate, M.W., 1963. Pumice eruption in the area of the South Sandwich Islands. *Geological Magazine*, 100(4), pp. 321-330, doi: 10.1017/S0016756800056053

Giachetti, T., Druitt, T.H., Burgisser, A., Arbaret, L. and Galven, C., 2010. Bubble nucleation, growth and coalescence during the 1997 Vulcanian explosions of Soufrière Hills Volcano, Montserrat. *Journal of Volcanology and Geothermal Research*, 193(3-4), pp. 215-231, doi: 10.1016/j.jvolgeores.2010.04.001

Giachetti, T. and Gonnermann, H.M., 2013. Water in volcanic pyroclast: Rehydration or incomplete degassing? *Earth and Planetary Science Letters*, 369, pp. 317-332, doi: 10.1016/j.epsl.2013.03.041

Giachetti, T., Gonnermann, H., Gardner, J., Shea, T. and Gouldstone, A., 2015. Discriminating secondary from magmatic water in rhyolitic matrix-glass of volcanic pyroclasts using thermogravimetric analysis. *Geochimica et Cosmochimica Acta*, 148, pp. 457-476, doi: 10.1016/j.gca.2014.10.017

Gifkins, C.C., McPhie, J. and Allen, R.L., 2002. Pumiceous rhyolitic peperite in ancient submarine volcanic successions. *Journal of Volcanology and Geothermal Research*, 114(1-2), pp. 181-203, doi: 10.1016/S0377-0273(01)00284-0

Giordano, D., Romano, C., Dingwell, D.B., Poe, B. and Behrens, H., 2004. The combined effects of water and fluorine on the viscosity of silicic magmas. *Geochimica et Cosmochimica Acta*, 68(24), pp. 5159-5168, doi: 10.1016/j.gca.2004.08.012

Giordano, D., Nichols, A.R. and Dingwell, D.B., 2005. Glass transition temperatures of natural hydrous melts: a relationship with shear viscosity and implications for the welding process. *Journal of Volcanology and Geothermal Research*, 142(1), pp. 105-118, doi: 10.1016/j.jvolgeores.2004.10.015

Giordano, D., Russell, J.K. and Dingwell, D.B., 2008. Viscosity of magmatic liquids: a model. *Earth and Planetary Science Letters*, 271(1-4), pp. 123-134, doi: 10.1016/j.epsl.2008.03.038

Gonnermann, H. M. and Manga, M., 2003. Explosive volcanism may not be an inevitable consequence of magma fragmentation. *Nature*, 426(6965), pp. 432-435, doi: 10.1038/nature02138

Gonnermann, H. M. and Manga, M., 2005. Nonequilibrium magma degassing: results from modeling of the ca. 1340 AD eruption of Mono Craters, California. *Earth and Planetary Science Letters*, 238(1), pp. 1-16, doi: 10.1016/j.epsl.2005.07.021

Gonnermann, H.M. and Gardner, J.E., 2013. Homogeneous bubble nucleation in rhyolitic melt: Experiments and nonclassical theory. *Geochemistry, Geophysics, Geosystems*, 14(11), pp. 4758-4773, doi: 10.1002/ggge.20281

Gottsmann, J. and Dingwell, D. B., 2001. The cooling of frontal flow ramps: a calorimetric study on the Rocche Rosse rhyolite flow, Lipari, Aeolian Islands, Italy. *Terra Nova*, 13(3), pp. 157-164, doi: 10.1046/j.1365-3121.2001.00332.x

Grindle, T.J. and Burcham Jr, F.W., 2003. Engine damage to a NASA DC-8-72 airplane from a high-altitude encounter with a diffuse volcanic ash cloud, NASA technical reports, NASA/TM-2003-212030, NAS 1.15:212030, H-2511.

Gruen, G., Weis, P., Driesner, T., Heinrich, C.A. and de Ronde, C.E., 2014. Hydrodynamic modeling of magmatic–hydrothermal activity at submarine arc volcanoes, with implications for ore formation. *Earth and Planetary Science Letters*, 404, pp. 307-318, doi: 10.1016/j.epsl.2014.07.041

Hall-Spencer, J.M., Rodolfo-Metalpa, R., Martin, S., Ransome, E., Fine, M., Turner, S.M., Rowley, S.J., Tedesco, D. and Buia, M.C., 2008. Volcanic carbon dioxide vents show ecosystem effects of ocean acidification. *Nature*, 454(7200), pp. 96-99, doi: 10.1038/nature07051

Hamada, M., Laporte, D., Cluzel, N., Koga, K.T. and Kawamoto, T., 2010. Simulating bubble number density of rhyolitic pumices from Plinian eruptions: constraints from fast decompression experiments. *Bulletin of Volcanology*, 72(6), pp. 735-746, doi: 10.1007/s00445-010-0353-z

Hartmann, W.K., Malin, M., McEwen, A., Carr, M., Soderblom, L., Thomas, P., Danielson, E., James, P. and Veverka, J., 1999. Evidence for recent volcanism on Mars from crater counts. *Nature*, 397(6720), pp. 586-589, doi: 10.1038/17545

Hauri, E., 2002. SIMS analysis of volatiles in silicate glasses, 2: isotopes and abundances in Hawaiian melt inclusions. *Chemical Geology*, 183(1), pp. 115-141, doi: 10.1016/S0009-2541(01)00374-6

Hauri, E., Wang, J., Dixon, J.E., King, P.L., Mandeville, C. and Newman, S., 2002. SIMS analysis of volatiles in silicate glasses: 1. Calibration, matrix effects and comparisons with FTIR. *Chemical Geology*, 183(1-4), pp. 99-114, doi: 10.1016/S0009-2541(01)00375-8

Head, J.W., Crumpler, L.S., Aubele, J.C., Guest, J.E. and Saunders, R.S., 1992. Venus volcanism: Classification of volcanic features and structures, associations, and global distribution from Magellan data. *Journal of Geophysical Research: Planets*, 97(E8), pp. 13153-13197, doi: 10.1029/92JE01273

Head III, J.W. and Wilson, L., 2003. Deep submarine pyroclastic eruptions: theory and predicted landforms and deposits. *Journal of Volcanology and Geothermal Research*, 121(3-4), pp. 155-193, doi: 10.1016/S0377-0273(02)00425-0

Hedenquist, J.W. and Lowenstern, J.B., 1994. The role of magmas in the formation of hydrothermal ore deposits. *Nature*, 370(6490), pp. 519-527, doi: 10.1038/370519a0

Helo, C., Longpré, M.A., Shimizu, N., Clague, D.A. and Stix, J., 2011. Explosive eruptions at mid-ocean ridges driven by CO_2-rich magmas. *Nature Geoscience*, 4(4), pp. 260-263, doi: 10.1038/ngeo1104

Hodder, A.P.W., 1978, Refractive index and hydration of rhyolitic glass from Holocene tephras, North Island, New Zealand. *New Zealand Journal of Geology and Geophysics*, 21(2), pp. 155-166, doi: 10.1080/00288306.1978.10424047

Horwell, C.J., Williamson, B.J., Llewellin, E.W., Damby, D.E. and Le Blond, J.S., 2013. The nature and formation of cristobalite at the Soufrière Hills volcano, Montserrat: implications

for the petrology and stability of silicic lava domes. *Bulletin of Volcanology*, 75(3):696, doi: 10.1007/s00445-013-0696-3

Houghton, B.F. and Wilson, C., 1989. A vesicularity index for pyroclastic deposits. *Bulletin of volcanology*, 51(6), pp. 451-462, doi: 10.1007/BF01078811

Houghton, B.F., Carey, R.J., Cashman, K.V., Wilson, C.J., Hobden, B.J. and Hammer, J. E., 2010. Diverse patterns of ascent, degassing, and eruption of rhyolite magma during the 1.8 ka Taupo eruption, New Zealand: evidence from clast vesicularity. *Journal of Volcanology and Geothermal Research*, 195(1), pp. 31-47, doi: 10.1016/j.jvolgeores.2010.06.002

Hynek, B.M., Phillips, R.J. and Arvidson, R.E., 2003. Explosive volcanism in the Tharsis region: Global evidence in the Martian geologic record. *Journal of Geophysical Research: Planets*, 108(E9):15, doi: 10.1029/2003JE002062

Ibáñez, J.M., De Angelis, S., Díaz-Moreno, A., Hernández, P., Alguacil, G., Posadas, A. and Pérez, N., 2012. Insights into the 2011–2012 submarine eruption off the coast of El Hierro (Canary Islands, Spain) from statistical analyses of earthquake activity. *Geophysical Journal International*, 191(2), pp. 659-670, doi: 10.1111/j.1365-246X.2012.05629.x

Ikegami, F., McPhie, J., Carey, R. J., Mundana, R., Soule, S. A. and Jutzeler, M., 2018. The eruption of submarine rhyolite lavas and domes in the deep ocean — Havre 2012, Kermadec arc. *Frontiers In Earth Science,* 6(147), doi: 10.3389/feart.2018.00147

Isgett, S.J., Houghton, B.F., Fagents, S.A., Biass, S., Burgisser, A. and Arbaret, L., 2017. Eruptive and shallow conduit dynamics during Vulcanian explosions: insights from the Episode IV block field of the 1912 eruption of Novarupta, Alaska. Bulletin of Volcanology, 79(8)58, doi: 10.1007/s00445-017-1138-4

Jenkins, S.F., Wilson, T.M., Magill, C., Miller, V., Stewart, C., Blong, R., Marzocchi, W., Boulton, M., Bonadonna, C. and Costa, A., 2015. Volcanic ash fall hazard and risk. *In Global Volcanic Hazards and Risk*, pp. 173-222.

Jokiel, P.L. and Cox, E.F., 2003. Drift pumice at Christmas Island and Hawaii: evidence of oceanic dispersal patterns. *Marine Geology*, 202(3-4), pp. 121-133, doi: 10.1016/S0025-3227(03)00288-3

Jutzeler, M., Marsh, R., Carey, R.J., White, J.D., Talling, P.J. and Karlstrom, L., 2014. On the fate of pumice rafts formed during the 2012 Havre submarine eruption. *Nature communications*, 5, pp. 3660(1-9), doi: 10.1038/ncomms4660

Kano, K., Yamamoto, T. and Ono, K., 1996. Subaqueous eruption and emplacement of the Shinjima Pumice, Shinjima (Moeshima) Island, Kagoshima Bay, SW Japan. *Journal of Volcanology and Geothermal Research*, 71(2-4), pp. 187-206, doi: 10.1016/0377-0273(95)00077-1

Kano, K., 2003. Subaqueous pumice eruptions and their products: A review. *Explosive subaqueous volcanism*, pp. 213-229, doi: 10.1029/140GM14

Kato, Y.U.Z.O., 1987. Woody pumice generated with submarine eruption. *Journal of the Geological Society of Japan*, 77, pp. 193-206.

Kelley, D., 2017. Volcanology: Vulcan rule beneath the sea. *Nature Geoscience*, 10(4), pp. 251-253, doi: 10.1038/ngeo2929

Kendrick, J.E., Lavallée, Y., Varley, N.R., Wadsworth, F.B., Lamb, O.D. and Vasseur, J., 2016. Blowing off steam: tuffisite formation as a regulator for lava dome eruptions. *Frontiers in Earth Science*, 4(41), doi: 10.3389/feart.2016.00041

Kokelaar, B.P. and Durant, G.P., 1983. The submarine eruption and erosion of Surtla (Surtsey), Iceland. *Journal of Volcanology and Geothermal Research*, 19(3-4), pp. 239-246, doi: 10.1016/0377-0273(83)90112-9

Kueppers, U., Scheu, B., Spieler, O. and Dingwell, D.B., 2006. Fragmentation efficiency of explosive volcanic eruptions: a study of experimentally generated pyroclasts. *Journal of Volcanology and Geothermal Research*, 153(1-2), pp. 125-135, doi: 10.1016/j.jvolgeores.2005.08.006

Kushnir, A.R., Martel, C., Bourdier, J.L., Heap, M.J., Reuschlé, T., Erdmann, S., Komorowski, J.C. and Cholik, N., 2016. Probing permeability and microstructure: Unravelling the role of a low-permeability dome on the explosivity of Merapi (Indonesia). *Journal of Volcanology and Geothermal Research*, 316, pp. 56-71, doi: 10.1016/j.jvolgeores.2016.02.012

Kushnir, A.R., Martel, C., Champallier, R. and Arbaret, L., 2017. In situ confirmation of permeability development in shearing bubble-bearing melts and implications for volcanic outgassing. *Earth and Planetary Science Letters*, 458, pp. 315-326, doi: 10.1016/j.epsl.2016.10.053

Le Losq, C., Neuville, D.R., Moretti, R. and Roux, J., 2012. Determination of water content in silicate glasses using Raman spectrometry: Implications for the study of explosive volcanism. *American Mineralogist*, 97(5-6), pp. 779-790, doi: 10.2138/am.2012.3831

Liu, Y., Zhang, Y. and Behrens, H., 2005. Solubility of H_2O in rhyolitic melts at low pressures and a new empirical model for mixed H_2O–CO_2 solubility in rhyolitic melts. *Journal of Volcanology and Geothermal Research*, 143(1-3), pp. 219-235, doi: 10.1016/j.jvolgeores.2004.09.019

Liu, E.J., Cashman, K.V., Rust, A.C. and Gislason, S.R., 2015(a). The role of bubbles in generating fine ash during hydromagmatic eruptions. *Geology*, 43(3), pp. 239-242, doi: 10.1130/G36336.1

Liu, E.J., Cashman, K.V. and Rust, A.C., 2015(b). Optimising shape analysis to quantify volcanic ash morphology. *GeoResJ*, 8, pp. 14-30, doi: 10.1016/j.grj.2015.09.001

Llewellin, E.W. and Manga, M., 2005. Bubble suspension rheology and implications for conduit flow. *Journal of Volcanology and Geothermal Research*, 143(1-3), pp. 205-217, doi: 10.1016/j.jvolgeores.2004.09.018

Magnall, N., James, M., Tuffen, H. and Vye-Brown, C., 2018. Commonalities in the emplacement of cooling-limited lavas: insights from the 2011-2012 Cordón Caulle rhyolitic eruption (*Doctoral dissertation, Lancaster University*).

Manga, M., Fauria, K.E., Lin, C., Mitchell, S.J., Jones, M., Conway, C.E., Degruyter, W., Hosseini, B., Carey, R., Cahalan, R. and Houghton, B.F., 2018. The pumice raft-forming 2012 Havre submarine eruption was effusive. *Earth and Planetary Science Letters*, 489, pp. 49-58, doi: 10.1016/j.epsl.2018.02.025

Manga, M., Mitchell, S. J., Degruyter, W. and Carey, R. J., (*In Press*) Transition of eruptive style: Pumice raft to dome-forming eruption at the Havre submarine volcano. *Geology*, doi: 10.1130/G45436.1

Manville, V., Segschneider, B., Newton, E., White, J.D.L., Houghton, B.F. and Wilson, C.J.N., 2009. Environmental impact of the 1.8 ka Taupo eruption, New Zealand: Landscape responses to a large-scale explosive rhyolite eruption. *Sedimentary Geology*, 220(3-4), pp. 318-336, doi: 10.1016/j.sedgeo.2009.04.017

Martin, E., Bindeman, I., Balan, E., Palandri, J., Seligman, A. and Villemant, B., 2017. Hydrogen isotope determination by TC/EA technique in application to volcanic glass as a window into secondary hydration. *Journal of Volcanology and Geothermal Research*, 348, pp. 49-61, doi: 10.1016/j.jvolgeores.2017.10.013

Masson, D.G., Harbitz, C.B., Wynn, R.B., Pedersen, G. and Løvholt, F., 2006. Submarine landslides: processes, triggers and hazard prediction. *Philosophical Transactions of the Royal Society of London A: Mathematical, Physical and Engineering Sciences*, 364(1845), pp. 2009-2039, doi: 10.1098/rsta.2006.1810

McIntosh, I. M., 2013. Bubble growth and resorption in magma: insights from dissolved water distributions in volcanic glass (*Doctoral dissertation, Durham University*).

McIntosh, I.M., Llewellin, E.W., Humphreys, M.C.S., Nichols, A.R.L., Burgisser, A., Schipper, C.I. and Larsen, J.F., 2014. Distribution of dissolved water in magmatic glass records growth and resorption of bubbles. *Earth and Planetary Science Letters*, 401, pp. 1-11, doi: 10.1016/j.epsl.2014.05.037

McIntosh, I.M., Nichols, A.R.L., Tani, K. and Llewellin, E.W., 2017. Accounting for the species-dependence of the 3500 cm^{-1} H_2O_T infrared molar absorptivity coefficient: implications for

hydrated volcanic glasses. *American Mineralogist*, 102, pp. 1677-1689, doi: 10.2138/am-2017-5952CCBY

McPhie, J. and Allen, R.L., 2003. Submarine, Silicic, Syn-Eruptive Pyroclastic Units in the Mount Read Volcanics, Western Tasmania: Influence of Vent Setting and Proximity on Lithofacies Characteristics. *Explosive subaqueous volcanism*, pp. 245-258, doi: 10.1029/140GM16

Mellors, R., Kilb, D., Aliyev, A., Gasanov, A. and Yetirmishli, G., 2007. Correlations between earthquakes and large mud volcano eruptions. *Journal of Geophysical Research: Solid Earth*, 112(B4), doi: 10.1029/2006JB004489

Meyer, J. and Wisdom, J., 2008. Episodic volcanism on Enceladus: Application of the Ojakangas–Stevenson model. *Icarus*, 198(1), pp. 178-180, doi: 10.1016/j.icarus.2008.06.012

McEwen, A.S., Keszthelyi, L., Spencer, J.R., Schubert, G., Matson, D.L., Lopes-Gautier, R., Klaasen, K.P., Johnson, T.V., Head, J.W., Geissler, P. and Fagents, S., 1998. High-temperature silicate volcanism on Jupiter's moon Io. *Science*, 281(5373), pp. 87-90, doi: 10.1126/science.281.5373.87

Millero, F.J. and Huang, F., 2009. The density of seawater as a function of salinity (5 to 70 g kg^{-1}) and temperature (273.15 to 363.15 K). *Ocean Science*, 5(2), pp. 91-100, doi: 10.5194/os-5-91-2009

Mitchell, S.J., McIntosh, I.M., Houghton, B.F., Carey, R.J. and Shea, T., 2018(a). Dynamics of a powerful deep submarine eruption recorded in H_2O contents and speciation in rhyolitic glass: The 2012 Havre eruption. *Earth and Planetary Science Letters*, 494, pp. 135-147, doi: 10.1016/j.epsl.2018.04.053

Mitchell, S.J., Biass, S., Houghton, B.F., Anderson, A., Bonny, E., Walker, B.H., Mintz, B.G., Turner, N.R., Frank, D., Carey, R.J. and Rosenberg, M.D., 2018(b). The interplay among clast size, vesicularity, postfragmentation expansion, and clast breakage: An example from the 1.8 ka Taupo eruption. *In Poland, M., Garcia, M., Camp, V., and Grunder, A., eds., Field Volcanology: A Tribute to the Distinguished Career of Don Swanson: Geological Society of America Special Paper*, 538(17), pp. 375-383, doi: 10.1130/2018.2538(17)

Mitchell, S. J., Houghton, B. F., Carey, R. J., Manga, M., Fauria, K., Jones, M. R., Conway, C. E., Soule, A. S., Wei, Z., & Giachetti, T., (*In review*) Submarine giant pumice: A window into the shallow conduit dynamics of a recent silicic eruption.

Mueller, S., Scheu, B., Spieler, O. and Dingwell, D.B., 2008. Permeability control on magma fragmentation. *Geology*, 36(5), pp. 399-402, doi: 10.1130/G24605A.1

Mundana, R. and Carey, R.J., 2017. Havre 2012 Submarine Eruption: The Role of Hydrostatic Pressure on the Morphology of a Silicic Lava Flow. *AGU Chapman Conference on Submarine Volcanism: New Approaches and Research Frontiers, Abstract*. 203454.

Murch, A., 2018. Ash Generation in the 2012 Eruption of Havre Volcano, Kermadec Arc: The Largest Deep Subaqueous Eruption of the Last Century (*Doctoral dissertation, University of Otago*).

Nanayama, F., Satake, K., Furukawa, R., Shimokawa, K., Atwater, B.F., Shigeno, K. and Yamaki, S., 2003. Unusually large earthquakes inferred from tsunami deposits along the Kuril trench. *Nature*, 424(6949), pp. 660-663, doi: 10.1038/nature01864

Newman, S., Stolper, E. M. and Epstein, S., 1986. Measurement of water in rhyolitic glasses; calibration of an infrared spectroscopic technique. *American Mineralogist*, 71(11-12), pp. 1527-1541.

Newman, S. and Lowenstern, J.B., 2002. VolatileCalc: a silicate melt–H_2O–CO_2 solution model written in Visual Basic for excel. *Computers & Geosciences*, 28(5), pp. 597-604, doi: 10.1016/S0098-3004(01)00081-4

Ni, H. and Zhang, Y., 2008. H_2O diffusion models in rhyolitic melt with new high pressure data. *Chemical Geology*, 250(1), pp. 68-78, doi: 10.1016/j.chemgeo.2008.02.011

Ni, H. and Zhang, L., 2018. A general model of water diffusivity in calc-alkaline silicate melts and glasses. *Chemical Geology*, 478, pp. 60-68, doi: 10.1016/j.chemgeo.2017.10.010

Nichols, A.R. and Wysoczanski, R.J., 2007. Using micro-FTIR spectroscopy to measure volatile contents in small and unexposed inclusions hosted in olivine crystals. *Chemical Geology*, 242(3), pp. 371-384, doi: 10.1016/j.chemgeo.2007.04.007

Nomikou, P., Carey, S., Papanikolaou, D., Bell, K.C., Sakellariou, D., Alexandri, M. and Bejelou, K., 2012. Submarine volcanoes of the Kolumbo volcanic zone NE of Santorini Caldera, Greece. *Global and Planetary Change*, 90, pp. 135-151, doi: 10.1016/j.gloplacha.2012.01.001

Nomikou, P., Carey, S., Bell, K.L.C., Papanikolaou, D., Bejelou, K., Cantner, K., Sakellariou, D. and Perros, I., 2014. Tsunami hazard risk of a future volcanic eruption of Kolumbo submarine volcano, NE of Santorini Caldera, Greece. *Natural hazards*, 72(3), pp. 1375-1390, doi: 10.1007/s11069-012-0405-0

Nowak, M. and Behrens, H., 2001. Water in rhyolitic magmas: getting a grip on a slippery problem. *Earth and Planetary Science Letters*, 184(2), pp. 515-522, doi: 10.1016/S0012-821X(00)00343-5

Owen, J., Tuffen, H. and McGarvie, D.W., 2013(a). Explosive subglacial rhyolitic eruptions in Iceland are fuelled by high magmatic H_2O and closed-system degassing. *Geology*, 41(2), pp. 251-254, doi: 10.1130/G33647.1

Owen, J., Tuffen, H. and McGarvie, D. W., 2013(b), Pre-eruptive volatile content, degassing paths and depressurization explaining the transition in style at the subglacial rhyolitic eruption of Dalakvísl, South Iceland. *Journal of Volcanology and Geothermal Research*, 258, pp. 143-162, doi: 10.1016/j.jvolgeores.2013.03.021

Papale, P. (1999). Strain-induced magma fragmentation in explosive eruptions. *Nature*, *397*(6718), pp. 425-428, doi: 10.1038/17109

Plank, T., Kelley, K.A., Zimmer, M.M., Hauri, E.H. and Wallace, P.J., 2013. Why do mafic arc magmas contain~ 4 wt. % water on average? *Earth and Planetary Science Letters*, 364, pp. 168-179, doi: 10.1016/j.epsl.2012.11.044

Polacci, M., Papale, P., Del Seppia, D., Giordano, D. and Romano, C., 2004. Dynamics of magma ascent and fragmentation in trachytic versus rhyolitic eruptions. *Journal of volcanology and geothermal research*, 131(1-2), pp. 93-108, doi: 10.1016/S0377-0273(03)00319-6

Pontbriand, C.W., Soule, S.A., Sohn, R.A., Humphris, S.E., Kunz, C., Singh, H., Nakamura, K.I., Jakobsson, M. and Shank, T., 2012. Effusive and explosive volcanism on the ultraslow-spreading Gakkel Ridge, 85° E. *Geochemistry, Geophysics, Geosystems*, 13(10), pp. 1-22, doi: 10.1029/2012GC004187

Potuzak, M., Nichols, A.R., Dingwell, D.B. and Clague, D.A., 2008. Hyperquenched volcanic glass from Loihi Seamount, Hawaii. *Earth and Planetary Science Letters*, 270(1), pp. 54-62, doi: 10.1016/j.epsl.2008.03.018

Price, J.F., Weller, R.A. and Schudlich, R.R., 1987. Wind-driven ocean currents and Ekman transport. *Science*, 238(4833), pp. 1534-1538, doi: 10.1126/science.238.4833.1534

Richet, P., Bottinga, Y., Denielou, L., Petitet, J.P. and Tequi, C., 1982. Thermodynamic properties of quartz, cristobalite and amorphous SiO2: drop calorimetry measurements between 1000 and 1800 K and a review from 0 to 2000 K. *Geochimica et Cosmochimica Acta*, 46(12), pp. 2639-2658, doi: 10.1016/0016-7037(82)90383-0

Riker, J.M., Blundy, J.D., Rust, A.C., Botcharnikov, R.E. and Humphreys, M.C., 2015. Experimental phase equilibria of a Mount St. Helens rhyodacite: a framework for interpreting crystallization paths in degassing silicic magmas. *Contributions to Mineralogy and Petrology*, 170(1), pp. 6, doi: 10.1007/s00410-015-1160-5

Risso, C., Scasso, R.A. and Aparicio, A., 2002. Presence of large pumice blocks on Tierra del Fuego and South Shetland Islands shorelines, from 1962 South Sandwich Islands eruption. *Marine Geology*, *186*(3), pp. 413-422, doi: 10.1016/S0025-3227(02)00190-1

Rossby, C.G., 1936. Dynamics of steady ocean currents in the light of experimental fluid mechanics. *Papers in Physical Oceanography and Meteorology (MIT-WHOI)*, 5(1), pp. 1-43, doi: 10.1575/1912/1088

Rotella, M.D., Wilson, C.J., Barker, S.J. and Wright, I.C., 2013. Highly vesicular pumice generated by buoyant detachment of magma in subaqueous volcanism. *Nature Geoscience*, 6(2) pp. 129-132, doi: 10.1038/ngeo1709

Rotella, M.D., Wilson, C.J., Barker, S.J., Cashman, K.V., Houghton, B.F. and Wright, I.C., 2014. Bubble development in explosive silicic eruptions: insights from pyroclast vesicularity textures from Raoul volcano (Kermadec arc). *Bulletin of Volcanology*, 76(8):826, doi: 10.1007/s00445-014-0826-6

Rotella, M.D., Wilson, C.J., Barker, S.J., Schipper, C.I., Wright, I.C. and Wysoczanski, R.J., 2015. Dynamics of deep submarine silicic explosive eruptions in the Kermadec arc, as reflected in pumice vesicularity textures. *Journal of Volcanology and Geothermal Research*, 301, pp. 314-332, doi: 10.1016/j.jvolgeores.2015.05.021

Rubin, K.H., Soule, S.A., Chadwick Jr, W.W., Fornari, D.J., Clague, D.A., Embley, R.W., Baker, E.T., Perfit, M.R., Caress, D.W. and Dziak, R.P., 2012. Volcanic eruptions in the deep sea. *Oceanography*, 25(1), pp. 142-157.

Rust, A.C. and Manga, M., 2002. Bubble shapes and orientations in low Re simple shear flow. *Journal of Colloid and Interface Science*, 249(2), pp. 476-480, doi: 10.1006/jcis.2002.8292

Rust, A.C. and Cashman, K.V., 2004. Permeability of vesicular silicic magma: inertial and hysteresis effects. *Earth and Planetary Science Letters*, *228*(1), pp. 93-107, doi: 10.1016/j.epsl.2004.09.025

Rust, A.C. and Cashman, K.V., 2011. Permeability controls on expansion and size distributions of pyroclasts. *Journal of Geophysical Research: Solid Earth*, 116(B11):202, doi: 10.1029/2011JB008494

Rutherford, M.J. and Hill, P.M., 1993. Magma ascent rates from amphibole breakdown: an experimental study applied to the 1980–1986 Mount St. Helens eruptions. *Journal of Geophysical Research: Solid Earth*, 98(B11), pp. 19667-19685, doi: 10.1029/93JB01613

Saar, M.O. and Manga, M., 1999. Permeability-porosity relationship in vesicular basalts. *Geophysical Research Letters*, 26(1), pp. 111-114, doi: 10.1029/1998GL900256

Sahagian, D.L. and Proussevitch, A.A., 1998. 3D particle size distributions from 2D observations: stereology for natural applications. *Journal of Volcanology and Geothermal Research*, 84(3-4), pp. 173-196, doi: 10.1016/S0377-0273(98)00043-2

Sano, K. and Toramaru, A., 2017. Cooling and crystallization of rhyolite–obsidian lava: Insights from micron-scale projections on plagioclase microlites. *Journal of Volcanology and Geothermal Research*, 341, pp. 158-171, doi: 10.1016/j.jvolgeores.2017.05.012

Sauter, E.J., Muyakshin, S.I., Charlou, J.L., Schlüter, M., Boetius, A., Jerosch, K., Damm, E., Foucher, J.P. and Klages, M., 2006. Methane discharge from a deep-sea submarine mud volcano into the upper water column by gas hydrate-coated methane bubbles. *Earth and Planetary Science Letters*, 243(3-4), pp. 354-365, doi: 10.1016/j.epsl.2006.01.041

Scaillet, B., Clémente, B., Evans, B.W. and Pichavant, M., 1998. Redox control of sulfur degassing in silicic magmas. *Journal of Geophysical Research: Solid Earth*, 103(B10), pp. 23937-23949, doi: 10.1029/98JB02301

Schindelin, J., Arganda-Carreras, I., Frise, E., Kaynig, V., Longair, M., Pietzsch, T., Preibisch, S., Rueden, C., Saalfeld, S., Schmid, B. and Tinevez, J. Y., 2012. Fiji: an open-source platform for biological-image analysis. *Nature methods*, 9(7), pp. 676-682, doi: 10.1038/nmeth.2019

Schipper, C.I., White, J.D., Houghton, B.F., Shimizu, N. and Stewart, R.B., 2010. Explosive submarine eruptions driven by volatile-coupled degassing at Lōihi Seamount, Hawaii. *Earth and Planetary Science Letters*, 295(3), pp. 497-510, doi: 10.1016/j.epsl.2010.04.031

Schipper, C.I., Castro, J.M., Tuffen, H., James, M.R., and How, P., 2013. Shallow vent architecture during hybrid explosive–effusive activity at Cordón Caulle (Chile, 2011–12): evidence from direct observations and pyroclast textures. *Journal of Volcanology and Geothermal Research*, 262, pp. 25-37, doi: 10.1016/j.jvolgeores.2013.06.005

Schipper, C.I., Castro, J.M., Tuffen, H., Wadsworth, F.B., Chappell, D., Pantoja, A.E., Simpson, M.P. and Le Ru, E.C., 2015. Cristobalite in the 2011–2012 Cordón Caulle eruption (Chile). *Bulletin of Volcanology*, 77(5):34, doi: 10.1007/s00445-015-0925-z

Schipper, C.I., Mandon, C., Maksimenko, A., Castro, J.M., Conway, C.E., Hauer, P., Kirilova, M. and Kilgour, G., 2017. Vapor-phase cristobalite as a durable indicator of magmatic pore structure and halogen degassing: an example from White Island volcano (New Zealand). *Bulletin of Volcanology*, 79(10):74, doi: 10.1007/s00445-017-1157-1

Schmidt, M.W. and Poli, S., 1998. Experimentally based water budgets for dehydrating slabs and consequences for arc magma generation. *Earth and Planetary Science Letters*, 163(1-4), pp. 361-379, doi: 10.1016/S0012-821X(98)00142-3

Seligman, A.N., Bindeman, I.N., Watkins, J.M. and Ross, A.M., 2016. Water in volcanic glass: From volcanic degassing to secondary hydration. *Geochimica et Cosmochimica Acta*, 191, pp. 216-238, doi: 10.1016/j.gca.2016.07.010

Sharqawy, M.H., Lienhard, J.H. and Zubair, S.M., 2010. Thermophysical properties of seawater: a review of existing correlations and data. *Desalination and water Treatment*, 16(1-3), pp. 354-380, doi: 10.5004/dwt.2010.1079

Shaw, A.M., Hauri, E.H., Fischer, T.P., Hilton, D.R. and Kelley, K.A., 2008. Hydrogen isotopes in Mariana arc melt inclusions: Implications for subduction dehydration and the deep-Earth water cycle. *Earth and Planetary Science Letters*, 275(1-2), pp. 138-145, doi: 10.1016/j.epsl.2008.08.015

Shea, T., Houghton, B.F., Gurioli, L., Cashman, K. V., Hammer, J.E. and Hobden, B.J., 2010. Textural studies of vesicles in volcanic rocks: An integrated methodology. *Journal of Volcanology and Geothermal Research*, 190, pp. 271–289, doi: 10.1016/j.jvolgeores.2009.12.003.

Shea, T., Hellebrand, E., Gurioli, L. and Tuffen, H., 2014. Conduit-to localized-scale degassing during Plinian Eruptions: Insights from major element and volatile (Cl and H_2O) analyses within Vesuvius AD 79 pumice. *Journal of Petrology*, 190(3), pp. 315-344, doi: 10.1093/petrology/egt069

Shea, T., 2017. Bubble nucleation in magmas: A dominantly heterogeneous process? *Journal of Volcanology and Geothermal Research*, 343, pp. 155-170, doi: 10.1016/j.jvolgeores.2017.06.025

Shea, T., Leonhardi, T., Giachetti, T., Lindoo, A., Larsen, J., Sinton, J. and Parsons, E., 2017. Dynamics of an unusual cone-building trachyte eruption at Pu ʻu Wa ʻawa ʻa, Hualālai volcano, Hawai ʻi. *Bulletin of Volcanology*, 79(4):26, doi: 10.1093/petrology/egt069

Smith, M.S. and Shepherd, J.B., 1993. Preliminary investigations of the tsunami hazard of Kick'em Jenny submarine volcano. *Natural hazards*, 7(3), pp. 257-277, doi: 10.1007/BF00662650

Smith, I.E. and Price, R.C., 2006. The Tonga–Kermadec arc and Havre–Lau back-arc system: their role in the development of tectonic and magmatic models for the western Pacific. *Journal of volcanology and geothermal research*, 156(3-4), pp. 315-331, doi: 10.1016/j.jvolgeores.2006.03.006

Sohn, R.A., Willis, C., Humphris, S., Shank, T.M., Singh, H., Edmonds, H.N., Kunz, C., Hedman, U., Helmke, E., Jakuba, M. and Liljebladh, B., 2008. Explosive volcanism on the ultraslow-spreading Gakkel ridge, Arctic Ocean. *Nature*, 453(7199), pp. 1236-1238, doi: 10.1038/nature07075

Song, W., Lavallée, Y., Hess, K.U., Kueppers, U., Cimarelli, C. and Dingwell, D.B., 2016. Volcanic ash melting under conditions relevant to ash turbine interactions. *Nature communications*, 7(10795), pp. 1-10, doi: 10.1038/ncomms10795

Soule, S.A., Nakata, D.S., Fornari, D.J., Fundis, A.T., Perfit, M.R. and Kurz, M.D., 2012. CO_2 variability in mid-ocean ridge basalts from syn-emplacement degassing: constraints on eruption dynamics. *Earth and Planetary Science Letters*, 327, pp. 39-49, doi: 10.1016/j.epsl.2012.01.034

Sparks, R.S.J., 1978. The dynamics of bubble formation and growth in magmas: a review and analysis. *Journal of Volcanology and Geothermal Research*, 3(1-2), pp. 1-37, doi: 10.1016/0377-0273(78)90002-1

Stern, R.J., 2002. Subduction zones. *Reviews of geophysics*, 40(4), pp. 3(1-13), doi: 10.1029/2001RG000108

Stevenson, D.J., 1982. Volcanism and igneous processes in small icy satellites. *Nature*, 298(5870), pp. 142-144, doi: 10.1038/298142a0

Stolper, E., 1982. The speciation of water in silicate melts. *Geochimica et Cosmochimica Acta*, 46(12), pp. 2609-2620, doi: 10.1016/0016-7037(82)90381-7

Stommel, H., 1948. The westward intensification of wind-driven ocean currents. *Eos, Transactions American Geophysical Union*, 29(2), pp. 202-206, doi: 10.1029/TR029i002p00202

Tan, K.M., Liddy, T., Anvar, A. and Lu, T.F., 2008. The advancement of an autonomous underwater vehicle (AUV) technology. *In Industrial Electronics and Applications, 2008. ICIEA 2008. 3rd IEEE Conference, IEEE*, pp. 336-341, doi: 10.1109/ICIEA.2008.4582535

Tani, K., Ishizuka, O., Nichols, A.R., Hirahara, Y., Carey, R., McIntosh, I.M., Masaki, Y., Kondo, R. and Miyairi, Y., 2013. December. Discovery of an active shallow submarine silicic volcano in the northern Izu-Bonin Arc: volcanic structure and potential hazards of Oomurodashi Volcano. *In AGU Fall Meeting Abstracts*.

Thorarinsson, S., Einarsson, T., Sigvaldason, G. and Elisson, G., 1964. The submarine eruption off the Vestmann Islands 1963–64. *Bulletin Volcanologique*, 27(1), pp. 435-445, doi: 10.1007/BF02597544

Toramaru, A., 1995. Numerical study of nucleation and growth of bubbles in viscous magmas. *Journal of Geophysical Research: Solid Earth*, 100(B2), pp. 1913-1931, doi: 10.1029/94JB02775

Toramaru, A., 2006. BND (bubble number density) decompression rate meter for explosive volcanic eruptions. *Journal of Volcanology and Geothermal Research*, 154(3-4), pp. 303-316, doi: 10.1016/j.jvolgeores.2006.03.027

Toramaru, A., Noguchi, S., Oyoshihara, S. and Tsune, A., 2008. MND (microlite number density) water exsolution rate meter. *Journal of Volcanology and Geothermal Research*, 175(1-2), pp. 156-167, doi: 10.1016/j.jvolgeores.2008.03.035

Toramaru, A., 2014. On the second nucleation of bubbles in magmas under sudden decompression. *Earth and Planetary Science Letters*, 404, pp. 190-199, doi: 10.1016/j.epsl.2014.07.035

Tuffen, H., Owen, J. and Denton, J., 2010. Magma degassing during subglacial eruptions and its use to reconstruct palaeo-ice thicknesses. *Earth-Science Reviews*, 99(1-2), pp. 1-18, doi: 10.1016/j.earscirev.2010.01.001

Tuffen, H., James, M.R., Castro, J.M. and Schipper, C.I., 2013. Exceptional mobility of an advancing rhyolitic obsidian flow at Cordón Caulle volcano in Chile. *Nature communications*, 4(2709), pp. 1-7, doi: 10.1038/ncomms3709

van Keken, P.E., Hacker, B.R., Syracuse, E.M. and Abers, G.A., 2011. Subduction factory: 4. Depth-dependent flux of H_2O from subducting slabs worldwide. *Journal of Geophysical Research: Solid Earth*, 116(B1):401, doi: 10.1029/2010JB007922

van Otterloo, J., Cas, R.A. and Scutter, CR., 2015. The fracture behaviour of volcanic glass and relevance to quench fragmentation during formation of hyaloclastite and phreatomagmatism. *Earth-Science Reviews*, 151, pp. 79-116, doi: 10.1016/j.earscirev.2015.10.003

Vaughan, R.G., Abrams, M.J., Hook, S.J. and Pieri, D.C., 2007. Satellite observations of new volcanic island in Tonga. *Eos, Transactions American Geophysical Union*, 88(4), pp. 37-41, doi:

Vaughan, R.G. and Webley, P.W., 2010. Satellite observations of a surtseyan eruption: Hunga Ha'apai, Tonga. *Journal of Volcanology and Geothermal Research*, 198(1-2), pp. 177-186, doi: 10.1029/2007EO040002

von Aulock, F.W., Kennedy, B.M., Schipper, C.I., Castro, J.M., Martin, D.E., Oze, C., Watkins, J.M., Wallace, P.J., Puskar, L., Bégué, F. and Nichols, A.R., 2014. Advances in Fourier transform infrared spectroscopy of natural glasses: From sample preparation to data analysis. *Lithos*, 206, pp. 52-64, doi: 10.1016/j.lithos.2014.07.017

von Lichtan, I.J., White, J.D.L., Manville, V. and Ohneiser, C., 2016. Giant rafted pumice blocks from the most recent eruption of Taupo volcano, New Zealand: Insights from palaeomagnetic and textural data. *Journal of Volcanology and Geothermal Research*, 318, pp. 73-88, doi: 10.1016/j.jvolgeores.2016.04.003

Vougioukalakis, G., Mitropoulos, D., Perissoratis, C., Andrinopoulos, A. and Fytikas, M., 1994. The submarine volcanic centre of Kolumbo, Santorini, Greece. *Bull. Geol. Soc. Greece*, 30(3), pp. 351-360.

Wallace, P.J., Dufek, J., Anderson, A.T. and Zhang, Y., 2003. Cooling rates of Plinian-fall and pyroclastic-flow deposits in the Bishop Tuff: inferences from water speciation in quartz-hosted glass inclusions. *Bulletin of Volcanology*, 65(2-3), pp. 105-123, doi: 10.1007/s00445-002-0247-9

Wallace, P.J., 2005. Volatiles in subduction zone magmas: concentrations and fluxes based on melt inclusion and volcanic gas data. *Journal of Volcanology and Geothermal Research*, 140(1-3), pp. 217-240, doi: 10.1016/j.jvolgeores.2004.07.023

Watkins, J.M., Manga, M. and DePaolo, D.J., 2012. Bubble geobarometry: A record of pressure changes, degassing, and regassing at Mono Craters, California. *Geology*, 40(8), pp. 699-702, doi: 10.1130/G33027.1

Watkins, J.M., Gardner, J.E. and Befus, K.S., 2017. Nonequilibrium degassing, regassing, and vapor fluxing in magmatic feeder systems. *Geology*, 45(2), pp. 183-186, doi: doi.org/10.1130/G38501.1

Webster, J.D., 1997. Chloride solubility in felsic melts and the role of chloride in magmatic degassing. *Journal of petrology*, 38(12), pp. 1793-1807, doi: 10.1093/petroj/38.12.1793

Webster, J.D., Vetere, F., Botcharnikov, R.E., Goldoff, B., McBirney, A. and Doherty, A.L., 2015. Experimental and modeled chlorine solubilities in aluminosilicate melts at 1 to 7000 bars and 700 to 1250 C: Applications to magmas of Augustine Volcano, Alaska. *American Mineralogist*, 100(2-3), pp. 522-535, doi: 10.2138/am-2015-5014

Webster, J.D., Goldoff, B.A., Flesch, R.N., Nadeau, P.A. and Silbert, Z.W., 2017. Hydroxyl, Cl, and F partitioning between high-silica rhyolitic melts-apatite-fluid (s) at 50–200 MPa and 700–1000 C. *American Mineralogist*, 102(1), pp. 61-74, doi: 10.2138/am-2017-5746

Wech, A., Tepp, G., Lyons, J. and Haney, M., 2018. Using earthquakes, T waves, and infrasound to investigate the eruption of Bogoslof volcano, Alaska. *Geophysical Research Letters*, 45(14), pp. 6918-6925, doi: doi.org/10.1029/2018GL078457

Wessel, P., Sandwell, D.T. and Kim, S.S., 2010. The global seamount census. *Oceanography*, 23(1), pp. 24-33.

White, J.D., Manville, V., Wilson, C.J.N., Houghton, B.F., Riggs, N.R. and Ort, M., 2001. Settling and deposition of AD 181 Taupo pumice in lacustrine and associated environments. Volcaniclastic Sedimentation in Lacustrine Settings; White, JDL, Riggs, NR, Eds, pp. 141-150, doi: 10.1002/9781444304251.ch7

White, J.D., Schipper, C.I. and Kano, K., 2015. Submarine explosive eruptions. *In The Encyclopedia of Volcanoes (Second Edition)*, pp. 553-569.

Whitham, A.G. and Sparks, R.S.J., 1986. Pumice. *Bulletin of Volcanology*, *48*(4), pp. 209-223, doi: 10.1007/BF01087675

Wilson, L. and Head, J.W., 2002. Heat transfer and melting in subglacial basaltic volcanic eruptions: implications for volcanic deposit morphology and meltwater volumes. *Geological Society, London, Special Publications*, 202(1), pp. 5-26, doi: 10.1144/GSL.SP.2002.202.01.02

Wohletz, K.H., 1983. Mechanisms of hydrovolcanic pyroclast formation: grain-size, scanning electron microscopy, and experimental studies. *Journal of Volcanology and Geothermal Research*, 17(1-4), pp. 31-63, doi: 10.1016/0377-0273(83)90061-6

Wright, I.C. and Gamble, J.A., 1999. Southern Kermadec submarine caldera arc volcanoes (SW Pacific): caldera formation by effusive and pyroclastic eruption. *Marine Geology*, 161(2), pp. 207-227, doi: 10.1016/S0025-3227(99)00040-7

Wright, I.C., Gamble, J.A. and Shane, P.A., 2003. Submarine silicic volcanism of the Healy caldera, southern Kermadec arc (SW Pacific): I–volcanology and eruption mechanisms. *Bulletin of Volcanology*, 65(1), pp. 15-29, doi: 10.1007/s00445-002-0234-1

Wright, I.C., Worthington, T.J. and Gamble, J.A., 2006(a). New multibeam mapping and geochemistry of the 30–35 S sector, and overview, of southern Kermadec arc volcanism. *Journal of Volcanology and Geothermal Research*, 149(3), pp. 263-296, doi: 10.1016/j.jvolgeores.2005.03.021

Wright, H., Roberts, J. J. and Cashman, K. V., 2006(b). Permeability of anisotropic tube pumice: Model calculations and measurements. *Geophysical research letters*, 33(17):316, doi: 10.1029/2006GL027224

Wysoczanski, R. and Tani, K., 2006. Spectroscopic FTIR imaging of water species in silicic volcanic glasses and melt inclusions: an example from the Izu-Bonin arc. *Journal of Volcanology and Geothermal Research*, 156(3), pp. 302-314, doi: 10.1016/j.jvolgeores.2006.03.024

Wysoczanski, R.J., Wright, I.C., Gamble, J.A., Hauri, E.H., Luhr, J.F., Eggins, S.M. and Handler, M.R., 2006. Volatile contents of Kermadec Arc–Havre Trough pillow glasses: Fingerprinting slab-derived aqueous fluids in the mantle sources of arc and back-arc lavas. *Journal of Volcanology and Geothermal Research*, 152(1), pp. 51-73, doi: 10.1016/j.jvolgeores.2005.04.021

Xu, Z. and Zhang, Y., 2002. Quench rates in air, water, and liquid nitrogen, and inference of temperature in volcanic eruption columns. *Earth and Planetary Science Letters*, 200(3-4), pp. 315-330, doi: 10.1016/S0012-821X(02)00656-8

Yuasa, M. and Kano, K., 2003. Submarine Silicic Calderas on the Northern Shichito-Iwojima Ridge, Izu-Ogasawara (Bonin) Arc, Western Pacific. *Explosive subaqueous volcanism*, pp. 231-243, doi: 10.1029/140GM15

Zhang, Y., Stolper, E.M. and Wasserburg, G.J., 1991. Diffusion of water in rhyolitic glasses. *Geochimica et Cosmochimica Acta*, 55(2), pp. 441-456, doi: 10.1016/0016-7037(91)90003-N

Zhang, Y., Belcher, R., Ihinger, P., Wang, L., Xu, Z. and Newman, S., 1997. New calibration of infrared measurement of dissolved water in rhyolitic glasses. Geo*chimica et Cosmochimica Acta*, 61(15), pp. 3089-3100, doi: 10.1016/S0016-7037(97)00151-8

Zhang, Y., 1999. H_2O in rhyolitic glasses and melts: measurement, speciation, solubility, and diffusion. *Reviews of Geophysics*, 37(4), pp. 493-516, doi: 10.1029/1999RG900012

Zhang, Y., Xu, Z., Zhu, M. and Wang, H., 2007. Silicate melt properties and volcanic eruptions. *Reviews of Geophysics*, 45(4):004, doi: 10.1029/2006RG000216

Zhang, Y. and Ni, H., 2010. Diffusion of H, C, and O components in silicate melts. *Reviews in Mineralogy and Geochemistry*, 72(1), pp.171-225, doi: 10.2138/rmg.2010.72.5

Zhang, L., Guo, X., Wang, Q., Ding, J. and Ni, H., 2017. Diffusion of hydrous species in model basaltic melt. *Geochimica et Cosmochimica Acta*, 215, pp. 377-386, doi: 10.1016/j.gca.2017.07.019

“An understanding of the natural world and what's in it is a source of not only a great curiosity, but great fulfillment”

— *Sir David Attenborough*

“Bubbles, bubbles, bubbles, bubbles. My bubbles.”

— *Bubbles,*
Finding Nemo